Contact region fidelity, sensitivity, and control in roll-based soft lithography
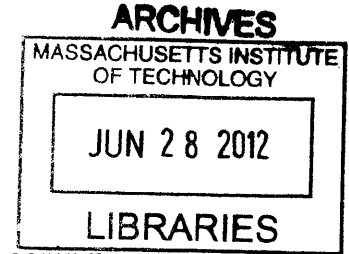
by

Joseph Edward Petrzelka

B.S., Iowa State University (2007)
M.S., Iowa State University (2009)

Submitted to the Department of Mechanical Engineering
in partial fulfillment of the requirements for the degree of
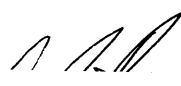
Doctor of Philosophy

at the

MASSACHUSETTS INSTITUTE OF TECHNOLOGY

June 2012

© Massachusetts Institute of Technology 2012. All rights reserved.

Author ....
Department of Mechanical Engineering
May 11, 2012

Certified by...
David E. Hardt
Ralph E. and Eloise F. Cross Professor of Mechanical Engineering
Thesis Supervisor

Accepted by ....
David E. Hardt
Chairman, Department Committee for Graduate Students

Contact region fidelity, sensitivity, and control in roll-based soft lithography

by

Joseph Edward Petrzelka

Submitted to the Department of Mechanical Engineering
on May 11, 2012, in partial fulfillment of the
requirements for the degree of
Doctor of Philosophy

Abstract

Soft lithography is a printing process that uses small features on an elastomeric stamp to transfer micron and sub-micron patterns to a substrate. Translating this lab scale process to a roll-based manufacturing platform allows precise control of the stamp contact region and the potential for large area, high rate surface patterning. In this manner, emerging devices can be produced economically, including flexible displays, distributed sensor networks, transparent conductors, and bio-inspired surfaces.

Achieving and maintaining collapse-free contact of the soft stamp features is a necessary condition for printing. In the first part of the thesis, stamp behavior is examined at two length scales. First, microfeature collapse is examined across a range of dimensionless aspect ratios and pattern ratios to determine the collapse mode and the feature stiffness. Second, behavior of roll-mounted stamps is investigated on the macroscopic scale.

The results of these analyses, simulations, and experiments show that contact is prohibitively sensitive as the feature scale shrinks to single microns or below. In the second part of the thesis, methods are developed to reduce the contact sensitivity. A compliant stamp architecture is introduced to tune the mechanical response of the stamp. Next, a new process for manufacturing cylindrical stamps is developed that removes limitations of planar stamp templates.

The third part of the thesis addresses process control. A parallel kinematic stage is designed to manipulate the height and pitch of a roll over a substrate with submicron precision. A hybrid state-space / classical feedback control approach is used to achieve high bandwidth servo control in the presence of coupling and unmodeled dynamics. Using optical instrumentation, the stamp contact pattern is monitored and can be controlled using camera images as a control variable. Ultimately, a practical method of impedance control is implemented that demonstrates excellent disturbance rejection.

The results of this thesis provide models for stamp behavior at the local microscale and the roll-based macroscale. These results illustrate the high sensitivity of contact to displacement disturbances in roll-based lithography, but also provide valuable design insight towards designing stamps and processing machinery that are robust to

these inherent disturbances.

Thesis Supervisor: David E. Hardt
Title: Ralph E. and Eloise F. Cross Professor of Mechanical Engineering

Acknowledgements

This thesis, or even studying at MIT, would never have been possible without the support of innumerable individuals. My trajectory has been altered in some way by almost every faculty member, project team, or support staff that I've encountered. I am sincerely grateful to everyone who has taken the time to teach, critique, mentor, or just listen. Several people have been overwhelmingly instrumental in my success, and warrant individual mention here:

Prof. David Hardt is arguably the best advisor I've ever encountered. His mentoring, guidance, latitude in research direction, and positive attitude have made my time at MIT a distinct pleasure. The committee members - Prof. Martin Culpepper and Dr. Brian Anthony - provided excellent insight and advice.

My transition to the mechanical engineering program at MIT would not have been possible without the support my peers. The LMP student community, especially Matt Dirckx, Melinda Hale, Bob Panas, and Maria Telleria. Surviving qualifiers and producing a thesis would not have been possible without countless consults, cubicle conversations, and lunches. My sanity would not be intact without Wil Selby and Ashley Browning, who reminded me to live life outside of 77 Massachusetts Avenue.

Finally, though perhaps most importantly, my wife, Jenna, has been incredibly supportive both during my MS and Iowa State and my PhD at MIT. Her belief in my goals and aspirations has propelled me well beyond what I might have ever achieved on my own.

Contents

11

List of Figures

15

List of Tables

Nomenclature

α Image foreshortening correction factor, page 293

α_s Timoshenko beam theory shear factor, page 180

β Image perspective correction factor, page 293

β Volume fraction of solids in photoresist solution, page 214

ϵ Error vector used to assess roll positioning stage repeatability, page 268

ϵ Material infinitesimal deformation gradient tensor, page 57

σ Material stress tensor, page 58

b Fluid body force, page 206

E Material strain tensor, page 57

F Material deformation gradient tensor, page 56

$G(s)$ Frequency domain transfer function matrix, page 279

H Material displacement gradient tensor, page 56

K State feedback matrix, page 277

u Actuator effort vector in roll positioning stage dynamic equation, page 262

u Material displacement vector, page 56

v Fluid velocity vector, page 206

$\boldsymbol{x}$ Dynamic state vector in roll positioning stage dynamic equation, page 262

$\boldsymbol{y}$ Output vector in roll positioning stage dynamic equation, page 262

$\boldsymbol{u_r}$ Reference roll contact force superimposed on roll during impedance control, page 310

δ Roll displacement towards substrate, page 112

δ^* Local effective roll displacement, page 164

δ_0 Equilibrium roll displacement (neglecting surface energy), page 119

δ_{eq} Equilibrium roll displacement (considering surface energy), page 119

$\delta_{flexure}$ Displacement of a flexural bearing comprised of individual flexure blades, page 250

ϵ Dimensional errors along $\hat{y}$ at the stamp contact interface, page 162

ϵ Surface strain at the root of a flexure blade, page 250

γ_s Material surface energy, page 67

$\hat{\delta}$ Nominal or mean roll displacement, page 164

κ Material bulk modulus, page 58

κ_0 Initial material bulk modulus (finite deformation elasticity), page 59

λ Material stretch, page 58

λ Wavelength of light, page 219

$\lambda_{epsilon}$ Roll displacement error wavelength, page 165

λ_f Fluid asperity wavelength in a centrifuge, page 211

λ_m Maximum locking stretch, Arruda-Boyce model, page 59

$\mathcal{C}_1$ Criterion for applicability of elastic layer model, page 127

$\mathcal{C}_2$ Criterion for applicability of elastic foundation model, page 129

$\mathcal{C}_3$ Criterion for applicability of elastic foundation model in backing layer stamps, page 183

$\mathcal{DC}(s)$ Decoupling criterion, page 279

μ Fluid dynamic viscosity, page 206

μ Material shear modulus, page 58

μ_0 Initial material shear modulus (finite deformation elasticity), page 59

ν Fluid kinematic viscosity, page 206

ν Material Poisson ratio, page 61

ω Centrifuge velocity in the $\hat{\psi}$ direction, page 206

ρ Beam radius of curvature, page 172

ρ Fluid density, page 206

ρ_m Material radius of curvature, page 173

σ Fluid surface tension, page 199

σ_∞ Stamp microfeature far-field pressure, page 68

σ_Y Yield stress, page 250

τ Net actuator torque on roll in the $\hat{\theta}$ direction, page 260

τ_f Fluid asperity decay time constant in a centrifuge, page 211

Θ Gaussian beam waist divergence angle, page 219

θ Incident angle of a light ray relative to a surface normal vector, page 289

θ Roll pitch as a degree of freedom in positioning stage, about $\hat{x}$, page 246

A Stamp microfeature aspect ratio, dimensionless, page 68

a Stamp microfeature spacing, page 67

b Thickness of flexure blade, page 249

b_c Buckling boundary condition, page 74

b_i Damping of each flexural bearing, $i = 1, 2$, page 261

$C_i(s)$ Frequency domain compensators in a $\mathbb{R}^\nabla$ system, $i = 1 \ldots n$, page 278

C_{10} Neo-Hookean material parameter, page 59

Cf Conformability, dimensionless ratio of surface energy and strain energy, page 69

D Collimated Gaussian beam diameter, page 220

D_1 Neo-Hookean material parameter, page 59

E Material elastic modulus, page 61

E^* Plane strain elastic modulus, page 70

E_0 Initial material elastic modulus (finite deformation elasticity), page 61

E_ϵ Roll displacement error in the spatial frequency domain, page 165

f Contact force between roll and substrate per unit length of roll, page 112

f Focal length, page 220

f Net actuator force on roll in the $\hat{y}$ direction, page 260

f_i Force of an actuator, $i = 1, 2$, page 250

g Gravitational field magnitude, page 206

GF Strain gage 'gage factor', page 255

h Fluid film height in a centrifuge drum, page 206

h Height of flexure blade, page 249

h Stamp microfeature height, page 67

I Beam moment of inertia, page 74

I Camera image in the form of an array of discrete pixels, page 299

I Gaussian beam irradiance, page 218

I^* Aggregate vector of image array I, page 300

I_0 Gaussian beam irradiance at the beam axis, page 218

I_1 First invariant of material deformation, page 59

J Material volume ratio, page 57

J Sprung rotational inertia of shaft and flexural bearings, page 261

K Stamp microfeature stiffness, dimensionless, page 69

k Stamp microfeature sheet stiffness, page 69

k^* Equivalent microfeature stiffness in stamps with backing features, page 181

k_b Sheet stiffness of stamp backing features, page 175

K_I Stamp microfeature stiffness (limit of small aspect ratio), page 71

k_i Stiffness of each flexural bearing, $i = 1, 2$, page 261

k_p Sheet stiffness of stamp printing features, page 175

k_{beam} Stiffness of flexure blade from beam theory, page 249

$k_{flexure}$ Stiffness of a flexural bearing comprised of individual flexure blades, page 250

K_{II} Stamp microfeature stiffness (limit of large aspect ratio), page 72

K_{pi} Position sensor gain, $i = 1, 2$, page 255

l Contact length between roll and substrate along the $\hat{x}$ direction, page 112

l Length along roll axis $\hat{z}$ between flexural bearing pivots, page 259

l Length of flexure blade, page 249

l_0 Equilibrium roll contact length, page 119

l_z Centrifuge drum length, page 206

l_z Stamp length along roll axis $\hat{z}$, page 112

m Sprung mass of shaft and air bushings, page 261

n Optical index of refraction, page 289

n Plastic yield safety factor, page 250

P Gaussian beam power, page 219

P Stamp microfeature pattern ratio, dimensionless, page 68

p Fluid hydrostatic pressure field, page 206

p Hydrostatic pressure field, page 60

$p(x)$ Contact pressure distribution between roll and substrate, page 112

p_0 Center (maximum) contact pressure between roll and substrate, page 112

p_c Stamp microfeature collapse pressure, page 109

q Beam loading function, page 177

r Centrifuge drum radius, page 206

r Roll radius, page 112

r^* Equivalent roll radius in a two-roll system, page 115

S Stamp microfeature far-field pressure, dimensionless, page 69

S_{buckle} Stamp microfeature buckling pressure, page 76

S_c Stamp microfeature collapse pressure, page 72

t Stamp thickness, page 67

U Strain energy, page 59

u Fluid velocity vector component in the $\hat{x}$ direction, page 207

u Material displacement component along $\hat{x}$, page 56

v Fluid velocity vector component in the $\hat{y}$ direction, page 207

v Material displacement component along $\hat{y}$, page 56

v_∞ Stamp microfeature far-field displacement, page 68

V_b Strain gage bridge driving voltage, page 255

V_{vi} Velocity sensor gain, $i = 1, 2$, page 256

w Beam neutral axis displacement, page 177

w Gaussian beam diameter, page 218

w Stamp microfeature width, page 67

w_0 Gaussian beam waist diameter, page 218

W_{ad} Interface work of adhesion, page 67

W_{ad}^* Effective interface work of adhesion, page 75

X Stamp microfeature far-field displacement, dimensionless, page 69

y Roll height as a degree of freedom in positioning stage, along $\hat{y}$, page 246

y_i Position of roll endpoints in a simply supported configuration, $i = 1, 2$, page 246

z_R Gaussian beam Rayleigh range, page 219

Part I

Introduction

Chapter 1

Introduction

Contact lithography holds the potential to pattern large areas of micro- and nano-scale features at high rates by using mechanical contact to replicate patterns. In recent years, interest has risen in adapting *contact lithography* processes to roll based platforms to enable large area printing of micro- and nano-scale features, including microcontact printing [87] and nanoimprint lithography [1]. Successful implementation of contact lithography in roll based platforms would enable scalable manufacturing of flexible engineered metasurfaces, electronics, displays, and sensor systems.

This thesis examines microcontact printing from the perspective of the elastomeric stamp contact interface. The three central parts of this thesis examine (*i*) fundamental contact phenomena, (*ii*) stamp design and manufacture, and (*iii*) process control schemes. Ultimately, the thesis contributes a holistic understanding of stamp deformation behavior, a new stamp architecture and casting technique for robust printing, and a machine model for precision roll-based manufacturing.

1.1   Thesis Contributions

This thesis provides contributions to both (*i*) the theoretical understanding of elastomeric stamp behavior and (*ii*) ways that this behavior can be used to create robust printing through new machine and process designs.

An experimental approach is developed to observe the load, displacement, and

collapse mode of microscale stamp features. The stiffness of individual stamp features is established as a function of feature geometry. Using this stiffness result, a unified theory is developed that maps feature collapse modes as a function of dimensionless geometrical, material, and load parameters. The experimental method developed is used to validate these models of stiffness and collapse mode. This result predicts the acceptable pressure or displacement imposed on any particular microfeature, which in turn guides robust stamp design and establishes an upper bound on feasible stamp contact stresses.

The contact pressure evolution in roll mounted stamps is derived by augmenting classical contact mechanics solutions in the limit of either very small or very compliant stamp features. The models developed are validated using numeric simulation and experimental studies on a custom designed lab scale rolling stage. The results of these models illustrate that the stamp contact behavior has a significant dependence on the microscale stamp features, even when the body of the stamp is many times thicker than the characteristic feature dimensions. Combining the prior bound on stamp contact stresses with these models provides feasible roll displacements or contact errors.

A feasible process window for roll based processing is developed using the roll based contact models. Design opportunities for a large (robust) process window are discussed and compared to reports in the literature. A new stamp architecture is developed to dramatically increase this process window beyond the ability of conventional stamp designs. Analytical, numerical, and experimental approaches prove that this new architecture greatly increases the permissible roll displacement before stamp feature collapse. Additionally, a new centrifugal casting process is developed for creating cylindrical stamps for roll based processing with high dimensional uniformity and continuous peripheral patterns.

A machine design is presented that provides precise submicron resolution positioning between a processing roll and substrate. Excellent linearity is achieved by supporting the roll in a parallel kinematic configuration with flexural bearings. A new controller architecture and synthesis strategy are developed for servo control of

the resulting complex dynamical system. Two process control strategies are demonstrated for maintaining a uniform area contact region during printing. The results of this machine design and control provide guidelines for manufacturing scale implementations of roll based contact lithography.

1.2 Lithographic Techniques

1.2.1 Conventional Lithography

Surface patterning, or lithography, has been an active area of development since the advent of the printing press in the 1400's. During the industrial revolution of the 1800's, roll-to-roll printing presses replaced plate presses [99], resulting in unprecedented rates of production for patterned materials.

Modern roll-to-roll printing presses are capable of printing flexible substrates at rates of meters per second with sub-millimeter resolution and registration between multiple colors. As in the beginning, printing at these rates is still accomplished using mechanical contact with the printing substrate, but has evolved into modern technologies like gravure, offset, and flexographic printing.

Each of these three processes - gravure, offset, and flexography - uses an impression, or backup, roller to engage a flexible substrate against a printing roller. Gravure printing uses a rigid cylinder with small engraved pockets to selectively transfer ink (housed in each pocket) to the substrate. Offset printing patterns ink on a metal roller, transfers the ink to a rubber roller, and finally to the printing substrate. Finally, flexography uses a patterned print roller with positive relief to transfer ink between an inking roll and the substrate. Since the 1990's, flexography has overtaken the gravure and offset printing processes as the process of choice when it comes to throughput and quality of printing [99].

Development of flexography may have begun as early as 1860, when rubber plates were used to transfer aniline dyes diluted with alcohol. The term *flexography* was coined in the 1950's, but the process didn't reach its current state until 1972 when

more advanced polymer printing plates were developed to replace molded rubber stamps.

Flexographic plates consist of a soft cushion layer, a polyester layer for transverse stiffness and dimensional stability, and a UV sensitive polymer layer, with a total thickness of about 3 mm. By selectivley exposing the UV sensitive polymer layer and developing with a solvent, these stamps can achieve feature resolutions as fine as 70 μm [99].

Modern flexography can be implemented on rolls up to 2 m in diameter on web widths of 3 m. Top web speeds can range from 5 to 12 m/s. Using a central impression roller (with multiple print rolls in a planetary arrangment) printing layers can be registered within 100 μm total indicated runout (TIR) [99].

1.2.2 Photolithography

Over the last 50 years, *photolithography* has been developed for semiconductor applications. Using selective exposure to light, photosensitive polymer resists can be patterned optically without mechanical contact, allowing unprecedented resolution, accuracy, and alignment.

As of 2010, modern photolithography operates at the 45 nm half-pitch node. The critical transistor gate dimension at this level is 25 nm with an allowable variation of 1.6 nm; overlay registration between layers is 18 nm [61]. There is a coordinated effort in industry (cf. International Technology Roadmap for Semiconductors) to continue reducing these characteristic dimensions per Moore's law [72].

The steady reduction of limits in photolithography has been brought about by parallel improvements in the polymer photoresists, optics, low wavelength light sources, and wafer flatness [61]. The resolutions and accuracies have been shrinking while overall throughput has increased, requiring dramatic innovations and improvements in the *wafer steppers* responsible for aligning photomasks, optics, and wafers during exposure. These wafer steppers are now capable of processing 200 wafers per hour, but at a capital equipment cost of $50 million USD each.

The high cost of capital equipment and photoresist materials results in a corre-

spondingly high cost of photolithographic patterning. A detailed analysis of manu-
facturing expenses shows a total patterning cost of tens of dollars per wafer in a high
volume production environment [61]. With 300 mm diameter wafers (0.07 m^2), this
corresponds to hundreds of dollars per square meter *per layer* of patterning. The
manufacturing cost of finished multilayer semiconductor devices can easily be tens of
thousands of dollars per square meter or more.

While photolithography is expensive, it represents the cutting edge of patterning
capabilities and the gold standard of quality against which emerging technologies
must compete.

1.2.3 Hybrid Lithography

The high cost and optical limits of photolithography have motivated the development
of alternative technologies. Of particular interest are nanoimprint lithography (NIL)
and microcontact printing (μCP), which use mechanical contact between a stamp
and substrate to transfer a pattern.

NIL uses a tool to transfer a three dimensional relief pattern to a polymer, either
through thermal embossing [13] or UV curing of a polymer during contact [34, 88].
To a first order, this process is rate limited by (i) viscous fluid flow, both into feature
relief and decay of a residual layer between the stamp and substrate, and (ii) energy
transfer cycles, either thermal or UV. Despite these rate limits, NIL remains a topic
of much interest because it has no inherent physical resolution limit (cf. diffraction
limit in optical lithography).

μCP transfers a two dimensional pattern from selective contact of a stamp, quite
similar to conventional flexography. The use of a conformable polymer for the stamp
and special monolayer inks allow reliable patterning of features down to about 200
nm. The two dimensional pattern can be subsequently processed by selective etching
or deposition to reveal three dimensional structures. While the ultimate resolution
is limited by use of soft conformable elastomers in stamps, μCP is rate limited by
diffusion of the molecular inks and can be performed at much higher rates than NIL.

These two methods appear to be a reversion to contact based methods that have

dominated economical production of printed matter since the advent of the printing press. In this thesis, these patterning techniques are classified as *contact lithography*: a hybrid class of patterning that aims to achieve resolutions characteristic of optical lithography but by more traditional mechanical means.

Each of these methods has in common the replication of patterns from a tool, which is itself often replicated from a master surface. In this fashion, the process can be quite economical by amortizing the effort and cost associated with creating a high resolution template over perhaps hundreds of printing tools that each pattern thousands of parts. Moreover, these contact based processes are amenable to roll-based manufacturing implementations, where μCP in particular has the possibility of extraordinarily large rate-resolution products.

1.3 Microcontact Printing

μCP was pioneered by Whitesides and colleagues [59]. In the seminal embodiment (Figure 1-1), μCP used a rubber or polydimethylsiloxane (PDMS) stamp. This stamp was inked with alkenethiols and contact with a gold surface, where the alkenethiol formed a self assembling monolayer (SAM) exactly one molecule thick. The SAM protected the gold during a mild ferro-cyanic wet etch, which selectively developed the transferred pattern.
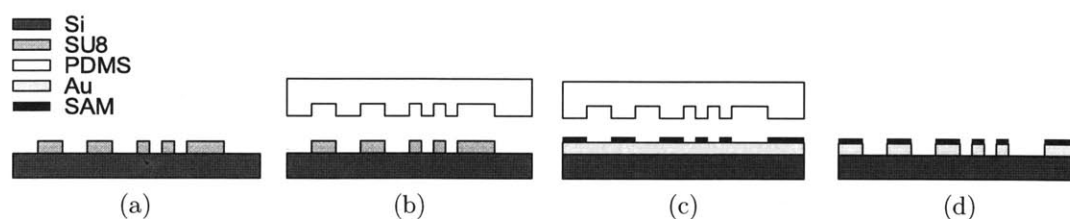
Figure 1-1: Process steps in microcontact printing: (a) a master template is created, typically using photolithography and a durable photoresist like SU8. (b) an elastomeric stamp, typically PDMS, is cast against the master template and parted, leaving a negative of the pattern geometry. (c) A SAM is selectively patterned on a separate substrate using the elastomeric stamp, typically a layer of gold on a silicon wafer. (d) The SAM protects the substrate layer during a wet etch to selectively expose the negative of the original master pattern.

This section examines the details of the ink, stamp, and substrate material systems used for μCP and their evolution since the invention of the process.

1.3.1 Monolayer Inks

SAMs are typically formed of a functionalized molecule that include a ligand group (head), an alkyl chain (tail), and an optional functional group.

μCP uses alkenethiols, a particular type of SAM. Alkenethiols, interchangeable referred to as thiols in this thesis, have an alkane tail formed by saturated C-C bonds and a sulfer head group. For example, the first three alkanes are methane (CH_4), ethane (C_2H_6), and propane(C_3H_8). Alkenethiols in μCP more typically use large molecular number tail groups, such as hexadecane ($C_{16}H_{34}$) or octadecane ($C_{18}H_{38}$).

Alkenethiols have a sulfer head group (e.g. octadecanethiolate $C_{16}H_{33}S$ is quite similar to octadecane, except that one hydrogen atom has been replaced with a sulfer atom). Sulfer has a high affinity for Group 11 metals (i.e. gold, silver, copper), promoting adhesion of the head group to the metal lattice. When a number of alkenethiols are present, they will *self organize* into a protective molecular layer where the head groups are in contact with the metal lattice and the tail groups are arranged normal to the surface (Figure 1-2).
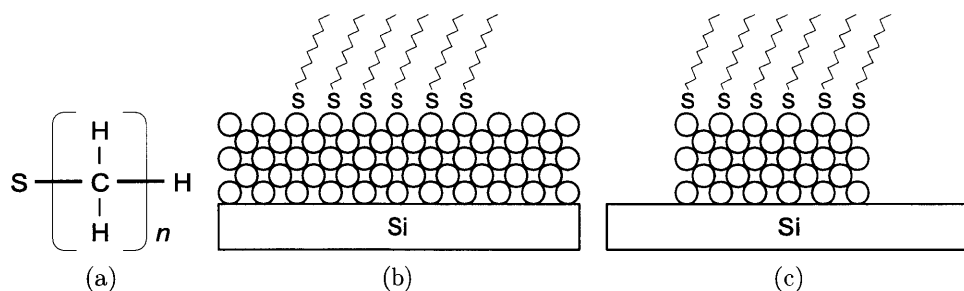
Figure 1-2: Self assembling monolayers as etch resists. (a) Alkenethiols are fully saturated hydrocarbons with a sulfer head; the species length n is typically 10-20 for microcontact printing. (b) The sulfer head has a high affinity for gold (among other materials) and will self create a self assembling monolayer on the face centered cubic lattice structure of gold. (c) This SAM protects the underlying gold during wet etching, acting as a selective etch resist.

In μCP, alkenethiols are introduced to the printing substrate through diffusion processes. Ideally, thiols only diffuse from the PDMS stamp to the substrate precisely where the two make contact. Alternatively, the thiol can diffuse along the substrate surface from the contact region or diffuse through the ambient from stamp recesses.

Thiols diffuse through PDMS obeying conventional mass transport laws, allowing the stamp-thiol system to be modeled using Fick's law [5]. This phenomena means that the PDMS stamp acts as an 'ink pad' to allow a number of stamping replications between inking steps.

This diffusion behavior is one reason that microcontact printing can achieve such high resolutions. In contrast to fluid inks typical of conventional lithographic processes, the molecular thiol ink diffuses to the substrate exactly in the area of contact but does not substantially alter the mechanical contact between the stamp and substrate. Most importantly, there are no effects of fluid dynamics to consider.

For a substantial review of SAMs, their recent history, and application to μCP, the reader is referred to [66].

1.3.2   Stamp Replication

Stamps for μCP are made of polymers formed against a master surface, or template. These master surfaces are almost exclusively a silicon wafer patterned with photoresist in conventional photolithography, or for very small features, electron beam lithography. The patterned surface typically has sufficient mechanical strength to permit forming the stamp directly against the photoresist pattern. Using this strategy of replication, the cost and effort of obtaining a single high resolution master can be amortized over a large number of replicated stamps.

The original report of μCP used both a conventional rubber stamp (for example the type used in flexography) and a PDMS stamp [59]. PDMS has been used almost exclusively thereafter because of its ability to precisely replicate small features and its favorable material properties.

Replication of features down to 200 nm were demonstrated almost immediately [58] and within several years features below 100 nm were reported [7] using com-

mercially available Sylgard 184 PDMS (Dow Corning). The use of this thermoset elastomer allows the thin prepolymer fluid to conform to a patterned surface in a liquid state and be cured to a crosslinked solid with negligible shrinkage or distortion.

Complete contact between the stamp and printing substrate is a necessary condition for selective thiol transfer and the high resolution of μCP. Complete contact can be guaranteed by choosing a stamp material that makes *conformal contact* with printing substrate, where the two surfaces automatically conform over small asperities without application of external pressure. PDMS is a good material for stamps because it achieves conformal contact over reasonable asperities; the ratio of surface energy γ_s (about 20 mJ/m^2) to elastic modulus E_0 (about 2 MPa) is quite large. The material radius of curvature $\rho_m = \gamma_s/E_0$ (as defined by [47]) of PDMS is about 10 nm. At this length scale the surface energy of the stamp is quite significant, creating *conformal contact* over a substrate with surface roughness on the order of ρ_m.

This high surface energy also presents problems. When features are on the order of 100 nm, elastic collapse occurs and the features adhere to one another, destroying any periodic pattern. To counter this, harder stamp materials have been developed. Formulations of hard-PDMS have been developed with elastic moduli around 8 MPa, though significantly more brittle than standard PDMS [89]. A UV-curable hard PDMS formulation was developed by [12], which speeds the curing time and eliminates shrinkage that occurs as a result of cooling from the thermal cure step. In addition to PDMS, block copolymer elastomers with moduli above 10 MPa have also been successfully used for μCP [100]. These block copolymers are thermoplastics rather than thermosets, requiring higher forming temperatures and pressures during stamp formation than PDMS. With any of these higher hardness stamps, additional contact pressure may be required for conformal contact if the radius of curvature ρ_m becomes too large relative to substrate roughness [47].

1.3.3 Material Systems

The invention of μCP did not hinge on the idea of pattern transfer by a stamp: this had in fact been a core concept of lithographic techniques since inception of the

printing press. Rather, the core discovery of μCP was the stamp, ink, and substrate material system that allowed for precise replication and transfer from the master wafer to the etched gold pattern. In the last twenty years, a number of researchers have discovered additional material systems that are compatible with elastomeric stamps.

Gold was the first material for patterning via microcontact printing and still remains the most popular due to its resistance to oxidation. The technique of patterning and etching using thiols has been shown to work on other noble metals from Group 11 in the periodic table, namely silver and copper [29]. Etching of palladium and aluminum films was also demonstrated with use of the appropriate SAM [29].

The gold structures formed by microcontact printing can themselves be used as etch resists. As one example, gold structures form a resist on the underlying silicon substrate such that three dimensional patterns can be formed using a potassium hydroxide (KOH) etch bath [64].

SAMs and their resulting structures can be used as a deposition resist. SAMs have been shown to form a direct resist to copper chemical vapor deposition (CVD) on silicon and aluminum oxides (SiO_2, Al_2O_3) [50]. Thiols on a substrate film form a resist for electroless deposition of nickel on gold film [58] or a specially synthesized polyimide substrate [68].

Deposition catalysts can also be patterned using the principles of μCP. A pattern, etch, and plate process developed by [29] allows patterning silver, copper, and nickel by electroless deposition on a gold film formed by print and etch. Gold can be deposited on commercial polyimide film using a process developed by [110]. Rather than printing a SAM, palladium colloids (small particles with single-nanometer dimensions) can be printed on silicon, glass, or polymers to act as a catalyst for electroless deposition of copper.

In addition to metals, organic materials can be patterned by microcontact printing. Patterns of carbon nanotube (CNT) forests have been defined in a three step process by printing palladium colloids, depositing silver by electroless deposition, and catalyzing CNT growth on the silver [44]. Polymer multilayer resists for etching have been developed [45] and polymer CVD has been demonstrated with patterns defined

by μCP of a precursor or photoinitiator [76]. Active organic materials have been patterned using μCP, for example organic light emitting diodes (OLEDs) [80].

This brief review of compatible material systems should serve to highlight the versatility of μCP in forming surface patterns and structures. The reader is referred to several substantial reviews to gain a broader appreciation for the material systems that can be produced using μCP as a patterning precursor [84, 81, 106, 20, 54].

1.3.4 Outlook

μCP attracted significant early research attention from IBM [19, 8, 7, 27, 28, 29, 62, 5]. It appears that the process never became developed to the point of mainstream manufacturing in the semiconductor industry, due in part to difficulties with cross-layer registration at nanometer scales and the industry's existing investment and continued advances in photolithography.

At the same time, high speed μCP has been demonstrated with stamp residence times on the order of milliseconds [37]. This maps directly to the feasibility of high speed roll to roll printing, which has been demonstrated at web speeds of 2 m/s [96, 92, 56, 4, 17, 107].

While μCP may not be appropriate for semiconductor fabrication that requires single nanometer resolution and accuracy, it can fill a niche in high resolution, high speed processing of large areas with characteristic feature dimensions of 100 nm or above. Candidate device architectures may be those with registration requirements of several μm rather than several nm (i.e. thin film transistor (TFT) matrix displays vs. integrated circuits) or where registration requirements are altogether absent (i.e. single layer metamaterials).

The outlook of μCP as a large area, high rate patterning technique is indeed positive. Elastomeric μCP stamps can act as a flexographic plate, so that μCP can be adapted to roll-based processing drawing on existing industry expertise. A successful manufacturing scale implementation would permit an unprecedented combination of feature resolution and manufacturing rate in a variety of material systems for emerging device architectures.

43

1.4 Printing Applications

Emerging device architectures require the rates and economy of traditional roll based printing, but with resolutions characteristic of modern photolithography. These include both active devices, such as large area displays or sensor networks, and passive devices, such as a metasurfaces that use a specific micro- or nano- scale pattern to achieve certain bulk optical, electrical, or mechanical behavior on a macroscopic scale.

Each of these applications has in common the requirements of (*i*) high resolution patterning (microscale or below) (*ii*) over very large areas (*iii*) at costs on the order of single dollars or cents per square meter. These common goals requires development of processes that match the resolution of photolithography with the processing paradigms of roll based flexography.

1.4.1 Active Surfaces

The transistor is the basic element at the center of modern electronic devices, whether logic devices such as central processing units or interfaces such as visual displays. TFTs have been instrumental in development of flat panel displays. Characteristic dimensions (transistor channel length and gate registration) of these devices are in the range of single microns [16].

The last decade has seen significant interest in development of flexible display technologies, transitioning flat panel displays from glass substrates to polymer films. These films would both open opportunities for new form factors and be amenable to economical roll-to-roll processing.

Developments in flexible displays would directly translate to other flexible electronic devices, including flexible sensor arrays. Commonly cited applications are in consumer electronics, medicine, and defense. Flextech is an industry consortium actively developing technologies toward this end, similar to the Sematech consortium that has been instrumental in semiconductor development across the .

As examples of success in flexible electronics, material systems have been developed for creating copper TFT interconnects using μCP [21] and μCP has been shown

a strong contender for patterning of TFT array contacts compared to alternative inkjet or screen printing technologies [79]. It has been argued that that μCP can provide the means for overcoming limits of conventional lithography, especially as related to low cost production of flexible displays and electronics [75].

1.4.2 Passive Surfaces

Beyond consumer electronics, μCP has great potential to become a dominant patterning technology to produce metasurfaces that require a pattern with high spatial frequency over a large area of substrate. While a number of such metasurfaces exist, two examples are provided here that are directly applicable to μCP.

Transparent conductive layers are required in flat panel display technologies and amorphous / polychrystaline photovoltaic modules. Indium tin oxide (ITO) has traditionally been used for these applications because of its good conducting behavior and high optical transmission. At the same time, indium is scarce and ITO is brittle, leading to failure in flexible devices. Alternative approaches must have a resistance less than 10 ohms per square and a visible spectrum transmission of greater than 90%. Sparse grids of metallic nanowires have shown promising results toward this goal [42], and could be patterned quite economically with μCP.

Superhydrophobic surfaces can be used to achieve dropwise condensation, dramatically improving heat transfer coefficients. These improved heat transfer coefficients map directly to higher efficiency in steam power cycles and desalination. Alternatively, the superhydrophobicity can be leveraged for a self cleaning effect, perhaps useful on solar cell modules to prevent reductions in photonic flux from surface fouling. [22] shows that dropwise condensation can be achieved on surfaces patterned with thiols by μCP. While thiols would not be a robust surface modifier in an industrial setting, it is possible that a μCP based patterning combined with polymer CVD of polytetrafluoroethylene (PTFE, i.e. Teflon) [76] can create a similar hydrophobic surface.

Table 1.1: A survey of stamp defect modes reported in literature

	Defect	Sources
Dimensional distortion	Ink swelling	[5, 37]
	Edge rounding	[47]
	Ink diffusion	[37, 5, 62]
Mechanical defects	Vertical collapse	[19, 47, 86, 31]
	Lateral collapse	[7, 19, 47, 86, 31, 91]
	Incomplete conformal contact	[47, 8]
	Buckling	[47, 31, 46, 91]
	Roof collapse	[106, 47, 91, 48, 8]
	Dynamic air entrapment	[96, 37]

1.5   Manufacturing Challenges

1.5.1   Feature Deformation

PDMS is a promising stamp material because it acts as a diffusion medium for thiol inks, ensures conformal contact, and replicates template geometry exceptionally well. At the same time, this soft elastomer is the source of a variety of printing defects due to phenomena like swelling, spontaneous collapse, or deformation under contact stresses. These stamp deformations have been the subject of much difficulty and research effort.

Table 1.1 summarizes stamp defect modes that have been identified in literature. These modes are classified here into dimensional and mechanical modes: the former affects the dimensional distribution of the transferred pattern, while the latter affects the integrity or fidelity of the pattern. Dimensional defect modes include ink swelling, curing shrinkage, rounding of punch edges by surface tension, and ink diffusion at feature edges. Mechanical defects (Figure 1-3) include vertical punch collapse, vertical punch buckling, lateral punch collapse, incomplete conformal contact, and roof collapse.

1.5.2 Accuracy

The flexibility of elastomeric PDMS stamps has been touted as a means of patterning curved objects [106]. This same phenomena makes it quite difficult to control the alignment and stretch of stamps when high accuracy is required. While high resolution is easy to achieve by replicating a master template, the absolute accuracy is difficult to maintain over large areas.

To control the lateral stretch of stamp patterns, many researchers cast stamps against rigid backplanes, for example quartz [55, 89]. On parting the stamp and the master template, the lateral dimensions of the stamp are maintained by the rigid backplane.

In other cases, a flexible (but transversely stiff) backplane is used, for example metal shim stock [96, 92, 56, 4, 17, 107, 40] or polymer films [60]. This approach is similar to the use of a polyester layer to maintain dimensional stability in flexographic plates [99].
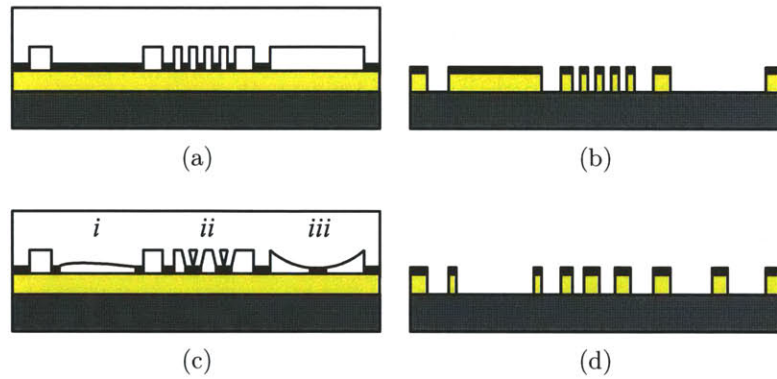
Figure 1-3: Effect of mechanical stamp deformation on pattern trasnfer. (a) Ideal stamp contact behavior and (b) resulting substrate pattern after development; (c) actual stamp contact behavior and (d) resulting substrate pattern after development. Mechanical contact defects like (i) air entrapment between the stamp and substrate, (ii) lateral feature collapse in small features with large aspect ratios, and (iii) roof collapse in wide feature spacings alter the actual contact pattern and result in a drastically different pattern transfer.

1.5.3 Machine Implementations

Manufacturing machines for μCP must address control of the stamp (i) contact pressure and (ii) registration. These two goals are often contradictory.

Contact integrity can be maintained by carefully controlling the pressure or displacement imposed on the elastomeric stamp. The majority of automated processing techniques reported have controlled the hydrostatic pressure applied behind the stamp, allowing it to conform to the substrate surface on the meso-scale while maintaining a uniform pressure at the substrate interface (Figure 1-4a) [18, 15]. While this approach leads to uniform pressure, alignment and dimensional accuracy are difficult to control.

To overcome these difficulties, other machines have been designed that utilize a rigid backplane behind the stamp, often to print on a silicon wafer substrate [9, 55]. In this rigid backplane case, feature deformation is determined by displacement boundary conditions. Roll-to-plate and roll-to-roll processing allow precise control of registration and contact propogation along a narrow zone in the roll nip, but impose similar displacement boundary conditions (Figure 1-4b).

Position and pressure errors are unavoidably introduced in each of these processing strategies, leading to either feature collapse or incomplete contact. Dimensional errors are introduced through machine, substrate, and stamp errors, especially as printing is scaled to manufacturing level implementations. These errors may be geometric in nature, for example an imperfect backplane, or temporal in nature, such as thermal variations or stamp swelling due to ink concentrations [5]. If the stamp is mounted to a rigid backing or roll, the stamp experiences uniform displacement with these spatially varying errors superimposed. Ultimately, these superimposed errors cause one region of the stamp to collapse while another region fails to make contact. Any successful manufacturing implementation *must* be robust to these errors.

1.5.4 Roll Based Processing

Roll based processing, or roll-to-roll manufacturing, is identified as an exemplary implementation of microcontact printing. There exist unequalled opportunities for attaining large rates and areas in a continuous process with roll-based processing. Roll based configurations typically provide narrow line contact between the stamp and substrate, which manages contact propagation, minimizes air entrapment at high speeds, and provides opportunities for active control of pressure and spatial registration. Moreover, roll based microcontact printing is able to leverage an existing body of knowledge in high precision roll-to-roll and web-handling techniques.

The first demonstration of roll based μCP was a simple experiment by Xia et al., where a stamp was mounted on a cylinder and rolled by hand over a 100 mm wafer [105]. A lack of uniformity is clearly evident in the images shown in this report, indicating the need for more precise control of the process.

A roll-based configuration for printing organic transistors was proposed by Rogers et al., where the PDMS stamp is mounted to a glass roller after plasma bonding, then
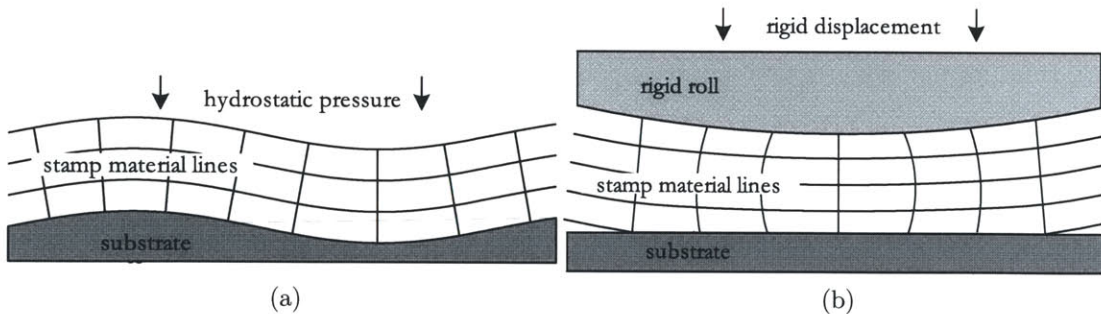
Figure 1-4: Stamp behavior differs based on imposing a uniform displacement or uniform pressure on the stamp. (a) A stamp under hydrostatic pressure can easily conform to substrates, even in the case of large substrate or stamp dimensional errors. In this case, there may also be transverse stiffening, such as backing the stamp with a metallic shim. In this printing configuration, it is difficult to control lateral pattern distortion and registration. (b) Printing using a rigid backing, particularly a roll, allows high rate printing with good control over pattern registration. However, this configuration results in fixed displacement boundary conditions, where very high pressures develop in the incompressible stamp material. This type of deformation is extremely sensitive to dimensional errors in the roll or substrate.

49

used to pattern a flexible substrate [87]. The same group has developed a method of creating a flexography-style PDMS stamp using a flexible Kapton backplane [60]. Methods of web handling and pressure control were not presented in these reports.

A series of high-speed roll-to-roll printing trials were performed at MIT, where closed loop tensioning and a compliant backup roller were used to modulate contact pressure [4, 17, 56, 96, 92, 107]. Stamps were cast with an integrated ferrous backplane, which was attached to a magnetic roller. This machine was demonstrated at a 2 m/s substrate speed, but exhibited air entrapment and had no means of actively regulating the stamp contact behavior.

1.5.5   Grand Challenge

This thesis poses a grand challenge of translating μCP from a bench level prototyping process to an industrial roll-to-roll process on par with flexography. This endeavor seeks to combine the merits of flexography and photolithography, two highly sophisticated manufacturing processes.

This challenge is daunting. The end result would be a factor of 1000 reduction in resolution in flexography (from 100 μm to 100 nm) while maintaining the same rate (meters per second web speed), accompanied by a factor of 100 improvement in alignment (100 μm TIR to 1 μm TIR). As compared to photolithography, a factor of 10000 reduction in cost per unit area is required (100's of dollars per square meter to single cents), with a corresponding factor of 1000 increase in processing rate. At these rates and resolutions, patterning features on a pitch of 1 μm across a 1 m substrate a web speed of 1 m/s requires patterning of no less than one terabit per second.

A manufacturing scale roll to roll system must contend with web handling, stamp inking, contact region control, inline inspection, and interlayer registration. While these certainly exist in conventional flexographic machinery, there must be dramatic improvements in each to improve pattern registration and accuracy. There must be an efficient and repeatable method of producing and mounting polymer stamps to roll based processing machinery. The effect of material and process variations on the final output must be well understood from a process control perspective. Any

one of these problems constitutes a significant research effort and moves well beyond demonstrations of benchtop feasibility.

Neglecting any particular choices of material system or device architecture, the fidelity of stamp contact is at the core of successful processing. This thesis focuses on this core tenet.

The broad goal of this thesis is thus to completely understand the contact behavior and sensitivity of roll mounted PDMS stamps with surface microfeatures (Figure 1-4b), with the goal to obtaining robust contact at the stamp interface. As this thesis will show, the process window for stable stamp contact often allows only a few microns of roll displacement; holding this tolerance becomes a significant engineering challenge. Hence beyond the fundamental understanding of contact behavior, parallel goals of this thesis are to develop designs or techniques for either broadening the process window or actively regulating the stamp contact behavior. The three central parts of this thesis reflect these goals towards process modeling and innovation.

1.6   Thesis Outline

This thesis is organized into three parts (excluding the introduction and conclusion), each addressing (*i*) fundamental stamp deformation behavior, (*ii*) robust stamp design and manufacture, and (*iii*) machinery and process control .

In Part II, Chapter 2 provides an introduction the mechanics of incompressible elastomers, such as PDMS used in μCP stamps. An example is given of calibrating material models by fitting constitutive model parameters to tensile test data.

Chapter 3 investigates the deformation of stamp microfeatures at a local scale. Analytical, numerical, and experimental approaches are taken to identify the dominant collapse mode as a function of dimensionless geometrical and material characteristics. The critical interface pressure is established for each collapse mode. A relationship between feature load and displacement is developed based on these same dimensionless characteristics.

Chapter 4 develops models of the contact pressure profiles at the stamp-substrate

interface in roll-based printing. The load-displacement behavior from Chapter 3 is incorporated in these models to identify the effect of stamp features on the corresponding pressure distributions. A strategy for incorporating the surface energy of the stamp in numerical simulations is developed and implemented. These results are validated experimentally.

In Part III, Chapter 5 develops a model of the process window as a function of roll displacement in roll-based μCP. This process window is related to error sources, showing that the process window is too narrow for practical implementation of a robust process. This observation is used to motivate design of a new stamp architecture that can be used to increase the process window. This architecture is explored analytically, numerically, and experimentally. A case study demonstrates the utility of this architecture.

Chapter 6 examines conventional stamp casting and develops a new method for creating cylindrical stamps especially for roll based processing. A prototype machine is designed and constructed to demonstrate this new stamp casting method. Analytical and experimental results show that microscale features can be produced in the stamp while maintaining excellent dimensional uniformity of the stamp.

In Part IV, Chapter 7 introduces the design of a precision roll positioning stage. Using a parallel kinematic design with flexural bearings, submicron resolution and repeatable motion are obtained between a 50 mm processing roll and substrate.

Chapter 8 discusses servo control of the parallel kinematic positioning stage from Chapter 7. To implement feedback control in the presence of mode coupling and unmodeled dynamics, a nested state-space / classical loop shaping control architecture is used. A decoupling criterion is derived that allows application of this control architecture. The parallel kinematic positioning stage is used as an example of controller synthesis with this nested conrol structure.

Chapter 9 demonstrates two methods of controlling the stamp contact behavior using the roll positioning stage. These two control strategies show good disturbance rejection, supporting a practical and robust manufacturing scale process implementation.

Part II

Contact Behavior

Chapter 2

Polymer Mechanics

This chapter provides a foundation for mechanical analysis of PDMS stamps in subsequent chapters through a review of relevant mechanics of material deformation. The presentation of mechanics here is limited to material pertinent to elastic deformation of elastomers, for example the PDMS used in soft lithography stamps.

The following sections introduce the material behavior of PDMS, develop general notation of material deformation, and introduce constitutive models of value to finite deformation elastomeric analysis. The final section describes how the constitutive models are calibrated using mechanical test data of elastomer specimens.

2.1   PDMS Composition

PDMS is a crosslinked polymer with a siloxane backbone; the corresponding monomer is shown Figure 2-1. PDMS can be readily obtained in industrial formulations, most commonly Dow Corning Sylgard 184 product. The PDMS is supplied as a two part pre-polymer, which is mixed at a specific ratio and allowed to cure. The prepolymer will cross link naturally over the period of a few days, or curing can be thermally accelerated to a matter of hours or minutes [103].

Crosslinked PDMS is a soft elastomer with elastic modulus on the order of 1.5 MPa. The exact modulus is quite sensitive to mixing ratios of the prepolymer and exact thermal cycle during curing [43]. This polymer has a moderate surface energy
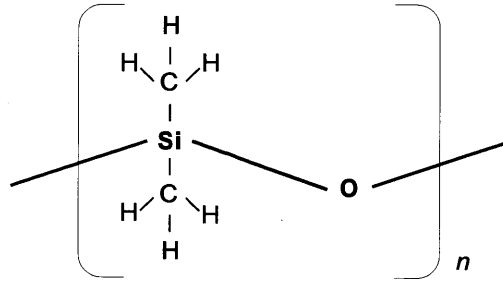
Figure 2-1: PDMS monomer; the polymer is formed with a silicon-oxygen backbone. Crosslinking occurs between polymer chains by removing the methyl (CH_3) groups.

of about 20 mJ/m^2 [11]. As with most elastomers, PDMS has a viscoelastic response with a characteristic relaxation timescale of about 5 s [63]. In this thesis, elastomeric stamps are modeled as a purely elastic material to examine quasi-static behavior.

2.2 Material Deformation

Displacement of a continuum material during deformation is given by vector u as a function of initial position X. The vector u represents the position change of a material point between its undeformed and deformed coordinates. (Throughout this thesis, the material deformation is often analyzed in two dimensional coordinates using u and v as the components of u along the $\hat{x}$ and $\hat{y}$ directions, respectively.)

The *strain* at a particular point is dependent not on u, but on the spatial derivative thereof. For example, a rigid translation of a body will result in a uniform finite u at all X, but will not strain or deform the body in any way. The spatial derivative of displacement gives rise to the displacement gradient tensor H and the deformation gradient tensor F:

$$H = \nabla u \tag{2.1}$$

$$F = H + 1 \tag{2.2}$$

The strain tensor $\boldsymbol{E}$ is given by

$$\boldsymbol{E} = \frac{1}{2}(\boldsymbol{F}^\top \boldsymbol{F} - \mathbf{1}) = \frac{1}{2}(\boldsymbol{H} + \boldsymbol{H}^\top + \boldsymbol{H}^\top \boldsymbol{H}) \tag{2.3}$$

In the special case that deformations are small, that is $|\boldsymbol{H}| \ll 1$, the strain tensor $\boldsymbol{E}$ reduces to the infinitesimal strain tensor $\boldsymbol{\epsilon}$:

$$\boldsymbol{\epsilon} = \frac{1}{2}(\boldsymbol{H} + \boldsymbol{H}^\top) \tag{2.4}$$

In terms of the displacement components, this strain field is

$$\epsilon_{ij} = \frac{1}{2}\left(\frac{\partial u_i}{\partial X_j} + \frac{\partial u_j}{\partial X_i}\right) \tag{2.5}$$

Deformation given by components of $\boldsymbol{\epsilon}$ must satisfy the compatibility equation, which links the strain field to the displacement field (for example, in 2D deformation there are two deformation directions, u_x and u_y, but three strain components ϵ_{xy}, ϵ_{yy}, and ϵ_{xy}, only two of which can be independent):

$$\nabla \times (\nabla \times \boldsymbol{\epsilon}) = \mathbf{0} \tag{2.6}$$

The volume change at each material point is a useful metric of deformation. The volume ratio $J > 0$ at each point is

$$J = \det \boldsymbol{F} \tag{2.7}$$

J gives the relative volume change at a point. For example, a general material in positive hydrostatic stress will expand ($J > 1$), while a material in negative hydrostatic stress will contract ($J < 1$). If the material is incompressible, $J = 1$ will always hold.

A general deformation leads to stress in material, characterized at each point by a stress tensor $\boldsymbol{\sigma}$ that must satisfy the equilibrium condition (neglecting body forces

and tractions):

$$\nabla \cdot \boldsymbol{\sigma} = \mathbf{0} \tag{2.8}$$

The way that the strain tensor $\boldsymbol{E}$ and stress tensor $\boldsymbol{\sigma}$ correspond at each material point depends on the particular material and its properties. This relationship is characterized by a constitutive model.

2.3 Constitutive Models

2.3.1 Small Deformation Elasticity

Small deformation isotropic elasticity is characterized by shear modulus μ and bulk modulus κ that relate stress $\boldsymbol{\sigma}$ and strain $\boldsymbol{\epsilon}$:

$$\boldsymbol{\sigma} = 2\mu\boldsymbol{\epsilon}' + \kappa(\operatorname{tr}\boldsymbol{\epsilon})\mathbf{1} \tag{2.9}$$

where the deviatoric strain tensor $\boldsymbol{\epsilon}' = \boldsymbol{\epsilon} - \frac{1}{3}(\operatorname{tr}\boldsymbol{\epsilon})\mathbf{1}$.

This constitutive model links elastic stress and strain in the familiar linear elastic relationship. From (2.9), changes in the state of stress will affect either the deviatoric material strain with a scaling determined by the shear modulus (e.g. the shear or elongation) or the volume ratio of the material with a scaling determined by the bulk modulus (e.g. uniform expansion or contraction).

2.3.2 Finite Deformation Elasticity

In finite deformation elasticity, material deformation is characterized by stretch $\lambda_i = 1 + E_{ii}$. In small deformation elasticity, strain $\boldsymbol{\epsilon}$ is a linear function of $\boldsymbol{u}$ because the term $\boldsymbol{H}^\top \boldsymbol{H}$ is neglected in (2.3). In general finite deformation elasticity, the strain tensor $\boldsymbol{E}$ is a nonlinear function of the deformation vector $\boldsymbol{u}$, requiring that constitutive behavior be characterized by an *energy function* rather than a linear relationship between stress and strain.

One of the most common forms of isotropic finite elasticity is the Neo-Hookean

model [85], which captures nonlinear behavior from large deformations:

$$U = C_{10}(I_1 - 3) + \frac{1}{D_1}(J - 1)^2 \tag{2.10}$$

where the first invariant I_1 is

$$I_1 = \bar{\lambda}_1^2 + \bar{\lambda}_2^2 + \bar{\lambda}_3^2 \tag{2.11}$$

with volume ratio $J = \lambda_1 \lambda_2 \lambda_3$ and deviatoric stretches $\bar{\lambda}_i = J^{-1/3}\lambda_i$. $C_{10} = \mu_0/2$ and $D_1 = 2/\kappa_0$ are material parameters. In this formulation, moduli are denoted with the subscript 0 (for example μ_0, κ_0), representing the linearized moduli at small deformations about $\lambda = 1$.

For λ_i near unity, $U = \frac{1}{2}\boldsymbol{\sigma} : \boldsymbol{\epsilon}$ and the Neo-Hookean model can be shown to reduce to the consitutive model for small deformation elasticity (2.9).

2.3.3   Stiffening Finite Deformation Elasticity

The Neo-Hookean model fails to capture stiffening behavior that is common at moderate λ in elastomers. While several models of this behavior exist (e.g. Yeoh [109] and Gent [30]), the Arruda-Boyce model [3] is introduced here because it is derived from physical mechanisms and requires only two parameters to calibrate (each with physical significance).

The Arruda-Boyce model explains stiffening by an examination of polymer chain behavior. At small stretches, the polymer can deform by rotation of atomic bonds, but at some point these bonds become fully aligned with the direction of rotation. This locking point is characterized by a maximum stretch, or λ_m. The chain behavior is described by the inverse Langevin function. This function is unwieldy, but can be approximated by the first five terms of a Pade approximation to arrive at a strain energy function given by:

$$U = C_1 \left[\sum_{i=1}^{5} \alpha_i \lambda_m^{-2(i-1)}(I_1^i - 3^i) \right] + \frac{1}{D_1} \left(\frac{J^2 - 1}{2} - \ln J \right) \tag{2.12}$$

59

where

$$\boldsymbol{\alpha} = \left\{ \begin{array}{c} 1/2 \\ 1/20 \\ 11/1050 \\ 19/7000 \\ 519/673750 \end{array} \right\} \tag{2.13}$$

and

$$\mu_0 = C_1 \left(1 + \frac{3}{5\lambda_m^2} + \frac{99}{175\lambda_m^4} + \frac{513}{875\lambda_m^6} + \frac{42039}{67375\lambda_m^8} \right) \tag{2.14}$$

Thus, the Arruda-Boyce model can be fully characterized by only the initial shear modulus μ_0 and the maximum stretch of the polymer chains λ_m.

This model can be shown to match the behavior of the Neo-Hookean model at moderate levels of λ_m, but departs at more extreme deformations to describe stiffening behavior (see for example Figure 2-3).

2.3.4   Incompressibility

Throughout this thesis, PDMS is assumed to be incompressible such that volume ratio $J = 1$. This assumption reduces the constitutive models above to more convenient forms. For example, the small deformation constitutive model (2.9) becomes

$$\boldsymbol{\sigma} = 2\mu\boldsymbol{\epsilon} + p\mathbf{1} \tag{2.15}$$

where p is some hydrostatic pressure field that does not affect the strain components.

The Neo-Hookean model (2.10) becomes:

$$U = C_{10}(I_1 - 3) \tag{2.16}$$

and the Arruda-Boyce model (2.12) reduces to:

$$U = C_1 \left[\sum_{i=1}^{5} \alpha_i \lambda_m^{-2(i-1)} (I_1^i - 3^i) \right] \tag{2.17}$$

60

Engineering solutions are often given in terms of elastic modulus E (not to be confused with strain tensor $\boldsymbol{E}$ or its individual elements E_{ij}) and Poisson ratio ν rather than shear modulus μ and bulk modulus κ. In an incompressible material, κ is infinite and ν is identically $\frac{1}{2}$. The elastic and shear moduli are related by

$$E = 2\mu(1 + \nu) \tag{2.18}$$

An equivalent linearized elastic modulus E_0 can be found using this relationship for finite deformation elasticity. In an incompressible material ($\nu = \frac{1}{2}$), the initial elastic modulus is identically

$$E_0 = 3\mu_0 \tag{2.19}$$

2.4 Material Characterization

Each of these constitutive models (small deformation, Neo-Hookean, and Arruda-Boyce) must be calibrated by fitting to experimental data. Perhaps the most popular characterization is the tensile test, which places the material specimen in a state of uniaxial stress.

The Neo-Hookean and Arruda-Boyce models can be rewritten in terms of the primary stretch λ_1 to calibrate the material constants in each model based on uniaxial tension data. For an incompressible material, $J = 1$ gives $\lambda_2 = \lambda_3 = 1/\sqrt{\lambda_1}$. The first invariant I_1 (2.11) in the uniaxial case is thus

$$\bar{I}_1 = \lambda_1^2 + 2\lambda_1^{-1} \tag{2.20}$$

Substituting the expression for the first invariant into the Neo-Hookean model (2.16) gives an incompressible energy function of

$$U = C_{10}(\lambda_1^2 + 2\lambda_1^{-1} - 3) \tag{2.21}$$

61

where the engineering stress can be found as $dU/d\lambda_1$:

$$\sigma_1 = \frac{dU}{d\lambda_1} = 2C_{10}(\lambda_1 - \lambda_1^{-2}) \tag{2.22}$$

Similarly, this form for the first invariant can be used to reduce the Arruda-Boyce model (2.17) to

$$\sigma_1 = 2C_1 \left(\lambda_1^2 - \frac{1}{\lambda_1} \right) \left[\sum_{i=1}^{5} i\alpha_i \lambda_m^{-2(i-1)} I_1^{(i-1)} \right] \tag{2.23}$$

Material parameters can be determined by fitting these uniaxial tension models to physical tensile test data that records σ_1 and λ_1. In experiments throughout this thesis, PDMS samples are characterized using a Zwick load frame equipped with a 20 N load cell. Test specimens are cut from PDMS sheets using a die with gage width and length of 4 and 20 mm, respectively (Figure 2-2a). These specimens are mounted in the jaws of a load frame (Figure 2-2b) and strained to $\lambda_1 = 2$ at a strain rate of 0.01/s.
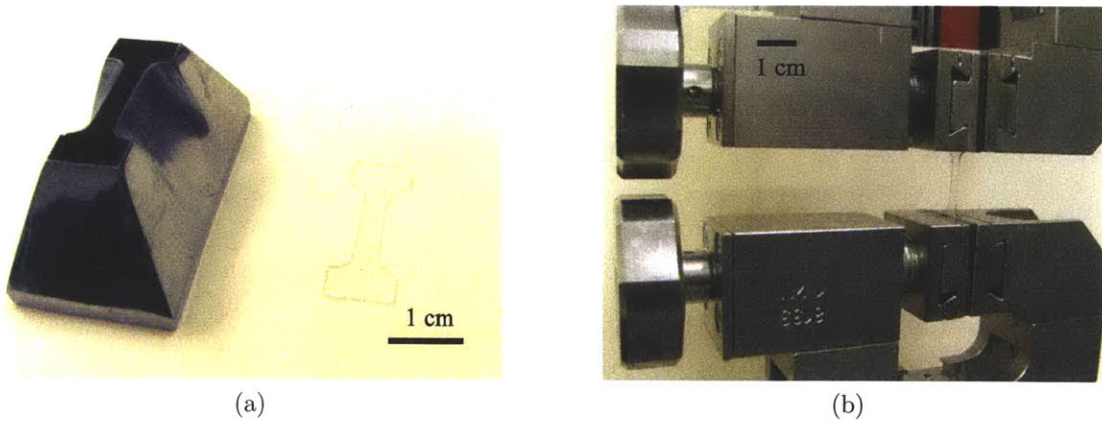
Figure 2-2: Uniaxial tensile testing specimen. (a) Die and corresponding PDMS tensile testing specimen; (b) specimen mounted in the jaws of a load frame.

The resulting experimental data resembles the 'S' curve typical of a strain-stiffening material (as described by the Arruda-Boyce model). Figure 2-3 shows a comparison of the Neo-Hookean models and Arruda-Boyce models overlaid on a single experimental data set. Each model was fit by regression; only data for small stretches ($\lambda_1 < 1.2$)

is used to fit the Neo-Hookean model.
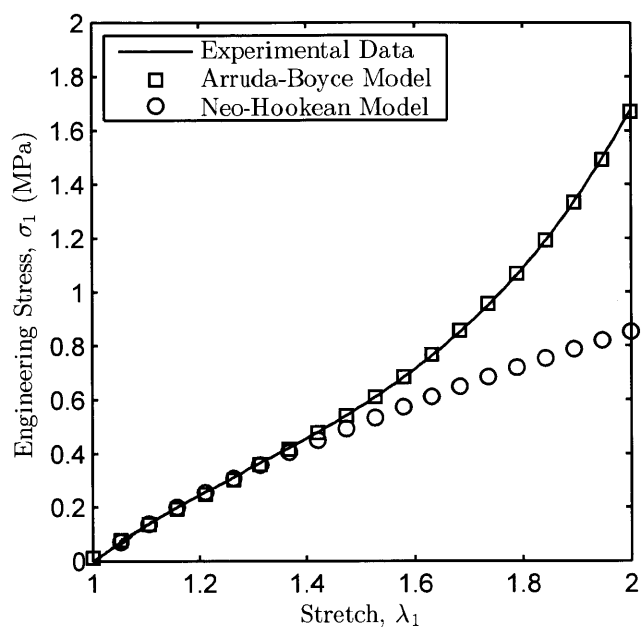
Figure 2-3: Experimental tensile test data with superimposed best fit Arruda-Boyce (μ_0= 0.43 MPa, λ_m=1.21) and Neo-Hookean (μ_0= 0.49 MPa) models.

Chapter 3

Stamp Feature Deformation

3.1 Feature Collapse

While the low shear modulus μ_0 of PDMS stamps allows conformal contact with printing substrates, it also permits undesired deformations at the local scale at modest contact pressures (Figure 3-1). Because μCP is based on selective stamp contact, stamp feature collapse results in failure of the printing process. Although other processing limits exist in μCP, achieving correct contact of the stamp features is a critical and necessary condition for successful pattern transfer.

(a)   (b)   (c)   (d)
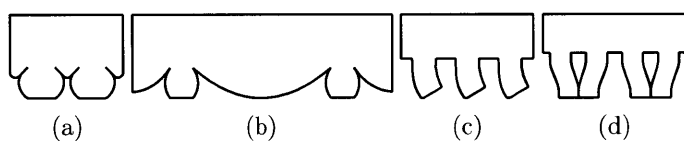
Figure 3-1: Microfeature collapse modes: (a) Sidewall collapse, where pattern collapse progresses from the pinned edges of contact as the feature sidewalls bulge; this is the most stable mode of deformation. (b) Roof collapse, where features spaced far apart permit the roof to collapse against the substrate. (c) Buckling, wherein tall features buckle under load. (d) Lateral collapse, where tightly grouped features adhere to their neighbors under with no external loading.

Contact integrity can be maintained by carefully controlling the pressure or displacement imposed on the elastomeric stamp. Position and pressure errors are inherently introduced in each of these processing strategies, leading to either feature

collapse or incomplete contact. To understand this sensitivity and resulting process limitations, one must first understand the mechanistic load-displacement behavior of the stamp features.

Many authors have examined defect modes in PDMS microfeatures, not limited to those illustrated in Figure 3-1. Interestingly, the behavior of elastomeric microfeatures is important not only for microcontact printing, but also to other fields like biomimetic surfaces for dry adhesion (i.e. synthetic gecko feet).

Models predicting the onset of roof collapse (Figure 3-1b) were investigated independently by IBM [8] and Hui et al. [47], while Sharp et al. [91] experimentally validated the latter. The behavior of roof collapse after the defect has been initiated has also been studied, especially the spread of collapse due to surface energy [112]. Roof collapse in the limit of small feature aspect ratios represents an analytically tractable case that can be solved using well known solutions of periodic cracks [57] and crack propagation [24]. Unfortunately, these models are not generally applicable to all practical or conceivable stamp feature designs.

Feature buckling (Figure 3-1c) has been predicted using an Euler buckling model [47]. Sharp et al. show that the attachment of the feature to the stamp is sufficiently rigid to consider it a fixed boundary condition, though their experimental results showed buckling at a pressure much less than predicted by a fixed-pinned Euler beam [91]. Buckling was again examined by the same group of researchers in the context of biomimetic adhesion [31, 46].

Early efforts at IBM identified feature instability (Figure 3-1d) as an important defect mode [7] and proposed onset of collapse based on empirical data. An analytic modeling strategy was proposed by Hui et al. [47], developed by balancing strain energy in each laterally adhering feature and the work of adhesion with its neighbor. This modeling approach was compared to experimental results by Glassmaker et al. [31] and Roca-Cusachs et al. [86], showing that the approach provides a reasonably accurate prediction of instability. This phenomena has also been widely studied in silicon microelectromechanical systems (MEMS), where small cantilevers will adhere to each other in bistable configurations [108].

All of these existing studies of PDMS microfeatures have reported critical pressures at which a particular collapse mode occurs. There has been no discussion of critical collapse displacements or even the stiffness, which would relate the load and displacement behaviors. Without understanding this relationship, the complex problem of macro-scale stamp deformation is intractable. To this end, this chapter seeks to establish the stiffness of PDMS microfeatures to relate load and displacement.

The remainder of this chapter provides a review of analytic results, a numeric investigation using finite element methods, and an experimental investigation of collapse. The primary purpose of this work is to develop and validate models for feature stiffness, although the onset of particular collapse mode (Figure 3-1) is simultaneously examined to demonstrate congruence with existing studies. Ultimately, the coherence of these models is demonstrated by using them to correctly predict experimental collapse modes.

3.2 Analytical Models

This section introduces notation and examines the deformation problem from an analytical perspective. The goal in the following is to develop a foundation for both the stiffness of the microfeature arrays and the onset of each failure mode shown in Figure 3-1.

3.2.1 Notation

The analysis and results in this paper examine a soft lithography stamp with periodic lines on its surface (resembling a series of parallel punches), a cross section of which is shown in Figure 3-2. The stamp is composed of an incompressible elastomer that can be characterized by a large deformation Neo-Hookean constitutive model with shear modulus μ_0 and elastic modulus $E_0 = 3\mu_0$. The stamp material has surface energy of γ_s (or work of adhesion W_{ad} with a substrate, as appropriate). The stamp has some bulk thickness t and the microfeatures on its surface that have width w, height h, and are regularly spaced at an interval a.
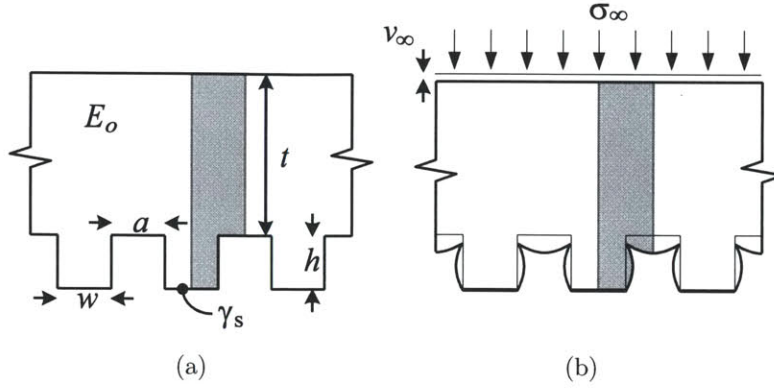
Figure 3-2: Stamp geometry and feature dimensions. (a) Cross section of nominal stamp configuration, labeled with characteristic dimensions and material properties. (b) Cross section of deformed stamp showing far field displacement and pressure. In both cross sections a unit cell is shown shaded.

During loading, the surface of each stamp feature experiences no-slip contact against the stamp substrate. The vertical faces of the unit cell shown in Figure 3-2 are free of shear stress and have no lateral displacement, as dictated by symmetry. The upper edge of the same unit cell is subject to some uniform pressure σ_∞ and uniform downward displacement v_∞.

Normalized parameters are introduced to describe the geometry, load, and displacement behavior of each stamp feature to scale the following numerical and experimental results. Geometrical quantities are normalized by the feature width w, resulting in an aspect ratio A and pattern ratio P:

$$A = \frac{h}{w} \tag{3.1}$$

$$P = \frac{a}{w} \tag{3.2}$$

Surface energy is normalized by the elastic modulus and feature dimension, re-

sulting in conformability Cf:

$$Cf = \frac{W_{ad}}{E_0 w} \tag{3.3}$$

Far field contact stress is normalized by elastic modulus:

$$S = \frac{\sigma_\infty}{E_0} \tag{3.4}$$

Displacement v_∞ is normalized by the maximum displacement of a feature $v_{\infty,max}$ (when the stamp features have deformed to fill all voids at the contact interface), resulting in a normalized displacement value X between zero and unity. Examining the unit cell of Figure 3-2 and applying incompressibility and continuity, it is evident that $v_{\infty,max} \cdot (a + w) = h \cdot a$. From this it follows that normalized displacement is:

$$X = v_\infty \frac{a + w}{ha} \in [0, 1] \tag{3.5}$$

Finally, dimensionless stiffness $K = dS/dX$ is introduced to relate the load and displacement behavior. This value can be related to sheet stiffness $k = d\sigma_\infty/dv_\infty$ by applying (3.4) and (3.5):

$$K = \frac{dS}{dX} = k \frac{ha}{E_0(a + w)} \tag{3.6}$$

3.2.2 Stiffness

Feature stiffness can be examined analytically in two limits: first where features are very short ($A \ll 1, A \ll P$), and second where the features are very tall and dense ($A \gg 1, P \ll 1$) (Figure 3-3).
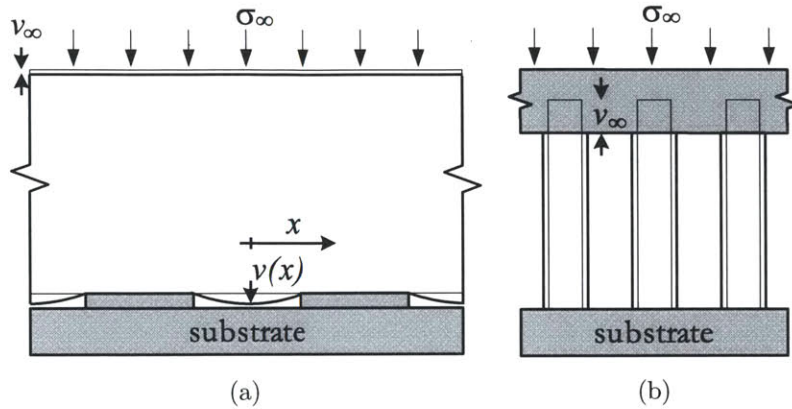
Figure 3-3: Stamp feature deformation in two analytical limits. (a) In the limit of very small aspect ratio, the stamp features can be considered rigid compared to the bulk stamp thickness. This configuration can be modeled as an infinite series of rigid punches on an elastic halfspace. (b) In the limit of very large aspect ratio, the bulk stamp can be considered rigid relative to the stamp features and the no-slip boundary condition can be neglected. This configuration can be modeled as a series of elastic columns compressed between frictionless plates. In both A and B, the rigid elements are shown shaded and the undeformed state of the elastic elements are shown thin.

In the first case, that is $A \ll 1$, Hui et al. [47] show that the deformation problem converges to the solution of an infinite series of rigid punches on an elastic halfplane (Figure 3-3a). The solution to this problem is identical to that for a series of colinear cracks in an elastic plane (where the cracks represent the gap space between punches). This configuration is examined by Koiter [57] using Muskhelishvili's complex field analysis [73]. Koiter derives a strain energy per crack for an elastic space; the corresponding energy for the halfplane is one half Koiter's result:

$$U = -\frac{(a + w)^2}{\pi} \frac{\sigma_\infty^2}{E^*} \log \cos \left(\frac{\pi}{2} \frac{a}{a + w} \right) \tag{3.7}$$

where $E^* = E/(1 - \nu^2)$ for plane strain.

The stiffness σ_∞/v_∞ can be derived from U using complementary energy and virtual work. It is a familiar result that the elastic energy stored in a compliant system scales with the square of displacement:

$$U = (a + w) \cdot \frac{1}{2} \left(\frac{d\sigma_\infty}{dv_\infty} \right) v_\infty^2 \tag{3.8}$$

This expression can be re-written using the identity $v_\infty = \sigma_\infty \cdot dv_\infty / d\sigma_\infty$:

$$U = (a + w) \cdot \frac{1}{2} \left(\frac{dv_\infty}{d\sigma_\infty} \right) \sigma_\infty^2 \tag{3.9}$$

Equating this relationship with Koiter's result (3.7) provides the stiffness σ_∞ / v_∞ of the features. Assuming an incompressible material ($\nu = 1/2$) in plane strain, this stiffness is

$$\frac{d\sigma_\infty}{dv_\infty} = -\frac{2\pi}{3} \frac{E}{a+w} \left[\log \cos \left(\frac{\pi}{2} \frac{a}{a+w} \right) \right]^{-1} \tag{3.10}$$

Converting to the dimensionless stiffness K (3.6) gives the stiffness in the first limit:

$$K_I = K|_{A \to 0, A/P \to 0} \tag{3.11a}$$

$$= \frac{2\pi}{3} \frac{AP}{(P+1)^2} \left[-\log \cos \left(\frac{\pi}{2} \frac{P}{P+1} \right) \right]^{-1} \tag{3.11b}$$

In the second limit, that is $A \gg 1$, the deformation problem approaches a series of closely spaced columns compressed between frictionless plates (Figure 3-3b). In this case, the stiffness of each column would be $df/dv_\infty = E^* w / h$. Converting this to a far field stiffness by $\sigma_\infty = f/(a+w)$ gives

$$\frac{d\sigma_\infty}{dv_\infty} = \frac{E^* w}{h} \frac{1}{a+w} \tag{3.12}$$

Assuming plane strain incompressibility and converting to dimensionless stiffness K (3.6) for the second limit results in

$$K_{II} = K|_{A \to \infty, P \to 0} \qquad \text{(3.13a)}$$

$$= \frac{4}{3} \frac{P}{(P+1)^2} \qquad \text{(3.13b)}$$

The value of stiffness K in the region between these two limits remains an open question. In Section 3.5, a general expression is developed for K by fitting the models of (3.11a) and (3.13a) to results from numerical simulations.

3.2.3 Collapse Onset

Collapse modes are dependent on some critical displacement and pressure. In the following, the critical point of feature collapse is examined where analytically possible, individually considering instantaneous collapse, roof collapse, buckling, and lateral collapse.

Sidewall Collapse

The critical point for sidewall collapse (Figure 3-1a) is trivial, since loss of line resolution does not occur until $X = 1$. From the definition of stiffness K, this results in a collapse pressure S_c of

$$S_c = K \qquad \text{(3.14)}$$

Roof Collapse.

When the roof collapse mode (Figure 3-1b) is observed for $A \ll 1$, the deformation converges to the that of an elastic halfplane loaded by an infinite series of rigid punches (Figure 3-3a). Koiter [57] provides the roof displacement for this problem in terms of

72

distance x from the center of the roof:

$$v(x) = \frac{2}{\pi} \frac{\sigma_\infty}{E^*} (a + w) \log \left[\frac{c(x) + \sqrt{c^2(x) - c^2(a/2)}}{c(a/2)} \right] \qquad (3.15a)$$

$$c(\chi) = \cos \left(\pi \frac{\chi}{a + w} \right) \qquad (3.15b)$$

Collapse occurs when $v(x = 0) = h$. Using (3.15) to solve for this point gives the corresponding collapse pressure:

$$\sigma_\infty = E^* \frac{\pi}{2} \frac{h}{a + w} \log^{-1} \left[\frac{1 + \sin \frac{\pi}{2} \frac{a}{a+w}}{\cos \frac{\pi}{2} \frac{a}{a+w}} \right] \qquad (3.16)$$

Assuming an incompressible material in plane strain ($E^* = \frac{4}{3} E_0$) and converting to dimensionless variables gives normalized collapse pressure S_c:

$$S_c = \frac{3\pi}{8} \frac{A}{P + 1} \log^{-1} \left[\frac{1 + \sin \frac{\pi}{2} \frac{P}{P+1}}{\cos \frac{\pi}{2} \frac{P}{P+1}} \right] \qquad (3.17)$$

Normalized displacement X at this collapse point can be found by integrating the displacement profile

$$X_c = \frac{\int_0^{a/2} v(x) dx}{v(0) \cdot \frac{a}{2}} \qquad (3.18)$$

In the limit that $P \ll 1$, a lower bound of $X_c = \pi/4$ can be found using (3.18) and an elliptical displacement profile given by Koiter. For larger P, the collapse point lies between this bound and $X = 1$. A practical lower bound on collapse pressure is thus given by

$$S_c = \frac{\pi}{4} K \qquad (3.19)$$

Buckling.

In the case of feature buckling (Figure 3-1c), the conventional model for Euler buckling [93] in plane strain can be applied. The critical buckling load f_{Euler} on each feature is

$$f_{\text{Euler}} = b_c \frac{\pi^2 E^* I}{L^2} \qquad (3.20)$$

73

where b_c is a boundary condition constant as given in Table 3.1 and I is the beam moment of inertia, identically $w^3/12$ for the microfeature geometry.

Table 3.1: Boundary condition constants for Euler column buckling

Boundary Condition	b_c
Fixed-fixed	4
Fixed-pinned	2
Pinned-pinned	1
Fixed-free	1/4

Putting this buckling load in terms of far field pressure $\sigma_\infty = f/(a + w)$, assuming incompressibility, and rearranging into normalized parameters gives the Euler buckling pressure as

$$S_{\text{Euler}} = b_c \frac{\pi^2}{9} \frac{1}{(P + 1)A^2} \tag{3.21}$$

This expression (3.21) is essentially the model for critical buckling pressure given by [47], but expressed in dimensionless variables for an incompressible material. At this point b_c remains a variable that is dependent on the load conditions: a substrate that is fixed laterally will resemble a series of fixed-pinned columns, while one that is free to translate laterally will resemble a series of fixed-free columns.

The work of adhesion W_{ad} between the stamp and the substrate results in a delayed onset of buckling (as observed in the experimental results of Sharp et al. [91]), where additional elastic energy is required to overcome the energy barrier of W_{ad}. To augment the traditional buckling model assumed by other authors, this thesis considers the balance of strain energy per unit area U and work of adhesion per unit area W_{ad} (Figure 3-4).

Assuming linear behavior, this balance can be written using complementary energy and sheet stiffness k. In the stable configuration, just before the point of buckling, the features will have only mechanical elastic energy:

$$U_{\text{Euler}} = \frac{1}{2} \frac{1}{k} \sigma^2 \tag{3.22}$$

74
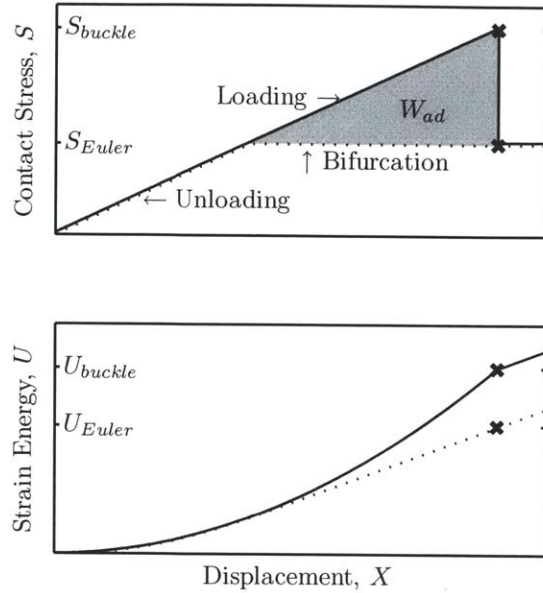
Figure 3-4: Loading and unloading paths for microfeature buckling in the presence of surface energy. The work of adhesion at the contact interface delays the onset of buckling during loading; the delay can be found by equating the difference in strain energies U_{buckle} and U_{Euler} with the work of adhesion.

In the buckled configuration, just after the point of buckling, the features will have a strain energy composed of the sum of the elastic mechanical energy at the Euler buckling point and the additional mechanical energy required to compress to the delayed buckling point in a state of bifurcation (Figure 3-4):

$$U_{\text{buckle}} = \frac{1}{2}\frac{1}{k}\sigma_{\text{Euler}}^2 + \frac{1}{k}\sigma_{\text{Euler}}(\sigma - \sigma_{\text{Euler}}) \tag{3.23}$$

The work of adhesion per unit area is the surface energy scaled by the stamp contact area (W_{ad} here denotes the work of adhesion between the stamp and substrate materials)

$$W_{ad}^* = W_{ad}\frac{w}{a + w} \tag{3.24}$$

The delayed buckling point can be found by equating the difference in strain energies U_{buckle} (3.22) and U_{Euler} (3.23) with the work of adhesion W_{ad}:

$$U_{buckle} - U_{Euler} = -W_{ad}^*$$ (3.25)

Substituting the corresponding expressions allows solving for the additional pressure required to cause buckling in the presence of surface energy:

$$\sigma - \sigma_{\text{Euler}} = \sqrt{k \cdot W_{ad} \frac{w}{a+w}}$$ (3.26)

Converting to dimensionless parameters provides a critical buckling load S_{buckle}:

$$S_{\text{buckle}} = S_{\text{Euler}} + \sqrt{\frac{2KCf}{AP}}$$ (3.27)

Lateral Collapse

Lateral collapse (Figure 3-1d) is predicted by balancing microfeature strain energy U and work of adhesion W_{ad} to find the minimum energy state of an arbitrarily tall feature. For a feature of height h with collapse contact length l_c ($l_c < h$) the critical height for spontaneous lateral collapse is $h_c = h - l_c$ (Figure 3-5a).

The critical collapse height h_c is found by first finding the equilibrium collapse length l_c. The equilibrium condition requires a minimum energy state, calculated using the necessary condition $d(U + W_{ad})/dl_c = 0$ [47]. Expanding this condition gives

$$\frac{d}{dl_c}\left(\frac{k_{beam}(a/2)^2}{2}\right) + \frac{d}{dl_c}\left(-l\frac{W_{ad}}{2}\right) = 0$$ (3.28)

where k_{beam} is the beam stiffness of a microfeature of length $h - l_c$, $a/2$ is the length that the same feature must deflect to contact a neighboring feature, and W_{ad} is the work of adhesion between the stamp material and itself. Rewriting this for some

76
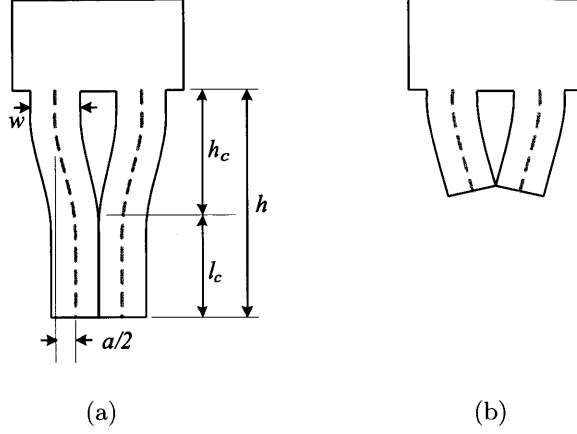
Figure 3-5: Schematic of feature lateral collapse. (a) Fixed-fixed beam configuration and characteristic dimensions. (b) Schematic of similar features collapsing in a cantilever beam mode.

arbitrary beam stiffness gives a critical condition of

$$\frac{d}{dl_c}(k_{beam}) = -\frac{d}{dh_c}(k_{beam}) = \frac{4W_{ad}}{a^2} \tag{3.29}$$

Prior studies have all assumed that the deformed shape of features is that of a fixed-fixed beam as shown in Figure 3-5a, where $k_{beam} = 12E^*I/(h_c)^3$ (I is the cross sectional moment of inertia) [47, 31, 86]. However, experimental observations (Figure 3-6) show that deformed features near the critical point assume the shape of a cantilever beam, where $k_{beam} = 3E^*I/(h_c)^3$ (Figure 3-5b).

Evaluating criterion (3.29) with the cantilever beam stiffness, letting $I = w^3/12$ for a rectangular beam in plane strain, and assuming incompressibility gives

$$\frac{Ew^3}{h_c^4} = \frac{4W_{ad}}{a^2} \tag{3.30}$$

Rearranging and converting to dimensionless parameters gives a critical condition for lateral collapse of

$$\frac{P^2}{4A^4} = Cf \tag{3.31}$$

77

(a) (b) (c)
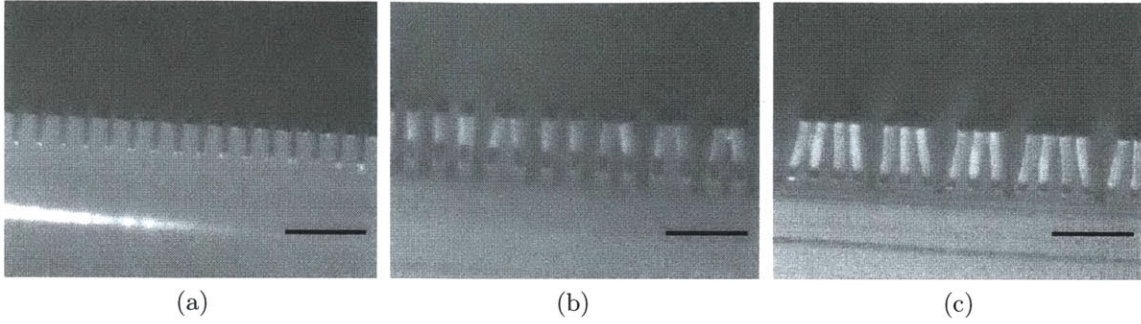
Figure 3-6: Micrographs of lateral feature collapse showing (a) stability ($w=20\mu$m, $a=10\mu$m, $h=30\mu$m), (b) onset of collapse ($w=20\mu$m, $a=16\mu$m, $h=54\mu$m), and (c) full collapse with a high mode number($w=20\mu$m, $a=10\mu$m, $h=77\mu$m). Scale bars: 100 μm.

This model in (3.33) is strictly valid only for small displacements of long beams, requiring $P \ll 1$ and $A \gg 1$. For aspect ratios smaller than $ca.$ 3, the model should include the shear stiffness of each beam. Timoshenko beam theory [98] includes this effect, where the corresponding cantilever beam stiffness is

$$k_{\text{beam}} = \left(\frac{h_c^3}{3E^*I} + \frac{\alpha_s h_c}{A\mu} \right)^{-1} \tag{3.32}$$

with cross sectional area A, moment of inertia I, shear modulus μ, and shear factor $\alpha_s = 6/5$ for rectangular features [98].

Applying this Timoshenko beam stiffness to (3.30) gives a more accurate criterion of

$$\frac{P^2}{4A^2} \frac{A^2 + \alpha_s/3}{(A^2 + \alpha_s)^2} = Cf \tag{3.33}$$

In the limit of large aspect ratio A, this expression derived with Timoshenko beam stiffness (3.33) converges to the criterion derived from Euler beam stiffness (3.31). This more accurate criterion is unfortunately implicit in aspect ratio A.

The strain energy at the contact point has been neglected for features undergoing cantilever deflection (Figure 3-5b); this will be small for features very near the critical height h_c. Despite this approximation, the expression given in (3.33) provides an accurate estimate of stability.

3.2.4 Summary

These models provide a means of estimating the onset point of each type of defect shown in Figure 3-1; (3.14), (3.17), and (3.27) give the collapse pressures for modes a, b, and c (respectively) while (3.33) gives the collapse criteria for mode d. Each critical collapse displacement X_c can be found from these critical pressures S_c by the relationship $S_c = KX_c$.

3.3 Numerical Simulation

A numerical investigation of microfeature behavior was conducted using finite element methods, particularly to determine the load-displacement behavior not described in the limits of (3.11a) and (3.13a). Features with aspect ratios from $A = [0.1 \dots 10]$ and pattern ratios from $P = [0.1 \dots 10]$ were simulated, resulting in 441 unique simulations as a function of varying geometry.

3.3.1 Geometry

The stamp deformation can be simulated using plane strain conditions when the stamp features are long parallel lines (giving $u_z = 0$). A cross section of these features is depicted in Figure 3-2. Symmetry provides a unit cell that is half of a characteristic feature as shown in grayscale. Normalized geometry was analyzed that was consistent with the dimensionless parameters introduced in Section 3.2.1. The contact width $w/2$ of each unit cell was unity for each geometry, while the height of the feature h and width of the unit cell roof $w/2$ were determined by the desired aspect ratio A and pattern ratio P (Figure 3-7a).

Table 3.2: Feature numeric simulation parameters

Geometric Parameter	Simulation Values	
Pattern Ratio, P	$10^{n/10}$,	$n = -10 \dots 10$
Aspect Ratio, A	$10^{n/10}$,	$n = -10 \dots 10$

The overall height of each unit cell was set to be the greater of three times the feature height h or unit cell width $\frac{1}{2}(a + w)$ to ensure a uniform far field pressure distribution at the top surface by Saint-Venant's principle [101].

Rigid geometry is used to represent the substrate. A rigid symmetry plane is used to constrain sidewall bulge to half of the roof width; the sidewalls of adjacent features with large aspect ratios can bulge and touch at this midplane. The use of these rigid elements (rather than very stiff deformable elements) results in a smaller, faster numerical implementation.

(a)   (b)
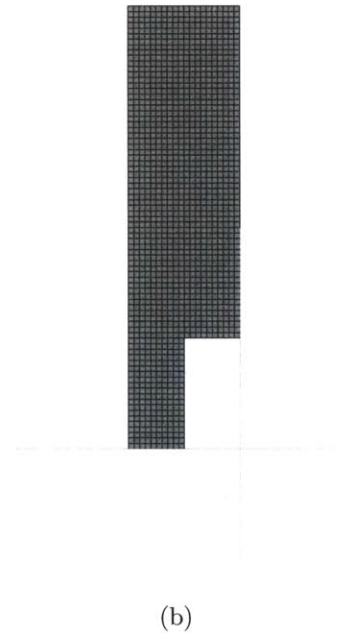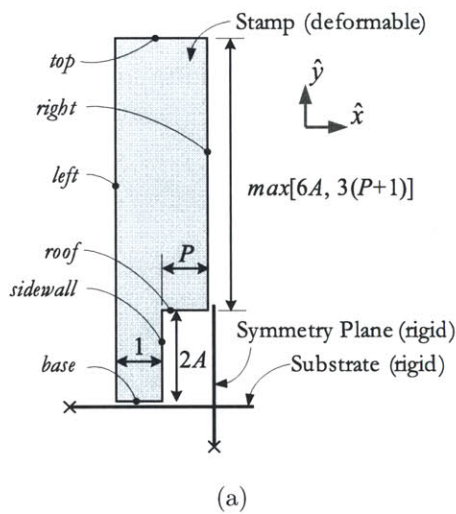
Figure 3-7: Feature numerical simulation geometry. (a) Example numerical simulation geometry showing characteristic dimensions, features, and rigid geometry; (b) example mesh with minimum of ten elements along an edge.

3.3.2 Meshing

Uniform rectangular mesh elements were used to mesh each unit cell. The mesh density was chosen so that minimum of ten mesh elements were used along the shortest edge of each simulation ($w/2$, $a/2$, or h) (Figure 3-7b). Testing of a higher mesh

80

density showed this to be sufficiently resolved for accurate results.

Large deformation plane strain elements with non-linear geometry conditions were used in each simulation (ABAQUS element type CPE4RH).

3.3.3   Material Model

An incompressible Neo-Hookean constitutive model was used in the simulations. Sensitivity testing did not show significant changes in the loading curve, collapse displacement, or deformed shape using a full Arruda-Boyce model [3]. Typical results (Figure 3-8) do not exhibit material stretches where the strain stiffening is important (above about $\lambda > 1.25$, cf. Figure 2-3) except near full collapse (Figure 3-8).

Incompressibility was assumed ($D_1 = 0$) and $E_0 = 3\mu_0 = 1$ was used to calculate material parameter C_{10} in the Neo-Hookean constitutive equation (2.10).

3.3.4   Boundary Conditions

Boundary conditions were used to impose symmetry and appropriate contact behavior (summarized in Table 3.3 and Table 3.4). Symmetry dictates no lateral translation or rotation at the left and right faces. Symmetry is imposed on sidewall bulging using a rigid symmetry plane coupled with a frictionless contact condition. The roof and sidewall faces have no-slip contact conditions (a.k.a. rough contact) with the rigid substrate element, as well as each other. The base of the feature has fixed displacement, emulating a no-slip contact condition but without the computational complexity of a contact condition.

Table 3.3: Microfeature simulation boundary conditions

Face	Boundary Condition
Left	$\hat{x}$ symmetry ($\partial v / \partial x = 0$, $u = 0$)
Right	$\hat{x}$ symmetry ($\partial v / \partial x = 0$, $u = 0$)
Top	Irrotational ($\partial v / \partial x = 0$, $u = 0$)
Base	Fixed ($u = v = 0$)

Table 3.4: Microfeature simulation contact conditions

Face 1	Face 2	Boundary Condition
Sidewall	Substrate	No slip (rough)
Sidewall	Symmetry Plane	Frictionless
Roof	Substrate	No slip (rough)
Roof	Sidewall	No slip (rough)

3.3.5 Loading

A rigid compressive displacement is imposed on the top surface of the unit cell (Figure 3-7a) from $X = 0$ to $X = 1$ in steps of $\Delta X = 0.01$.

3.3.6 Implementation

The numerical model was implemented in ABAQUS 6.10.

Scripts were used to automate execution of the simulations. ABAQUS can be executed either through the available user interface or at the command line. When a model is built in the ABAQUS interface, a Python language journal (.jnl) file is saved. ABAQUS can be executed from the command line by changing this journal file to a Python script file (.py) can calling "abaqus cae noGUI=JOURNALFILE.py", similar to executing a recorded macro command.

A master program was written in C++ to iterate through each combination A and P shown in Table 3.2. At each point, this master program alters the geometrical parameters in the slave Python script and executes ABAQUS through the command line. It required several days of computation time to simulate all permutations of A and P.
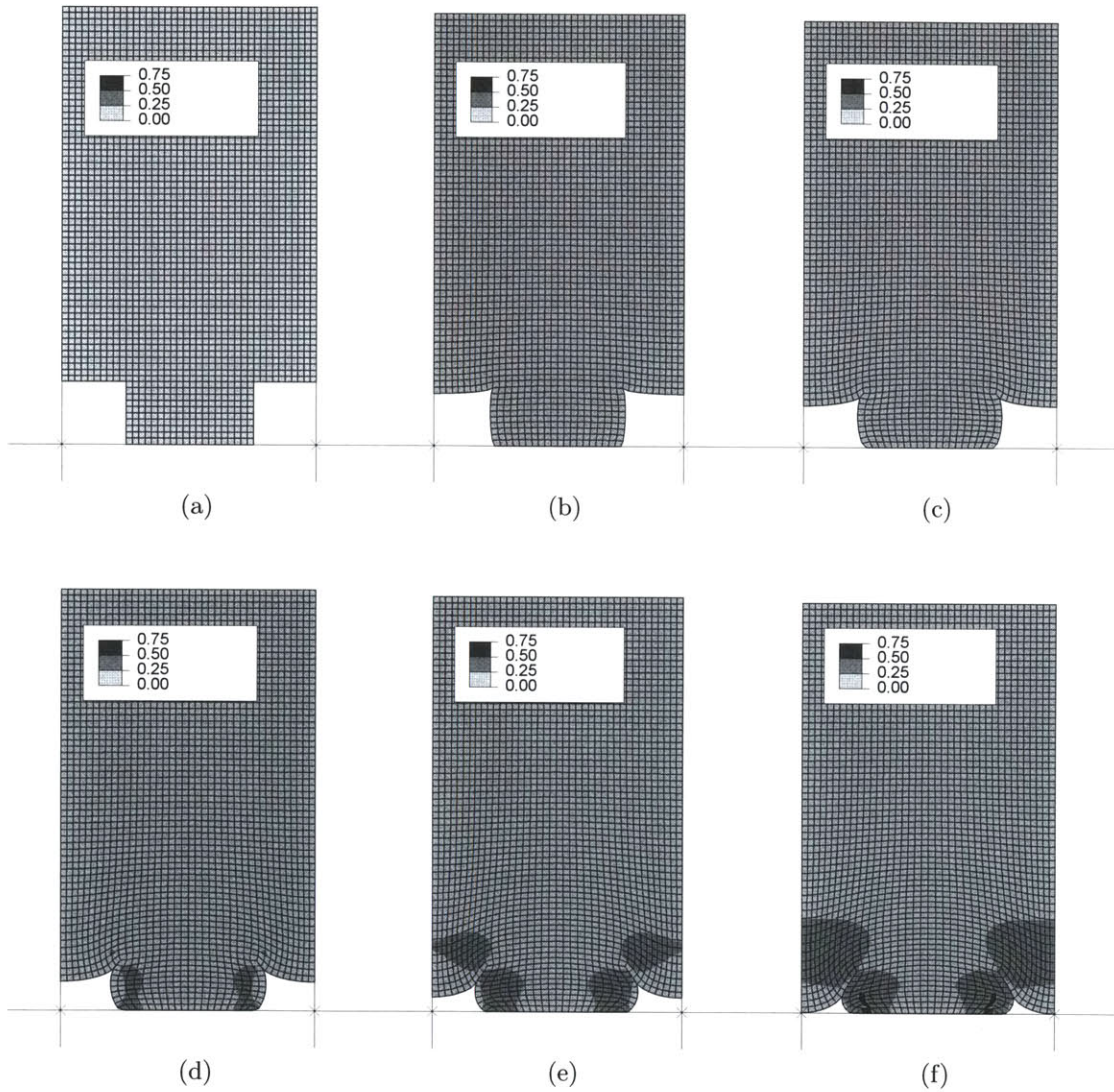
Figure 3-8: Example numerical simulation steps showing maximum principle strain $(1-\lambda)$; the feature in this figure has aspect ratio $A = 0.5$ and pattern ratio $P = 1.0$. The simulated unit cell has been mirrored for clarity. The deformed geometry is shown for (a) $X = 0$, (b) $X = 0.2$, (c) $X = 0.4$, (d) $X = 0.6$, (e) $X = 0.8$, and (f) $X = 0.94$ where roof collapse occurs.

3.3.7 Interpreting Results

During each simulation the internal energy U, displacement v_∞, and roof displacement $v(x = 0)$ of the model were recorded to allow reconstruction of the load-displacement curve $S(X)$ and collapse point X_c.

From the principle of virtual work, the strain energy in the simulation is the integral of force along the path of displacement. Writing force as the product of far field pressure and area gives

$$U = \int \sigma_\infty \frac{a + w}{2} dv_\infty \tag{3.34}$$

Differentiating twice with respect to v_∞ gives

$$\frac{d^2 U}{dv_\infty^2} = \frac{a + w}{2} \frac{d\sigma_\infty}{dv_\infty} \tag{3.35}$$

This result can be related to the dimensionless quantities to extract dimensionless stiffness K from each simulation. In the simulated geometry, $w = 2$, $a = 2P$, $h = 2A$, and $E = 1$. Using these values and the relationships in (3.34) and (3.35) gives

$$K = \frac{d^2 U}{dX^2} \frac{AP}{(1 + P)^2} \tag{3.36}$$

Stiffness K is a function of position X and, neglecting elastic instability (i.e. buckling), increases monotonically with X. The exact stiffening behavior depends on the feature geometry. For example, the simulation shown in Figure 3-8 stiffens slightly at $X = 0.4$ where the roof and sidewall make contact, and severely at $X = 0.94$ where the roof collapses. To generalize the behavior across all geometries, an ideal behavior is assumed that has constant stiffness $K = K_0$ for $X \in [0, 1)$ and infinite stiffness at $X = 1$ due to incompressibility. This approach is illustrated on a load-displacement plot in Figure 3-9.

The exact point of roof collapse X_c is detected in the simulations when $v(x = 0) = -h = -2A$ (Figure 3-10).

84
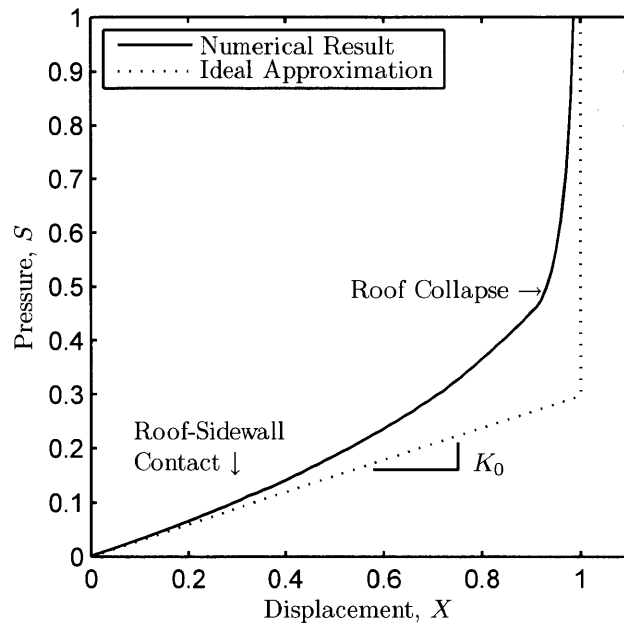
Figure 3-9: Dimensionless load-displacement behavior of feature in numerical simulation. Substantial stiffening occurs when the deformation imposes new boundary conditions, such as roof/sidewall contact or roof collapse. This behavior is approximated by an ideal load-displacement curve.
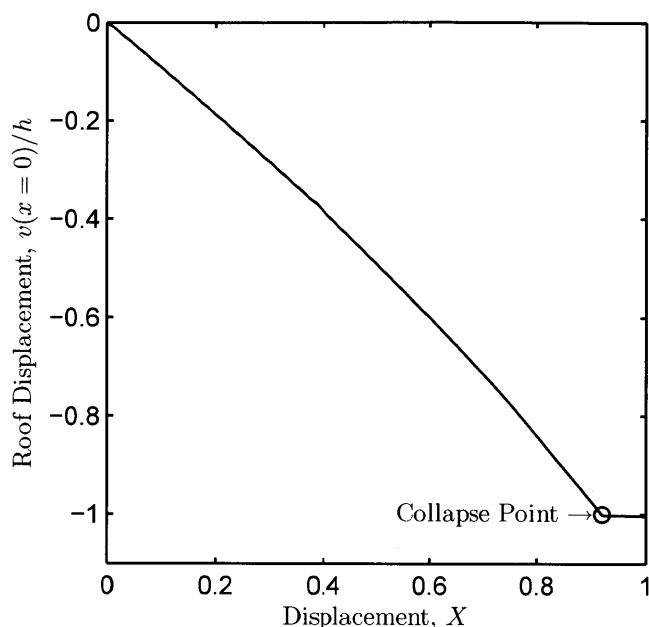
Figure 3-10: Roof displacement plot and corresponding roof collapse point from numerical simulations.

3.4 Experimental Methods

This section describes the experimental methods that were used to simultaneously measure the (i) load, (ii) displacement, and (iii) contact pattern of compressed micro features. This experimental protocol represents the first time that these three measurements have been made simultaneously for PDMS microfeatures. It is quite difficult to isolate the displacement behavior of these very small features; the key to the approach taken here is to use a very thin but very wide stamp specimen so that the body of the stamp appears very stiff compared to the microfeatures. The stiff stamp body allows extraction of a meaningful measurement of feature behavior from the resulting experimental data.

3.4.1 Experiment Design

A set of experiments were designed to test the behavior of polydimethylsiloxane (PDMS) features across a range of reasonable A and P values. A photomask was

designed with 20 μm and 50 μm line and post features on varying pitches (Table 3.5). Control areas were included on the photomask to create regions of (i) no photoresist and (ii) fully crosslinked photoresist . Each pattern was organized into 12.5 mm square regions.

Selectively exposing a layer of photoresist with this photomask creates a master template with a variety of pattern ratios P and an aspect ratio defined by the thickness of the photoresist. Because multiple feature scales and pattern ratios are incorporated in each master template, very few master wafers and stamps need to be made to span a large portion of the $A - P$ space. The post features on the master templates were not used in this particular set of experiments.

3.4.2 Test Specimens

A master surface was created by patterning a wafer with SU8 resist (Microchem). Each wafer contained 20 and 50 μm wide lines on six different pitches and included control regions with no features, as defined by the photomask described above. Four wafers were developed with different resist thicknesses and measured using a Zygo interferometer. This approach resulted in four different aspect ratios (A) and six pattern ratios (P) for each feature size (Table 3.6).

PDMS stamps were cast 200 μm thick using vacuum-assisted injection molding between two precision ground aluminum plates separated by a shim. The mold was cured at 60° C for two hours and subsequently parted using pressurized ethanol. The stamp was diced into 12.5 mm square samples using a razor blade.

Each PDMS sample was mounted on a glass slide with the microfeatures facing

Table 3.5: Mask Design

Parameter	Value
Sample Area [mm]	12.5 $\times$ 12.5
Feature Width, w [μm]	20, 50
Pattern Ratio, P	0.3, 0.5, 0.8, 1, 1.5, 3
Control	Full Exposure / No Exposure

Table 3.6: Feature experimental parameters

Geometric Parameter	Experimental Values
Feature Width, w [μm]	20, 50
Pattern Ratio, P	0.3, 0.5, 0.8, 1, 1.5, 3
Resist Thickness, h [μm]	17, 30, 54, 77

upward. To mount each sample, the slide was flooded with ethanol, the sample floated into place, and the ethanol allowed to evaporate. This technique eliminated both air pockets and residual stresses in the thin PDMS stamps.

3.4.3 Experimental Protocol

An optical prism and steel hemisphere (Figure 3-11) was placed on top of each sample. The prism permits observation of the contact region during loading, while the hemisphere provides a single contact point on which to exert a vertical load with no lateral tractions.

(a)   (b)   (c)
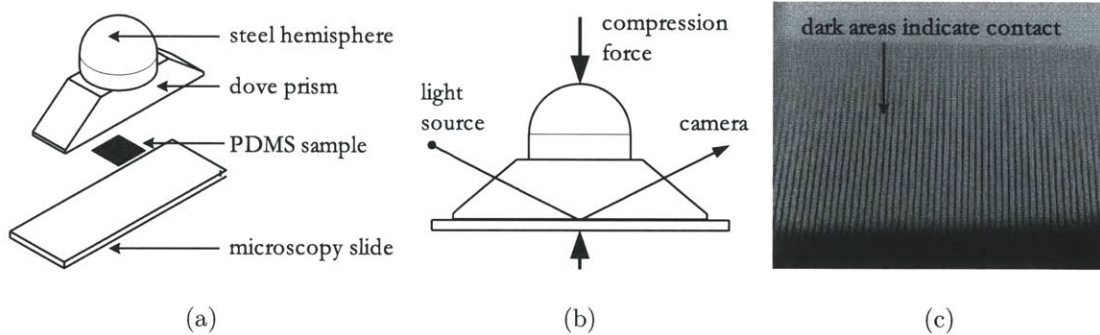
Figure 3-11: Experimental construct and contact visualization. (a) PDMS samples were mounted on glass slides with the microfeatures facing away from the slide. A 15 mm dove prism with a 25 mm hardened steel hemisphere (combined weight of 1.2 N) was placed on top of the sample using an alignment fixture. (b) The entire assembly was compressed between the platens of a load frame. A light source and camera were placed at opposite ends of the dove prism to capture the stamp contact pattern during loading. (c) A typical contact image of 50 μm wide lines as viewed by the camera.

The sample, with the prism and hemisphere, were mounted in an Instron load

frame and compressed at a rate of 1 μm/s. The samples were precycled once to 80 N to ensure full contact and alignment between the load frame elements before ramping to a final value of 350 N (0.5 MPa and 2.25 MPa mean contact pressure, respectively). Displacement was measured via a linear variable differential transformer (LVDT), force by a 1 kN load cell, and contact collapse was monitored by a camera through the optical prism. The optical prism and loading components resulted in a preload of 1.2 N (7.68 kPa) that was not captured by the load cell.

(a)   (b)
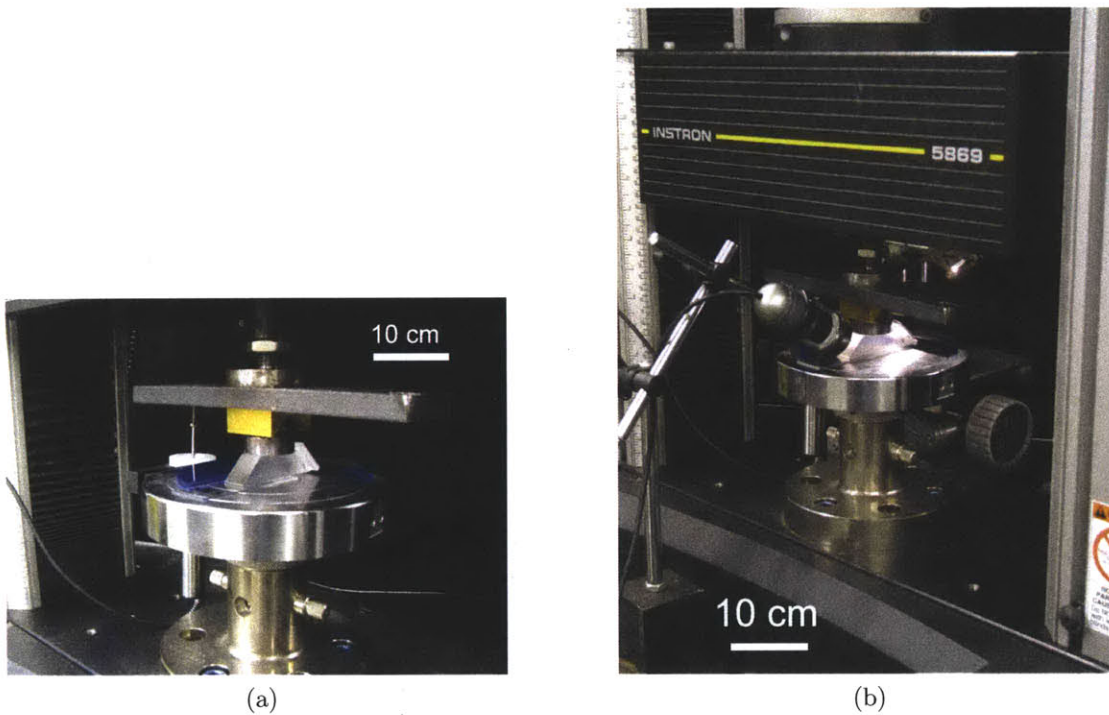
Figure 3-12: Feature loading experimental apparatus. (a) The experimental construct was compressed in an Instron load frame. The sample was located on the lower platen with an alignment fixture and compressed through contact of a steel hemisphere and v-groove coupling. Displacement between the lower platen and v-groove mount was measured with an LVDT. (b) A light source and camera were positioned on opposite sides of the prism to visualize the contact interface during loading.

The collapse mode (Figure 3-1) of each sample was determined by inspection of the camera frames (Figure 3-13). Sidewall collapse was identified when the field of view became uniformly dark, roof collapse was identified when the pitch of the pattern doubled before full collapse, and buckling was identified when the width of

the features suddenly and dramatically decreased, resulting in a lighter field of view.
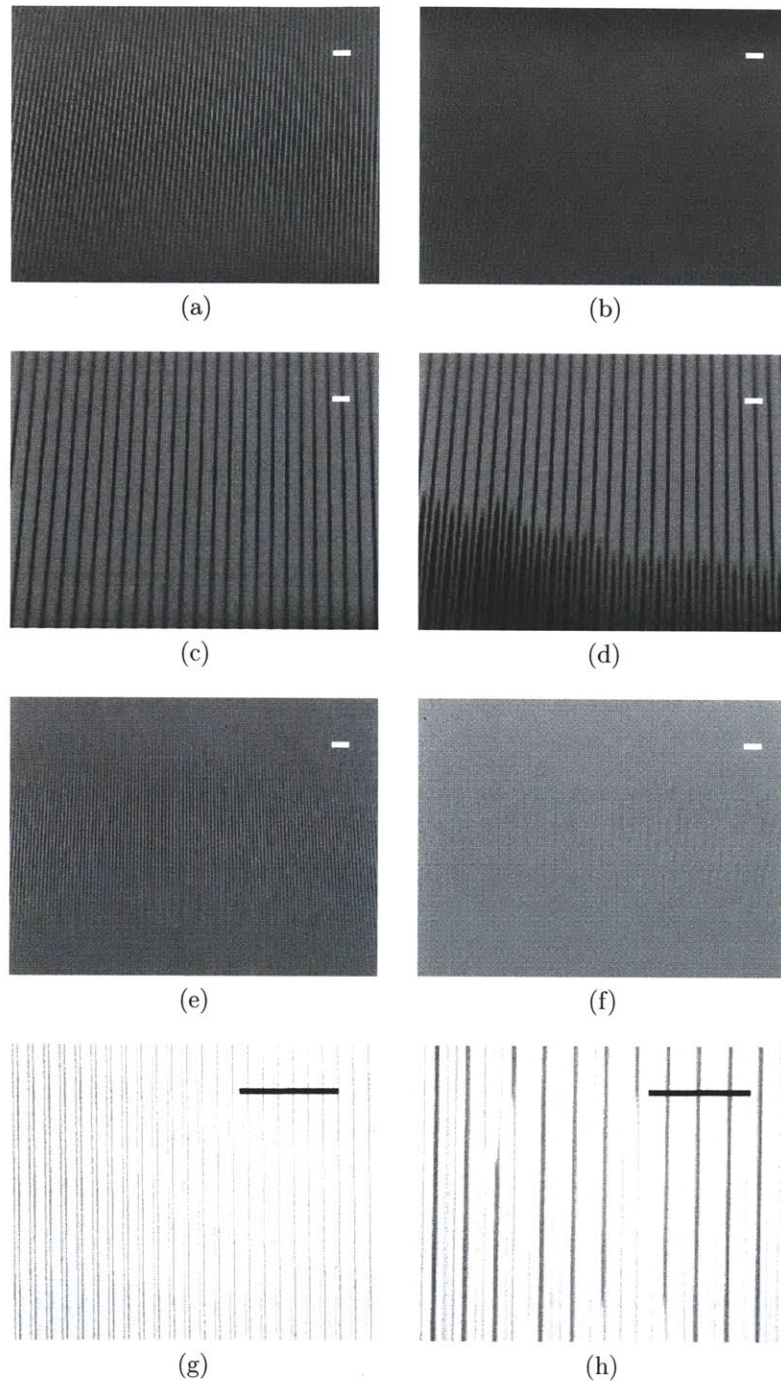
Figure 3-13: Experimental feature collapse images. Images before and after (a-b) sidewall collapse (w=50μm, a=40μm, h=54μm), (c-d) roof collapse (w=50μm, a=150μm, h=17μm), (e-f) buckling (w=20μm, a=30μm, h=54μm), and (g-h) lateral collapse (w=20μm, a=10μm, h=30,54μm). (a-f) were observed using the experimental setup described; (g-h) are optical micrographs of the stamp features. Scale bars: 200 μ m.

3.4.4 Data Collection

A PC was used to log data from the load frame and camera. This approach allowed exact correlatiion of the load-displacement data and camera images in real time during the experiment.

The Instron 5800 load frame used in these experiments has facilities for analog output of the measurement signals. The LVDT position signal and load cell force signal were output on two separate analog channels of the load frame. These analog signals were interfaced with the data logging computer via a National Instruments PCIe-6343 data acquisition card.

The camera (Dino-Lite AM413T) is supplied with a USB interface.

A Windows program was written in C++ to record data from the load frame and camera using C++ API's supplied by National Instruments and Dino-Lite. Each camera frame was converted from a 24 bit RGB image to an 8 bit grayscale image by averaging each color channel. This 8 bit pixel data was saved to an indexed binary file for each camera frame. The unfiltered analog signals were recorded at 10 kHz, registered against a timestamp and image index, and saved to a binary file with double floating point precision.

3.4.5 Material Characterization

The elastic modulus of PDMS is highly dependent on mixing and curing parameters. To experimentally determine material properties, two tensile test samples were cut from a portion of each stamp. The exact thickness of each specimen was measured with a Zygo interferometer. The specimens were tested according to the protocol described in Section 2.4; the initial elastic modulus $E_0 = 3\mu_0$ of each stamp was determined by fitting an incompressible Neo-Hookean constitutive model (2.16) to the experimental data at low stretches ($\lambda_1 < 1.2$).

All specimens were cast, tested, and characterized within a period of several days. It is not believed that any significant temporal drift in material parameters occurred over this time period.

3.4.6 Measurement Repeatability

The repeatability of each measurement type was examined with a repeatability study. Roof collapse measurements were repeated using a sample with w=50 μm, A=0.6, P=3.0. The initial stiffness, maximum displacement, collapse force, and onset of collapse displacement were measured independently six times. Buckling measurements were repeated using a sample with w=50 μm, A=1.54, P=3.0. Buckling force at loading and unloading was measured independently six times. By inspection, each set of six loading curves appeared nearly identical. The 95% confidence intervals (CI) associated with the results of these tests are summarized in Table 3.7.

Table 3.7: Feature measurement repeatability, showing sample mean μ, sample standard deviation s, and a 95% confidence interval (95% CI)

Measurement	μ	s	95% CI
Initial stiffness[N/μm]	1.32	0.09	$\pm$0.23
Maximum displacement [μm]	22.3	0.43	$\pm$1.10
Collapse force [N]	35.8	1.03	$\pm$2.64
Collapse displacement [μm]	17.9	0.51	$\pm$1.32
Buckling (loading) [N]	15.1	0.20	$\pm$0.52
Buckling (unloading) [N]	9.40	0.09	$\pm$0.23

3.5 Results

This section presents the stiffness and collapse mode of each experiment and compares these results to FEA results. Each of the following subsections discuss these phenomena and their comparison with analytic models from Section 3.2. These results provide collapse mode boundaries to predict the type of failure that will first occur for a particular stamp pattern.

3.5.1 Stiffness

Load-displacement data from the numeric simulations exhibited common characteristics: deformation would initially progress linearly for $X \ll 1$, exhibit large defor-

mation stiffening at moderate X, and finally converge to an asymptote at $X = 1$ due to incompressibility (Figure 3-9). To characterize the behavior of each simulation, an initial stiffness $K = dS/dX$ was fit for $X \leq 0.01$.

The analytic stiffness results from (3.11a) and (3.13a) apply only in the appropriate limits (Figure 3-14).
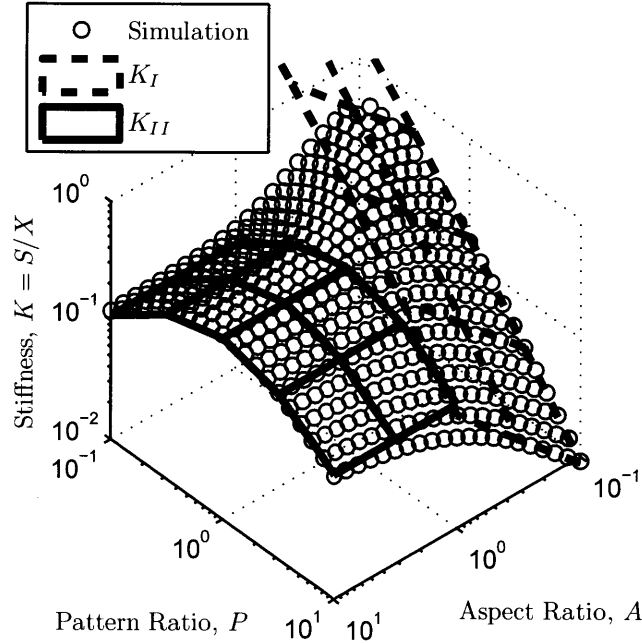
Figure 3-14: Feature stiffness from (3.11a) and (3.13a) shown superimposed over FEA stiffness results. The models and simulations show excellent coherence in the appropriate limits

From Figure 3-3, all deformation in the first limit occurs in the roof of the features (resulting in stiffness K_I), while in the second limit all deformation happens in the features themselves (resulting in stiffness K_{II}). If the models in these two limits are independent, a general model of stiffness can be developed by simply considering the two limits as springs in series, that is:

$$\frac{1}{K} \approx \frac{1}{K_I} + \frac{1}{K_{II}} \tag{3.37}$$

For tall features that are spaced far apart, this series approximation fits the FEA

94
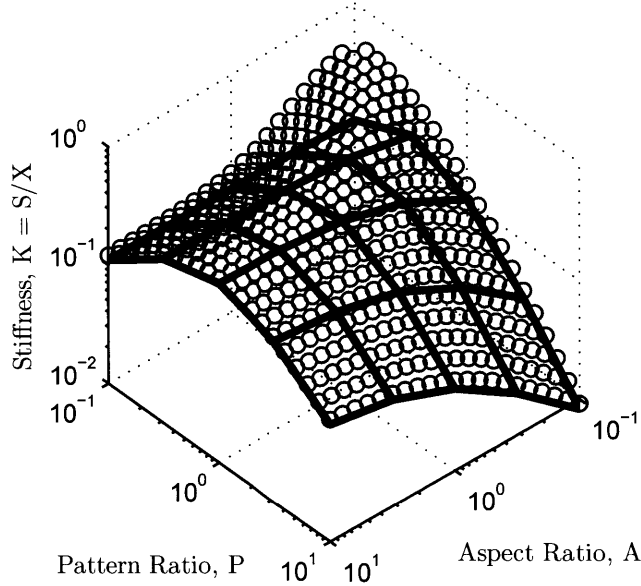
Figure 3-15: Series spring model of feature stiffness using K_I and K_{II} from (3.37) shown superimposed over FEA stiffness results. The tentative model and simulation results agree well except for the rear quadrant with small A and small P.

data well. However, for short, closely spaced features $(A, P \ll 1)$ the series model underestimates the actual stiffness from the FEA simulations (Figure 3-15). In this region, the no-slip boundary condition at the feature interface results in much higher stiffness than predicted by the frictionless column model of K_I. To empirically adjust (3.37) where $A, P \ll 1$, a correction factor is incorporated of the form

$$\frac{(A + P)^n + m}{(A + P)^n} \tag{3.38}$$

which converges to unity for large $(A+P)$. Using these modifications, constants n and m were fit by regression (1 and 0.6, respectively). This procedure results in a general closed form model for stiffness K (Figure 3-16), which can be shown to converge to the form of (3.11a) and (3.13a) in the appropriate limits:

$$K = \frac{1}{K_I(A, P)^{-1} + K_{II}(A, P)^{-1}} \frac{(A + P) + 0.6}{(A + P)} \tag{3.39}$$

95
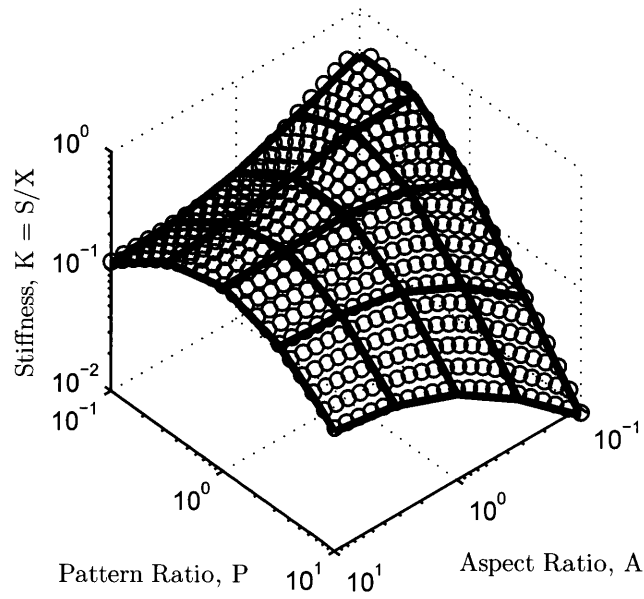
Figure 3-16: Final closed form model of feature stiffness from (3.39) shown superimposed over FEA stiffness results. This single model shows excellent agreement with the simulation results.

The maximum displacement $v_{\infty,max}$ and initial stiffness k (in Pa/m) were calculated to characterize each experimental load-displacement curve. Load-displacement curves were first corrected by subtracting the compliance of control specimens (without features) to isolate the behavior of the microfeatures (Figure 3-17).
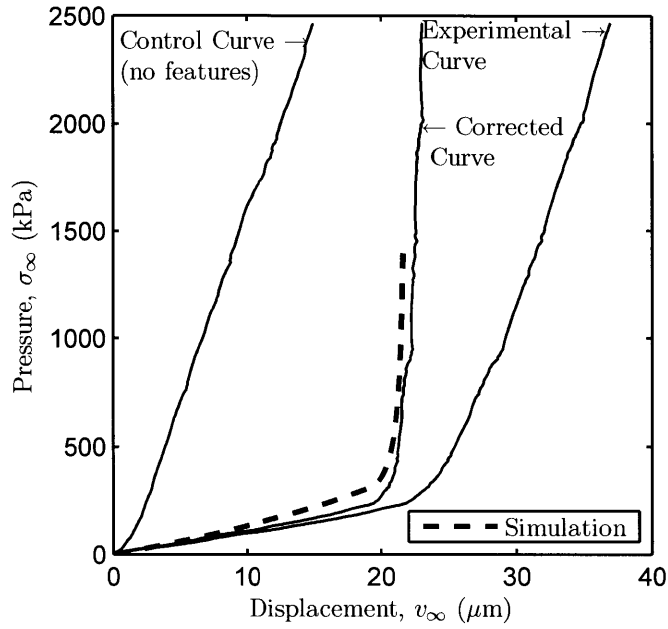
Figure 3-17: Experimental load-displacement curves showing the control sample (with no features), the sample of interest (with features), and the corrected curve where the control effect has been subtracted. After correction for the control stiffness, the data represents the response of only the features and fits well with the corresponding FEA results.

The maximum displacement $v_{\infty,max}$ was determined from the corrected data, showing good agreement with the maximum displacement based on incompressibility (Figure 3-18).
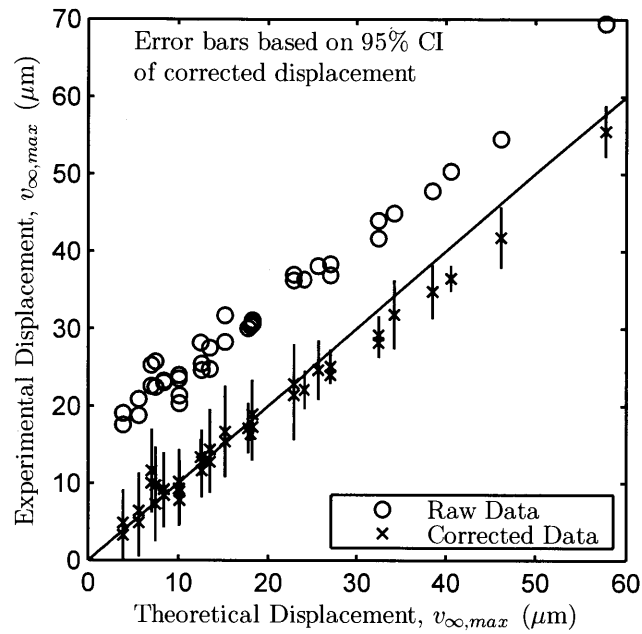
Figure 3-18: Theoretical and experimental maximum feature displacement $v_{\infty,max}$, both before and after correction of the experimental data with the control sample data. The theoretical maximum displacement is based on incompressibility at $X = 1$. After correction, the prediction and measurement match within experimental uncertainty.

Experimental stiffness was found by fitting a least-squares line to the load-displacement data. The experimental stiffness results are summarized in Figure 3-19, where they are plotted against the values predicted from the empirical model of (3.39).
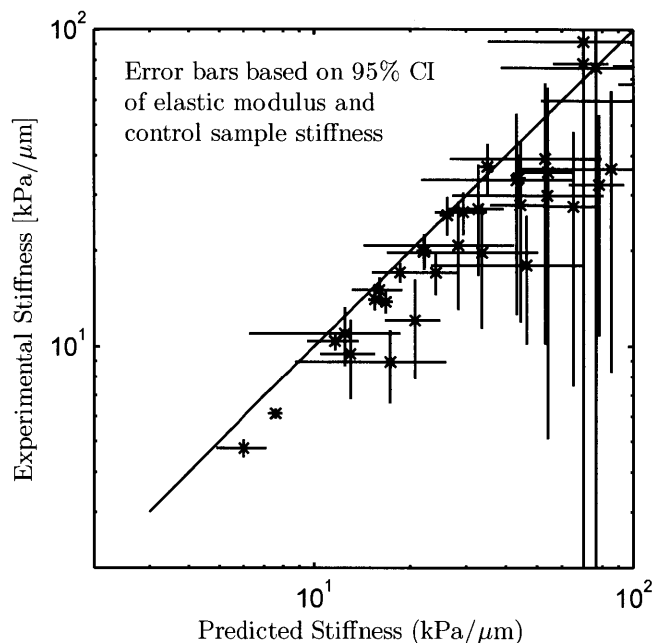
Figure 3-19: Predicted stiffness values from the proposed model (3.39) versus the experimentally measured values. Error bars along the prediction axis represent a 95% confidence interval based on variation in measurements of the elastic modulus, while error bars along the experimental measurement axis represent a 95% confidence interval based on control sample variation. The model and experimental values agree well within the experimental uncertainty, though this uncertainty is large for high stiffness features that are on the order of the control sample stiffness.

3.5.2 Roof Collapse

The collapse point in each numerical simulation was interpreted as the time when the roof first made contact with the substrate (Figure 3-8). The far-field pressure and displacement were recorded at this point for each simulation.

Images recorded during the loading experiments were used to determine the point of roof collapse. During the experiments, roof collapse began from the center of samples, and within some finite displacement spread to the entire stamp (these edge

effects are evident in the partial collapse shown in Figure 3-13d). The collapse points reported in the following figures are the critical point at which collapse was first observed.

Both the numeric and experimental collapse pressures agree well with the model presented in (3.17). The experimental roof collapse pressure is plotted versus the predicted stiffness in Figure 3-20. (3.18) predicts that collapse occurs at $X > \pi/4$. This corresponds to a lower bound on collapse pressure $S = \pi/4 \cdot K$, which is plotted against the experimental data in Figure 3-20.
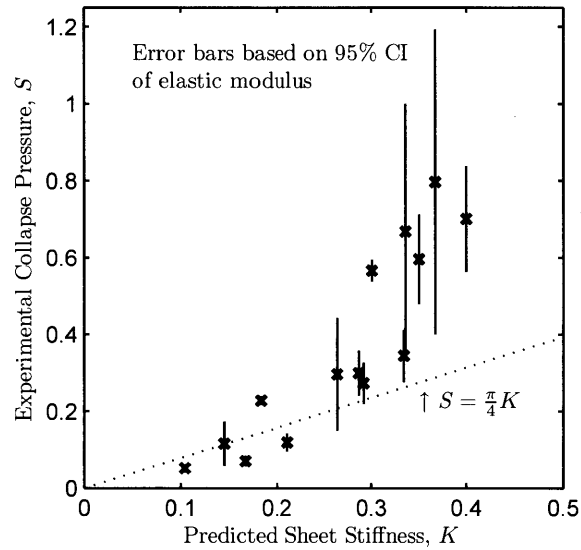
Figure 3-20: Experimental roof collapse pressure as a function of predicted stiffness. The collapse pressure has a lower bound of $S = \pi/4 \cdot K$. The experimental data support this lower bound, while some values fall substantially above this bound due to large deformation stiffening before collapse.

Simulations validated that roof collapse occurs in the range $X = [\pi/4, 1)$ as predicted using (3.18). The roof collapse observed during experiments fell within this same range (Figure 3-21).
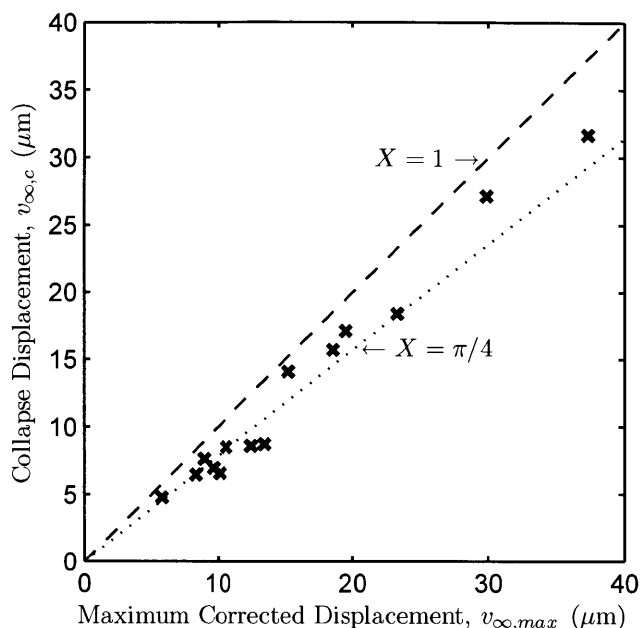
Figure 3-21: Roof collapse displacement $v_{\infty,c}$ from experimental data set as a function of maximum displacement $v_{\infty,max}$. Each simulation exhibited the onset of roof collapse between $X = \pi/4$ and $X = 1$ as predicted analytically.

3.5.3 Buckling

Buckling during experiments occurred instantaneously and completely across the stamp at a particular load, allowing determination of a single collapse pressure and displacement. The collapse pressure upon loading and unloading was determined from local extrema in the corrected load-displacement curve (Figure 3-22).

The critical buckling pressures are compared to the model in (3.27) in Figure 3-23. Because coefficient b_c in (3.27) is highly sensitive to boundary conditions, b_c is fit by least-squares regression to the unloading data in each plot. These coefficients range from 0.20 to 0.44; one can conclude that the fixed-free boundary condition ($b_c = 1/4$) provides a practical lower bound on buckling pressures. Using these boundary condition coefficients and a value of $W_{ad} \approx 200$ mJ/m^2 for PDMS on glass [2], the model presented in (3.27) is plotted in each figure using stiffness K proposed in (3.39). Curves for pinned-pinned and fixed-free boundary conditions are shown in

101
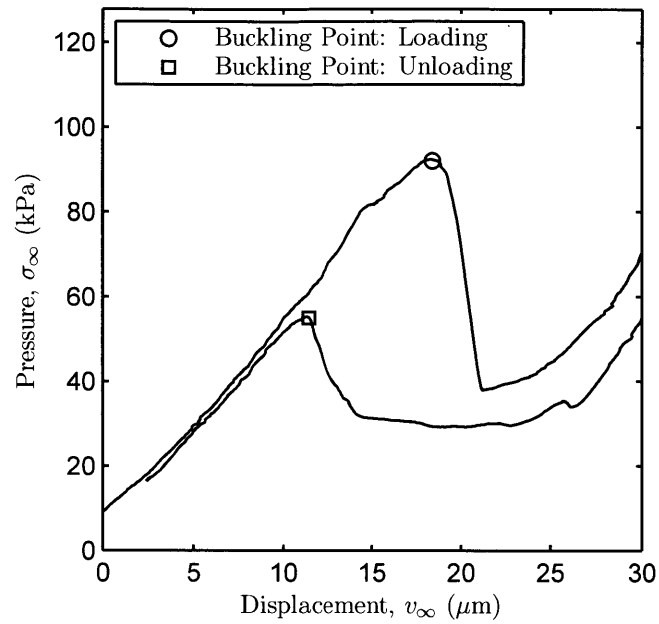
Figure 3-22: Typical experimental load-displacement curve for buckling. The loading and unloading buckling pressure for each sample were determined from the local maxima on each respective curve.

each figure for reference.
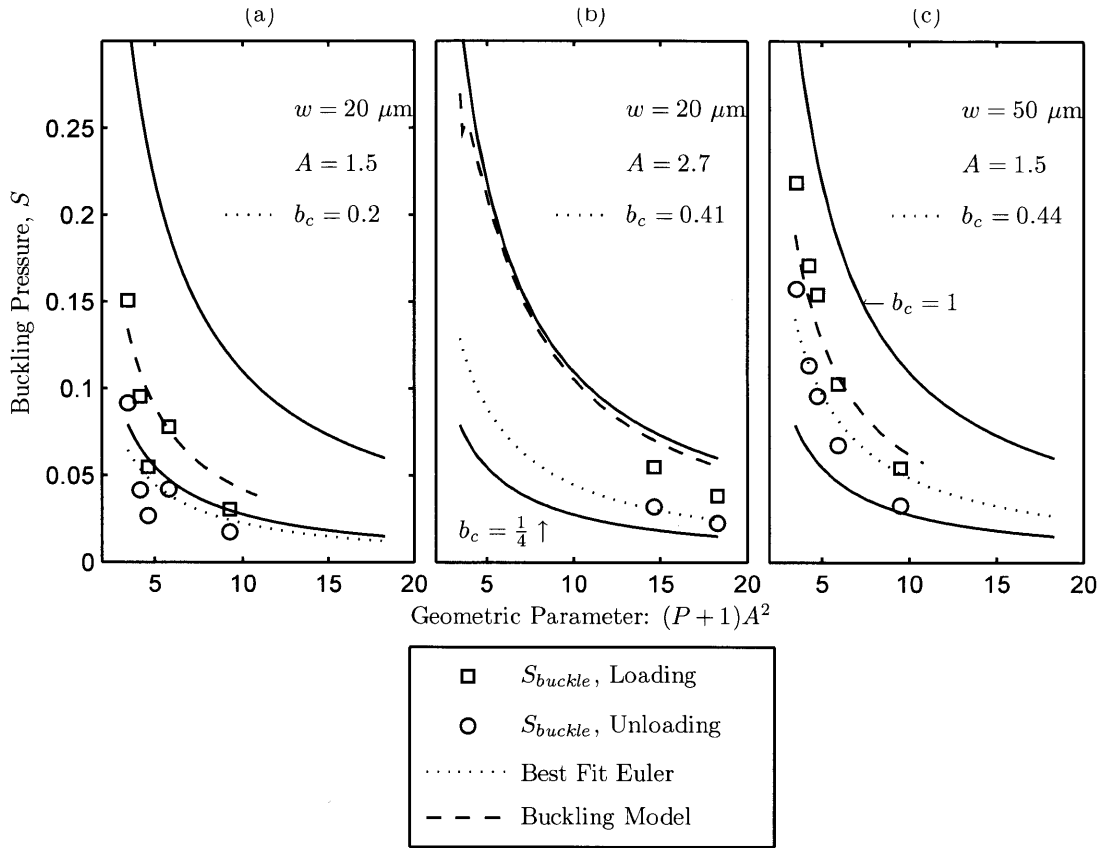
Figure 3-23: Critical experimental buckling pressures sorted by aspect ratio. Boundary condition coefficient b_c is fit to each set of unloading collapse points using (3.21) and the loading model of (3.27) is plotted for each aspect ratio using this b_c. Curves for $b_c = 1/4$ (fixed-free) and $b_c = 1$ (pinned-pinned) are shown for reference.

3.5.4 Failure Mode Prediction

Based on the models and empirical observations presented here, boundaries are developed that predict the particular mode of collapse. These boundaries can be used as a design tool to understand the expected collapse mode, for example to optimize feature aspect ratio. Failure mode is predicted with the following precedence:

(i) The condition for lateral collapse is examined to determine the inherent stability of features.

(ii) The critical collapse pressure for buckling is examined to determine stability under load.

103

(*iii*) Roof collapse and sidewall collapse are differentiated by the feature geometry.

The condition for lateral collapse is given by (3.33), where conformability Cf is calculated using the work of adhesion between the stamp material and itself. If this condition is violated, the features will not be useable for printing.

$$\frac{P^2}{4}\frac{A^2 + \alpha_s/3}{(A^3 + \alpha_s A)^2} < Cf \tag{3.40}$$

Buckling is a dominant mode when the critical pressure is less than the pressure of either roof collapse or lateral collapse. From (3.14) and (3.18) collapse occurs at approximately $X_c = \pi/4$, giving an ultimate collapse pressure of approximately $S_c = \pi/4 \cdot K$. A criterion for buckling is thus $S_{\text{buckle}} < \pi/4 \cdot K$, given by (3.23) and (3.39) respectively. In this criterion, conformability Cf is calculated using the work of adhesion between the stamp and substrate materials:

$$b_c\frac{\pi^2}{9}\frac{1}{(P+1)A^2} + \sqrt{\frac{2KCf}{AP}} < \frac{\pi}{4}K \tag{3.41}$$

If neither lateral collapse nor buckling occurs, the features experience either roof collapse or sidewall collapse. In both numeric and experimental results, roof collapse occurred only when $A < P$. Identically, only when the feature spacing a is greater than the feature spacing height h (such as shown in Figure 3-1b) can the roof touch the substrate. In the alternative case that $A > P$, the sidewalls of each feature bulge and touch the substrate as $X \to 1$. The empirically developed condition for roof collapse is thus

$$A < P \tag{3.42}$$

Each of these boundaries was computed numerically and superimposed on the experimental results in Figure 3-24. For numeric calculation of the boundaries, material parameters are assumed to be an elastic modulus E_0=1.5 MPa, PDMS-PDMS work of adhesion W_{ad}=44 mJ/m^2 [11], PDMS-glass work of adhesion W_{ad}=200 mJ/m^2 [2], and the average experimental buckling boundary condition constant $b_c = 0.4$ (Fig-

ure 3-23). These boundaries for observed collapse mode show excellent agreement with the experimental data.
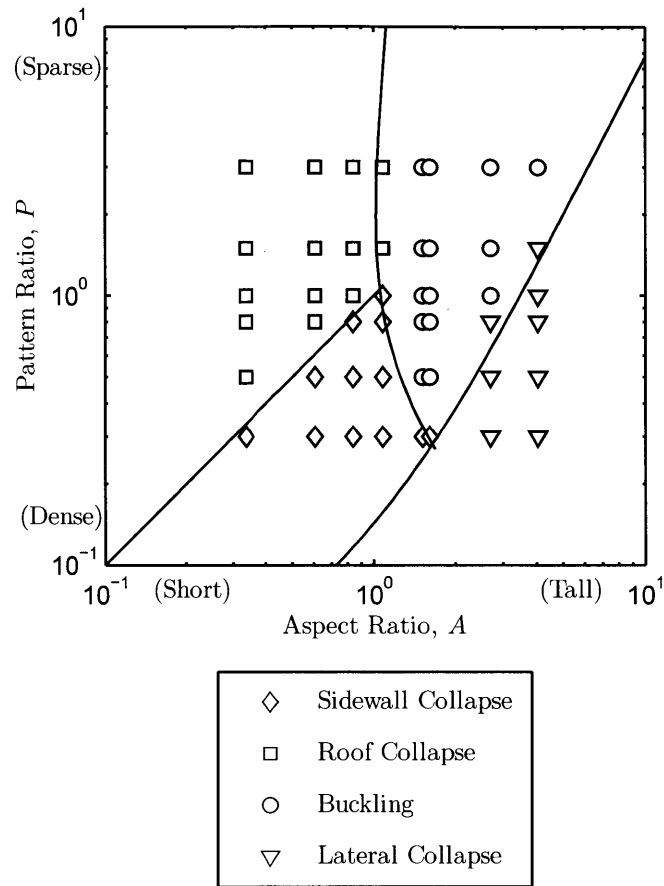
Figure 3-24: Feature collapse modes from experimental observations are plotted as a function of aspect ratio A and pattern ratio P. Boundaries from the proposed models are superimposed for reference, showing excellent prediction of collapse mode regimes.

3.6 Discussion

3.6.1 Experimental Agreement

The experimental data matches the analytical and numerical results well. Deviation from the expected values is due to difficulties in experimentally isolating the behavior of the microfeatures from the behavior of the stamp thickness.

In calculations of stiffness, it was assumed that the stamp body and stamp features are independent (Figure 3-17); in reality the behavior of the stamp body changes because the microfeatures alter the boundary condition against the observation prism. This assumption gives corrected experimental curves that are less stiff than the true feature behavior; this effect is visible in Figure 3-19 where the experimental values tend to be just less than the predicted values. Moreover, the uncertainty associated with high k features are due to difficulty in resolving the feature and control behavior when they are of similar magnitudes.

In Figure 3-20, the reported experimental collapse pressure is the *mean* pressure on the experimental sample when collapse is first observed, often at a small point of maximum pressure at the center of the sample. Thus, the true *local* pressure that causes collapse is expected to be greater than the experimental values reported. This observation explains why several values fall below the expected collapse pressure bound ($S = \pi/4 \cdot K$).

3.6.2 Scaling

The results have been reported in dimensionless quantities to allow extrapolation to other scales, especially sub-micron or nano-scale features. While these features would be too small to effectively characterize using the experimental methods described here, it is believed that the models will accurately describe collapse behavior across these scales.

The reported difficulties associated with nano-scale printing can be explained using the models in this chapter. As the feature scale shrinks, the conformability Cf

106

increases. This has the effect of shifting the buckling boundary to the right and the lateral collapse boundary to the left (Figure 3-25), such that lateral collapse becomes a limiting design factor. Features on the order of 100 nm often experience lateral collapse in PDMS, leading to development of harder elastomeric stamp materials [89, 12, 100, 82]. The example of collapsed 350 nm PDMS gratings given in [82] is just on the critical boundary predicted by (3.33).
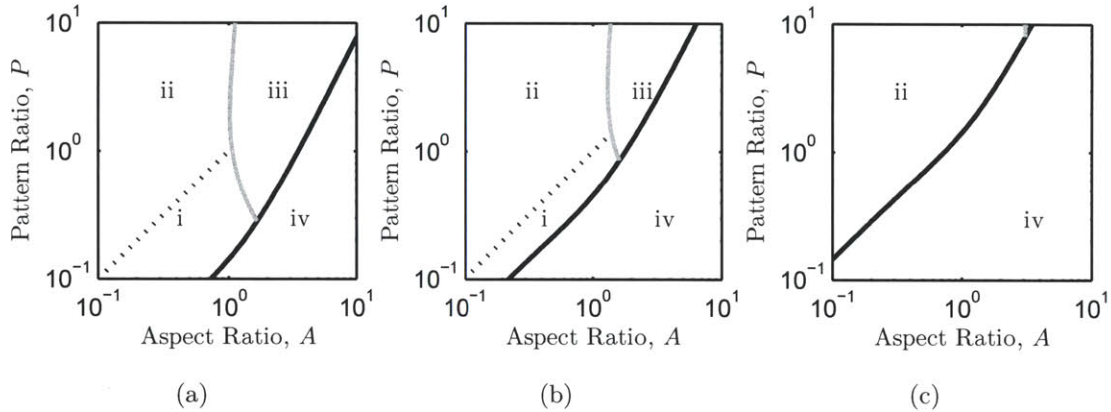
Figure 3-25: Predicted collapse mode boundaries as a function of feature scale for (a) 20 μm, (b) 2 μm, and (c) 200 nm features. Collapse modes are (i) sidewall collapse, (ii) roof collapse, (iii) buckling, and (iv) lateral collapse. Material properties of PDMS-PDMS $W_{ad} = 0.044$ mJ/m^2, PDMS-substrate $W_{ad} = 0.2$ mJ/m^2, and elastic modulus $E_0 = 1.5$ MPa are assumed.

This scaling result shows that at the nanoscale, the dominant defect modes are roof collapse and lateral collapse.

3.6.3 Alternative Geometry

This chapter analyzes regular grating patterns because they are a commonly fabricated structure and admit a tractable plane strain analysis. An extension of this study is a similar analytical and experimental approach towards arrays of post features. In many of the analyses (derivation of column stiffness, buckling, and lateral collapse), this can be accomplished by assuming plane stress rather than plane strain, giving $E^* = E$ rather than $E^* = \frac{4}{3}E$.

More interesting geometry, such as metallic interconnects and contacts, form regular grids of feature patterns. The behavior of these two dimensional patterns can be approximated by the equivalent plane strain behavior of a cross section using the models given here (for example, a stamp with 5 μm tall, 5 μm wide feature that forms a 50×100 μm grid around display pixels can be modeled as a grating with $w = h = 5$ μm and $a = 45$ μm). This approach will provide a conservative estimate of collapse behavior. If more accurate models of behavior are required, the results of this study show that finite element simulations provide very accurate predictions and that an ideal linearized approximation of feature behavior (Figure 3-9) gives a strong lower bound on expected collapse pressures.

3.7 Summary

This chapter characterized the deformation of PDMS microfeatures through analytical, numerical, and experimental results. A model for feature stiffness ((3.39)) has been developed by studying the load response across two orthogonal geometric parameters (aspect ratio A and pattern ratio P).

These results are also able to predict the collapse mode that a particular set of features will experience. (3.14), (3.17), and (3.18) predict the critical collapse pressure and displacement for sidewall and roof collapse modes. Buckling predictions were augmented with the effect of work of adhesion, and in these experiments show that features buckle as if they are fixed-free columns (3.27). The buckling point may be greatly delayed if the stamp is fixed relative to the backplane, resulting in a fixed-pinned architecture. Lateral collapse is more accurately predicted by adjusting the collapsed mode shape to that of a cantilever beam (3.33). These models predict buckling and lateral collapse at about one-half the aspect ratio predicted by the results of Hui et al. [47]. Using these more accurate predictions of collapse mode, the feature aspect ratio can be optimally designed to provide the maximum pressure or displacement before feature collapse.

The model for feature stiffness K provides a link between load and displacement

behavior of μCP stamp features. This stiffness, along with the maximum displacement at $X = 1$, permits observing two inherent load and displacement limits. First, the permissible load can never be greater than the order of K. Regardless of the particular choice of A and P, K never exceeds unity, hence imposed pressures should never exceed the elastic modulus of the stamp material. Second, displacements imposed on stamp features must never be greater than the characteristic feature dimension because buckling and lateral collapse occur above aspect ratios of about unity.

Ultimately, this chapter has developed and experimentally validated a general model for the load-displacement behavior of elastomeric microfeatures across a practical range of feature patterns and aspect ratios. This work provides new analytic and empirical models to create a coherent framework for predicting feature stiffness k and collapse pressure p_c. In subsequent chapters, this enables examination of macro scale stamp deformation behavior and design of robust stamp geometry.

Chapter 4

Roll Based Contact Mechanics

4.1 Roll Based Stamp Contact

While several demonstrations of roll based μCP have been reported [105, 87, 4, 17, 56, 96, 92, 107], there is little understanding regarding phenomena specific to the roll-substrate interface. Independent of particular inks or substrate materials, the integrity and quality of the stamp contact pattern at this interface is paramount to success of the process. The corresponding high surface energy and low elastic modulus of PDMS stamps guarantees conformal contact over nanoscale asperities, but permits stamp feature deformation and collapse at moderate contact pressures. As demonstrated in Chapter 3, commonly identified collapse modes (Figure 4-1) occur at contact pressures much less than the elastic modulus of the stamp material.

(a)　　　　(b)　　　　(c)　　(d)
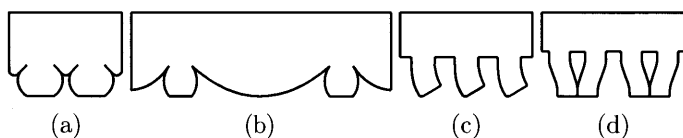
Figure 4-1: Elastomeric stamp features deform or collapse in modes like (a) bulging, (b) roof collapse, or (c) buckling when compressed at the contact interface. If the aspect ratio of features is too large (d) the features will adhere to each other even in the absence of contact forces.

In this chapter, the contact pressure at the stamp interface is considered a surro-

gate for contact pattern quality. Finite compressive pressures below a certain threshold will guarantee contact but not cause feature collapse. The results of Chapter 3 clearly delineate the boundaries between expected feature collapse mode and provide models for critical contact pressures at collapse. Despite this work, it remains to be seen how this feature behavior translates to a roll-based contact regime such as that in roll-to-roll or roll-to-plate printing.

The displacement-dependent stamp deformation between rigid rolls is difficult from the perspective of both analysis and implementation. In analysis, the finite stiffness of the microfeatures has a non-negligible effect on the contact pressure distribution. In implementation, any asperities or dimensional errors are superimposed on the displacement boundary conditions, resulting in a very sensitive process. To address these challenges, this chapter uses analytical, numerical, and experimental investigations of stamp contact mechanics between a rigid roll and a rigid substrate to identify the relationship between roll displacement and contact pressure.

During printing the stamp is assumed to be in a condition of plane strain along the length l_z of the roll, admitting a two dimensional analysis of the stamp cross section in the x, y plane (Figure 4-2). The deformation of the stamp between a rigid roll and rigid substrate is determined by the displacement δ of the roll towards the substrate along $\hat{y}$, with some resulting pressure distribution $p(x)$ with maximum pressure p_0, contact force per unit length f, and contact length $2l$. In this chapter, deformation between a rigid roll and a rigid substrate is considered; Section 4.2.1 will justify this approach by showing that the results can be mapped to a general case of deformation between two surfaces of arbitrary radii.

This work considers a thin elastic stamp of thickness t (typically less than 1 mm) bonded to a roll of radius r (typically on the order of cm) (Figure 4-3). Retaining the notation of Chapter 3, the surface of the stamp has a series of protruding features of width w, height h, and spacing a (typically at the microscale). The stamp is assumed to be of an incompressible elastomer with elastic modulus E_0. The stamp is bonded to the roll, providing a zero displacement boundary condition at the roll surface. Likewise, a no-slip boundary condition is assumed at the contact interface from the

112

large work of adhesion W_{ad} between the stamp and substrate.

The sensitivity of contact length $2l$ and contact pressure p to roll displacement δ must be well understood. From a process control perspective, this sensitivity determines disturbance rejection, where displacement disturbances might result from positioning errors or geometrical errors in the roll equipment, stamp, or substrate. This chapter examines the contact mechanics of the roll-stamp construct to elucidate these relationships.

Stamp behavior will be explored in two practical limits (Figure 4-4): (i) very small
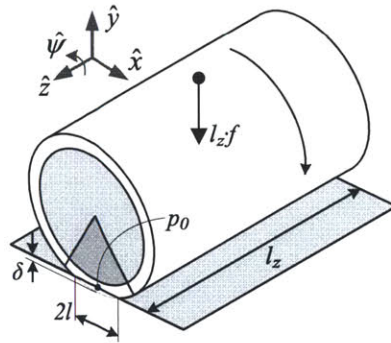
Figure 4-2: An elastic stamp bonded to a rigid roll and translated over a rigid substrate can be analyzed in plane strain.
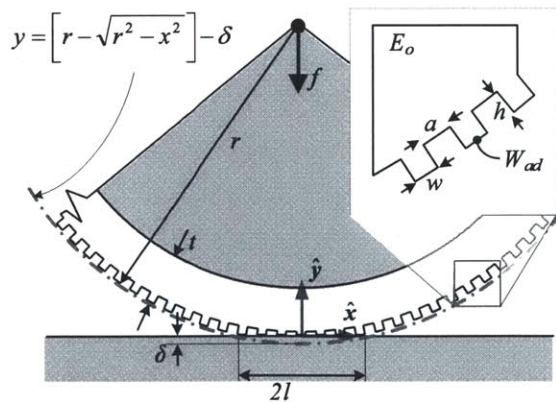
Figure 4-3: Cross section view of stamp showing coordinate frame, stamp dimensions, material properties, and contact variables.

(i.e. micron or submicron) stamp features and (*ii*) very large or compliant stamp features. The utility of these contact models will be demonstrated in subsequent chapters to derive the process sensitivity and guide robust stamp design.
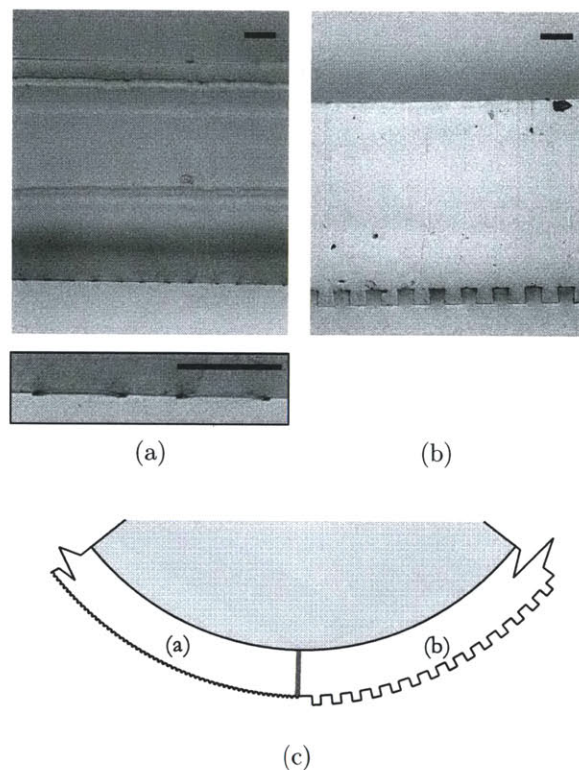
Figure 4-4: Two analytical limits of stamp architecture: (a) very small features and (b) very compliant features. These cases are illustrated with micrographs of stamp cross sections with (a) 3 μm tall lines in a hexagon pattern and (b) 50 μm tall lines in a grating pattern; subimage in (a) shows magnified 3 μm features (scale bars: 100 μm). (c) Schematic of corresponding stamps mounted to a roll.

4.2 Contact Mechanics

This section reviews pertinent principles of contact mechanics to provide a framework for subsequent presentation of analytical and numerical approaches. Requisite concepts of contact mechanics are reviewed in the context of elastomeric stamp contact: (*i*) a parabolic curvature mapping approach, (*ii*) models of contact mechanics

between cylinders (i.e. printing rolls), and (*iii*) the effect of a large work of adhesion at the stamp-substrate interface .

4.2.1 Curvature Mapping

Referring to Figure 4-3b, the nominal surface of the stamp can be described throughout the range of motion by a circle in the x, y plane:

$$y = \left(r - \sqrt{r^2 - x^2} \right) - \delta \tag{4.1}$$

The square root in this expression can be rewritten as a series expansion

$$y = -\delta + r \left[1 - \sqrt{1 - \frac{x^2}{r^2}} \right] \tag{4.2a}$$

$$= -\delta + r \left[1 - \left(1 - \frac{1}{2} \frac{x^2}{r^2} - \frac{1}{8} \frac{x^4}{r^4} + \cdots \right) \right] \tag{4.2b}$$

When the contact length l is small compared to the roll radius r, assuming $x \ll r$ allows removing higher order terms in the series expansion, resulting in a parabolic approximation of the roll profile:

$$y = \frac{1}{2} \frac{x^2}{r} - \delta \tag{4.3}$$

If two adjacent rolls of radius r_1 and r_2 are compressed together (rather than a single roll of radius r against a rigid plane), the contact problem can be mapped to a single roll of radius r^* compressed against a rigid plane. This result follows from a difference of each parabolic roll profile (at $\delta = 0$):

$$y_1 - y_2 = \frac{x^2}{2r_1} + \frac{x^2}{2r_2} = \frac{x^2}{2r^*} \tag{4.4}$$

where

$$r^* = \frac{r_1 \cdot r_2}{r_1 + r_2} \tag{4.5}$$

115

This parabolic approximation and curvature mappings are ubiquitous in contact mechanics [51], including derivation of the familiar Hertz solutions. These expressions lead to a more tractable analysis and allow developing generalized relationships for varying combinations of roll radii. In particular, the generalization of r^* permits analyzing and testing the case of a roll pressing against a rigid plane without loss of applicability to other cases, such as processing a flexible web through the nip of a printing roll and backup roll.

4.2.2 Hertz Contact

Contact between homogeneous bodies of curvature is well understood through Hertz contact mechanics [39]. In this derivation, Hertz assumes (*i*) small deformations, (*ii*) large radii of curvature ($r^* \gg l$), and (*iii*) frictionless contact.

The assumption of large radii of curvature allows analyzing the corresponding deformation of a planar elastic halfplane with local surface tractions. In this analysis, an equivalent elastic modulus is calculated:

$$\frac{1}{E^*} = \frac{1 - \nu_1^2}{E_1} + \frac{1 - \nu_2^2}{E_2} \tag{4.6}$$

Hertz solves for the general case of two bodies defined major and minor radii of curvature (see [51] for an easily accessible and tutorial review). In the special case of $r_{\mathrm{major}} = \infty$ the solution for contact between two cylinders arises. When the axes of the cylinders are aligned, the behavior at the contact interface is given by

$$l = \sqrt{2r^*\delta} \tag{4.7}$$

$$p(x) = E^* \sqrt{\frac{\delta}{2r^*} \left[1 - \left(\frac{x}{\sqrt{2r^*\delta}} \right)^2 \right]} \tag{4.8}$$

$$p_0 = E^* \sqrt{\frac{\delta}{2r^*}} \tag{4.9}$$

$$f = \frac{\pi}{2} \delta E^* \tag{4.10}$$

In the case that a soft, incompressible ($\nu = 0.5$) elastic stamp pressing against a relatively rigid substrate or rigid backup roll, $E^* = E_0/(1 - \nu^2)$ evaluates to $\frac{4}{3}E_0$.

4.2.3 Elastic Layer

Application of the Hertz solution to elastomeric stamps mounted on rigid roll machinery is an abuse of the underlying assumptions: the thin elastomeric layer has a boundary condition at the roll interface not accounted for by Hertz theory and the stamp experiences no-slip contact rather than frictionless contact.

A number of models have been published that treat the case of a thin elastic layer on rigid machinery, motivated especially by analysis of rubber coatings on processing rolls. A thorough review of these *elastic layer* approaches is provided by [51].

Meijers [70] develops the integral equations that govern elastic layer contact for a layer that is rigidly bonded to a substrate at one interface and compressed with a roller in friction free contact at the other. He pursues numerical solutions in two limits, (*i*) small contact lengths ($l \ll t$) and (*ii*) large contact lengths ($l \gg t$). His paper shows that these limits converge for moderate contact lengths l, allowing accurate calculation of contact pressures over a complete range of displacements. The resulting expressions for contact pressure are quite unwieldy and not repeated here.

Bentall and Johnson [6] examine a similar case of an elastic tire, which is fixed to a rigid roll and compressed against a rigid planar substrate with frictionless contact. Their paper includes a general derivation that considers a roll of finite stiffness (relaxing the assumption of rigidity). An approximate solution for an incompressible elastic layer on a rigid roll is derived for $l \gg t$:

$$l = \sqrt{6r^*\delta} \tag{4.11}$$

$$p(x) = \frac{3}{2}\frac{E_0 r^* \delta^3}{t^3}\left[1 - \left(\frac{x}{\sqrt{6r^*\delta}}\right)^2\right] \tag{4.12}$$

Johnson [51] shows that the more exact solution by Meijers converges to this approximate solution (4.12) for $l \gg t$ and to the Hertz solution (4.8) for $l \ll t$.

In general, the formulation of the elastic layer problem seems dependent on the relative thickness of the layer and makes it quite difficult to develop a simple expression that gives accurate but intuitive insight into the contact behavior. As an example, it would be advantageous to have a straightforward expression like the pressure distribution in Hertz contact (4.9) to clearly illustrate the effect of system variables on contact pressure evolution.

4.2.4   Elastic Foundation

Johnson [51] introduces the *elastic foundation* model as a method to approximate contact behavior. He notes that the difficulties associated with calculating contact stresses lie in the coupling between material deformations at each point. If each material point can be assumed decoupled, then a much simpler mathematical expression for contact behavior can be applied.

For example, Johnson's elastic foundation approach can be applied to the elastic layer problem when the Poisson ratio ν is near zero, that is, material deformation in one direction does not affect the state of stress in orthogonal directions. If this is the case, the contact pressure at each point x can be independently calculated based on the local displacement $\delta(x)$ and layer thickness $t(x)$, giving

$$p(x) = E_0 \frac{\delta(x)}{t(x)} \tag{4.13}$$

4.2.5   Work of Adhesion

Common stamp materials (e.g. PDMS) for contact lithography have large ratios of surface energy to elastic modulus W_{ad}/E_0. This work of adhesion must be captured in the models above to accurately model the contact behavior. Generally speaking, the work of adhesion at the contact interface results in larger contact lengths and lower contact forces than otherwise predicted.

Contact length and displacement are linked variables that can be found using an energy approach. The equilibrium state will be that which minimizes the total system

energy U, which consists of external work, strain energy, and surface energy (work of adhesion). This miminum energy state must satisfy the necessary condition that the first derivative of energy is zero; this can be achieved through two approaches. In the first approach, the displacement is assumed constant at δ_0 and the necessary condition becomes

$$\frac{dU_{\text{external}}}{dl} + \frac{dU_{\text{strain}}}{dl} + \frac{dU_{\text{adhesion}}}{dl} = 0 \tag{4.14}$$

where the external work is constant because of fixed displacement. Alternatively, a constant contact length l_0 is assumed, giving a necessary condition

$$\frac{dU_{\text{external}}}{d\delta} + \frac{dU_{\text{strain}}}{d\delta} + \frac{dU_{\text{adhesion}}}{d\delta} = 0 \tag{4.15}$$

where the energy of adhesion is constant because of the fixed contact length.

Johnson, Kendall, and Roberts (JKR) [52] adopted the latter approach (4.15) to extend the Hertz contact solution to include the effects of adhesion. This approach considers two related deformation paths (Figure 4-5): First, the strain energy to compress two bodies together to some displacement δ_0 and contact length $2l_0$ is calculated. Second, the strain energy is found that results when relaxing from δ_0 to δ_{eq} while maintaining the same contact length $2l_0$. Equilibrium occurs at the point where the interface energy $W_{ad} \cdot 2l_0$ is equal to the difference in the two strain energy paths.

This same energy approach can be applied to the stamp contact problem, where the first load path requires a strain energy U_I

$$U_I = \int_0^{\delta_0} f(\delta)d\delta \tag{4.16}$$

and the second path results in a strain energy U_{II}

$$U_{II} = \int_{\delta_0}^{\delta_{eq}} f_{II}(\delta)d\delta \tag{4.17}$$

where $f_{II}(\delta)$ is the load path as displacement is relaxed. For small deformation elasticity where deformation is a linear problem, relaxation along path II with fixed

119

contact length occurs at the instantaneous stiffness found at δ_0 during loading along path I. This observation gives $f_{II}(\delta)$ as

$$f_{II}(\delta_{eq}, \delta_0) = f(\delta_0) + \left.\frac{df}{dz}\right|_{\delta_0} \cdot (\delta_{eq} - \delta_0) \tag{4.18}$$

Since there is a pattern on the stamp, the work of adhesion must be scaled by the fraction of the stamp area that is in contact with the substrate

$$W_{ad}^* = W_{ad}\frac{w}{a + w} \tag{4.19}$$

From Figure 4-5, it follows that equilibrium requires

$$U_I(\delta_{eq}) + U_{II}(\delta_{eq}, \delta_0) - W_{ad}^* \cdot 2l(\delta_0) = 0 \tag{4.20}$$
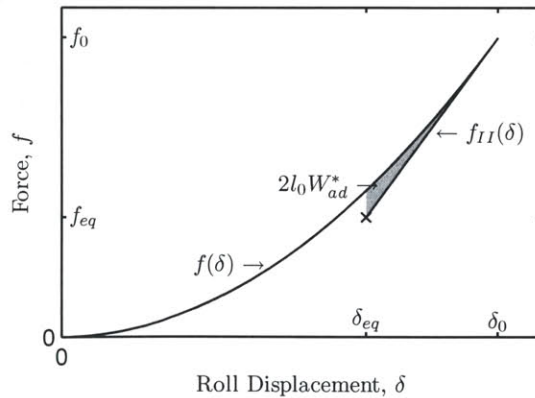
Figure 4-5: Load path for determining static equilibrium while accounting for surface energy. The construct is loaded to δ_0 considering only strain energy, then relaxed to δ_{eq} while holding contact length l_0 constant. The energy difference between the load curves represents the energy stored at the contact interface.

120

4.3 Feature Continuum Viewpoint

Referring to Figure 4-6, the individual stamp features can be considered as a continuum if they are small compared to the thickness t of the stamp and the contact length $2l$. Using this continuum approximation of feature behavior allows separation of the stamp into two continuum domains: (I) the stamp body and (II) the stamp features. This continuum viewpoint results in an elastic bilayer problem (Figure 4-6) composed of a rigid roll, an elastic layer of thickness t (Layer I), and an elastic layer of thickness h (Layer II).
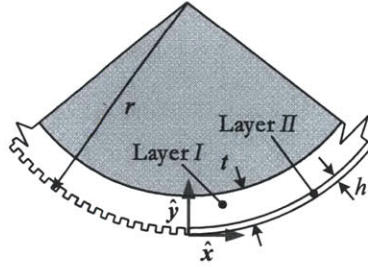
Figure 4-6: Bilayer approach to considering microfeature behavior. Two elastic layers exist on a rigid roll, where Layer I has the properties of PDMS and Layer II has properties determined by a continuum approximation of the stamp microfeatures.

While the stamp material in Layer I is assumed isotropic and incompressible, the anisotropic behavior of the features in Layer II is best described by orthotropic elasticity:

$$\begin{Bmatrix} \sigma_{xx} \\ \sigma_{yy} \\ \sigma_{xy} \end{Bmatrix} = \begin{bmatrix} E_{xx} & 0 & 0 \\ 0 & E_{yy} & 0 \\ 0 & 0 & \mu_{xy} \end{bmatrix} \begin{Bmatrix} \epsilon_{xx} \\ \epsilon_{yy} \\ \epsilon_{xy} \end{Bmatrix} \tag{4.21}$$

This model reflects the constitutive behavior of stamp features by incorporating directionally dependent behavior. The shear modulus μ_{xy} of the continuum approximation is the material shear modulus scaled by the volume fraction occupied by features:

$$\mu_{xy} = \frac{E_0}{3} \frac{w}{a+w} \tag{4.22}$$

121

Features cannot transmit lateral shear stresses to adjacent features, hence the circumferential modulus is negligible ($E_{xx} = 0$).

E_{yy} is the compressive modulus, which can be determined numerically or experimentally for various stamp patterns. When the stamp pattern is a grating, the results of Chapter 3 can be used to predict the microfeature sheet stiffness. This model gives dimensionless stiffness K as a function of dimensionless feature aspect ratio $A = h/a$ and pattern ratio $P = w/a$:

$$K = \frac{1}{K_I(A,P)^{-1} + K_{II}(A,P)^{-1}} \frac{(A+P) + 0.6}{(A+P)} \tag{4.23a}$$

$$K_I = \frac{2\pi}{3} \frac{AP}{(P+1)^2} \left[-\log\cos\left(\frac{\pi}{2}\frac{P}{P+1}\right) \right]^{-1} \tag{4.23b}$$

$$K_{II} = \frac{4}{3} \frac{P}{(P+1)^2} \tag{4.23c}$$

which can be converted to sheet stiffness k (in units of Pa/m) by

$$k = \frac{E_0(a+w)}{ha} K \tag{4.24}$$

The effective modulus $E_{yy} = hk$ in the radial (compressive) direction follows from this sheet stiffness.

The constitutive behavior in (4.21) applies to Layer II in Figure 4-6 and is strictly valid for small deformations. Sheet stiffness k approximates an ideal feature behavior (Figure 3-9). This approximation remains reasonably valid until feature collapse (though fails to capture large-deformation stiffening); it follows from (3.5) that this approximation is valid up to small finite compression that satisfies

$$\epsilon_{yy} > -X_c \frac{a}{a+w} \tag{4.25}$$

Though this constitutive model fails to accurately describe deformations beyond this limit, these deformations are not of practical interest because the process window has been exceeded by feature collapse.

4.4 Analytical Models

Analysis of stamp deformation can be approached by matching the stress and strain fields at the interface between Layer I and Layer II in Figure 4-6. This section analyzes the pressure distribution at the stamp-substrate interface for each limit illustrated in Figure 4-4, namely very small or very compliant features.

4.4.1 Small Features

The stamp features do not appreciably influence the displacement field in the stamp body when they are very small ($h \ll \delta$, Figure 4-4a). This assumption allows imposing the displacement boundary conditions directly on the stamp body (neglecting the features) to solve for the resulting pressure and contact distribution at the contact interface. The pressure distribution is hence identical to that on a smooth stamp with no features, allowing application of classical contact mechanics solutions.

The contact behavior of an elastic stamp wrapped around a rigid roll deviates significantly from the Hertz solution when the contact half-width l is on the order of the stamp thickness t. For even moderate displacements, accurate models require application of elastic layer solutions, where the stamp constitutes an elastic body compressed between a rigid roll and rigid substrate (Section 4.2.3).

Elastic layer derivations presented in the literature assume a frictionless contact condition at the elastic layer interface. Conversely, the large work of adhesion between PDMS stamps and substrate materials creates a no-slip condition at this interface. The following derivation examines an approximate solution for the desired boundary conditions. The resulting expression for pressure distribution will be similar to (4.12), which is simple enough to offer intuitive insight into the contact behavior.

An approximate solution can be derived for an incompressible stamp in the case that the stamp thickness is much less than both the contact length and roll radius:

$$t \ll l, r^*$$
(4.26)

Referring to Figure 4-7, a material deformation field (u and v in the $\hat{x}$ and $\hat{y}$

123

directions, respectively) must be found that satisfies zero slip at the stamp interfaces

$$u(y = 0, t) = 0 \qquad (4.27)$$

zero displacement at the roll interface

$$v(y = t) = 0 \qquad (4.28)$$

and the prescribed deformation imposed by the rigid substrate from (4.3)

$$v(y = 0) = \delta - \frac{x^2}{2r^*} \qquad (4.29)$$

The displacement fields u and v can be related by inspection of the control volume shown in Figure 4-7. Continuity and incompressibiliy require that the material displaced at $y = 0$ between $x = [0, \chi)$ be the same volume as that displaced through a vertical bisection at $x = \chi$:
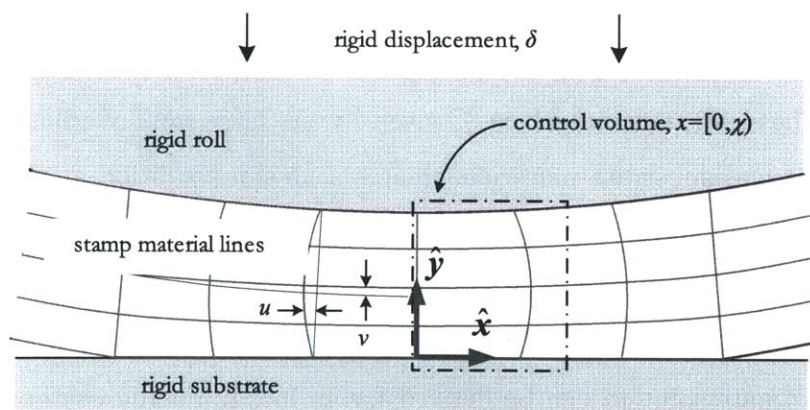
Figure 4-7: An incompressible elastic stamp with no-slip boundary conditions results in parabolic displacement profiles u and correspondingly large hydrostatic pressures. The control volume shown is used to relate roll displacement to the net stamp deformation.

124

$$\int_0^x v(y=0)dx = \int_0^t u(x=\chi)dy \qquad (4.30)$$

This relationship yields an approximate contact length l by solving for displacement field $u(x=l)=0$ (as at the edge contact in Figure 4-7):

$$l = \sqrt{6r^*\delta} \qquad (4.31)$$

Small deformation isotropic elasticity must satisfy equilibrium (2.9) and compatibility (2.6). It was shown that the equilibrium condition reduces to (2.15) for an incompressible material. In plane strain ($u_z = 0$), these tensor equations can be rewritten as a pair of differential equations involving the displacement field u,v and pressure field p:

$$\frac{1}{\mu_0}\frac{\partial p}{\partial x} + \frac{\partial^2 u}{\partial x^2} + \frac{\partial^2 u}{\partial y^2} = 0 \qquad (4.32)$$

$$\frac{1}{\mu_0}\frac{\partial p}{\partial y} + \frac{\partial^2 v}{\partial x^2} + \frac{\partial^2 v}{\partial y^2} = 0 \qquad (4.33)$$

where μ_0 is the shear modulus, identically $E_0/3$ for an incompressible material. Similarly, the assumption of incompressibility reduces the continuity equation to

$$\frac{\partial u}{\partial x} + \frac{\partial v}{\partial y} = 0 \qquad (4.34)$$

And compatibility to

$$\frac{d^2\epsilon_{xx}}{dy^2} + \frac{d^2\epsilon_{yy}}{dx^2} + \frac{d^2\epsilon_{xy}}{dxdy} = 0 \qquad (4.35)$$

Analysis can be simplified by eliminating negligible terms in (4.32) and (4.33); dimensionless quantities are required to determine the relative magnitude of each term. The characteristic dimensions of the problem are $x \propto l$ and $y \propto t$. The characteristic vertical displacement is $u_y \propto \delta$; applying the continuity equation gives $u_x \propto \delta l/t$. The material shear modulus μ_0 can be used as a characteristic pressure. Normalizing variables by these quantities gives dimensionless variables of order unity $\tilde{p} = p/\mu_0$, $\tilde{v} = v/\delta$, $\tilde{x} = x/l$, $\tilde{y} = y/t$, and $\tilde{u} = ut/\delta l$. These variables are substituted

125

into (4.32) and (4.33), where small terms are cancelled assuming $\delta \ll t \ll l$:

$$\frac{\partial \tilde{p}}{\partial \tilde{x}} + \frac{\delta}{l} \frac{\partial^2 \tilde{u}}{\partial \tilde{x}^2} + \frac{\delta l^2}{t^3} \frac{\partial^2 \tilde{u}}{\partial \tilde{y}^2} = 0 \tag{4.36}$$

$$\frac{\partial \tilde{p}}{\partial \tilde{y}} + \frac{\delta t}{l^2} \frac{\partial^2 \tilde{v}}{\partial \tilde{x}^2} + \frac{\delta}{l} \frac{\partial^2 \tilde{v}}{\partial \tilde{y}^2} = 0 \tag{4.37}$$

These scaling arguments reduce (4.32) and (4.33) to a much simpler form:

$$\frac{1}{\mu_0} \frac{\partial p}{\partial x} + \frac{\partial^2 u}{\partial y^2} = 0 \tag{4.38}$$

$$\frac{1}{\mu_0} \frac{\partial p}{\partial y} = 0 \tag{4.39}$$

(4.39) shows that pressure p is a function of x only. It follows that (4.38) admits a parabolic deformation field u (Figure 4-7) that satisfies the displacement boundary condition in (4.27)

$$u = \frac{1}{2\mu_0} \left(ty - y^2 \right) \frac{dp}{dx} \tag{4.40}$$

The displacement field u is related to roll displacement δ by applying the control volume in (4.30) and boundary condition dictating $v(y = 0)$ as a function of δ (4.29):

$$\int_0^x \left(\delta - \frac{x^2}{2r^*} \right) dx = \int_0^t \left(\frac{1}{2\mu_0} \left(ty - y^2 \right) \frac{dp}{dx} \right) dy \tag{4.41}$$

Evaluating these integrals and solving for the pressure gradient gives the pressure gradient as a function of roll displacement

$$\frac{dp}{dx} = \frac{12\mu_0}{t^3} \left(\delta x - \frac{x^3}{6r^*} \right) \tag{4.42}$$

The pressure $p(x)$ at any point along the interface can now be found by integrating this pressure gradient and substituting $l = \sqrt{6r^*\delta}$ from (4.31):

$$p(x) - p(l) = \int_x^l \frac{dp}{d\chi} d\chi = \frac{6\delta^2 r E_0}{t^3} \left[1 - \left(\frac{x}{\sqrt{6\delta r}} \right)^2 \right]^2 \tag{4.43}$$

By inspection, the maximum contact pressure p_0 occurs at the center of the roll contact region

$$p_0 = 6\frac{r^*\delta^2}{t^3}E_0 \qquad (4.44)$$

Integrating the contact pressure p across the contact interface give the contact force f per unit length:

$$f = \int_{-l}^{l} p(x)dx = \frac{32\sqrt{6}}{5}\frac{\delta^{5/2}r^{*3/2}}{t^3}E_0 \qquad (4.45)$$

This solution for contact behavior is valid when the elastic layer is thin and the contact length is large over the range of relevant roll displacements, as required by (4.26). This assumption can be quantified by finding the contact length at which a critical feature collapse pressure p_c is reached. From the solution for center contact pressure p_0, the collapse displacement δ_c is

$$\delta_c|_{p_0=p_c} = \sqrt{\frac{t^3}{6r^*}\frac{p_c}{E_0}} \qquad (4.46)$$

The corresponding contact length at this displacement is found using (4.31):

$$l_c|_{p_0=p_c} = \sqrt{6r^* \cdot \delta|_{p_0=p_c}} \qquad (4.47)$$

Substituting δ_c from (4.46) and requiring $l_c \gg t$ gives a criterion for model validity of

$$C_1 = \sqrt[4]{\frac{6r^*}{t}\frac{p_c}{E_0}} \gg 1 \qquad (4.48)$$

This criterion is strong when the elastic layer is very thin ($r^*/t \gg 1$) and the features have a large collapse pressure p_c. As an example, features with an aspect ratio and pattern ratio of unity will collapse at about $p_c = \frac{\pi}{4}KE_0$, where $K = 0.28$ (Chapter 3). The criterion developed above (4.48) is well satisfied (i.e. $C_1 \geq 3$) when $r^*/t > 48$, for example a 500 μm thick stamp on a 25 mm radius roll.

The kinematically admissible solution derived here is expected to overpredict contact pressure when (4.48) is weakly satisfied.

4.4.2 Compliant Features

When the stiffness of the stamp features is much less than the stamp stiffness in the $\hat{y}$ direction, the stamp body can be assumed rigid and the contact pressure distribution can be calculated from the features alone.

The effective Poisson ratio ν of the feature continuum approximation is zero; each microfeature deforms independently of every other (Section 4.3). This allows accurate application of the elastic foundation model (Section 4.2.4) because the pressure-displacement relationship is independent at each point along the contact interface.

A similar application of this approach has been used to analyze PDMS fibrillar structures for dry adhesion (e.g. biomimetic gecko feet) [74, 33].

Pressure at each point x along the interface is independent of the neighboring behavior, so that contact pressure is simply a function of the parabolic displacement profile (4.3):

$$p(x) = k \cdot v_{y=0}(x) = k \left(\delta - \frac{x^2}{2r^*} \right) \tag{4.49}$$

By inspection, the maximum contact pressure again occurs at the center of the roll

$$p_0 = k\delta \tag{4.50}$$

Contact length is given by the chordal intersection of the roll and substrate, obtained from the parabolic approximation of contact in (4.3):

$$l = \sqrt{2r^*\delta} \tag{4.51}$$

Integrating contact pressure over this length gives the contact force

128

$$f = \int\limits_{-l}^{l} p(x)dx = \frac{4}{3}k\sqrt{2r^*\delta^3} \qquad (4.52)$$

This solution is valid only when the features are very compliant relative to the stamp body of thickness t. This requires that the feature deformation is much greater than the stamp body deformation:

$$v|_{y=0,body} \ll v_\infty|_{features} \qquad (4.53)$$

At the feature collapse pressure p_c, the feature deformation will be $v_\infty = p_c/k$, where k is the feature stiffness (found either experimentally, numerically, or through the closed form model (4.24) developed in Chapter 3). The deformation of the stamp body is estimated using the model (4.44) developed in the previous section, where $v|_{y=0,body} = \delta$:

$$v|_{y=0,body} = \sqrt{\frac{t^3}{6r^*}\frac{p_c}{E_0}} \qquad (4.54)$$

Substituting these expressions into (4.53) gives a criterion of applicability

$$C_2 = \frac{E_0}{kt}\sqrt{\frac{6r^*}{t}\frac{p_c}{E_0}} \gg 1 \qquad (4.55)$$

This criterion is strong when the feature height h is a significant fraction of the stamp thickness t. As an example, features with an aspect ratio and pattern ratio of unity will collapse at about $p_c = \pi/4 \cdot KE_0$, where $K = 0.36$ (Chapter 3) and will have a stiffness of $k = 2E_0K/h$ (4.24). Assuming a roll radius of r^*=25 mm and a stamp thickness of 500 μm, the criterion (4.55) is well satisfied (i.e. $C_2 \geq 3$) for $h \geq 78\mu$m. Smaller feature heights h satisfy (4.55) when larger roll radii or smaller stamp thicknesses are used. The solution derived here is expected to overpredict contact pressure when (4.55) is weakly satisfied.

4.4.3 Surface Energy

The two models developed in this section have not taken into account the effect of surface adhesion. To include the effect of significant work of adhesion W_{ad}, the procedure developed in Section 4.2.5 can be applied. Finding df/dz is straightforward for the contact models derived in this section, but (4.20) results in implicit equations that must be solved numerically.

4.5 Numerical Simulation

Finite element methods were used to both validate the analytical models in their appropriate limits and to explore contact behavior in analytically intractable regimes, for example where the stiffness of the stamp body and the stamp features are of similar magnitudes.

4.5.1 Geometry

The roll-mounted stamp deformation is simulated using plane strain analyses, which holds for configurations where the length of contact along the roll axis is much greater than the contact width $2l$. Symmetry allows simulating the behavior of only half the contact region (Figure 4-8).

Normalized geometry and material parameters were used in the simulation so that the results can easily be adapted to different material parameters or roll scales. The characteristic length scale and pressure are $(t + h)$ and E_0, respectively. Normalizing by these quantities gives dimensionless feature height $\tilde{h}$ and radius $\tilde{r}$

$$\tilde{h} = \frac{h}{t + h} \tag{4.56}$$

$$\tilde{r} = \frac{r}{t + h} \tag{4.57}$$

Material parameters are normalized to give conformability Cf

$$Cf = \frac{W_{ad}^*}{E_0(t + h)} \qquad (4.58)$$

The loading parameters are normalized to give displacement $\tilde{\delta}$, contact length $\tilde{l}$, pressure $\tilde{p}$, force $\tilde{f}$, and energy $\tilde{U}$:

$$\tilde{\delta} = \frac{\delta}{t + h} \qquad (4.59)$$

$$\tilde{l} = \frac{l}{t + h} \qquad (4.60)$$

$$\tilde{f} = \frac{f}{E_0(t + h)} \qquad (4.61)$$

$$\tilde{p}_0 = \frac{p_0}{E_0} \qquad (4.62)$$

$$\tilde{U} = \frac{U}{E_0(t + h)^2} \qquad (4.63)$$

The simulation modelled a stamp region with an arclength three times the predicted contact length given by (4.31) (Figure 4-8a). This approach keeps the finite element model relatively small (as opposed to simulating a full roll), but emulates the full construct by Saint-Venant's principle [101].

A rigid element is used to represent the substrate. No element was created to represent the rigid roll interface; this is accomplished by later imposing a rigid displacement at the inner diameter of the stamp.

4.5.2 Meshing

Uniform rectangular mesh elements were used to mesh each unit cell. A minimum of 50 mesh elements were used per unit stamp thickness; this dense mesh is required to provide high resolution contact length data (Figure 4-8b).

Large deformation plane strain elements with non-linear geometry conditions were used in each simulation (ABAQUS element type CPE4RH).

(a)

(b)
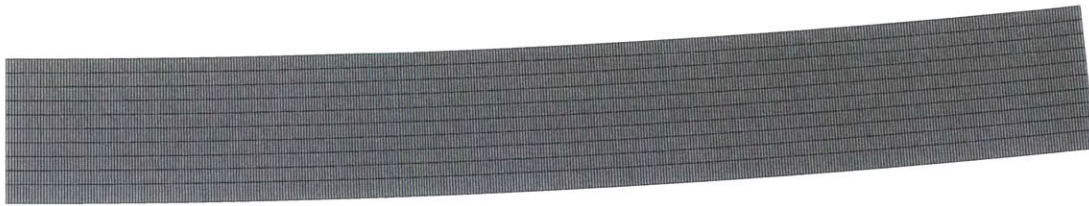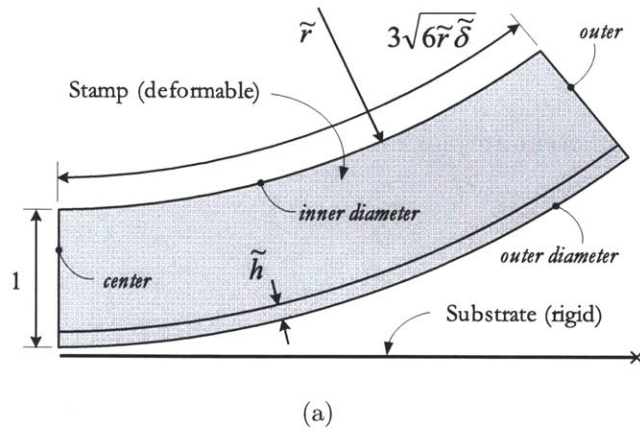
Figure 4-8: Finite element implementation of elastic stamps mounted to a rigid roll showing (a) multiple domains for stamp feature continuum approximation with characteristic dimensions and (b) typical mesh

4.5.3 Material Model

Stamp features were modeled as a continuum material as proposed in Section 4.2. An orthotropic linear elastic constitutive model was applied to the mesh elements in the corresponding region of the stamp; each parameter was set to match the feature continuum model (4.21).

An incompressible Neo-Hookean hyperelastic constitutive model (2.10) was applied to the remainder of the mesh elements representing the bulk thickness t of the stamp. Material parameters were scaled to $E_0 = 1$ so that the results reflect the dimensionless contact parameters.

4.5.4 Boundary Conditions

Boundary conditions were used to impose symmetry and appropriate contact behavior (summarized in Table 4.1 and Table 4.2). Symmetry dictates no lateral translation or rotation at the center face. Displacements and stresses must disappear far from the contact interface, requiring a rigid irrotational displacement at the outer face. The inner diameter is limited to rigid displacements in the vertical direction to emulate being fixed to a rigid roll. The outer diameter of the stamp has an irreversible no-slip contact condition: once the stamp face contacts the substrate it is not allowed to separate.

Table 4.1: Roll-based stamp simulation boundary conditions

Face	Boundary Condition
Center	X symmetry ($\partial v/\partial x = 0$, $u = 0$)
Outer	Irrotational ($\partial v/\partial x = 0$, $u = 0$)
Inner Diameter	Rigid displacement ($u = 0$)

Table 4.2: Roll-based stamp simulation contact conditions

Face 1	Face 2	Boundary Condition
Outer diameter	Substrate	Irreversible no slip (rough)

4.5.5 Loading

A two-stage load path was used in each simulation to capture the effect of surface energy (Figure 4-9): the stamp was compressed to some finite displacement $\tilde{\delta}_0$ by and subsequently relaxed while maintaining a constant area of contact (imposed by the irreversible contact condition between the stamp and substrate). This loading was accomplished by imposing a rigid displacement $\boldsymbol{u} = [0 \quad \tilde{\delta}]^\top$ on the inner diameter of the stamp.

This load path emulates the JKR contact analysis used to find equilibrium between a contact force and surfaces with a finite work of adhesion as given by (4.20).

This approach requires a number of simulations at varying levels of $\tilde{\delta}_0$ for each stamp configuration to reconstruct contact behavior as a function of displacement $\tilde{\delta}$ (Figure 4-8).

(a)

(b)

(c)

Figure 4-9: Typical roll-based stamp simulation results. Finite element model shown at (a) zero displacement, (b) displacement to $\tilde{\delta}_0$, and (c) relaxation to $\tilde{\delta}_{eq}$ to simulate the effect of large W_{ad}^*. The geometry has been mirrored for clarity.

4.5.6 Implementation

The numerical simulation was implemented in ABAQUS 6.10, a commercial finite element software package.

Scripts were used to automate execution of the simulations. ABAQUS can be executed either through the available user interface or at the command line. When a model is built in the ABAQUS interface, a Python script is saved in a corresponding journal (.jnl) file. ABAQUS can be executed from the command line by changing this jounal file to a Python script (.py) can calling "abaqus cae noGUI=JOURNALFILE.py".

A master program was written in C++ to iterate through different initial displacements $\tilde{\delta}_0$ for each stamp geometry. At each point, this master program alters the loading parameters in the slave Python script and executes ABAQUS through the command line.

4.5.7 Interpreting Results

Each simulation recorded the normalized roll displacement $\tilde{\delta}$, contact area $\tilde{l}$, contact force $\tilde{f}$, strain energy $\tilde{U}$, and center pressure $\tilde{p}_0$. For these dimensionless parameters, (4.20) can be rewritten as

$$\tilde{U}_I(\tilde{\delta}_{eq}) + \tilde{U}_{II}(\tilde{\delta}_{eq}, \tilde{\delta}_0) - Cf \cdot \tilde{l}(\tilde{\delta}_0) = 0 \qquad (4.64)$$

where $\tilde{U}_I$ and $\tilde{U}_{II}$ are the strain energies during the first and second loading steps, respectively.

Each simulation, with a distinct $\tilde{\delta}_0$ and $\tilde{l}_0$, was interpolated to find the equilibrium displacement $\tilde{\delta}_{eq}$ as a function of conformability Cf. Combining these curves from multiple simulations creates a surface in the $\tilde{l}_0, Cf$ plane that gives the equilibrium values of $\tilde{\delta}$, $\tilde{f}$, and $\tilde{p}_0$ (Figure 4-10).
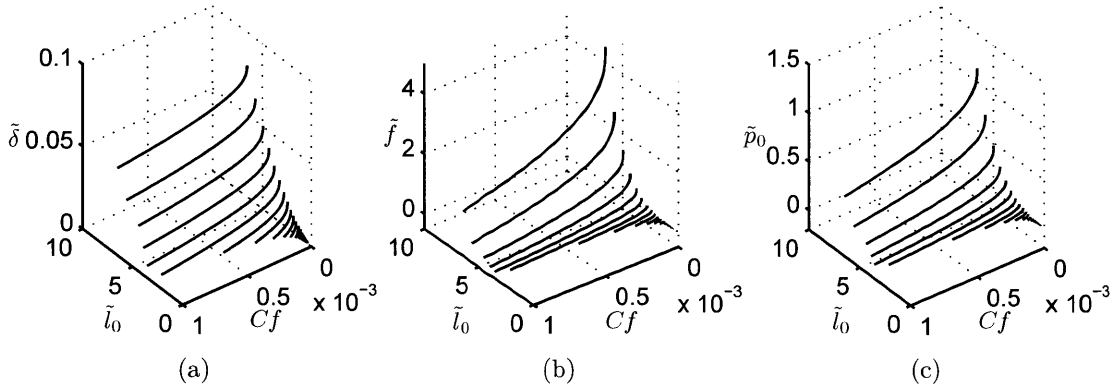
Figure 4-10: Typical contact simulation results. Simulated contact equilibrium curves are constructed as a function of conformability $Cf = W_{ad}^*/(t+h)E_0$. Sets of these curves form surfaces that can be interpolated across to find the behavior of a system with a particular Cf, including (a) roll displacement $\tilde{\delta}$, (b) roll force $\tilde{f}$, and (c) roll center pressure $\tilde{p}_0$.

4.6 Experimental Methods

4.6.1 Experiment Design

Two sets of experiments were designed to investigate the contact models derived in this chapter. Stamps without features were used to investigate the elastic layer model, while stamps with 50 μm features were used to verify the elastic foundation model. The exact combinations of stamp parameters are summarized in Table 4.3; each experiment was repeated three times to establish confidence in the results. A representative displacement and contact profile was selected from the three replicates for analysis.

Table 4.3: Stamp topologies and material parameters as tested in roll contact experiments. Stamp thickness t, feature width w, feature height h and feature spacing a were varied.)

	t (μm)	w (μm)	h (μm)	a (μm)	E_0 (MPa) (95% CI)
(a)	317	–	–	–	1.73 ± 0.12
(b)	698	–	–	–	1.61 ± 0.12
(c)	978	–	–	–	1.84 ± 0.10
(d)	311	50	47	50	1.37 ± 0.14
(e)	311	50	47	150	1.37 ± 0.14
(f)	590	50	47	50	1.51 ± 0.11
(g)	590	50	47	150	1.51 ± 0.11

4.6.2 Test Specimens

Stamps were fabricated by casting PDMS precursor (Dow Corning Sylgard 184) against a patterned silicon wafer in a mold cavity. The wafers were patterned with photoresist (MicroChem SU8 2025) and passivated with hexamethyldisilazane for 10 minutes in a vacuum desiccator. The mold was formed by holding a patterned silicon wafer in a vacuum chuck and assembling a polymethylmethacrylate (PMMA, a.k.a. acrylic) spacer and an aluminum plate on top (Figure 4-11). The PMMA spacer thickness and relief pattern defined the stamp thickness and dimensions; each stamp was 60 mm wide.
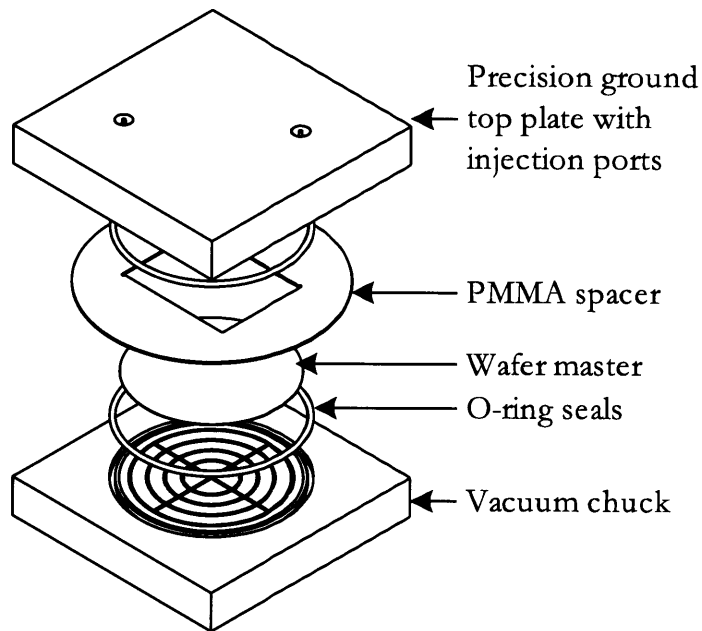
Figure 4-11: Mold used for casting stamps; fastening hardware, ejection port, and integrated heater omitted for clarity. The PMMA spacer defines the exact profile and thickness of each stamp, while the wafer imparts the stamp feature geometry.

Sylgard 184 PDMS precursor (Dow Corning) was mixed at the manufacturer's recommended 10:1 ratio (base:curing agent) and degassed under vacuum. The mold cavity was filled by supplying prepolymer to one injection port while applying vacuum to the opposing port. After curing for 2 hours at 60° C, the mold was parted with

pressurized ethanol through an ejection port, the stamp removed from the wafer, and rinsed thoroughly with ethanol (Figure 4-12).

(a)   (b)
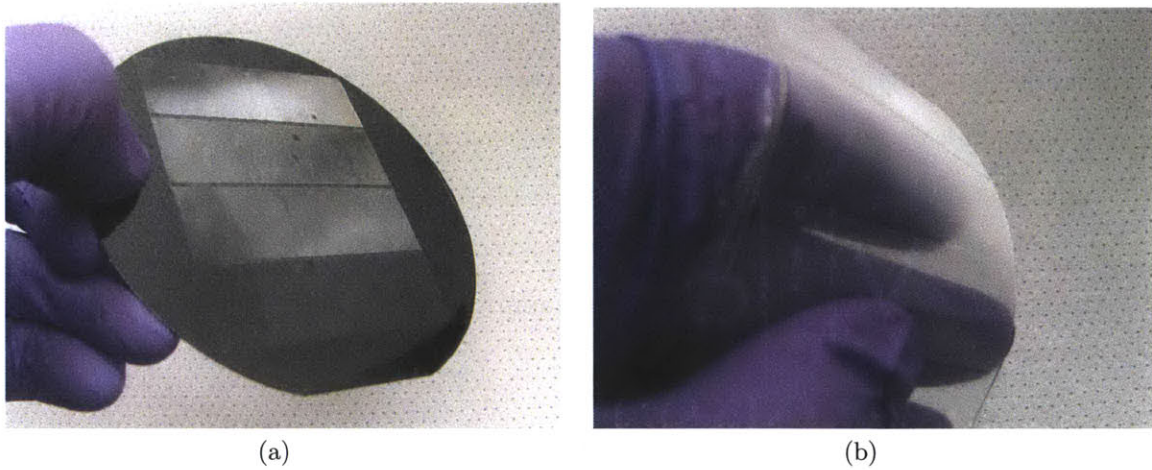
Figure 4-12: Stamp replication from a master template. (a) Master wafer with different 50 μm feature patterns over a width of 60 mm, (b) PDMS stamp with replicated feature patterns.

4.6.3   Experimental Apparatus

A precision roll positioning stage with equivalent roll radius $r^* = 25.4$ mm was used to measure the contact force, displacement, and contact area of different stamp configurations (Figure 4-13a). The stage was operated in a force control mode to maintain zero net torque on the roll pitch while varying the force imposed between the roll and substrate. Calibration experiments demonstrated the stage to have δ and f resolution of *ca.* 180 nm and 50 mN and accuracy of 300 nm and 150 mN, respectively. Further details on the experimental apparatus design are provided in Chapter 7.

Each stamp was loaded against a rigid planar substrate with a trapezoidal cycle that ramped between 0 N and 40 N at 2 N/s with a hold time of 5 s. This trapezoidal load profile was smoothed with a first order low-pass filter at 1 rad/s to minimize inertial affects at the ramp extrema (Figure 4-14).

(a)   (b)
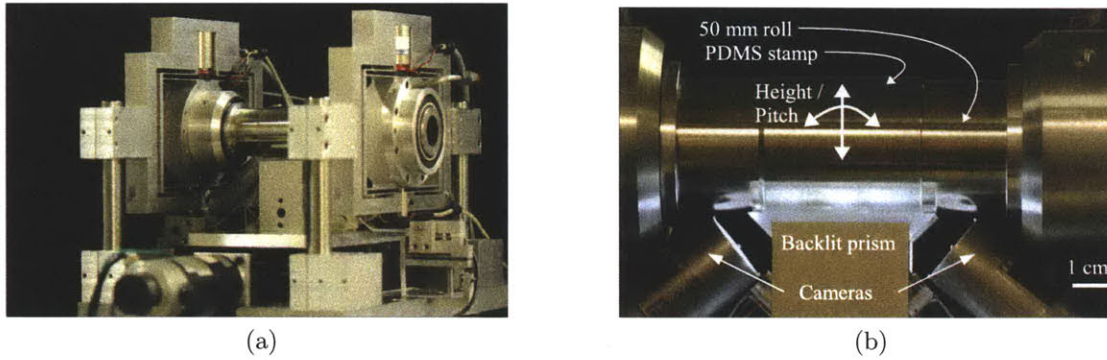
Figure 4-13: Precision roll positioning stage (a) can manipulate roll height and pitch over an optical prism (b) for contact experiments
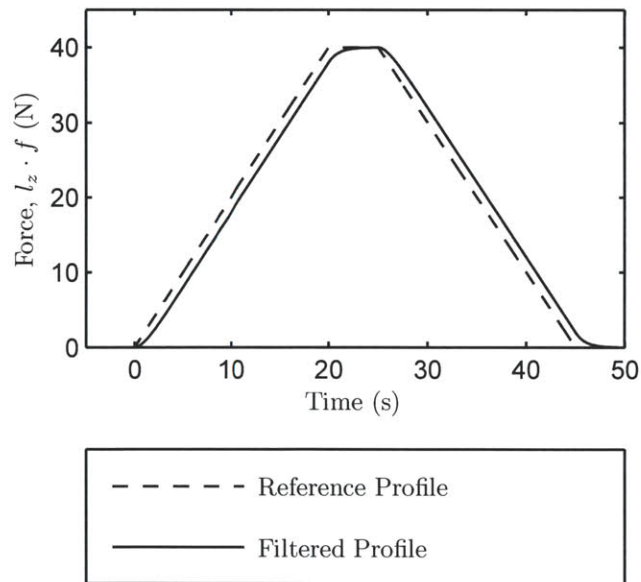
Figure 4-14: Experimental load profile for roll-based stamps. The experimental samples were loaded between 0 and 40 N at a rate of 2 N/s and with hold times of 5 s. The load profile was smoothed with a low pass filter to minimize inertial effects at the ramp extrema.

4.6.4 Data Collection

The contact area was monitored using an optical prism as the rigid substrate in the positioning stage. Lights and cameras were mounted at angles that would normally result in total internal reflection of the light through the prism (Figure 4-13b). The similar indices of refraction between the PDMS stamp and prism cause disruption of internal reflection wherever the two make contact. This observation technique captures accurate light field *in situ* images of contact during the load cycle (Figure 4-15a). Post processing of the images was used to correct for camera perspective and measure the contact width (Figure 4-15b). (Further details on this visualization technique are given in Chapter 9.)

(a)   (b)
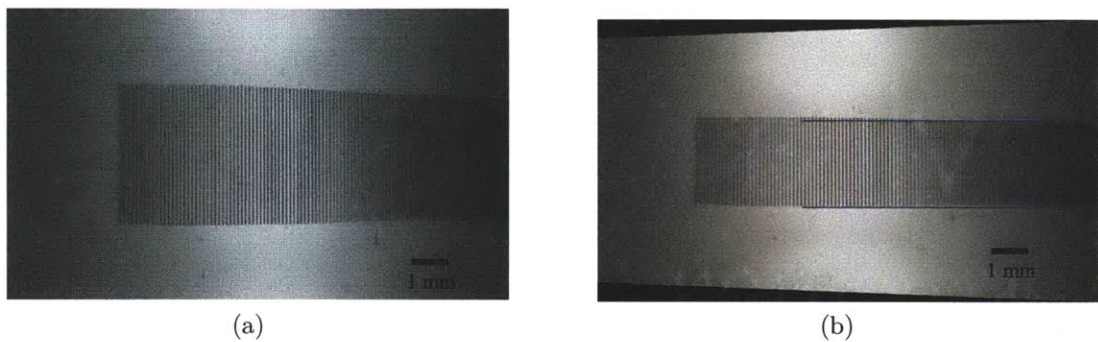
Figure 4-15: (a) Raw and (b) corrected image used in measuring contact area ($a = w = 50\mu$m). Each raw image was corrected for the perspective transformation and image foreshortening that results from an inclined camera angle.

A Windows program was written in C++ to record data from the roll positing stage and camera using C++ API's supplied by National Instruments and Dino-Lite (respectively).

Camera frames were recorded at 10 frames per second and converted from a 24 bit RGB image to an 8 bit grayscale image by averaging each color channel. This 8 bit pixel data was saved to an indexed binary file for each camera frame.

The analog roll position signals were recorded at 10 kHz, registered against a timestamp and image index, and saved to a second binary file with double floating point precision.

4.6.5   Material Characterization

After completing the loading experiments, five coupons were cut from each stamp with a gage length of 20 mm and width of 4 mm. Each coupon was subjected to a tensile test in a Zwick load frame equipped with a 20 N load cell. Elastic moduli were determined by fitting a large deformation Neo-Hookean model for moderate stretches up to $\lambda_1 = 1.2$. Additionally, cores were cut from each stamp and measured using a Zygo interferometer to determine the actual thickness and feature height of each stamp.

All specimens were cast, tested, and characterized within a period of several days. It is not believed that any significant temporal drift in material parameters occurred over this time period.

4.6.6   Experiment Accuracy

The accuracy of experimental results was limited by three factors: (i) machine accuracy, (ii) material property uncertainty, and (iii) stamp asperities.

The machine accuracy has an effect on the observed zero position of the roll. For example, an error in the machine force of ϵ will result in an error in the registration of load-displacement data. This force error can be related to a corresponding displacement error by $\epsilon/k_{\mathrm{stamp}}$, where k_{stamp} is the initial stiffness of the stamp construct.

Uncertainty in material properties gives a varying elastic modulus, which will directly affect the observed force on the roll. This uncertainty must be taken into account when comparing the experimental results to analytical or numerical models. Moreover, a varying elastic modulus changes the relative effect of the work of adhesion W_{ad} and will affect the equilibrium contact length and force.

Finally, small micro-scale asperities in the stamp result in variable behavior at small forces and displacements. Generally speaking, these asperities tend to reduce the observed stiffness; this effect disappears once moderate forces and displacements are reached. To counter this problem, load-displacement curves are registered with each other at some finite load (5 N is used in this chapter) rather than the equilibrium

point (0 N). An example of this effect is summarized in Figure 4-16.
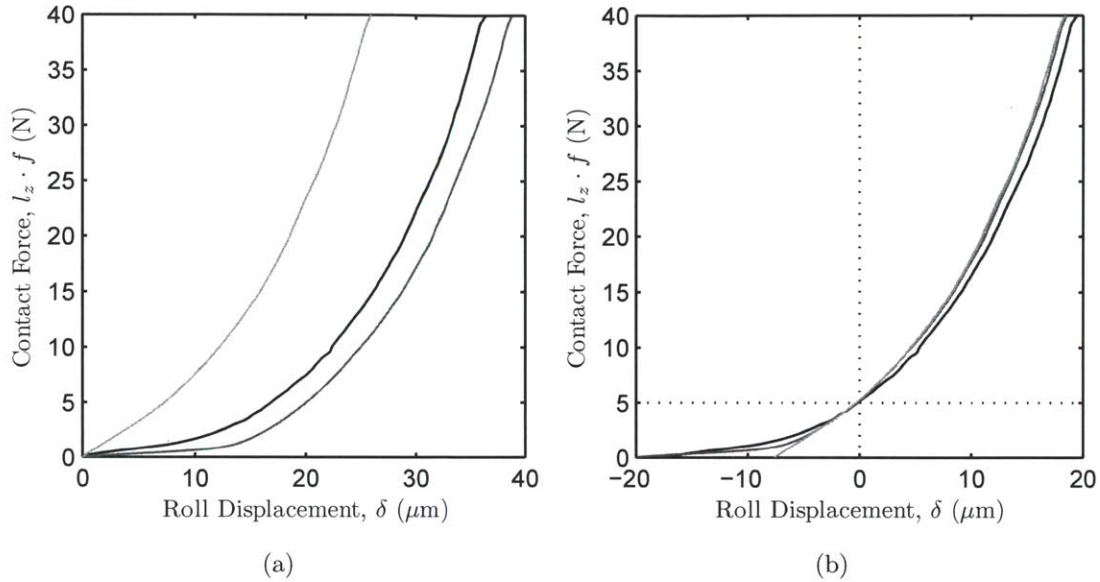
Figure 4-16: Typical experimental replications of load-displacement behavior. (a) Experimental roll based load-displacement curves from three different locations on the same stamp and (b) the same curves registered at some finite load (5 N). The data shows good repeatability when registered at a finite load; the range of energy integral under each curve is less than 5%.

4.7   Results

This section compares the analytical models to numeric simulations to illustrate their goodness of fit in the appropriate limits. Following this, experimental results are compared to numerical simulations.

4.7.1   Elastic Layer Simulation

Figure 4-17 shows a comparison of the elastic layer model with numerical simulations representing Table 4.3a-c. In this limit of very small features the elastic layer model applies, where the maximum contact pressure p_0, contact length $2l$, and contact force f are given by (4.44), (4.31), and (4.45), respectively. Hertz contact results from (4.7),

144

(4.9), and (4.10) are also superimposed to illustrate the divergence of this elastic layer case from the well known Hertz solutions.

Results are scaled for $r^* = 25.4$ mm and the work of adhesion is assumed zero. The reported contact pressure p_0 is normalized by elastic modulus E_0, while force f is reported per unit length of contact interface and also normalized by E_0.

In these results, the elastic layer model converges to the numerical simulations as l/t increases as required by the condition in (4.26). As expected, the kinematically admissible solution overpredicts the actual contact pressures. For each of the three cases in Figure 4-17, $\mathcal{C}_1 = l/t$ evaluates to 1.5, 2.1, and 4.7. It is interesting to note that the expression for contact pressure p_0 (4.44) remains quite accurate even when $\mathcal{C}_1 = l/t \gg 1$ is not strongly satisfied, though the models for contact length and force diverge more quickly from the simulation results.
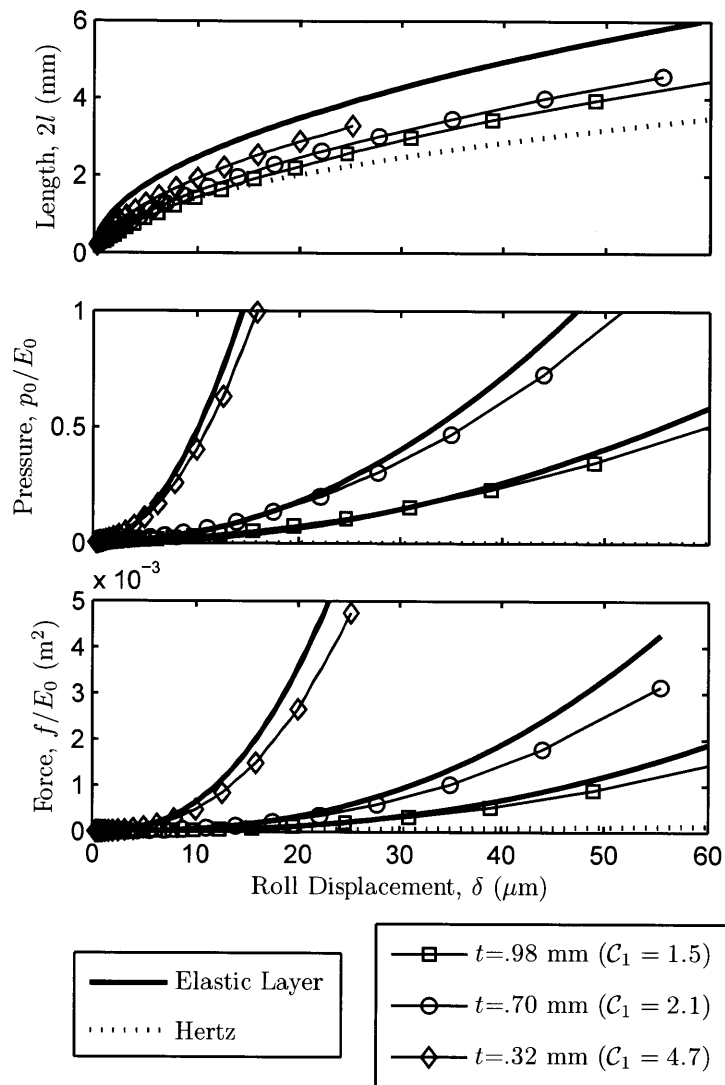
Figure 4-17: Comparison of finite element results and the elastic layer model for maximum contact pressure p_0, contact force f, and contact length $2l$. The approximate elastic layer model and numerical results converge as $\mathcal{C}_1 = l/t \gg 1$; at a contact length $2l$ of 3 mm, $\mathcal{C}_1 = l/t$ evaluates to 1.5, 2.1, and 4.7, respectively. Results have been scaled for $r^* = 25.4$ mm.

4.7.2 Elastic Foundation Simulation

Figure 4-18 compares the elastic foundation model with corresponding numerical results for the geometry of Table 4.3e,g. In this limit of very compliant features the elastic foundation model applies, where the maximum contact pressure p_0, contact length $2l$, and contact force f are given by (4.50), (4.51), and (4.52), respectively. Roll radius $r^* = 25.4$ mm and dimensionless feature stiffness $K = 0.17$ were assumed for the model and simulations. The contact force is normalized by elastic modulus and reported per unit length of roll.

The comparison in Figure 4-18 shows the elastic foundation model converges to the simulation results when condition (4.55) is satisfied; C_2 evaluates to 4.7 and 1.8, respectively.

It was assumed in the the derivation of the feature continuum approximation that all displacements were moderate and less than the feature collapse height, requiring the criterion in (4.25). The features used in this simulation ($w = 50$ μm, $a = 150$ μm, $h = 47$ μm) will collapse at about 28 μm of displacement, as predicted by (3.18). As roll displacement δ nears this point in Figure 4-18, the numerical results stiffens beyond the analytical prediction. The results beyond this point will be inaccurate once feature collapse occurs.
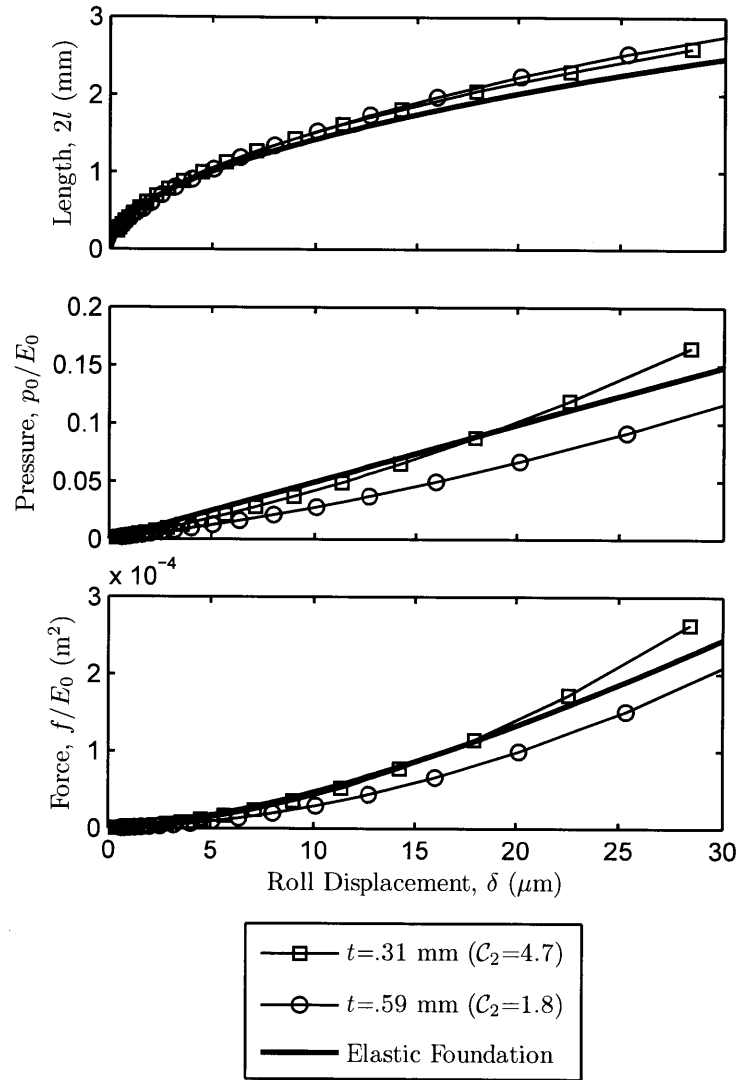
Figure 4-18: Comparison of finite element results and the elastic foundation model. The model and simulation match well when $C_2 \gg 1$. Results have been scaled for r^* = 25.4 mm and stamp features with $w = 50$ μm, $a = 150$ μm, and $h = 47$ μm.

4.7.3 Work of Adhesion

Figure 4-19 shows the influence of work of adhesion W_{ad} between zero and 200 mJ/m^2 on simulation results. These simulation assumed a roll radius $r^* = 25.4$ mm, stamp thickness $t = 700$ μm , and elastic modulus E_0=2.0 MPa. Each simulation result was translated by some arbitrary displacement so that $f(\delta = 0) = 0$; this translation gives the force and displacement relationship that would be observed experimentally. The contact force is normalized by elastic modulus and reported per unit length of roll.

Even though the stamp conformability $Cf = W_{ad}^*/E_0(t + h)$ is small, a dramatically different different force and pressure relationship is observed in the numerical simulations for different surface energies. Higher work of adhesion results in larger contact pressures, forces, and areas at all points (relative to the equilibrium point where $f = 0$). The presence of surface energy results in finite contact pressures and contact widths even at zero applied force f.
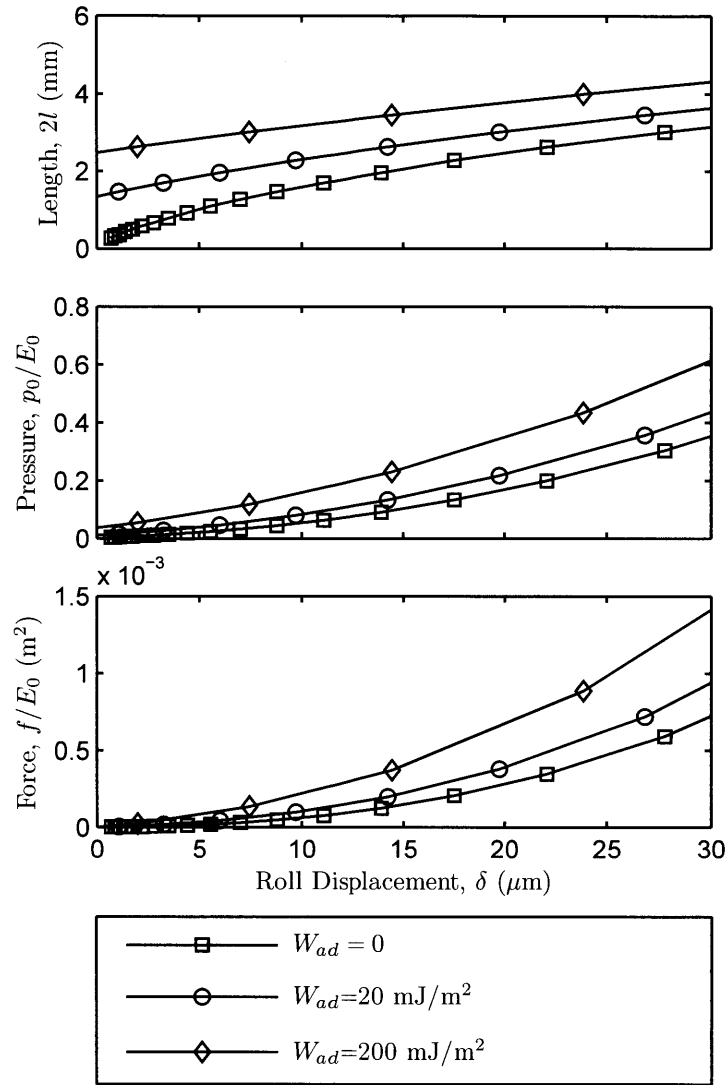
Figure 4-19: Contact behavior for a 0.7 mm elastic layer with varying W_{ad} at the contact interface. Even though conformability $Cf = W_{ad}^*/E_0(t + h)$ is small, the presence of surface energy results in dramatically different observed contact behavior. Results have been scaled for $r^* = 25.4$ mm and $E_0 = 2.0$ MPa.

4.7.4 Experimental Data

Work of Adhesion

The sensitivity of the observed force to work of adhesion makes it difficult to exactly correlate the experimental data to numerical simulation results, especially since the work of adhesion of PDMS can vary significantly. Values between 30 and 300 mJ/m^2 have been reported for the work of adhesion between PDMS and glass [41, 91].

The high material damping of PDMS will result in a lower apparent work of adhesion on advancing contact and a higher apparent work of adhesion on receding contact [94]. This phenomena is apparent in the experimental data, where significant hysteresis is observed between advancing and receding contact in the loading cycle (Figure 4-20). This hysteresis is due to viscoelastic material effects that are not included in the equilibrium contact equation (4.20), but can be explained by using different values for W_{ad} during advancing or receding contact.
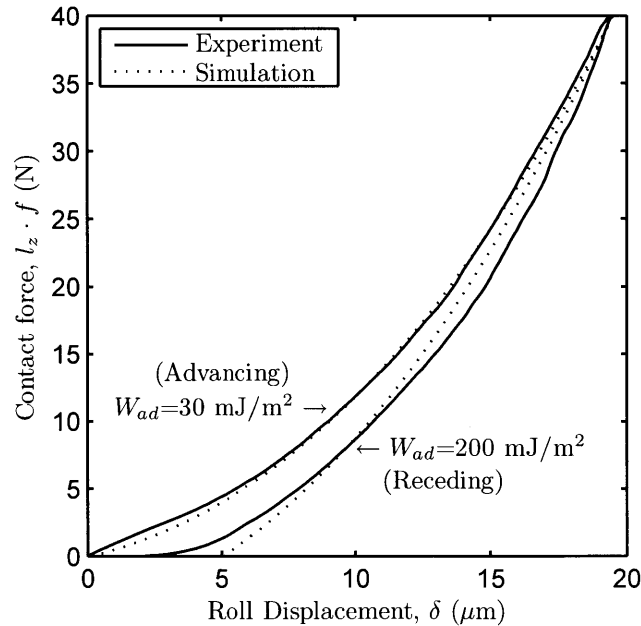
Figure 4-20: Experimental load-displacement data for a stamp with no features (t=698 μm, r^*=25.4 mm, E_0=1.61 MPa). Numerical simulations match the advancing behavior with W_{ad}=30 mJ/m^2 and the receding behavior with W_{ad}=200 mJ/m^2.

151

Figure 4-20 shows that W_{ad}=30 mJ/m^2 is consistent with the experimental behavior during advancing contact. In the following presentation of results, the advancing portion of the experimental data is compared with numerical simulations that assume this corresponding work of adhesion.

Experimental Uncertainty

Three dominant sources of experimental error are discussed in Section 4.6.6: (*i*) stamp asperities, (*ii*) material property uncertainty, and (*iii*) machine accuracy. In the following comparisons of experimental data with simulation results, each of these errors must be accounted for. The effect of stamp asperities is mitigated by registering the experimental and simulation data at some finite load (5 N) where the asperities have a diminished effect (Figure 4-16). The remaining error sources (material property uncertainty and machine accuracy) are addressed by creating an error band about the nominal simulation behavior.

This error band is constructed using both the 95% confidence interval of stamp modulus E_0 (Table 4.3) and the 95% confidence interval of machine accuracy ($\pm 1.96\sigma_{\text{machine}}$), based on a low frequency accuracy standard deviation $\sigma_{\text{machine}} = 75$ mN. For example, the upper bound on force is determined by mapping the dimensionless simulation results to dimensional variables using the upper confidence interval limit on E_0. Similarly, the lower bound is determined using the lower confidence interval limit on E_0. An additional uncertainty of $\pm 1.96\sigma_{\text{machine}}/k_{\text{stamp}}$ is added these limits to account for the machine accuracy, where k_{stamp} is the nominal simulated stiffness about the registration point (5 N).

$$l_z \cdot f_{\text{bounds}} = l_z \cdot f_{\text{simulation}}(E_0 \pm CI) \mp 1.96 \frac{\sigma_{\text{machine}}}{k_{\text{stamp}}(E_0)} \tag{4.65}$$

$$2l_{\text{bounds}} = 2l_{\text{simulation}}(E_0 \pm CI) \pm 1.96 \frac{\sigma_{\text{machine}}}{k_{\text{stamp}}(E_0)} \tag{4.66}$$

Summary of Results

The following plots compare experimental and numerical results for the stamp parameters shown in Table 4.3. Figure 4-21 shows cases a-c, representing very small features and elastic layer contact. Figure 4-22 shows cases d-e, representing elastic foundation contact with large compliant features on a thin stamp. Figure 4-23 shows cases f-g, representing an intermediate stamp with similar feature and stamp body stiffness.

The reported force measurements in Figures 4-21 - 4-23 correspond to the actual force superimposed on a 60 mm wide stamp; contact length $2l$ reported is the average of two contact images at different points along the roll axis. Measurement uncertainty is expressed by an error zone about the nominal simulation result, reflecting both a 95% confidence interval of elastic modulus E_0 as reported in Table 4.3 and a 95% confidence interval of the experimental apparatus accuracy (low frequency $\sigma = 75$ mN).

These experimental results support the accuracy of the analytical and numerical modeling approaches. The experimental and simulation data match well given the difficulty associated with making accurate measurements of this contact behavior. Exploration of these models is motivated by the need to understand the sensitivity of the process to small perturbations and asperities; these same inherent variations make an accurate measurement difficult to obtain. The load-displacement data does not always match the simulations well at small loads and displacements where small asperities dominate the contact behavior. Throughout the entire range of displacements, the total contact area is highly sensitive to the work of adhesion and often varies dramatically between camera frames (the average of the two camera images is shown in the results). These discrepancies are believed to be associated with the difficulty in obtaining a 'perfect' experimental construct rather than fundamental flaws in the models.
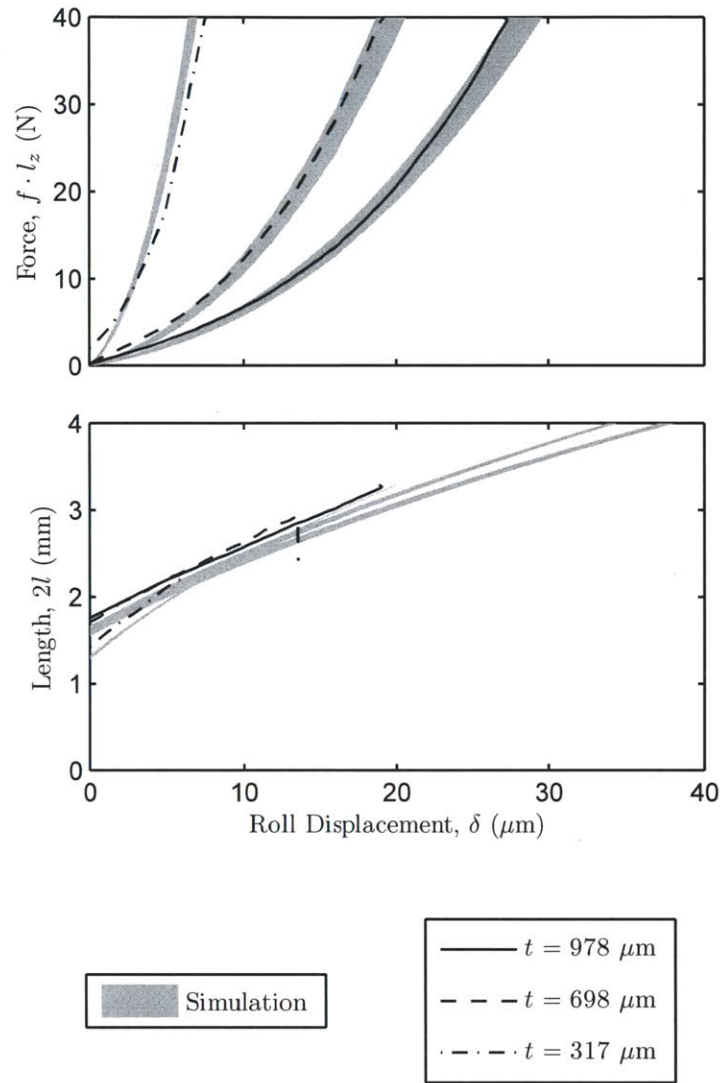
Figure 4-21: Experimental results for solid stamps with no features, emulating an elastic layer with submicron features. Simulation results are shown in gray with width corresponding to experimental uncertainty (see text). Experimental samples correspond to Table 4.3a,b,c.
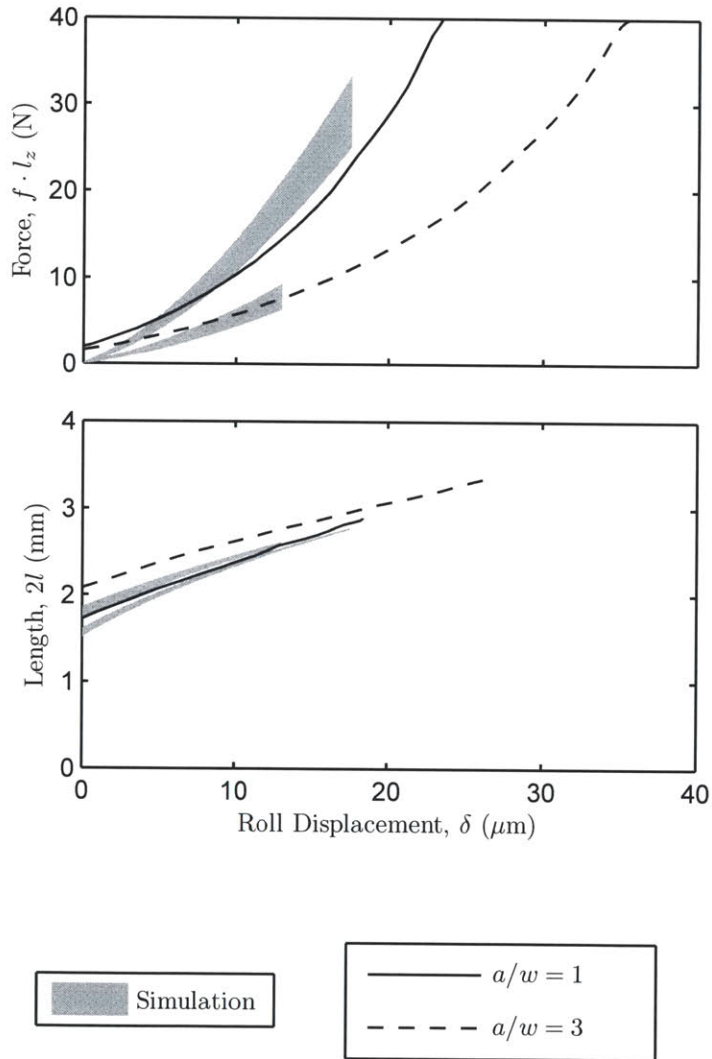
Figure 4-22: Experimental results for patterned stamps with nominal thickness of 200 μm. Simulation results are shown in gray with width corresponding to experimental uncertainty (see text). Experimental samples correspond to Table 4.3d,e.
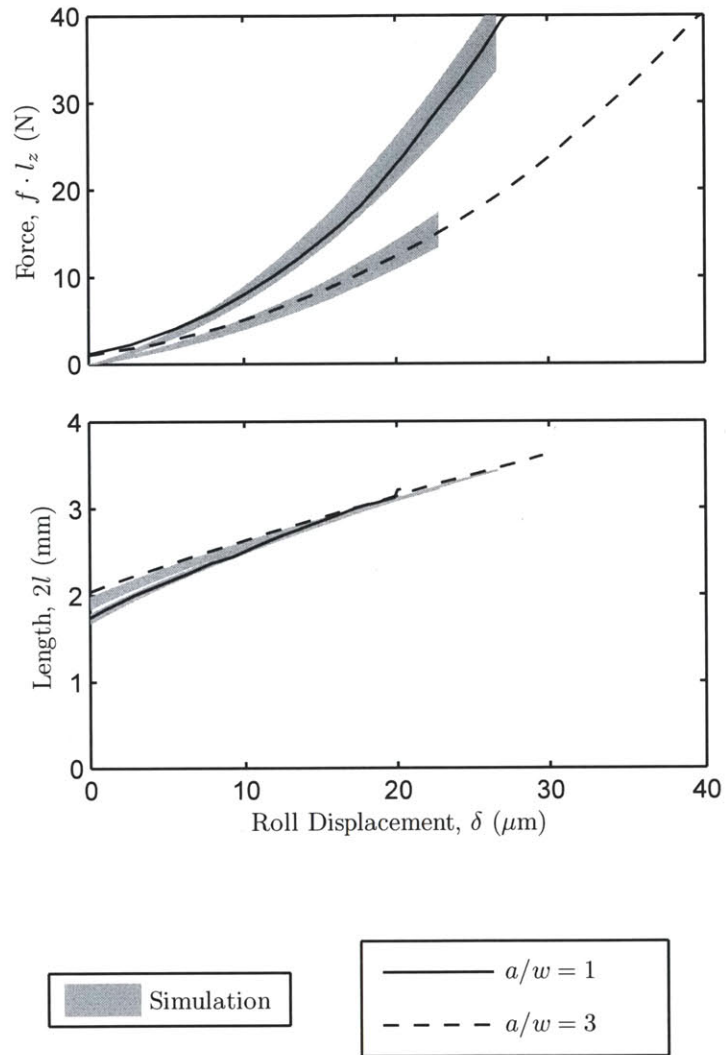
Figure 4-23: Experimental results for patterned stamps with nominal thickness of 500 μm. Simulation results are shown in gray with width corresponding to experimental uncertainty (see text). Experimental samples correspond to Table 4.3f,g.

4.8 Discussion and Summary

The analytical models agree well with the numerical results in the appropriate limits. While the elastic layer model does not always accurately predict the contact force or area, it gives an accurate estimate of contact pressure. In each case shown in Figure 4-17 the model and the simulation show the same trends, such that the model can be considered a valid for determining scaling laws and sensitivities.

The elastic foundation model matches the simulation behavior for large values of the criterion $r/t \gg 1$ and strains that satisfy $\epsilon_{yy} > X_c \cdot a/(a + w)$ (4.25). The latter is satisfied until a displacement of 35 μm; the simulations show stiffening as this limit is approached that the model does not capture (Figure 4-18). The elastic foundation provides a good estimate of contact behavior when the features are much more compliant than the stamp body.

This study examined quasi-static contact between the roll-mounted stamp and a rigid substrate. When this process is implemented in a dynamic state, i.e. the roll moves relative to the substrate, both advancing and receding contact will be observed. This combination of contact states will result in asymmetrical contact with simultaneous advancing and receding contact on opposite sides of the roll (cf. Figure 4-20).

The patterns used in this study were all continuous about the perimeter of the stamp (in the $\hat{\psi}$ direction, Figure 4-2). Patterns consisting of posts, intermittent lines, or lines oriented along the axis $\hat{z}$ of the roll, the discontinuities in $\hat{\psi}$ must be taken into account when considering the work of adhesion. These discontinuities prevent features from being 'pulled' into contact with the substrate until some portion of the feature makes contact; when features are very small this will result in effectively zero work of adhesion during advancing contact. On receding contact, however, these patterns will have an even larger apparent work of adhesion because a separate crack must be initiated at each discontinuity.

Maintaining selective contact between a stamp and a substrate is paramount to the success of contact lithography processes. In μCP, the stamp features can collapse

at moderate pressures, often at less than 10% of the elastic modulus E_0 (as evidenced by $K \leq 0.1$ in Figure 3-16). This collapse leads to a destruction of the intended pattern transfer during printing. In roll based printing, the success of contact is thus dependent on the pressure distribution in the contact region.

The models, numerical simulation, and experimental validation in this chapter show that the contact behavior of roll mounted PDMS stamps has a strong dependence on the size and stiffness of microfeatures. Given the relative scale of the stamp features in comparison to the stamp body, this result is at first nonintuitive. It is shown that this behavior is driven largely by the incompressible nature of the stamp materials used in soft lithography. As seen in Figures 4-17, large pressures ($> 0.1E_0$) can be reached in single microns of roll displacement δ for reasonable roll and stamp dimensions. This results in a very narrow process windowws and a very high sensitivity to stamp or substrate asperities and roll positioning errors.

Analytical results are provided in two limits, where the maximum contact pressure for very small features and very large features is given by (4.44) and (4.50), respectively. The approximate analytical results are shown to match finite element and experimental data well, but remain simple enough to allow practical engineering insight. For example, these expressions can be used to predict the process window for a particular printing operation as a function of roll displacement or geometric disturbance rejection. In Part III of this thesis, viewing this process window as a function of stamp parameters will illuminate design tradeoffs for creating compliant stamps and robust printing performance.

Part III

Robust Stamp Design

Chapter 5

Stamp Architecture

5.1 Process Sensitivity

In Part II of this thesis, it was shown that features can collapse at pressures that are only a few percent of the elastic modulus, and moreover, that these pressures can evolve at only single microns of roll displacement. The results of Part II can be used to derive process sensitivity models and inform design of robust stamps. At the center of this exercise lies *disturbance rejection*: how well can a particular stamp maintain faithful contact in the face of varying contact pressures or displacements?

In the case of roll-based lithography, the contact behavior must be able to reject position disturbances, which may occur from simple misalignment of the roll machinery or more spatially complex geometrical errors manifested through roll runout, stamp thickness variations, or substrate asperities. This chapter will introduce a number of errors that can easily produce several microns of variation along the roll length, enough in fact to exceed the printing process window. The printing features will either fail to make contact or collapse under excessive pressure if these position disturbances are too large; either of these events results in process failure.

By analyzing the spatial frequency content of these errors, it will be shown that the most problematic variations are those at with a spatial wavelength that lies between the feature scale and the roll length. These variations can only be attenuated by actuation at high spatial frequencies or an appropriately compliant stamp; the latter

would be preferable from a cost and complexity perspective. To this end, this chatper will examine opportunities for robust (compliant) stamp design and propose a new compliant stamp architecture.

5.1.1 Error Sources

Disturbances in roll-based contact lithography come from a number of sources and are manifest across multiple length scales. Figure 5-1 gives several examples of these errors and their sources.
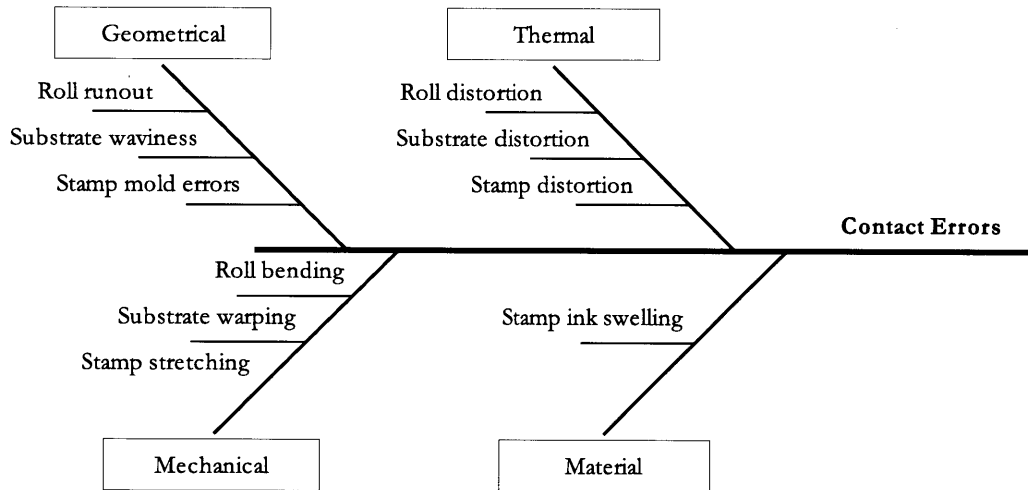
Figure 5-1: Fishbone diagram of disturbance sources in roll based printing. Displacement errors can be characterized as geometrical, thermal, mechanical, or material. Each of these specific error sources can easily contribute one or more microns of variation, resulting in a cumulative error that is greater than the collapse displacement of sensitive stamps.

Dimensional errors ϵ may come from fundamental geometrical inaccuracies in the processing equipment, temporally dependent thermal distortions, load-induced distortions, or diffusive processes in the stamp material itself.

Geometrical inaccuracies include roll and bearing runout and substrate waviness. At a smaller scale, the surface roughness of the same components becomes important. The stamp dimensions are typically determined by the mold that the stamp is cast

in; any variations in this mold are superimposed at the roll nip region by replication in the stamp itself.

Thermal errors can dramatic, especially as the scale of processing equipment increases. The error $\epsilon_{\text{thermal}}$ associated with expansion of a component is given by

$$\epsilon_{\text{thermal}} \approx l\alpha\Delta T \tag{5.1}$$

where l is a characteristic dimension, α is the coefficient of expansion, and ΔT is the change in temperature. Steel has a coefficient of expansion $\alpha \approx 10$ ppm/°C, while PDMS has a coefficient of $\alpha \approx 900$ ppm/°C [67], almost two orders of magnitude higher. Thus, a single degree change in temperature will alter the diameter of a 100 mm roll by 1 μm, while a 1 mm thick PDMS stamp would also expand by 1 μm.

Mechanical deformations will occur during loading. While the roll loads are small in microcontact printing compared to, for example, coating or sheet forming processes, small deflections will still occur in bearings, rolls, and even rigid substrate carriers. An interesting example of mechanical deformation is stamp stretching: if the stamp is not perfectly mounted to the processing roll thickness variations will occur. Incompressibility gives that the stamp material volume ratio is unity (2.7): $J = \lambda_r\lambda_z\lambda_\psi = 1$. This constraint on volume ratio J can be rearranged to show that a thickness error $\epsilon_{\text{stretch}}$ associated with non-uniform stamp stretching ($\lambda_z, \lambda_\psi \neq 1$) during mounting scales with stamp thickness t and is given by

$$\epsilon_{\text{stretch}} = (\lambda_r - 1)t = (\lambda_z^{-1}\lambda_\psi^{-1} - 1)t \tag{5.2}$$

For example, a local mounting stretch of $\lambda_z = 1.01$ will cause not only a 1% distortion in the stamp pattern, but also a 10 μm thickness variation through a $t = 1$ mm stamp.

Material properties can change as a function of environmental parameters. For example, PDMS is used because it absorbs alkenethiols and acts as an ink pad, or reservoir, during printing. This beneficial behavior can become detrimental; high concentrations of thiols will cause PDMS to swell up to 6% [5]. Others suggest operating at less than a 40 mM ink concentration to keep this swelling below 0.5%

[37]. Even so, 0.5% results in a characteristic 5 μm variation through a 1 mm stamp thickness.

5.1.2 Process Window

These errors ϵ_i have varying temporal and spatial frequencies. These errors can be modelled as variations from the nominal roll displacement $\hat{\delta}$ along the roll axis $\hat{z}$. This perspective results in a locally varying roll displacement δ^* that has an error content ϵ as a function of cylindrical coordinate $[z, \psi]$ at any point in time:

$$\delta^*(z, \psi) = \delta_0 + \epsilon(z, \psi) \tag{5.3}$$

The magnitude of δ^* must lie within the process window $(0, \delta_c)$ for all z and ψ for a robust printing process, where δ_c is a critical feature collapse displacement. There are three ways to improve the process performance: increase robustness (increase δ_c), decrease disturbances (decrease ϵ), or add a control effort u:

$$\delta^*(z, \psi) = \hat{\delta} + \epsilon(z, \psi) + u(z, \psi) \qquad \in (0, \delta_c) \tag{5.4}$$

The remaining chapters of the thesis approach this process window from all three perpectives. In this chapter, an effort will be made to decrease the stamp sensitivity by making it more compliant under compression. In Chapter 6 a new method of producing a more accurate stamp with smaller thickness errors will be developed. Finally, in Chapters 7 and 8 develop a two degree-of-freedom roll positioning stage for low spatial frequency actuation $u(z, \psi)$ and Chapter 9 studies methods of in-process feedback control using this stage.

5.1.3 Spatial Frequency

Analyzing error ϵ from the perspective of spatial frequency content provides powerful insights. Here error E_ϵ is defined in the frequency domain (inverse of wavelength λ_ϵ)

as the Fourier transform of ϵ:

$$E_\epsilon(1/\lambda_\epsilon) = \mathcal{F}\left(\epsilon(z, \psi)\right) \tag{5.5}$$

The frequency content of E_ϵ can be divided into four basic ranges of spatial frequency (Figure 5-2): low (roll length), midrange (stamp thickness to roll length), high (feature scale discontinuities), and ultra (nanoscale surface roughness).
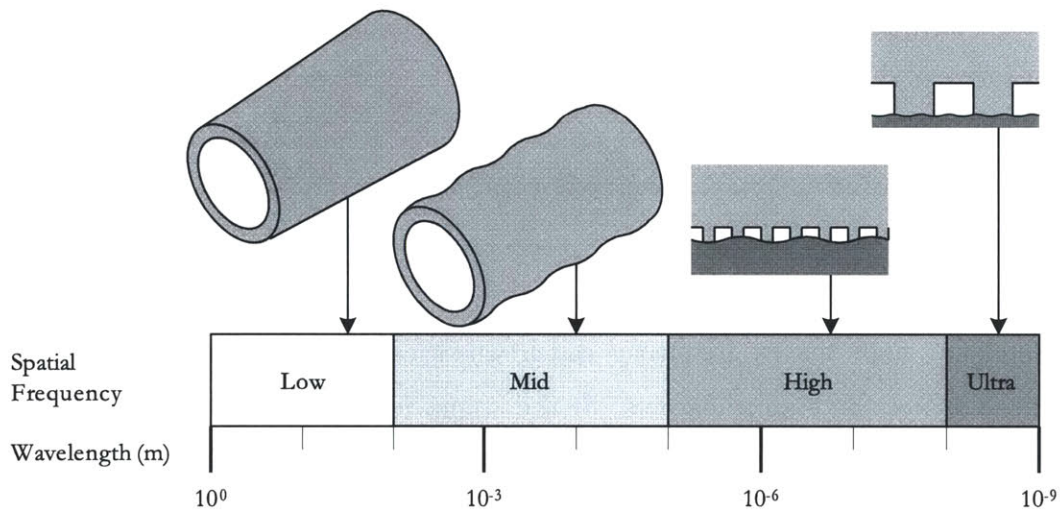
Figure 5-2: Process disturbances viewed in the frequency domain. The effect of process disturbance ϵ depends on the spatial frequency content as captured by its Fourier transform E_ϵ. Errors have different effects at different frequencies, for example (*i*) low frequencies with wavelength on the order of the roll length, (*ii*) mid range frequencies with wavelength on the order of the roll radius or stamp thickness, (*iii*) high frequencies with wavelength on the order of the feature scale, or (*iv*) ultra-high frequencies with wavelength less than the feature scale.

It is assumed that the magnitude of these disturbances is much less than the wavelength ($E_\epsilon/\lambda_\epsilon \ll 1$), which is a good assumption for the physical phenomena described in the wishbone diagram. For example, thermal distortion will not create asperities larger than a fraction of the wavelength in metallic roll equipment that has a high diffusivity and low coefficient of expansion. Similarly, mechanical bending or stretching will not result in large error magnitudes relative to the error wavelength.

165

This assumption gives that the error E_ϵ is Brownian with respect to spatial frequency.

Nanoscale surface roughness (ultra-high spatial frequency) is typically not a problem in microcontact printing because PDMS has been specifically chosen to make conformable contact with the substrate. A criterion for spontaneous conformable contact can be derived by balancing the work of adhesion with the strain energy required for the stamp material to conform to surface asperities [8]:

$$E_\epsilon \approx \sqrt{\frac{W_{ad}\lambda_\epsilon}{2.2E^*}} \tag{5.6}$$

or, in terms of dimensionless variables (assuming incompressibility with $\nu = 1/2$)

$$\frac{E_\epsilon}{\lambda_\epsilon} \approx \sqrt{\frac{1}{3}Cf} \tag{5.7}$$

where the relevent conformability is $Cf = W_{ad}/\lambda_\epsilon E_0$.

Similarly, high spatial frequency disturbances can be accommodated by small deformations of the stamp features. If the stamp features have an aspect ratio of order one, they can easily accommodate a value of ϵ that is a fraction of their height.

Midrange and low spatial frequency errors are thus the most problematic in soft lithography. These errors force deformations in the entire stamp, resulting in far field pressures that are often substantial enough to cause feature collapse. Very low frequency errors can be accommodated by active positioning of the roll relative to the substrate, which is examined in Part IV of this thesis. Midrange errors are much more difficult: they either require active control of the stamp displacement with a corresponding spatial frequency, which may be complicated and expensive, or require a stamp that can tolerate the error magnitude ϵ, which can be quite difficult to achieve through conventional stamp design practices. The distinct purpose of this chapter to examine the latter: how can the stamp be appropriately designed to provide a sufficiently large process window?

The following sections examine stamp design from two perspectives. First, the consequences of local feature deformation (Chapter 3) are used to understand optimal

feature design, namely choice of feature aspect ratio A. Second, the results from the analysis of the roll based contact mechanics analysis (Chapter 4) are used to provide insight into higher level stamp architecture, especially stamp thickness t and material composition. The results of these analyses will show that stamps are highly sensitive to disturbances and that there is little opportunity to adjust this during the design phase. Ultimately, this observation motivates a new stamp architecture that allows tuning the contact sensitivity.

5.2   Robust Stamp Design

5.2.1   Feature Design

A holistic approach to feature deformation was taken in Chapter 3 to map out the dominant stamp defect modes as a function of stamp geometry (aspect ratio A and pattern ratio P) and load conditions (far field pressure S and displacement X). Figure 3-24 showed that collapse mode could be predicted by aspect ratio A and pattern ratio P. In practice, the pattern ratio P of a stamp is often dictated by a desired device architecture or pattern, leaving the aspect ratio A as the only free variable in stamp feature design. The goal of design is to maximize the real far field pressure σ_∞ or displacement v_∞ that the stamp can withstand.

Using the same results that led to Figure 3-24, the critical collapse load and displacement can be computed as a function of aspect ratio and pattern ratio. Once the collapse mode has been determined, the appropriate collapse pressure can be determined using either (3.27) for buckling or (3.19) for roof and sidewall collapse. This critical collapse pressure $S_c = \sigma_{\infty,c}/E_0$ can be plotted as a function of aspect ratio A and pattern ratio P (Figure 5-3a).

The critical collapse displacement X_c can be found using the feature stiffness K:

$$X_c = \frac{S_c}{K} \tag{5.8}$$

This dimensionless displacement can be converted to physical feature displacement

v_∞ using the relationship in (3.5):

$$v_{\infty,c} = w\frac{S_c}{K}\frac{AP}{P+1} \tag{5.9}$$

Displacement $v_{\infty,c}$ is plotted in Figure 5-3b for the example of $w = 20$ μm features.

Inspection of Figure 5-3 gives design insight into robust feature design. It is the goal of any such design to maximize either the pressure or displacement that any particular feature pattern can sustain before collapse. From these plots it is evident that these two variables are synonymous: maximizing S_c for some particular P also maximizes $v_{\infty,c}$. This maximum occurs along the boundary of the buckling collapse mode; a larger aspect ratio increases feature robustness until buckling occurs, at which point larger aspect ratio becomes detrimental.

An important observation of this exercise is that features can only tolerate a far field displacement that is on the order of their characteristic width w, and a pressure that is on the order of the material shear modulus $\mu_0 = \frac{1}{3}E_0$. If the printing pattern is sparse, the pattern ratio P becomes large and tolerable pressures drop to only a few percent of E_0.
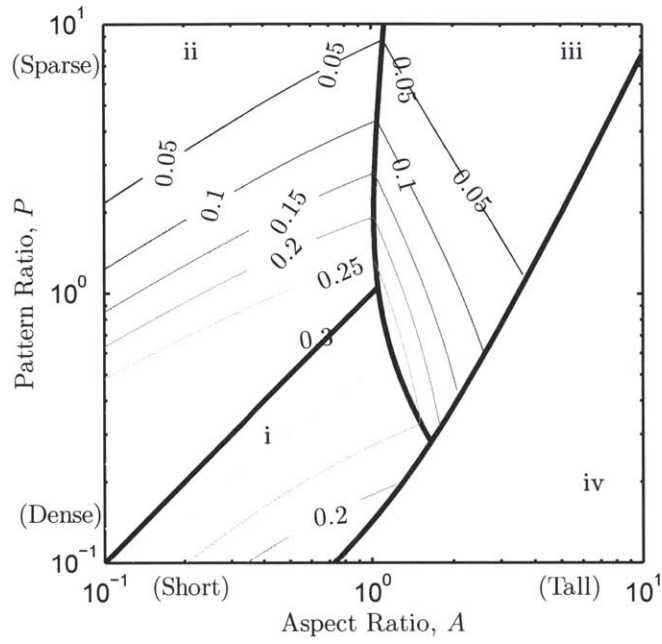
(a)
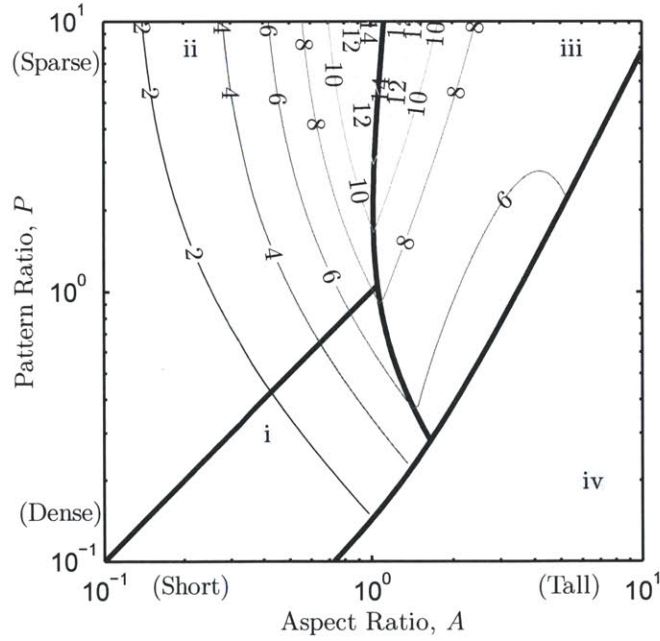
(b)

Figure 5-3: Critical collapse points during stamp loading: (a) contact pressure $S_c = p_c/E_0$ and (b) displacement $v_{\infty,c}$ (μm) for a stamp with w=20 μm. Collapse modes are (i) sidewall collapse, (ii) roof collapse, (iii) buckling, and (iv) lateral collapse. Material properties of PDMS-PDMS $W_{ad} = 44$ mJ/m^2, PDMS-substrate $W_{ad} = 200$ mJ/m^2, and elastic modulus $E_0 = 1.5$ MPa are assumed.

169

5.2.2 Stamp Design

An estimate of the acceptable position error (equivalently, disturbance) can be made by considering the elastic layer and elastic foundation models developed in Chapter 4. The maximum contact pressure p_0 must remain below some critical level p_c where stamp features collapse, as determined by the results in Chapter 3. A model for the collapse displacement δ_c of the roll can be constructed using results from the two analytical limits of roll behavior in Chapter 4:

In the case of very small or very stiff features, the elastic layer model (4.44) gives the critical roll displacement δ_{cI} as

$$\delta_{cI} = \sqrt{\frac{p_c t^3}{6 E_0 r^*}} \qquad (5.10)$$

where t is the stamp thickness, r^* is the equivalent roll radius, and E_0 is the stamp modulus.

In the case of very compliant features the elastic foundation model (4.50) gives δ_{cII} as

$$\delta_{cII} = \frac{p_c}{k_p} \qquad (5.11)$$

where k_p is the stiffness of the printing features on the stamp.

An estimate of permissible displacement using a conventional stamp architecture (i.e. with no backing layer) is obtained by assuming that both the features and stamp body deform as springs in series, requiring in a sum of displacement δ_{cI} and δ_{cII} in response to a contact pressure of p_c:

$$\delta_c = \frac{p_c}{k_p} + \sqrt{\frac{p_c t^3}{6 E_0 r^*}} \qquad (5.12)$$

This model is expected to give a *conservative* estimate of permissible displacement. In making the approximation of series springs, it is assumed that the boundary of the stamp body still experiences zero slip relative to the substrate. In reality, this boundary can move slightly under load as the features deform in shear.

In the limit of large features, the first term in (5.12) gives a significant contribution

to total displacement. Substituting expressions for p_c and k_p from (3.4) and (3.6) (respectively),

$$\frac{p_c}{k} = \frac{S_c E_0}{\frac{P+1}{P} \frac{K}{h} E_0} \tag{5.13a}$$

$$= \frac{S_c}{K} \frac{P}{P+1} h \tag{5.13b}$$

This result shows that the first term in (5.12) can never be larger than the feature scale, because (*i*) $S_c/K = X_c$ is never greater than unity, (*ii*) $P/(P+1)$ is never greater than unity, and (*iii*) h can never be greater than about the feature width w (cf. limiting aspect ratio $A = 1$ in Figure 5-3a).

This observation indicates that for very small patterns (micron and submicron), significant displacements in the system to tolerate ϵ must come from the stamp body, represented by the second term in (5.12). Sparse patterns (large P) have very small collapse pressures, often only a few percent of the stamp modulus (5% of E_0 or less). The results of Chapter 4 showed that these pressures can be reached at very small displacements δ (see for example Figure 4-17 where these pressures can occur at only a few μm).

If catastrophic pressures occur at displacements of only single microns, it will be very difficult to implement a manufacturing scale process that is robust to disturbances ϵ that are of the same order. The process design task is thus to design a stamp that maximizes δ_c in (5.12) regardless of the scale of printing features.

There are two clear design variables that arise from (5.12): stamp thickness and stamp material properties. Each variable is examined in the following subsections with the goal of maximizing δ_c.

Stamp Thickness

Increasing the thickness t of the stamp will increase δ_c, though this improvement comes at the cost of higher stamp pattern distortion and poor adhesion between the stamp and roll.

171

Application of beam theory predicts that strain at the stamp surface will increase with stamp thickness t. In Euler beam theory, radius of curvature ρ induces a variable strain throughout the beam thickness that is zero at the neutral axis:

$$\epsilon_{xx} = \frac{y}{\rho}, \qquad y \in [-t/2, t/2] \tag{5.14}$$

From this relationship, the surface strain $\epsilon_{xx}(y = t/2)$ is proportional to $t/2r$. As an example, a stamp with thickness $t = 1$ mm will have a surface strain of 2% when mounted to a roll with $r = 25.4$ mm. This strain causes a distortion in the stamp pattern, which may or may not be tolerable for the application at hand. It is clearly desirable to minimize this effect, though there are certainly opportunities to account for this deformation (i.e. create the stamp with a feature pitch 2% smaller than desired).

A similar application of beam theory shows that bending energy increases dramatically with stamp thickness. Using Euler beam theory, the energy per unit length of the stamp is

$$\frac{dU}{dx} = \frac{1}{2}\frac{M^2}{E_0 I} \tag{5.15}$$

With the relationships $M = E_0 I/\rho$ and $I = t^3/12$, this becomes

$$\frac{dU}{dx} = \frac{E_0 t^3}{24\rho^2} \tag{5.16}$$

When a stamp is mounted to a roll ($\rho = r$, where r is the roll radius), this strain energy must be overcome by the work of adhesion W_{ad} between the stamp and roll. This requirement that $dU/dx < W_{ad}$ limits the stamp thickness to

$$\frac{t/2r}{<} \sqrt[3]{3Cf} \tag{5.17}$$

where conformability $Cf = W_{ad}/rE_0$.

As an example, the 25.4 mm radius roll used in the experimental sections of this

thesis can only support a stamp that is slightly more than 1 mm thick (assuming values of E_0=2 MPa and W_{ad}=20 mJ/m^2). During the experimental work reported in this thesis, it was found that stamps thicker than about 500 μm were difficult to reliably mount to the roll. Even if the stamp is cast against a metal shim that is magnetically mounted to the roll (as described by [17]), the bond between the stamp and shim is not permanent and only as strong as the work of adhesion.

Only chemical bonds can overcome this limit. As an example, benchtop experiments during this research demonstrated a bond between PDMS and aluminum can be formed using cyanoacrylate (Loctite 420) after priming the PDMS surface (Loctite 770). Peel tests caused the PDMS to tear, indicating that the bond formed with this adhesive is stronger than PDMS itself. Other researchers have used the strategy of creating a plasma bond between the PDMS and a glass roll [111, 49], drawing inspiration from bonding of PDMS microfluidic chips to glass slides. Unfortunately, these irreversible bonding methods present significant challenges in implementation.

At this juncture, the design tradeoffs of surface strain and adhesion make it difficult to arbitrarily increase the thickness of stamps. This limitation constrains the ability to increase the process window δ_c (5.12) through adjusting stamp thickness t.

Stamp Material

When the conformability $Cf = \gamma_s/E_0 w$ of features approaches one, surface forces begin to dominate elastic forces. Equivalently, the radius of curvature of the material can be defined as $\rho_m = \gamma_s/E_0$ [47], indicating the length scale where $Cf = 1$. In the example of PDMS, $\rho_m = 10$ nm (E_0=2 MPa, γ_s=20 mJ/m^2). This characteristic length presents a particular challenge in very small features below 100 nm, resulting in edge rounding and poor feature definition [82, 89] in addition to the limit of lateral collapse introduced in Chapter 3.

Stiffer materials (higher E_0) give a smaller ρ_m, providing accurate replication of smaller features. With this motivation, stiff elastomeric materials have been investigated for contact lithography. Hard PDMS (h-PDMS) formulations have been reported with an elastic modulus of about 8-9 MPa [89, 12]. This higher modulus

173

comes at the expense of much smaller fracture strains, about 7% compared to well over 100% for traditional PDMS.

Simply employing a stamp material with a higher modulus offers no improvement in δ_c. Any change in elastic modulus E_0 does not affect the deformation in this displacement boundary value problem; p_c and k_p in (5.12) are likewise linear functions of E_0 and cancel out any uniform change in modulus.

However, using a hard material for the stamp features (modulus E_0') and a softer material for the stamp body *can* increase δ_c (as proposed by [89]). This architecture increases p_c and k_p in (5.12) by a factor of E_0'/E_0, giving an improvement of $\sqrt{E_0'/E_0}$ in δ_c. With the published values of E_0', this composite stamp architecture can offers a factor of 2 improvement in δ_c.

The conclusion is drawn from this analysis that there exists no method to *dramatically* alter the process limit δ_c of stamps using the conventional stamp architecture.

5.2.3 Compliant Architecture

The preceding discussion shows a lack of flexibility in stamp design to achieve a robust printing process with large δ_c. When features are large, the first term in (5.12) is large and the features themselves absorb a significant portion of the contact energy. For example, 50 μm features result in a forgiving process with δ_c on the order of tens of microns. Conversely, small features have a correspondingly higher stiffness and direct the majority of contact energy to the stamp body. These small features result in very small δ_c, typically on the order of several microns.

The key observation of this section is the following: large, compliant stamp features decouple the contact sensitivity from the stiff mechanics of the incompressible stamp body. Unfortunately, the stamp features are dictated by the device architecture being printed. An innovative approach introduced here is to include a *second* set of features in the stamp architecture; a logical point to incorporate these is at the interface between the roll and the stamp (Figure 5-4).

Introducing this *backing layer* improves stamp design flexibility to achieve a process that can tolerate large disturbances compared to varying stamp thickness or

modulus. If a backing layer (with stiffness k_b) is added to the stamp, (5.12) becomes

$$\delta_c = \frac{p_c}{k_p} + \sqrt{\frac{p_c t^3}{6 E_0 r^*}} + \frac{p_c}{k_b} \qquad (5.18)$$

The final term in (5.18) provides significant design flexibility to create a stamp with some desired printing pattern, thickness, and roll diameter while retaining the ability to tailor the stamp compliance and resulting process window 5-5.
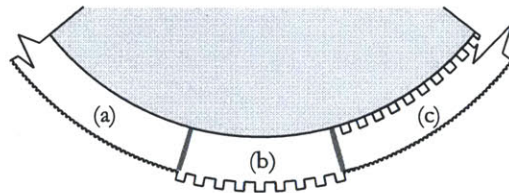
Figure 5-4: Motivation for backing layer architecture. (a) Large features absorb significant contact energy before collapse, while (b) small features cannot absorb much contact energy and collapse at much smaller roll displacements. (c) Incorporating large backing features allows a stamp with small printing features to absorb large amounts of contact energy before collapse for robust printing.

(a) (b)
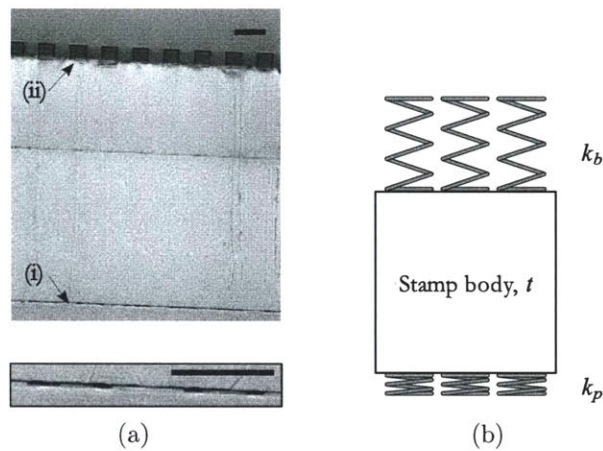
Figure 5-5: Compliant stamp architecture with two feature layers. (a) Cross section micrograph of a stamp with (i) printing features and (ii) backing features; inset is a zoomed view of the printing features (scale bars 100 μm). This stamp was formed by laminated two thin stamps together in a back-to-back configuration. (b) This architecture is more compliant; the backing features have stiffness k_b that is presumably much lower than the stiffness k_p of the printing features. This design allows tuning the mechanical behavior of the stamp independently of the stamp thickness t, allowing the stamp to absorb more mechanical energy before the printing features collapse.

5.3 Contact Analysis

A stamp with a backing layer resembles a beam suspended between two beds of springs (printing features and backing features) with stiffness k_p and k_b, respectively. The contact behavior of the beam can be examined by considering the displacement w of the stamp body from its nominal position (Figure 5-6).

Figure 5-6: Beam theory analogy of backing layer behavior. The stamp body forms a beam suspended between two layers of features that act as individual springs with stiffness k_p and k_b. The load q on some differential element dx of the stamp body is dependent on the local displacement of the neutral axis $w(x)$.

The beam load function q can be derived by considering a differential element of the beam dx. Assuming that the stamp body is rigid in compression, all deformation must occur in either the printing features or the backing features. The displacement on the backing features is the same as the beam displacement $w(x)$, giving a load function dependent only on this displacement and the backing feature stiffness k_b:

$$q_b(x) = k_b w(x) \qquad (5.19)$$

The load function of the printing features is more complex. The nominal displacement will be the difference between the substrate boundary condition $(\delta - x^2/2r^*)$ and the beam deformation. However, these features are only engaged in the contact region

where $x \in [-l, +l]$, giving a piecewise load function:

$$q_p = \begin{cases} k_p \left(\delta - \frac{1}{2r^*}x^2 - w \right) & x < l \\ 0 & x > l \end{cases} \tag{5.20}$$

Combining these individual loading functions gives the complete loading function $q = q_b + q_p$:

$$q = \begin{cases} k_p \left(\delta - \frac{1}{2r^*}x^2 \right) - (k_b + k_p)w & x < l \\ -k_b w & x > l \end{cases} \tag{5.21}$$

The boundary conditions on the stamp body are dictated by symmetry at $x = 0$

$$\left. \frac{dw}{dx} \right|_{x=0} = 0 \tag{5.22}$$

$$\left. V \right|_{x=0} = 0 \tag{5.23}$$

and vanishing deformation far from the contact region

$$\left. w \right|_{x=\infty} = 0 \tag{5.24}$$

$$\left. M \right|_{x=\infty} = 0 \tag{5.25}$$

5.3.1 Euler Beam Theory

The simplest form of beam deformation is Euler beam theory, governed by moment-induced bending. The the curvature ρ of the beam is proportional to the moment M in the beam

$$\rho = \frac{M}{E^*I} \tag{5.26}$$

The shear V at each point x along the beam axis is the local derivative of the moment at that point:

$$V = \frac{dM}{dx} \tag{5.27}$$

And the rate of change of shear gives the load distribution q at each point on the beam:

$$q = \frac{dV}{dx} \tag{5.28}$$

Finally, the displacement $w(x)$ of the beam must be linked to the local curvature:

$$\frac{1}{\rho} = \frac{\frac{d^2 w}{dx^2}}{\left(1 + \left[\frac{dw}{dx}\right]^2\right)} \tag{5.29}$$

For small displacements, dw/dx is small, giving

$$\frac{1}{\rho} = \frac{d^2 w}{dx^2} \tag{5.30}$$

Hence, by combining the preceding equations, the stamp displacement in Euler beam bending is governed by the relationship

$$\frac{d^4 w}{dx^4} = \frac{q}{E^* I} \tag{5.31}$$

Substituting the loading function (5.21) into the governing equation gives a piecewise differential equation of the form

$$\begin{cases} \frac{d^4 w}{dx^4} + \frac{k_b + k_p}{E^* I} w = \frac{k_p}{E^* I} \left(\delta - \frac{1}{2r^*} x^2\right) & x < l \\ \frac{d^4 w}{dx^4} + \frac{k_b}{E^* I} w = 0 & x > l \end{cases} \tag{5.32}$$

The characteristic equation of this system is of the form $\lambda^4 + a = 0$, giving roots λ that are two pairs of complex conjugates $\pm \sqrt[4]{a} \frac{\sqrt{2}}{2}(1 \pm i)$. Letting $\beta = \sqrt[4]{a} \frac{\sqrt{2}}{2}$ results in a homogeneous solution of the form

$$w_{HS} = e^{\beta x} \left(c_1 \cos \beta x + c_2 \sin \beta x\right) + e^{-\beta x} \left(c_3 \cos \beta x + c_4 \sin \beta x\right) \tag{5.33}$$

This homogenous solution gives $w(x)$ that *oscillates* well beyond the contact region defined by $x < l$. This behavior is unexpected in the actual physical system: one would imagine that the stamp displacement simply *decays* to zero beyond the contact region.

5.3.2 Timoshenko Beam Theory

In reality, the stamp is able to not only bend, but shear, giving a much smaller transient beyond the contact region. Timoshenko beam theory incorporates this shear deformation [98]. The beam slope Φ is now defined, and again determined by the moment in the beam:

$$\frac{d\Phi}{dx} = \frac{M}{EI} \tag{5.34}$$

However, the derivative of w is now dependent on shear deformation as well

$$\frac{dw}{dx} = \Phi - \frac{\alpha_s V}{GA} \tag{5.35}$$

where G is the shear modulus and A is the cross sectional area of the beam. Correction factor α_s is of order unity; for rectangular beam profiles Timoshenko gives $\alpha_s = 6/5$ [98]. This gives a governing differential equation of

$$\frac{d^4 w}{dx^4} = \frac{1}{EI} q - \frac{\alpha_s}{GA} \frac{d^2 q}{dx^2} \tag{5.36}$$

Substituting the loading function q gives

$$\begin{cases} \frac{d^4 w}{dx^4} - \alpha_s \frac{k_b + k_p}{GA} \frac{d^2 w}{dx^2} + \frac{k_b + k_p}{E^* I} w = \frac{k_p}{E^* I} \left(\delta - \frac{1}{2r^*} x^2 \right) + \alpha_s \frac{k_b}{GAr^*} & x < l \\ \frac{d^4 w}{dx^4} - \alpha_s \frac{k_b}{GA} \frac{d^2 w}{dx^2} + \frac{k_b}{E^* I} w = 0 & x > l \end{cases} \tag{5.37}$$

This differential equations has a characteristic equation of form $\lambda^4 - a\lambda^2 + b = 0$. It can be shown (assuming $\nu = 1/2$) that for $k_b > 4\alpha_s^2 E/t$ this characteristic equation has two pairs of identical real roots. These real roots β and γ result in a homogeneous

solution of form

$$w_{HS} = (c_1 + c_2 x)e^{\beta x} + (c_3 + c_4 x)e^{\gamma x} \tag{5.38}$$

This solution gives exponential decay of the beam displacement, matching physical expectations much better than the Euler solution.

5.3.3   Elastic Layer

The beam theory analysis can be forgone when the bending energy is very small compared to the strain energy in the features. In this limit, an elastic foundation model will give accurate estimates of center contact pressure p_0.

Similar to the elastic layer analysis of large compliant features in Section 4.4.2, the pressure is assumed independent at each point. This assumption amounts to permitting discontinuities in $w(x)$, in contrast to the beam bending models that require $\mathbb{C}^4$ continuity in $w(x)$. The net force q on each differential element dx must be zero; it follows from the loading function (5.21) that

$$w = \begin{cases} \frac{k_p}{k_b + k_p} \left(\delta - \frac{1}{2r^*} x^2 \right) & x < l \\ 0 & x > l \end{cases} \tag{5.39}$$

The pressure at each point along the interface is identically q_p, giving

$$p(x) = \frac{k_b k_p}{k_b + k_p} \left(\delta - \frac{1}{2r^*} x^2 \right) \tag{5.40}$$

At this point, equivalent stiffness k^* is defined as

$$k^* = \frac{k_b k_p}{k_b + k_p} \tag{5.41}$$

The contact behavior can now be derived following the reasoning in Section 4.4.2 (see (4.49), (4.51), and (4.52)), substituting $k = k^*$. This gives roll contact center

181

pressure p_0, contact half length l, and contact force f as

$$p_0 = k^*\delta \tag{5.42}$$

Assuming the contact area to be defined by a chordal intersection gives

$$l = \sqrt{2r^*\delta} \tag{5.43}$$

Integrating the pressure across this area gives force:

$$f = \frac{4}{3}k^*\sqrt{2r^*\delta^3} \tag{5.44}$$

For this approach to be accurate, the bending energy $U_{bending}$ must be small compared to the elastic energy $U_{feature}$ stored in the features during deformation:

$$U_{beam} \ll U_{features} \tag{5.45}$$

Euler beam theory gives the bending energy per unit length as

$$\frac{dU_{beam}}{dx} = \frac{M^2}{2E_0 I} \tag{5.46}$$

where the moment M in the beam is proportional to the moment of inertia I ($t^3/12$) and inversely proportional to the radius of curvature ρ:

$$M = \frac{E_0 I}{\rho} \tag{5.47}$$

Substituting these expressions give the bending energy in terms of the contact variables:

$$\left.\frac{dU_{beam}}{dx}\right|_{x=0} = \frac{t^3}{24r^{*2}}E_0 \tag{5.48}$$

At the critical collapse point the strain energy in compressed features at the center

of the contact interface is

$$\frac{dU_{feature}}{dx}\bigg|_{x=0} = \frac{1}{2}k^*\delta_c^2 = \frac{1}{2k^*}p_c^2 \tag{5.49}$$

Applying (5.48) and (5.49) to (5.45) yields the criterion that

$$\mathcal{C}_3 = 12\frac{p_c}{E_0}\frac{p_c}{k^*t}\frac{r^{*2}}{t^2} \gg 1 \tag{5.50}$$

This criterion holds when the backing layer is compliant and when the stamp is very thin. A typical printing configuration might have small printing features with $w = h = a = 1$ μm and much larger backing features with $w = 50$, $h = a = 100$ μm. Chapter 3 shows that these printing features will have a collapse pressure of about $p_c = \pi/4 \cdot KE_0$, where $K = 0.36$ for features with an aspect ratio A and pattern ratio P of unity. The stiffness of the printing features k_p and backing features k_b can be found using (4.24) ($720000E_0$ and $4200E_0$, respectively). Using these stiffness values, the criterion developed above is satisfied ($\mathcal{C}_3 \geq 3$) for stamp thickness t less than 3.1 mm.

5.3.4 Numerical Solution

The beam-based equations are solved numerically for particular values of δ using the given boundary conditions. The contact length l is determined by minimizing the sum of strain energy in the stamp features, strain energy in the stamp body, and work of adhesion:

$$U = U_b + U_p + U_{\text{beam}} + U_{\text{adhesion}} \tag{5.51}$$

where each energy component is given by

$$\frac{dU_b}{dx} = \frac{1}{2}k_b w^2 \tag{5.52}$$

$$\frac{dU_p}{dx} = \begin{cases} \frac{1}{2}k_b\left(\delta - \frac{1}{2r^*}x^2 - w\right)^2 & x < l \\ 0 & x > l \end{cases} \tag{5.53}$$

$$\frac{dU_{\text{beam}}}{dx} = \frac{1}{2}\frac{1}{E^*I}M^2 + \frac{1}{2}\frac{\alpha_s}{AG}V^2 \tag{5.54}$$

$$\frac{dU_{\text{adhesion}}}{dx} = \begin{cases} -W_{ad}^* & x < l \\ 0 & x > l \end{cases} \tag{5.55}$$

For a stable numerical implementation, each spatial variable (δ, x, w, l) is transformed into a dimensionless variable of order unity by normalizing by the stamp thickness t. Likewise, each energy (U_i and W_{ad}) is normalized by k^*t^3. Figure 5-7 compares the solution for each model presented above (Euler beam theory, Timoshenko beam theory, and elastic layer).
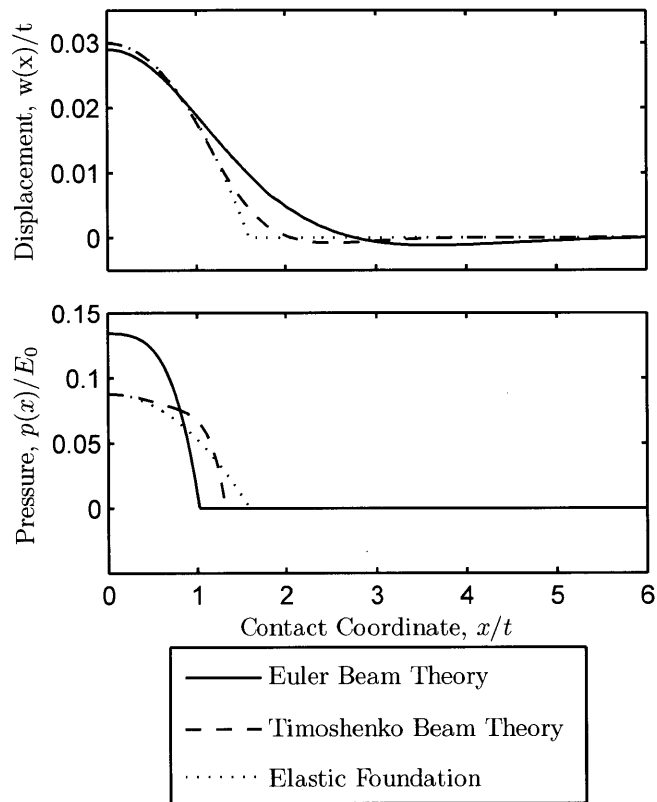
Figure 5-7: Calculated contact behavior for backing layer beam theory models. Stamp body displacement w and contact pressure p are shown as a function of position x from the center of the roll for a roll radius of $r^* = 40t$. Numerical solutions of the Euler, Timoshenko, and elastic foundation boundary value problems are shown. These results show that the Euler model overpredicts center contact pressure p_0 and affects w over an excessive range of x; the Timoshenko model gives a more accurate behavior prediction. The elastic foundation model predicts p_0 as well as the Timoshenko model.

5.4 Results

The same numerical simulation routine and experimental protocol were used as described in Sections 4.5 and 4.6. This section compares the analytical and numerical results, shows experimental verification, and provides a discussion of the data.

The experimental samples are summarized in Table 5.1. In practice, these were the exact stamps used during experiments of roll contact mechanics (Table 4.3) but were mounted with the stamp features against the roll interface.

Table 5.1: Experimental parameters for stamps with backing layers, including the stamp thickness t, feature width w, feature height h, feature gap a, and elastic modulus E_0 with a 95% confidence interval. These stamps were mounted with the features against the roll, leaving the flat side of the stamp at the contact interface.

	t (μm)	w (μm)	h (μm)	a (μm)	E_0 (MPa) (95% CI)
(a)	311	50	47	50	1.37 ± 0.14
(b)	311	50	47	150	1.37 ± 0.14
(c)	590	50	47	50	1.51 ± 0.11
(d)	590	50	47	150	1.51 ± 0.11

5.4.1 Numerical Data

Simulations of backing layers (assuming infintessimally small printing features) were done in the same manner as described in Section 4.5, but with the feature layer adjacent to the roll interface rather than the substrate interface to emulate backing features.

Figure 5-8 shows simulation results for identical features that have been placed at the printing interface and the substrate interface. In both cases, the features absorb a majority of the vertical roll displacement. This observation supports the hypothesis that backing features placed at the roll interface can absorb disturbances and prevent collapse of very small printing features.
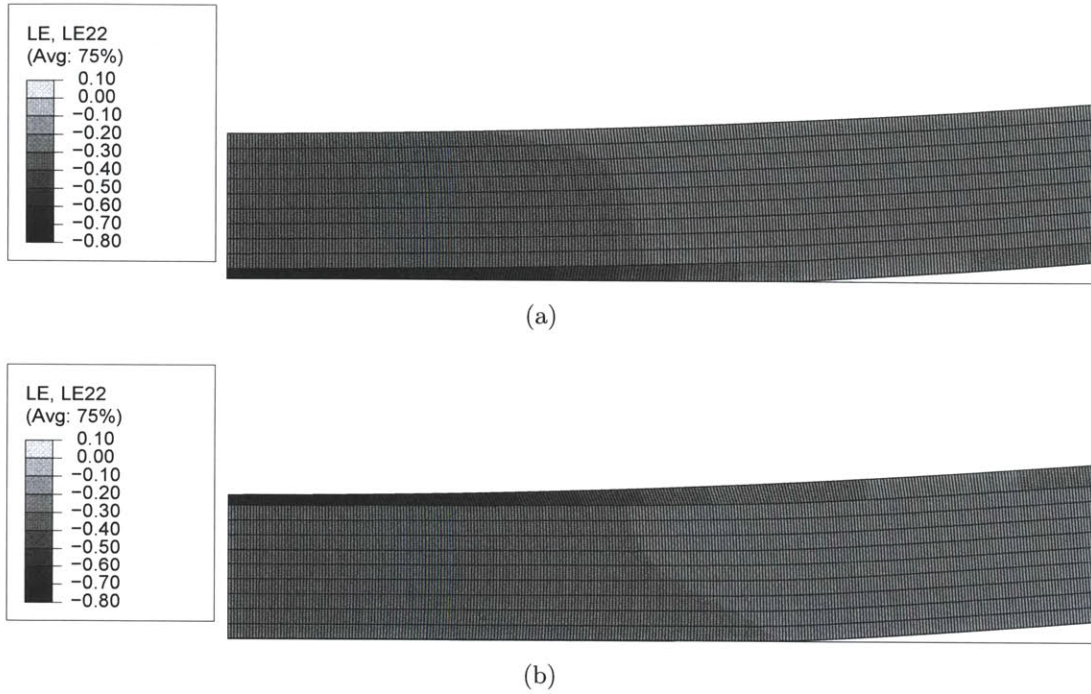
Figure 5-8: Comparison of numerical simulations for identical (a) printing features and (b) backing features. In both cases the majority of strain energy is absorbed by the features, as shown by strain in the vertical direction ϵ_{yy}.

The mechanical response of these two cases (corresponding to Table 5.1a-b) is plotted in Figure 5-9 assuming a roll radius of 25.4 mm. The contact pressure p is normalized by E_0 and the contact force f is reported per unit length of roll, normalized by E_0.

The stamps plotted in Figure 5-9 have $\mathcal{C}_2 = 7.68 \gg 1$ (4.55) and $\mathcal{C}_3 = 119 \gg 1$ (5.50). Because $\mathcal{C}_2 \gg 1$ the elastic foundation model will give accurate results, and because $\mathcal{C}_3 \gg 1$ the bending energy of the stamp body can be neglected. The numerical results support this conclusion, showing that the behavior of each stamp is nearly identical and follows the prediction of the elastic layer model until near the theoretical collapse point at δ_c=28 μm.
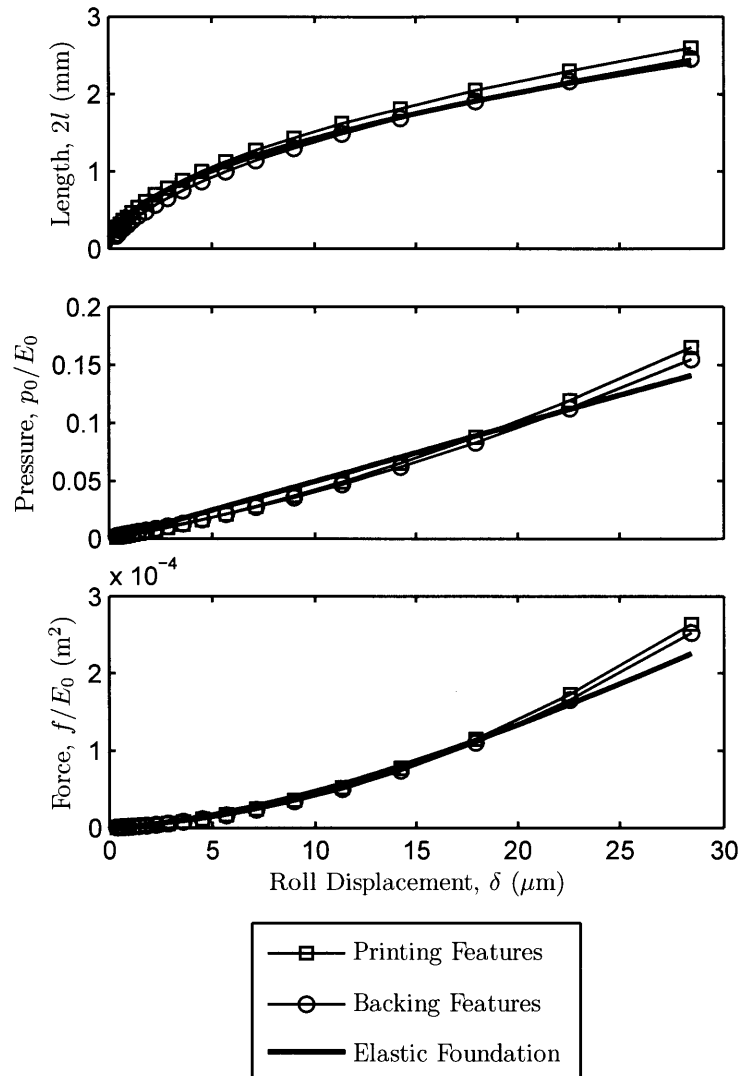
Figure 5-9: Comparison of numerical simulations and elastic foundation model for a stamp mounted in both the printing and backing configurations, assuming a stamp with dimensions shown in Table 5.1b compressed on a roll with $r^* = 25.4$ mm. These models show nearly identical behavior in this case where beam bending energy is small ($\mathcal{C}_3 = 119 \gg 1$).

5.4.2 Experimental Data

The following plots compare experimental and numerical results for the stamp parameters shown in Table 5.1. In short, Figure 5-10 shows results for a 0.31 mm thick stamp and Figure 5-11 shows results for a 0.59 mm thick stamp. In both figures, the corresponding data from the experiments in Chapter 4 to allow comparison of identical stamps with features in either the printing or backing configuration.

The reported force measurements in Figures 5-10 and 5-11 correspond to the actual force superimposed on a $l_z = 60$ mm wide stamp; contact length $2l$ reported is the average of two contact images at different points along the roll axis. Measurement uncertainty is expressed by an error zone about the nominal simulation result, reflecting both a 95% confidence interval of elastic modulus E_0 as reported in Table 5.1 and a 95% confidence interval of the experimental apparatus accuracy (low frequency σ = 75 mN) (see Section 4.7.4). As in Chapter 4, a work of adhesion W_{ad}=30 mJ/m^2 was assumed.

When mounted in a backing layer configuration, the flat surface of the stamp was exposed to the printing interface. Since there were no printing features on the stamp in this orientation, a collapse pressure $p_c = 0.05E_0$ (corresponding to a sparse pattern with $A = 1$, $P = 9$) was assumed to calculate $\mathcal{C}_3$ (5.50). Because $\mathcal{C}_3$ is much greater than unity in each case, the beam bending energy is expected to be negligible so that the stamps behave regardless of mounting direction (printing versus backing). Indeed, this behavior is observed, where each load-displacement curve appears nearly identical within the bounds of uncertainty.

In each experimental case, the force f is slightly lower when the stamps are mounted in a backing configuration. This phenomena is perhaps due to a larger effective work of adhesion W_{ad}^*: when the stamps are in a backing configuration, the smooth surface in contact with the substrate interface has an effective pattern ratio $P = 0$, resulting in larger W_{ad}^* per (4.19).

Figure 5-10: Experimental results for patterned stamps with nominal thickness of 200 μm. Simulation results are shown in gray with width corresponding to measurement uncertainty (see text). Experimental samples correspond to Table 5.1a-b; W_{ad} of 30 mJ/m^2 and $p_c = 0.05E_0$ assumed.
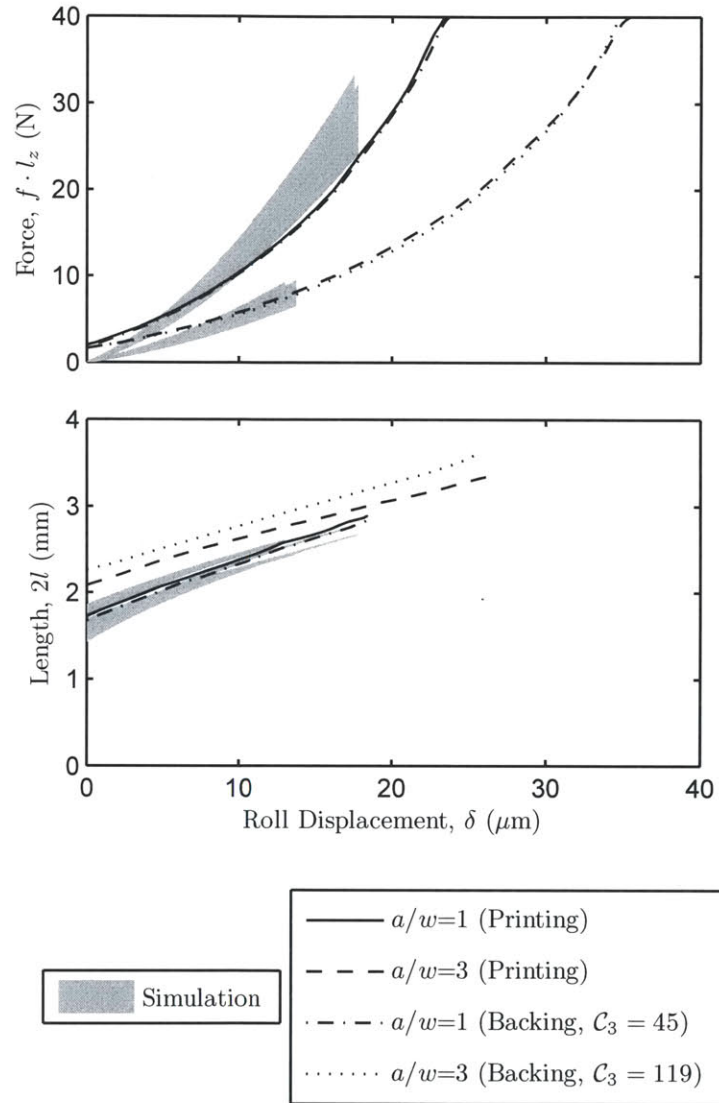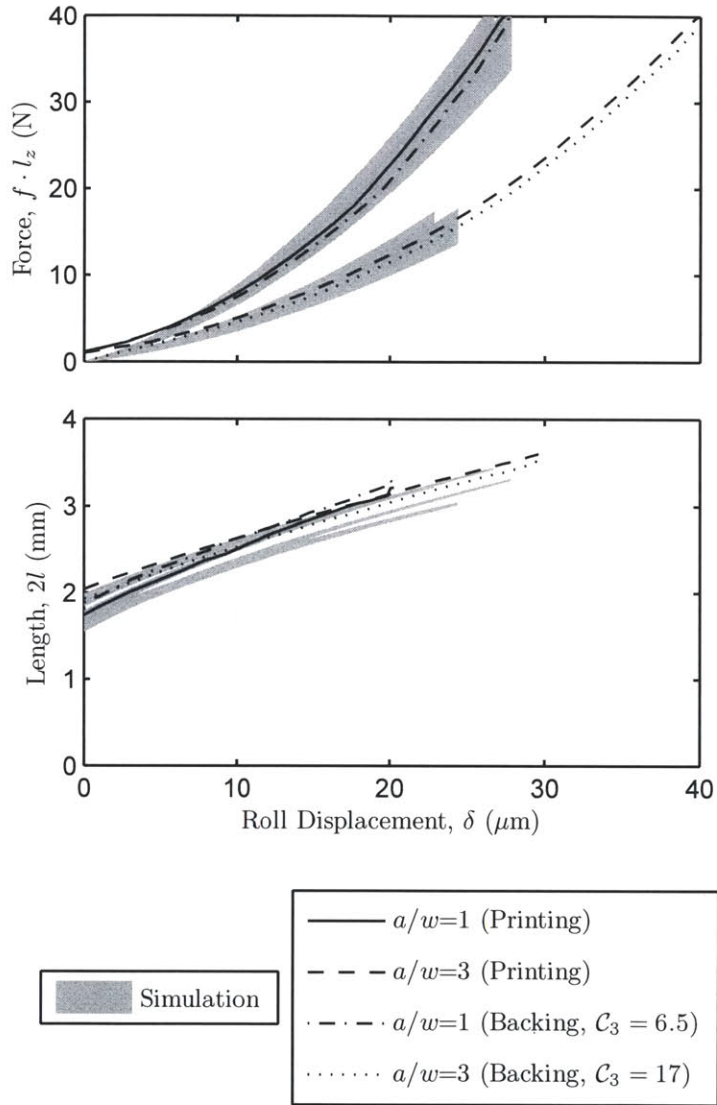
Figure 5-11: Experimental results for patterned stamps with nominal thickness of 500 μm. Simulation results are shown in gray with width corresponding to measurement uncertainty (see text). Experimental samples correspond to Table 5.1c-d; W_{ad} of 30 mJ/m^2 and $p_c = 0.05E_0$ assumed.

5.4.3 Discussion

A new stamp architecture was proposed, operating on the hypothesis that stamp features at the stamp-roll interface could alter the mechanical response of the stamp to improve rejection of asperities and positioning errors. An analogy was drawn between stamps with backing features and beam theory, leading to a model for contact behavior based on Timoshenko beam theory. A scaling argument based on strain energies showed that for many practical stamp designs, the bending energy of the stamp can be neglected. In this case, the behavior of the stamp can be described by an elastic foundation model.

The numerical and experimental results support this hypothesis, showing that microfeature patterns affect stamp mechanical behavior similarly regardless of their location (at the roll interface or at the substrate interface). In each experimental case, criterion $C_3 \gg 1$ was satisfied.

These results are powerful: in a printing configuration, large features can absorb a much larger displacement before collapse pressures are reached at the contact interface. As an example of this, compare the pressure evolution in Figure 4-17 (very small features) and Figure 4-18 (large features). Small features can often not be avoided at the contact interface because they are dictated by the desired pattern transfer. Using this new stamp architecture, large features can be introduced at the roll interface to tune the mechanical response of the stamp even when very small features are used for printing.

5.5 Case Study

A sparse honeycomb pattern (Figure 5-12a) is used as a design case study to illustrate the effect of including a backing layer. This pattern would be useful for creating transparent conductive electrodes, but is very difficult to print because it collapses (Figure 5-12b) at small displacements and low pressures.

(a)   (b)
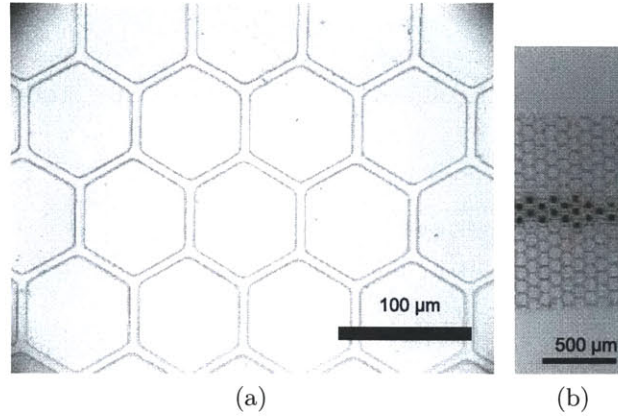
Figure 5-12: Hexagonal pattern used in backing layer case study. (a) Micrograph of a 300 μm thick stamp with honeycomb pattern: edge length of 50 mm, feature width 5 μm, and feature height 3 μm. (b) Image from experimental apparatus showing collapse propagating from the center of the contact zone at only a few microns of roll displacement.

Table 5.2: Case study stamp parameters

Parameter	Value
t	300 μm
w	5 μm
h	3 μm
a	80 μm
r^*	25.4 mm

Using the stamp parameters in Table 5.2, (3.39) predicts a dimensionless stiffness of $K = 0.022$. These sparse features are expected to experience roof collapse at a pressure of $p_c = \frac{\pi}{4} K E_0$ (Chapter 3). The feature stiffness k is given by (4.24). Using this collapse pressure and stiffness in (5.12) predicts a critical collapse displacement of $\delta_c = 4$ μm.

Two backing layers were tested in the configuration shown in Figure 4-4d) to evaluate their impact on process robustness, measured by maximum roll compression before feature collapse. Two separate stamps (Table 5.1a-b) were laminated against the honeycomb stamp (Figure 5-12) to form the desired stamp architecture. Table 5.3 shows the corresponding predictions for critical collapse displacement, neglecting the

additional stamp thickness.

Table 5.3: Predicted collapse displacement of case study pattern

	A_b	P_b	δ_c [μm]
(a)	-	-	3.9
(b)	0.95	1	5.1
(c)	0.95	3	7.4

These laminated stamps were tested using the same machine and protocol described in Section 4.6. Figure 5-13 shows the resulting load-displacement behavior of each stamp truncated to the point where collapse was observed in the contact images. Force f is reported as the actual force applied to the $l_z = 60$ mm wide stamp during the experiment.

Figure 5-13: Experimental load-displacement behavior to collapse point for a sparse hexagonal printing pattern. Compared to a control case with no backing layer (a), backing layers of increasing compliance (b,c) allow both higher force f and higher displacement δ before collapse.
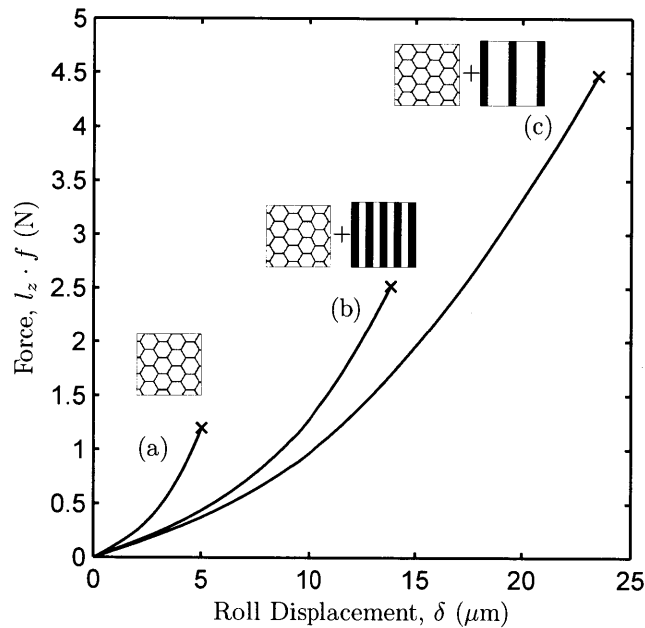
The results of the backing layer experiment are dramatic. The control experiment

(Figure 5-13a) exhibits collapse near the 4 μm predicted value. The stamp can tolerate both more displacement *and* more force before the delicate pattern features collapse by adding backing layers with increasing compliance (Figure 5-13b-c).

The observed collapse displacements are much greater than originally predicted (Table 5.3). This is likely due to two effects: (*i*) a larger stamp thickness that occurred when laminating the two stamp patterns together and (*ii*) a relaxation of the no-slip boundary condition imposed on the stamp body as the backing layer is allowed to not only compress, but shear.

The conclusion from this case study is that the inclusion of a backing layer enables a more robust printing process, especially through tailoring the mechanical behavior of a stamp independent of the particular printing pattern or stamp thickness t.

5.6 Summary

This chapter used stamp deformation results from Part II to guide a discussion of error sources, process limits, and ultimately development of a new stamp architecture for roll based printing that is more robust to displacement disturbances than conventional designs.

The review of error sources showed that mechanical, thermal, and geometric effects can often contribute several microns *each* to the total positioning error ϵ observed at the roll and substrate. This error enters the process as a disturbance to nominal roll displacement $\bar{\delta}$, sometimes causing the local displacement δ^* to fall outside the process window of $(0, \delta_c)$ (5.4). Moreover, δ_c is often smaller than the magnitude ϵ of possible disturbances because of the high collapse pressures that rapidly develop at the stamp contact interface.

To improve robustness to ϵ, especially at mid-range spatial frequencies (Figure 5-2), a new stamp architecture was designed in order to dramatically increase permissible displacement δ_c even when very small micron or submicron patterns are being printed.

Analysis shows that features placed on the reverse side of the stamp (i.e. at the

195

roll bonding interface) will result in the same mechanistic behavior as if they were mounted on the front of the stamp, as long as criterion $\mathcal{C}_3 \gg 1$. The numerical and experimental validations support this analysis. In a case study using a very sensitive printing pattern, this stamp architecture was shown to significantly increase the load and displacement that the stamp construct can tolerate before feature collapse is observed.

Chapter 6

Stamp Casting

6.1 Stamp Replication

The economies of contact lithography are realized by massively parallel replication of features between a stamp and substrate. The stamp itself is a product of surface replication; in both μCP and NIL stamps are patterned by forming against a master surface.

The methods of manufacturing the master surface and subsequently producing stamps are a critical technological hurdle in large area contact lithography. In this chapter, conventional methods of master preparation and stamp production are reviewed. This discussion will show that there remain a number of challenges in the path of truly large scale patterning. The remainder of the chapter is dedicated to introducing and developing a new way of making stamps that are both more precise and inherently scalable compared to silicon-based master templates.

6.1.1 Master Templates

At the heart of contact lithography lies the master template. This surface dictates the ultimate resolution, accuracy, and fidelity that can be achieved in any subsequent patterning step.

While the end goal of contact lithography is often to break the rate limits of

conventional lithography, it is interesting that each template is almost exclusively produced using conventional lithography. This processing choice leverages a well developed, highly accurate system. Eventually, the high cost of producing the template by conventional means is amortized over a large number of reproduced surfaces.

The approaches towards manufacturing templates can be classified into one of two categories: monocrystalline or resist based.

Monocrystalline templates are formed by etching patterns into silicon wafers. Optical lithography is first used to define a pattern in a photoresist. This photoresist acts as a mask during subsequent reactive ion etching (RIE), which forms relief structure in the surface of the wafer.

Resist-based templates are also typically based on silicon wafer substrates, but in contrast to reactive ion etching, the resist itself forms the relief structure. The most common photoresist for these templates is a permanent epoxy-based resist (e.g. Microchem SU8); SU8 was originally developed for MEMS applications [65] but has become widely used for patterning templates for soft lithography and microfluidics fabrication. SU8 can be processed in thicknesses less than 1 μm to greater than 100 μm with large aspect ratios, giving similar geometric capabilities as RIE.

Each template fabrication method has its own advantages. The monocrystalline templates have exceptionally high structural integrity (though small features promote brittle fracture). These templates are typically used for high temperature or high pressure embossing, for example thermal nanoimprint lithography [14], microembossing [25], or casting of amorphous alloys [38]. While resist-based templates are not as mechanically sound, they offer superior surface finish; the base of each replicated feature is defined by the polished substrate rather than an RIE surface with nanoscale surface roughness.

Because of the superior surface finish and low relative cost (no etching equipment required), resist based templates are used almost exclusively for soft lithography, including microcontact printing.

6.1.2 Conventional Stamp Casting

For a manufacturing application, replication of stamps from a master template must satisfy two requirements. First, the stamp must exactly replicate each micro or nanoscale feature on the template. Second, the macroscopic dimensions of the stamp must be precisely controlled. The latter requirement is often the more difficult to satisfy.

Section 5.1 developed a process window in terms of allowable roll displacement δ_c or error distribution $\epsilon(z, \psi)$. In that discussion, it was shown that catastrophic pressures develop at the printing interface at only several microns of displacement. This same process window maps directly to the tolerance that must be placed on the thickness of stamps.

Two general approaches to stamp casting have been reported in the literature: open face casting [60, 49] and injection molding [40, 17, 55].

Open face casting is performed by placing the master template on a horizontal surface, forming a dam around it, and pouring prepolymer over the surface. Gravity is allowed to equilibrate the free surface of the prepolymer before it cures. This method is able to produce very flat and smooth free surfaces, with the exception of edge effects near the dam driven by surface tension σ. The thickness t of the stamp is determined by mass conservation within the dam. Any error in leveling the horizontal surface will be manifest as a taper ϵ_{taper} in the cured stamp.

Injection molding is performed by forming a mold around the master surface and using a pressure differential to introduce prepolymer. In contrast to conventional injection molding, the pressure gradient in this process may be formed by pulling a vacuum on the mold rather than applying pressure to the feedstock; this can help degas the precursor and prevent gas entrapment in the cured stamp. The mean thickness $\bar{t}$ in this process can be controlled more carefully by the mold and gravity has nominally no effect on stamp taper. At the same time, any surface roughness or waviness of the mold will be imparted on the stamp.

6.1.3 Conventional Stamp Mounting

Once stamps are cast, they must be mounted to rolls. The accuracy of the final stamp construct can be no better than the accuracy of this mounting process, regardless of the accuracy of the master template. With this in mind, the transfer process must both (*i*) bond the stamp to the roll and (*ii*) provide a means of aligning the stamp to the roll. .

In planar stamping (i.e. patterning of silicon wafers), it is common to cast the stamp between the master template and a rigid backplane [55, 89]. In this manner, dimensional accuracy imparted by the master is maintained by this rigid backplane that becomes an integral part of the stamp.

In roll based processing, a similar concept has been reported where stamps are cast against a flexible (but transversely rigid) backplane, for example ferrous shim stock [96, 92, 56, 4, 17, 107, 40] or polymer films [60]. These films can subsequently be mounted to rolls using magnetic attraction or double sided adhesive tape, respectively.

Other approaches directly mount the stamp to the roll from the master surface using an irreversible bond. As one example, it is well known that a strong bond can be formed between PDMS and glass after plasma treatment of both surfaces. This technique has been used to bond stamps directly to glass processing rolls [111, 49]. While quite common, this plasma bonding technique is sensitive to plasma treatment parameters, requires specialized plasma treatment equipment, and requires a glass roll. As an alternative permanent bonding method, bench level tests during this thesis showed that cyanoacrylate (Loctite 401) will form suitable bonds between PDMS and metal rolls with an appropriate primer (Loctite 770).

6.1.4 Challenges

Distinct challenges exist in each of these areas (master templates, stamp casting, and stamp mounting), especially as processing rolls are scaled larger towards practical manufacturing sizes.

As rolls increase in diameter and length, stamp dimensions (nominally a rectangle

with dimension of roll length and roll circumference) will outgrow conventional wafer processing technology. Opportunity certainly exists to adapt larger scale lithographic processing, such as that used in manufacture of flat panel displays. Regardless of the approach, it is likely that some entirely new technology will be required to manufacture master templates with scalable dimensions.

Even if a large area template is made, it will be quite difficult to cast stamps with extremely uniform dimensions. Stamp dimensions ϵ must be controlled within the process window δ_c as given by (5.4), placing bounds on acceptable manufacturing tolerances. For example, maintaining thickness uniformity within a tolerance of single microns will be quite difficult when stamps are scaled to large dimensions (i.e. one meter), but will be paramount for achieving a robust process. This level of stamp uniformity represents a daunting challenge of dimensional control within a few parts per million.

Mounting large stamps accurately will require new approaches or specialized precision alignment machinery. Non-uniform mounting leads to both pattern distortions and variations in stamp thickness (5.2). As discussed in Section 5.2.2, wrapping a flat stamp around a cylindrical roll results in a residual stress distribution and pattern distortion on the surface of the stamp.

A challenge that has not been addressed is the ability to eliminate discontinuities in roll mounted stamps, i.e. how to create a stamp that creates a *continuous* pattern around the periphery of a roll. In conventional printing, e.g. flexography, roll equipment is simply made large enough (more than 1 m in diameter if necessary) that an entire printing panel (newspaper page; packaging box panel, etc) can be mounted. The repeating patterns in thin film transistor arrays or engineered metasurfaces could be made using much smaller and less expensive rolls and stamps if a single continuous pattern could be replicated in the stamp without discontinuities.

Based on these challenges, several requirements are proposed for an 'ideal' stamp production method. The resulting stamp should:

(*i*) possess no fundamental scaling limitations

(*ii*) exhibit micron-level thickness uniformity

(*iii*) be in a stress-free state when mounted

(*iv*) have a pattern continuously about the periphery

6.2 Cylindrical Stamps

The problems persistent in conventional stamp casting motivate development of an improved stamp manufacturing method. The entire process should be re-examined rather than trying to optimize individual steps within the confines of traditional processing techniques.

A stamp must be cast against a cylindrical master if it is to have a stress-free state when mounted to a roll. Moreover, adopting a cylindrical master allows the opportunity to create a *continuous* stamp that completely wraps the processing roll.

Cylindrical processing requires redevelopment of not only the stamp casting process, but also master template patterning. Conventional optical lithography is typically limited to planar substrates and cannot be directly adapted to surfaces with curvature.

Photoresist remains an attractive patterning medium because of the high resolutions attainable. Photoresist patterning can also reach high levels of accuracy in a non-contact process with no disturbance forces (compared to, for example, micromachining or embossing).

Photoresist can be patterned on a curved surface using direct write lithography with a single focused light source. Rather than selectively exposing a resist on on a wafer stepper or aligner using a mask, the resist can be patterned using the serial process that is used to make the mask itself.

Very uniform coatings can be applied in a centrifuge. A drum of radius r spinning at a high speed ω will create a uniform free surface just as in open face casting. The Bond number $Bo = \rho r \omega^2 h^2 / \sigma$ will increase as a result of the high centripetal acceleration, reducing edge effects driven by surface tension σ in a fluid layer of density

ρ and height h. At the same time, the Galileo number $Ga = r\omega^2 h^3/\nu^2$ will increase for a given fluid with kinematic viscosity ν, resulting in much faster convergence to the uniform free surface. These effects can be leveraged to create uniform layers of photoresist and prepolymer on the interior of a centrifuge drum.

Using a centrifuge-based approach to master template fabrication and stamp casting can be done by depositing three distinct layers within a centrifuge drum (Figure 6-1 b, c, and d respectively):

(i) Planarizing layer (photoresist)

(ii) Patterning layer (photoresist)

(iii) Stamp layer (PDMS)
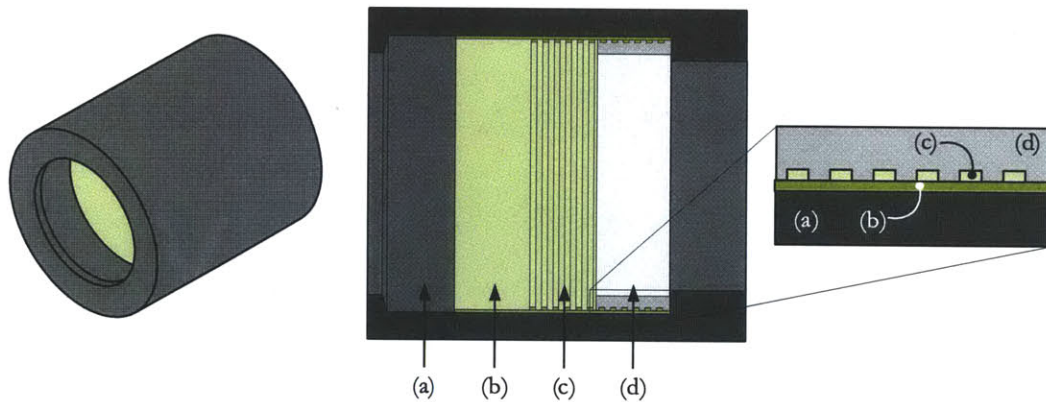
Figure 6-1: Coating steps required to create a patterned cylindrical stamp: (a) machined drum surface, (b) planarizing layer, (c) patterning layer, (d) stamp layer.

In the first step, a layer of photoresist is deposited on the inner surface of a drum by *centrifugal coating*, as opposed to spin coating on a wafer. The entire layer of photoresist is cured; in the case of a negative photoresist this can be accomplished by uniform exposure. This critical step provides a precise and uniform datum surface, (nominally) regardless of the quality of the drum surface.

Next, a second layer of photoresist is deposited on the inner surface of the same drum by centrifugal coating. This photoresist is selectively exposed by a direct-write

laser system. After exposure, the resist is developed to create a pattern that will eventually be transferred to the stamp surface.

In the third step, polymer precursor is deposited on the inner surface of the same drum (for example PDMS precursor). The PDMS is allowed to cure while the drum is spinning, which may be accelerated by heating the drum.

Finally, the cured stamp (Figure 6-2) is removed from the drum and mounted to a roll. The third step can be repeated a number of times to create additional stamps from the same template that was patterned in the first two steps.
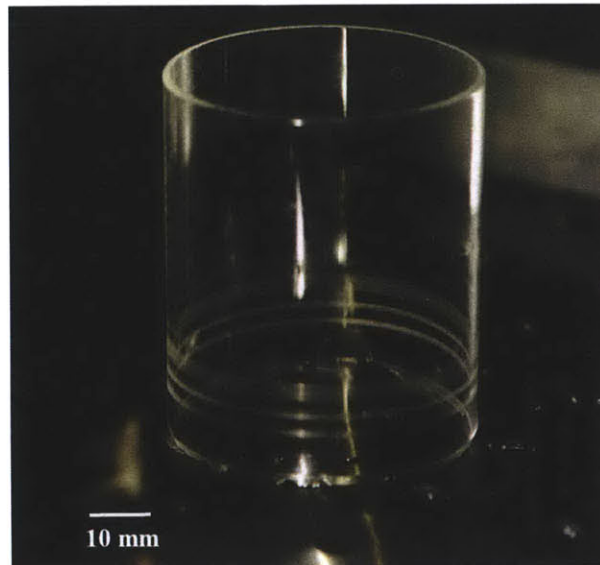
Figure 6-2: PDMS stamp made with the proposed centrifuge process

Ordinarily centrifugal casting is performed with phase-change materials (i.e. molten iron for pipes or melted thermoplastics for bushings [32]). In this adaptation, the chemical curing (as opposed to thermally dependent solidification) of photoresists and PDMS precursors allows carefully tuning the spin time and curing point to reach an optimally uniform surface independent of the thermal history of the process.

The remaining sections develop an analytical model of centrifugal coating, discuss the design of a direct write laser system, and highlight experimental results from a proof of concept implementation.

6.3 Centrifugal Coating

This section examines the governing fluid dynamics of a centrifugal coating process.

Photolithographic processes ubiquitously use spin coating to deposit a uniform layer of fluid. In this process, fluid is dispensed at the center of a wafer (or other substrate), which is then rotated at high speeds (often several thousand rpm) to create a thin layer of fluid. During the spinning, centrifugal forces are balanced by viscous forces, resulting in a final film thickness that scales inversely with the square root of rotational speed. Higher order effects, due to solvent evaporation and non-Newtonian flow, result in slight deviations from this scaling law and a final film that is slightly thicker at the center of the substrate [26].

Alternatively, high speed centrifuging of liquid on the interior of a drum is a uniquely stable case of flow on a cylindrical surface. If the flow is on the outside of the drum ('coating flow'), surface tension gives rise to edge effects at slow rotation speeds, ribs form at moderate speeds, and the fluid is shed from the cylinder by centrifugal forces at high speed [83, 35, 69, 53, 71].

On the inside of a drum ('rimming flow'), ribs or 'disks' form at low speeds [83]. Only at high rotational speeds does a uniform layer form on the inner surface of a rotating cylinder, stabilized by centrifugal forces.

In contrast to spin coating, the final film thickness in centrifugal coating can be governed by mass conservation rather than rotational velocity. Longer spin times can be used to eliminate defects like bubbles that plague thick films of photoresist. Finally, the film thickness on a perfectly cylindrical surface will not have the thickness variation present in the radial direction during spin coating.

The following subsections present the derivation of a coating model, followed by a discussion of implications on photoresist and PDMS films.

6.3.1 Fluid Dynamics

The transient behavior of a fluid inside a rotating drum is considered here, where the drum is of radius r, length l_z, and the fluid layer has a variable thickness $h(\psi)$ that

is a function of the local coordinate inside the drum. The drum is spinning rapidly at a constant speed ω with its axis oriented horizontally in a constant gravitational field g (Figure 6-3).
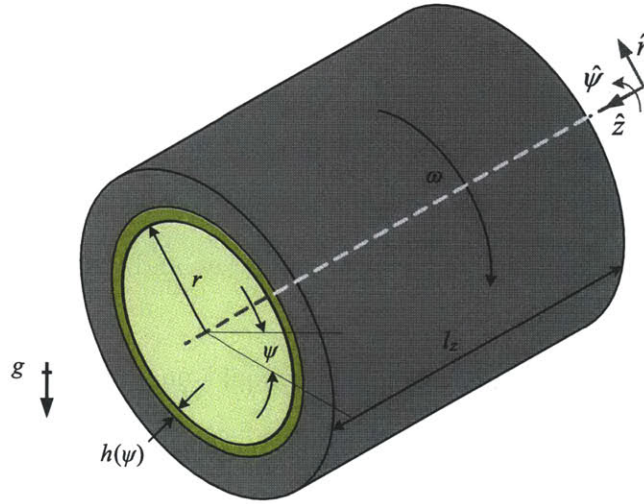
Figure 6-3: Cylindrical coordinate system and characteristic dimensions for a horizontal centrifuge drum with a layer of coating fluid on its interior.

In the following analyses, it will be assumed that the centripetal acceleration is much greater than gravity ($\omega^2 r \gg g$) and that the fluid layer is everywhere thin ($h(\psi) \ll r$).

The Navier-Stokes equation for incompressible flow of a Newtonian fluid is

$$\rho \left(\frac{\partial v}{\partial t} + v \cdot \nabla v \right) = -\nabla p + \mu \nabla^2 v + b \tag{6.1}$$

where ρ is the fluid density and μ is the dynamic viscosity, linked by kinematic viscosity $\nu = \mu/\rho$. v, p, and b are the velocity field, pressure field, and body forces (respectively). Continuity of an incompressible fluid requires that

$$\nabla \cdot u = 0 \tag{6.2}$$

This problem can be analyzed in rectilinear coordinates $\hat{x}$ and $\hat{y}$ with velocity field

206

components u and v (respectively) when the fluid layer is thin relative to the drum radius (Figure 6-4).
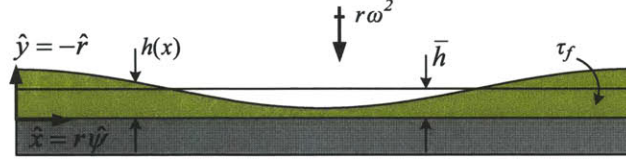

Figure 6-4: Rectilinear approximation of a coating flow flow inside a centrifuge drum. The centrifugal acceleration $r\omega^2$ creates a stabilizing body force that causes sinusoidal asperities (as shown) to decay to a uniform free surface of height $\bar{h}$. Analysis shows that asperity decay occurs as a first order system with fluid decay time constant τ_f.

For small Reynolds number flows $Re = \rho v l / \mu$ (where v and l are a characteristic velocity and dimension) the inertial terms on the left hand side of (6.1) can be shown negligible. For a horizontal centrifuge, the body force of a point located at angle ψ on the centrifuge drum is

$$\boldsymbol{b} = \begin{bmatrix} b_\psi \\ b_r \end{bmatrix} = \begin{bmatrix} g\cos(\omega t + \psi) \\ g\sin(\omega t + \psi) + \rho r\omega^2 \end{bmatrix} \tag{6.3}$$

For high speeds ω, gravity g is very small and its oscillation has a time average of zero, justifying the assumption that $\boldsymbol{b} = [0, \rho r\omega^2]^\mathsf{T}$. Expanding the rectilinear notation in (6.1) with this assumption gives two partial differential equations that relate the pressure field p and the velocity field $[u, v]$:

$$0 = -\frac{\partial p}{\partial x} + \mu\left(\frac{\partial^2 u}{\partial x^2} + \frac{\partial^2 u}{\partial y^2}\right) + 0 \tag{6.4a}$$

$$0 = -\frac{\partial p}{\partial y} + \mu\left(\frac{\partial^2 v}{\partial x^2} + \frac{\partial^2 v}{\partial y^2}\right) - \rho r\omega^2 \tag{6.4b}$$

Continuity (6.2) likewise becomes

$$\frac{\partial u}{\partial x} + \frac{\partial v}{\partial y} = 0 \tag{6.5}$$

The boundary conditions on the fluid are given by a no-slip condition at the drum interface and zero shear at the free surface:

$$u|_{y=0} = 0 \tag{6.6}$$

$$\mu \frac{\partial u}{\partial x}\bigg|_{y=h(x)} = 0 \tag{6.7}$$

Additionally, the pressure at the free surface is taken to be zero:

$$p|_{y=h(x)} = 0 \tag{6.8}$$

To reduce these differential equations to a more tractable form, dimensionless variables of order unity are considered. Length scales x and y are normalized by characteristic lengths r and $\bar{h}$, while pressure is normalized by centrifugal pressure $\rho\omega^2 rh$:

$$\tilde{x} = \frac{x}{r} \tag{6.9}$$

$$\tilde{y} = \frac{y}{\bar{h}} \tag{6.10}$$

$$\tilde{p} = \frac{p}{\rho\omega^2 r\bar{h}} \tag{6.11}$$

$$\tilde{u} = \frac{u}{u^*} \tag{6.12}$$

where u^* is some (as yet) unknown characteristic velocity. Applying these variables to the continuity equation gives

$$\tilde{v} = \frac{v}{u^*}\frac{r}{h} \tag{6.13}$$

Converting the system of differential equations (6.4) to these dimensionless variables gives

208

$$0 = -\frac{\partial \tilde{p}}{\partial \tilde{x}} \frac{\rho \omega r h}{\mu} + \frac{u^*}{\omega r} \frac{r}{h} \left(\frac{\partial^2 \tilde{u}}{\partial \tilde{x}^2} \frac{h^2}{r^2} + \frac{\partial^2 \tilde{u}}{\partial \tilde{y}^2} \right) \qquad (6.14a)$$

$$0 = -\frac{\partial \tilde{p}}{\partial \tilde{y}} \frac{\rho \omega r h}{\mu} + \frac{u^*}{\omega r} \left(\frac{\partial^2 \tilde{v}}{\partial \tilde{x}^2} \frac{h^2}{r^2} + \frac{\partial^2 \tilde{v}}{\partial \tilde{y}^2} \right) - \frac{\rho \omega r h}{\mu} \qquad (6.14b)$$

It was assumed that $h \ll r$, which permits neglecting $\partial u / \partial x$ in (6.14a). Assuming also that

$$\frac{u^*}{\omega r} \ll \frac{\rho \omega r h}{\mu} \qquad (6.15)$$

the velocity gradients can be ignored in (6.14b) (this assumption will be checked once the characteristic velocity u^* is known). Dropping these terms simplify the original differential equations to

$$0 = -\frac{\partial p}{\partial x} + \mu \frac{\partial^2 u}{\partial y^2} \qquad (6.16a)$$

$$0 = -\frac{\partial p}{\partial y} - \rho r \omega^2 \qquad (6.16b)$$

Integrating $\partial p / \partial y$ (6.16b) across the fluid height $h(x)$ with the boundary condition (6.8) of zero pressure at the free surface, gives pressure p as a function of height y:

$$p(x, y) = \rho r \omega^2 (h(x) - y) \qquad (6.17)$$

From which $\partial p / \partial x$ follows directly:

$$\frac{\partial p}{\partial x} = \rho r \omega^2 \frac{dh}{dx} \qquad (6.18)$$

This result for $\partial p / \partial y$ enters (6.16a) as a forcing function. Because $\partial p / \partial x$ is a function of x alone, (6.16a) can be solved for velocity field u by integration and application of the boundary conditions in (6.6) and (6.7):

209

$$u = \frac{1}{\mu}\frac{\partial p}{\partial x}\left(\frac{y^2}{2} - yh(x)\right) \tag{6.19}$$

At this juncture, the assumption of (6.15) can be checked. Substituting $u^* = u(y = h(x))$ and $\partial p/\partial x$ above into (6.15) gives

$$\frac{dh}{dx} \ll \frac{2r}{h} \tag{6.20}$$

Assuming smooth asperities, dh/dx will be of order h/r. This allows rewriting (6.20) as $h^2/r^2 \ll 1$, which clearly holds given the original assumption that $h \ll r$.

Next, the volume flow rate Q through a plane in x is given by integrating the flow profile u (6.19) between 0 and $h(x)$:

$$Q(x) = \int\limits_0^{h(x)} u(x)dy = \frac{1}{3\mu}\frac{dp}{dx}h^3(x) \tag{6.21}$$

If variations in height $h(x)$ are small around $\bar{h}$, flow rate can be approximated as

$$Q(x) = \frac{1}{3\mu}\frac{dp}{dx}\bar{h}^3(x) \tag{6.22}$$

this flow rate Q must be related to the instantaneous change in height profile $h(x)$ to find the rate of decay of sinusoidal asperities (e.g. Figure 6-4). Applying a control volume in an infinitesimally small volume about some x coordinate, one can show that the temporal derivative of height is related to the spatial derivative of flow rate:

$$\frac{dh}{dt} = -\frac{dQ}{dx} \tag{6.23}$$

Substituting the volume flow rate Q from (6.21) gives

$$\frac{dh}{dt} = -\frac{d}{dx}\left(\frac{\rho r \omega^2}{3\mu}\frac{dh}{dx}\bar{h}^3(x)\right) \tag{6.24}$$

This partial differential equation relates the temporal and spatial aspects of the

fluid film profile h. The form of (6.24) admits a decaying sinusoidal solution for h with wavelength λ_f:

$$h(x,t) = \bar{h} + e^{-t/\tau_f} \cos\left(2\pi \frac{x}{\lambda_f}\right) \qquad (6.25)$$

applying this solution form to (6.24) and solving for the asperity decay time constant in the fluid layer τ_f gives

$$\tau_f = \frac{3\mu\lambda_f^2}{4\pi^2\rho r \omega^2 \bar{h}^3} \qquad (6.26)$$

This result shows that sinusoidal height asperities decay as a first order system with a time constant given by (6.26).

When the centrifuge drum is perfectly horizontal, the free surface of the fluid layer will conform to a perfect cylinder about the drum's axis of rotation. At high rotational speeds, the system is insensitive to gravitational effects from leveling errors, but not completely decoupled. To analyze the effect of leveling errors, consider the body force b on an arbitrary fluid element in r, z coordinates when the drum has some leveling error ϵ_{axis} (Figure 6-5):

$$b_r = \rho\omega^2 r + \rho g \cos(\epsilon_{\text{axis}}) \cos(\omega t + \psi) \qquad (6.27a)$$

$$b_z = \rho g \sin \epsilon_{\text{axis}} \qquad (6.27b)$$

The time average of b_r is $\rho\omega^2 r$. For small ϵ_{axis}, the mean body force vector will be an angle of ϕ from $\hat{r}$:

$$\epsilon_{\text{fluid}} = \tan^{-1} \frac{\rho g \sin \epsilon_{\text{axis}}}{\rho\omega^2 r} = \frac{\epsilon_{\text{axis}} g}{\omega^2 r} \qquad (6.28)$$

Because $\omega^2 r$ is typically much greater than g (often by a factor of 100 or more), an error ϵ_{axis} in leveling is greatly attenuated (by the same factor of 100 or more). For example, if the centrifuge axis is level within $\epsilon_{\text{axis}} = 1$ degree (20 mrad) the free surface would exhibit a taper of only $\epsilon_{\text{fluid}} = 200$ μrad.
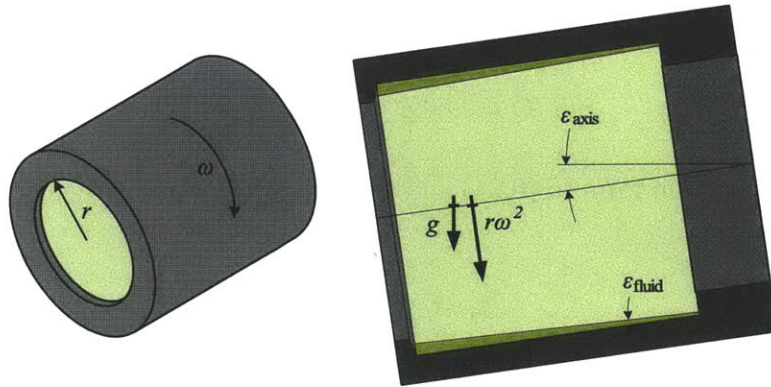
Figure 6-5: The horizontal centrifuge arrangement is insensitive to leveling errors ϵ_{axis}. Because the centrifugal acceleration $r\omega^2$ is typically much greater than gravity g, the leveling error is greatly attenuated and is manifest as a much smaller taper ϵ_{fluid} in the fluid free surface.

6.3.2 Photoresist

The first step of depositing a photoresist layer is paramount to obtaining a uniform stamp thickness. This creates an ideal cylindrical surface that is replicated by the outer diameter of the cast PDMS, independent of the quality (roughness, eccentricity, or cylindricity) of the drum surface.

Solvents are used to tune the fluid properties of resists for coating. Spin coating typically governed by dynamic viscosity and speed; thickness goes with the square root of speed [26]. The solvent is evaporated from the photoresist before exposure or development.

The same principle is used in this centrifugal coating application to adjust the time constant τ_f of centrifugal coating. The photoresist is entirely too viscous to spread in a thin layer (several microns) even in a rapidly spinning centrifuge. For example, coating a 50 μm thick layer of SU8 2015 (ν=1250 cSt) in a 50 mm diameter centrifuge spinning at 300 rad/s would result in an excruciatingly long time constant τ_f of nearly one day.

Solvent is added to the photoresist to both (*i*) reduce the viscosity (Figure 6-6) and (*ii*) increase the effective height of the fluid film. These combined effects

dramatically reduce the time constant for equilibriation. For example, a typical time constant is only a fractional second for a dilute (ν=2.5 cSt) 500 μm film in a 50 mm diameter centrifuge spinning at 300 rad/s. In fact, the drum must be spinning much slower when the fluid layer is introduced to avoid transient turbulent flow as the fluid matches the speed of the drum (the relevant Reynolds number is $Re = \omega r h / \nu$).
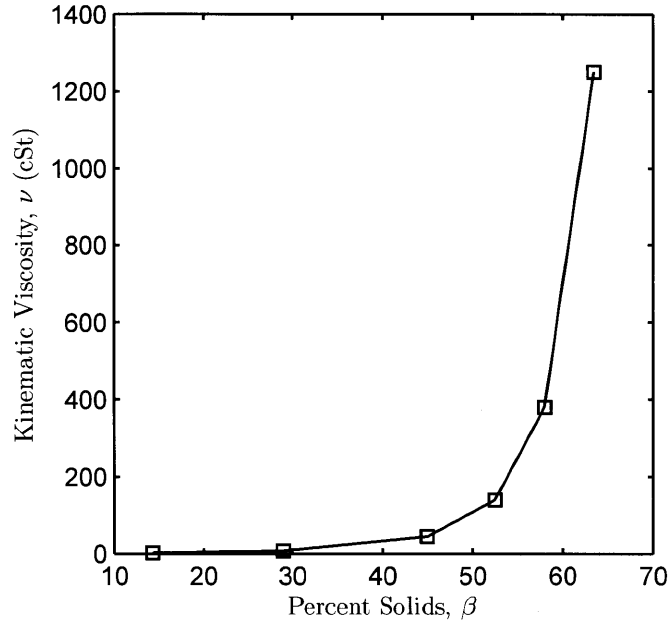

Figure 6-6: Kinematic viscosity $\nu = \mu / \rho$ of SU8 with respect to solids fraction (Microchem).

The evaporating solvent limits the ability of the planarizing layer to compensate for long wavelength errors in the centrifuge drum. While the diluted photoresist converges to a uniform free surface, the evaporation of solvent leaves a resist layer that is a *fraction* of the original fluid height. When the evaporation time constant τ_e becomes shorter than the fluid equilibration time constant τ_f, the fluid can no longer reach the ideal free surface before additional solvent evaporates. This crossover point is inevitable as τ_f increases with about h^{-3} while τ_e will remain constant. Nevertheless, the planarizing layer can easily remove drum imperfections at small spatial wavelengths (e.g. machining marks) and *attenuate* long wavelength errors

213

(e.g. drum eccentricity or taper).

The thickness of the photoresist is determined by mass conservation and can be related to the initial volume of photoresist V:

$$\beta V = 2\pi r \bar{h} l_z \qquad (6.29)$$

where β is the solids fraction in the photoresist, r is the drum radius, $\bar{h}$ is the mean resist thickness, and l_z is the length of the drum along its axis. This can be rearranged to give the relationship

$$\frac{V}{\bar{h}} = \frac{2\pi r l_z}{\beta} \qquad (6.30)$$

which can be use to calculate the required volume of photoresist for a particular film thickness $\bar{h}$.

6.3.3 PDMS

PDMS is prepared by mixing a base and curing agent in a ratio of about 10:1. This mixture will cure by crosslinking at ambient temperature in about 24 hours, though heating can significantly reduce the curing time to a matter of minutes.

This temperature-dependent effect is used to an advantage in the centrifuge process developed here. The PDMS prepolymer can be allowed to centrifuge to a uniform free surface for several minutes, then heated and cured after the fluid has equilibriated. An exceptionally uniform free surface can be achieved because there is no mass transfer (i.e. solvent evaporation) or appreciable volume change upon curing.

PDMS has a density of about 1.04 g/cm^3 and a viscosity of 3.5 Pa·s (Dow Corning). Using a 25 mm radius centrifuge spinning at 300 rad/s, this results in a fluid decay constant of $\tau_f = 3$ s for $\bar{h} = 1$ mm.

By inspection, the time constant τ_f (6.26) shows that a thicker stamp (larger h) will converge to a free surface faster, and thus allow a higher throughput when casting stamps. Section 5.2 shows that thicker stamps provide a larger processing window before feature collapse modes are observed. These two phenomena are complementary

214

6.4 Machine Design

This section presents a machine designed ot provide a test bed for testing the centrifugal stamp casting process introduced in this chapter. This machine was designed to allow both (*i*) rotation of a hollow drum, acting as a centrifuge, and (*ii*) translation of a stage parallel to the drum axis, allowing manipulation of a laser writing head.

The following subsections examine the specific design of the centrifuge, optics, system assembly, and control.

6.4.1 Centrifuge

The centrifuge shaft must be carefully designed to provide repeatable motion, high speed operation, and a high temperature tolerance. The drum (and thus shaft) temperatures must be able to reach at least 100° C for solvent evaporation, photoresist crosslinking, and PDMS crosslinking.

A set of back-to-back angular contact bearings are used to support a steel shaft in this initial design (Figure 6-7). This arrangement provides very good shaft constraint (axial, radial, and pitch), but allows the shaft to expand relative to the bearing housing.

The difficulties related to thermal expansion are not trivial in this bearing design. The elongation of the shaft at an elevated temperature is given by

$$\Delta l = \alpha l \Delta T \tag{6.31}$$

For a shaft length of about 50 mm between bearing and a temperature differential of 75 C, steel ($\alpha = 10 \cdot 10^{-6}$ /C) will expand by 38 μm. A set of Belleville washers are used to maintain bearing preload as the shaft expands through this distance.

A 70 mm face plate is integrated into the shaft for mounting centrifuge drums. The drum is located to the faceplate around a center boss and secured with capscrews.

A DC motor is coupled to the opposite end of the shaft using a flexible coupling to account for shaft misalignment. For a centrifuge, the motor speed is typically more important than torque; the only significant dynamics occur when starting or stopping rotation. An available DC brush servo motor was used to drive the centrifuge (Table 6.1).

Table 6.1: DC brush motor characteristics

Specification	Value
Maximum Speed, ω	3000 rpm
Torque constant, K_t	0.137 N·m/A
Winding resistance, R	1.9 Ω
Winding inductance, L	3.3 mH
Inertia, J	0.186 g·m^4
Encoder resolution	1000 lines/rev

The assembled shaft faceplate has 7 μm of radial runout and 15 μm of axial runout.

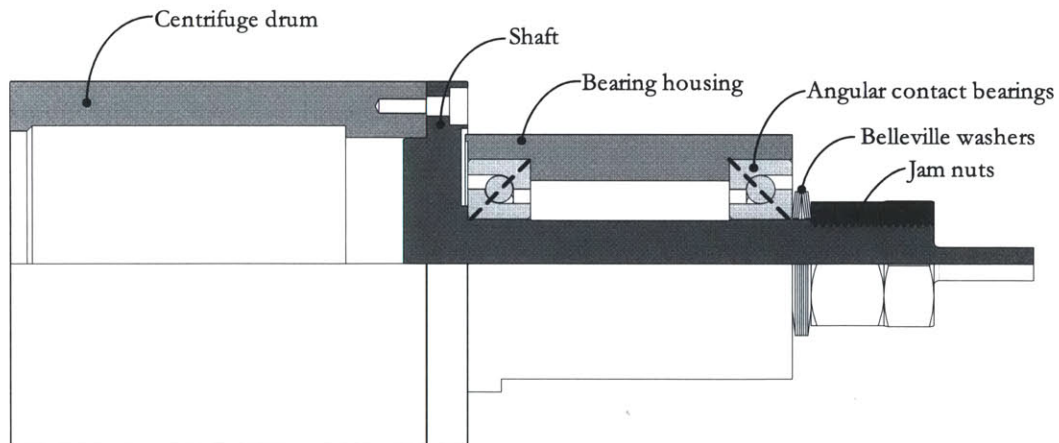Drums are turned on a mandrel so that the mounting face, outer diameter, and

Figure 6-7: Centrifuge bearing design. Back-to-back angular contact bearings were used to constrain the shaft axially and radially. Belleville washers provided a compliant preload between the jam nuts and washers to accommodate large thermal expansions during heating of the centrifuge drum. The centrifuge drums are interchangeable on the shaft.

inner bore can be machined in one setup. This maintains accuracy and results in a balanced rotating assembly. The finished drums typically measure at about 3 μm of total indicated runout (TIR) on the lathe before removal.

TIR of about 30 μm is typical after mounting each drum to the centrifuge shaft. This runout is due to both alignment errors and propogation of runout in the centrifuge shaft. The centrifuge (Figure 6-8) runs very smoothly with no vibrations at 300 rad/s, though no formal measurement was made of rotating assembly balance.
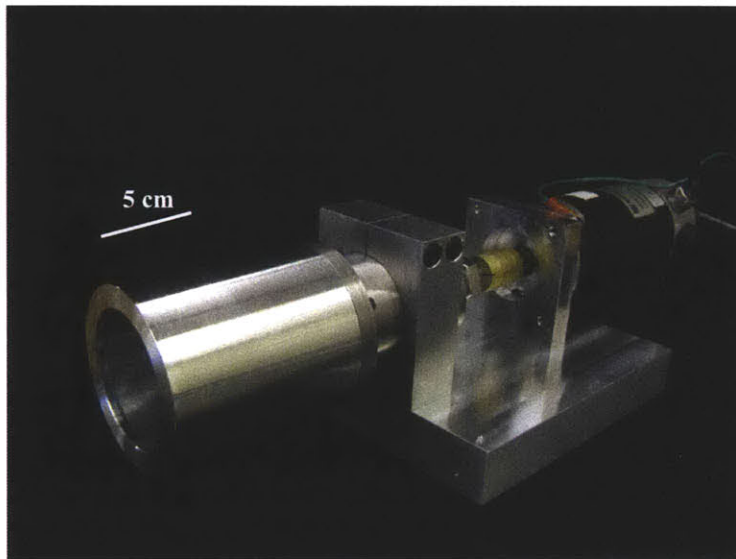

Figure 6-8: Assembled centrifuge. The bearing set and drive motor are mounted to a common base with a kinematic coupling.

6.4.2 Direct Write Optics

Photoresist patterning requires selective exposure to a UV light source. Depending on the resist, this exposure will cause cause either cross linking or degradation so that the pattern can be developed in a solvent.

A direct write laser system is designed for this machine. A set of focusing optics are used to direct a collimated laser beam to a small spot on the inner surface of the centrifuge drum. The ultimate patterning resolution of the system will be dictated by the minimum spot diameter achievable.

Gaussian Behavior

Laser beams are characterized by a Guassian profile: the irradiance (power density) follows a bell shaped distribution with the maximum intensity at the center of the beam. The irradiance profile I is given as a function of radius r from the beam axis [36]:

$$I(r) = I_0 e^{-2r^2/w^2} \tag{6.32}$$

where I_0 is the irradiance at the beam axis and w is the characteristic radius of the beam (Figure 6-9). From this relationship, it is clear that w is the radius at which $I(r)$ drops to $1/e^2$ (or 14%) of the maximum I_0.
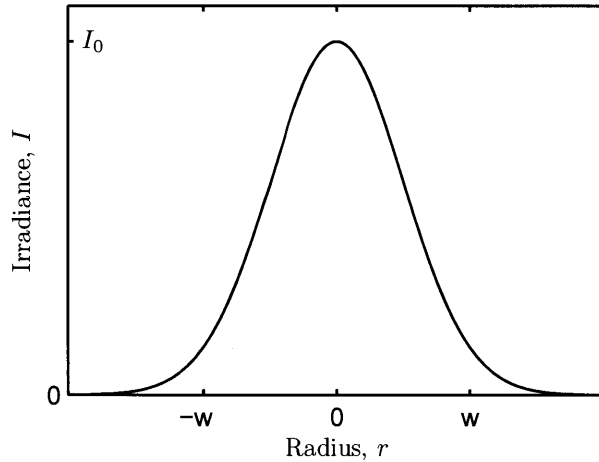

Figure 6-9: Gaussian beam irradiance profile; the beam irradiance drops from its maximum power density I_0 to I_0/e^2 at the characteristic beam radius w.

Focusing a Gaussian beam results in a finite spot size determined by diffraction limits (Figure 6-10). The profile $w(z)$ of the beam radius along the beam axis $\hat{z}$ is given by [36]

$$w(z) = w_0 \left[1 + \left(\frac{\lambda z}{\pi w_0^2} \right)^2 \right]^{1/2} \tag{6.33}$$

where the minimum radius w_0 at the beam waist is a function of wavelength λ and beam divergence angle Θ:

$$w_0 = 1.22 \frac{\lambda}{\Theta} \tag{6.34}$$

218

Integrating the irradiance profile over the beam area gives the total transmitted power P:

$$P = \frac{1}{2}\pi I_0 w^2 \qquad (6.35)$$

The *Rayleigh range* is where the beam area doubles, or equivalently the radius increases by $\sqrt{2}$:

$$z_R = \frac{\pi w_0^2}{\lambda} \qquad (6.36)$$

The depth of focus (centered about the beam waist) is typically considered $2z_r$ (twice the Rayleigh range).
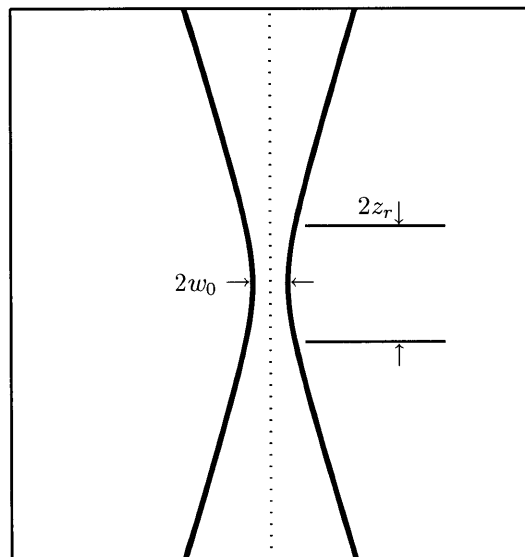
Figure 6-10: Gaussian beam waist. A beam with a convergence angle of Θ with have a Rayleigh range z_r and a waist radius w_0.

The relationship in (6.36) shows the primary tradeoff in laser focusing: smaller spot diameters result in a smaller depth of focus. In other words, a higher resolution system becomes increasingly sensitive to the relative positioning of the optics and desired image plane. In the case of this direct write system, a smaller depth of focus requires higher accuracy in the positioning of the optics and centrifuge drum.

Table 6.2: Direct write laser specifications

Specification	Value
Power, P	80 mW
Wavelength, λ	405 nm
Beam diameter, D	6 mm
Maximum trigger frequency	1 MHz

Optics Design

A single element focusing system is designed for direct write operations in the centrifuge drum (Figure 6-11). In this relatively simple architecture, a single plano-convex lens is used to focus a collimated laser beam to a single spot.
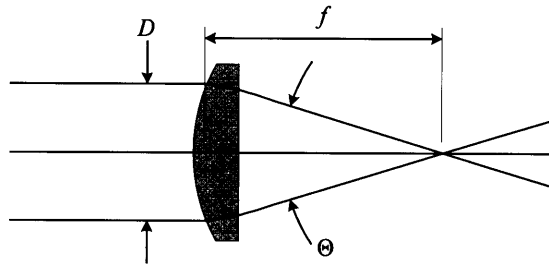

Figure 6-11: Single element focusing architecture using a single plano-convex lens to focus a collimated laser beam to a concentrated spot. Characteristic dimensions used in the design analysis are shown.

The Guassian beam waist equations can be rewritten in terms of design variables, where D is the collimated laser beam diameter and f is the focal length of the lens. A 405 nm wavelength, 80 mW power laser with a 6 mm beam diameter was selected as a light source (Table 6.2). Figure 6-12 shows the design balance between spot diameter $2w_0$ and depth of focus $2z_r$ for these laser parameters.

For this initial design, a lens with focal length $f = 75$ mm was chosen to provide reasonably small spot size ($2\omega_0 = 12$ μm) while still providing a relatively large depth of focus ($2z_r = 0.6$ mm).
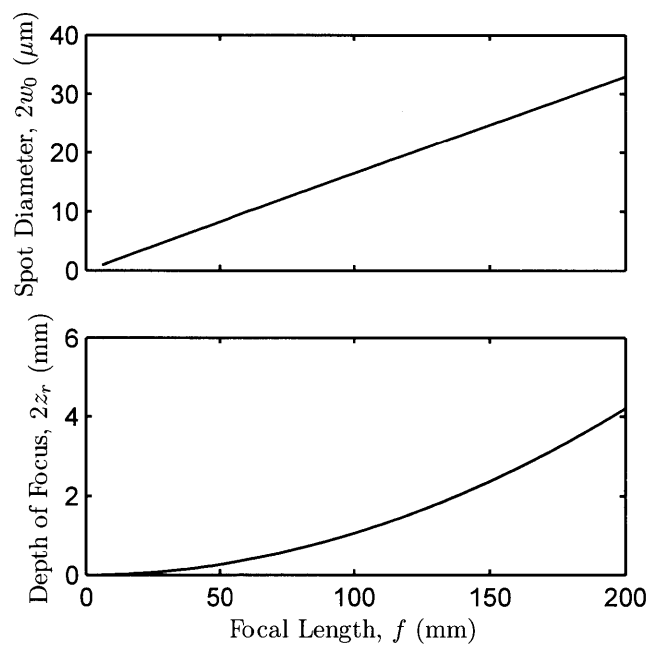
Figure 6-12: Laser focusing design tradeoffs. A shorter focal length f provides a smaller spot diameter $2w_0$, but also results in a much shallower depth of focus $2z_r$.

Traditional direct write systems are designed for planar substrates, where there is little or no space constraint. When writing on the inner diameter of a drum, the beam path must enter along the axis of the drum and be redirected towards the drum surface. This redirection is accomplished by incorporating a right angle prism in the optics stack (Figure 6-13).
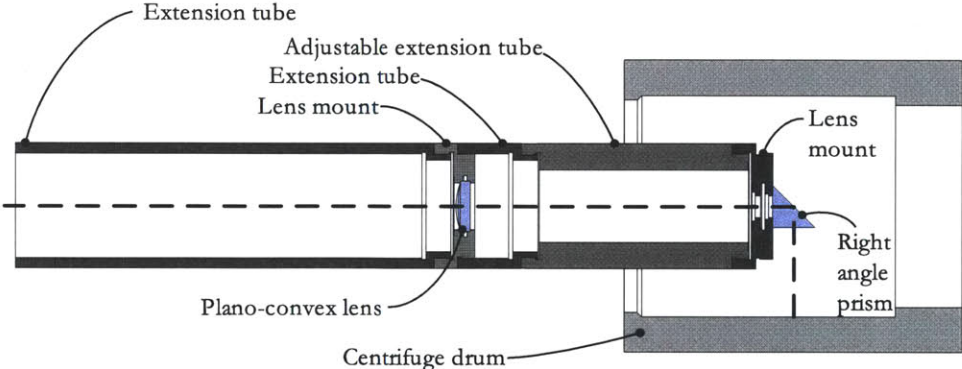
Figure 6-13: Laser optics design using C-mount components. The beam travels through a stack of C-mount components located coaxially with the centrifuge drum. A right angle prism is used to redirect the focused beam towards the drum surface.

Standard C-mount components were used to build the optics assembly. An adjustable body tube was placed between the lens element and the prism to adjust the beam focus to the drum surface. The entire optics stack was mounted to an aluminum baseplate (Figure 6-14).

Figure 6-14: Assembled focusing optics, mounted on a base with a kinematic coupling.

6.4.3 System Integration

The centrifuge drum and laser optics must be capable of relative motion to pattern the entire drum surface. Cylindrical motion coordinates are used, where the drum is able to spin in its own bearings (along $\hat{\psi}$) and the laser optics travel relat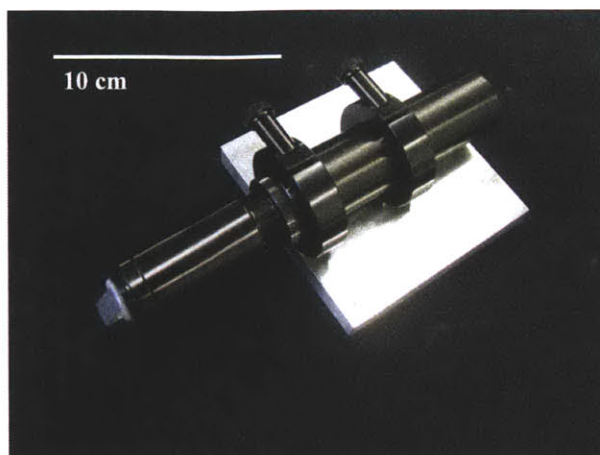ive to the drum axis ($\hat{z}$). These two degrees of freedom allow patterning the entire area of the centrifuge drum at a constant radius r.

The motion of the optics relative to the drum along $\hat{z}$ can be accomplished by moving the either the optics or the drum. In this design, the optics are chosen as the moving element because they have much lower mass. An available linear motion stage with crossed roller bearings and a lead screw drive was selected as the motion platform. The stage was driven with a motor identical to the one used in the centrifuge drive (Table 6.1).

The centrifuge (Figure 6-8) and focusing optics (Figure 6-14) must be precisely aligned, but should also be fixed in such a way to allow disassembly. Each component must be removable, for example to allow draining solvent from the centrifuge drum. To this end, the centrifuge and laser optics are located to the machine base using three groove kinematic couplings (Figure 6-15).

All components are arranged on an optical breadboard to provide flexibility and modularity. The centrifuge kinematically couples to a baseplate that mounts directly

223

to the breadboard. The focusing optics kinematically couple to the moving surface of the motion stage where the laser is permanently fixed; the motion stage is in turn mounted to the breadboard.

The assembled machine is shown in Figure 6-16, where the position of the laser optics along the axis of the centrifuge drum can clearly be seen.

The laser beam was collimated and aligned using a target reticle at each end of the focusing tube (without focusing elements). The laser focus was adjusted to be at the inner surface of the centrifuge drum. Once the system was aligned and focused,
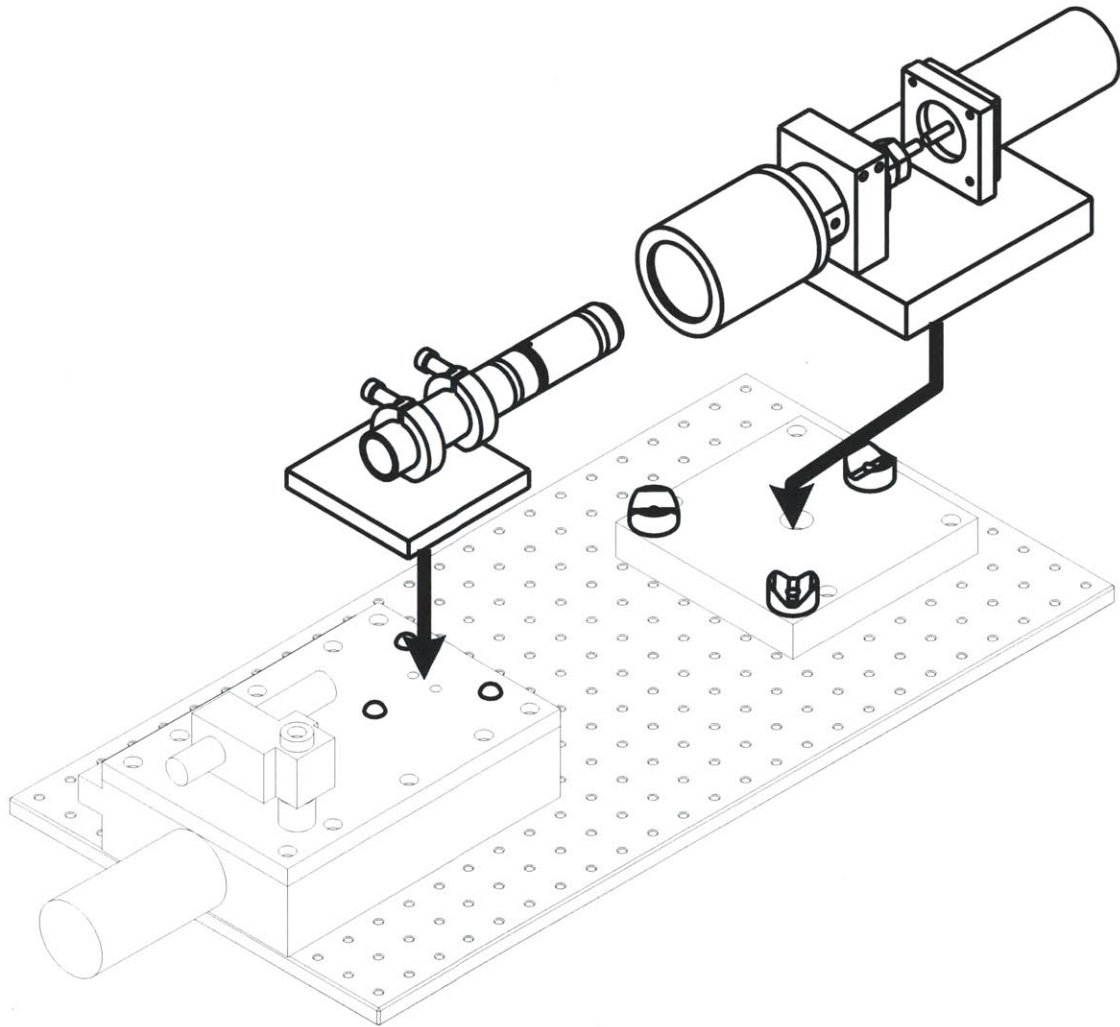
Figure 6-15: Schematic of direct write system, showing removal of laser optics and centrifuge drum from their kinematic mounts.

the individual subassemblies could be removed and replaced without misalignment.

6.4.4 Servo Control

Each of the two servo motors is driven by a linear current amplifier. The servo motor encoders and amplifiers are interfaced to a PC using a National Instruments
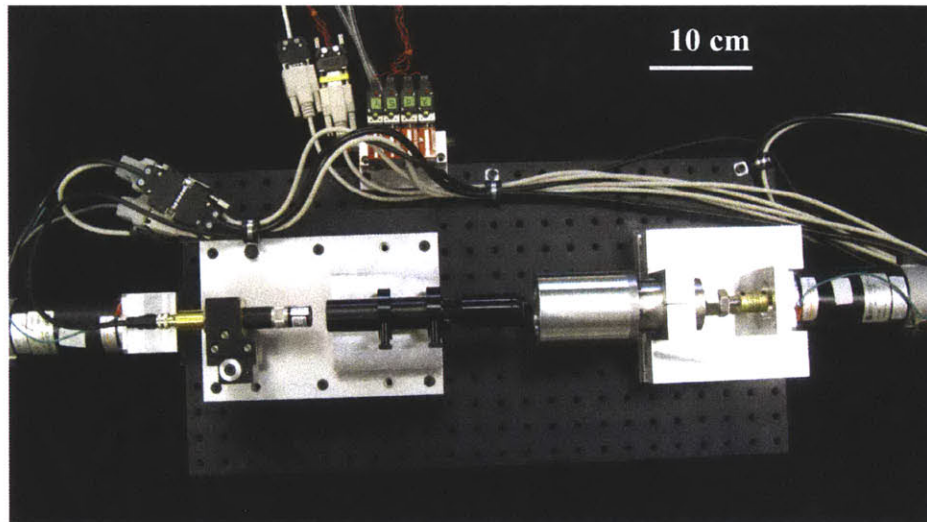
(a)
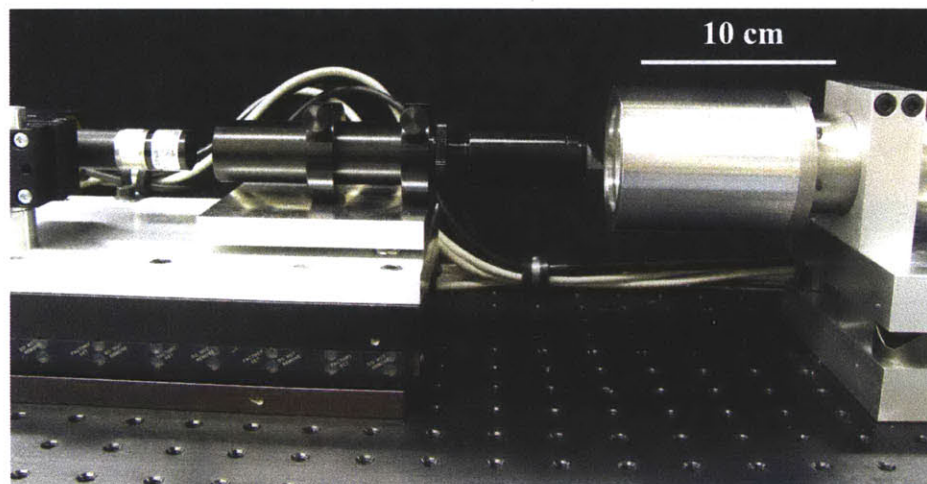
(b)

Figure 6-16: Assembled direct-write system. (a) The individual components are mounted to an optical breadboard. (b) The laser and focusing optics travel along the axis of the centrifuge drum.

PCIe-6343 data acquisition card. Closed loop feedback control is performed using the National Instruments Labview platform.

Centrifuge Control

The controller architecture for velocity control of the centrifuge drum is shown in Figure 6-17.
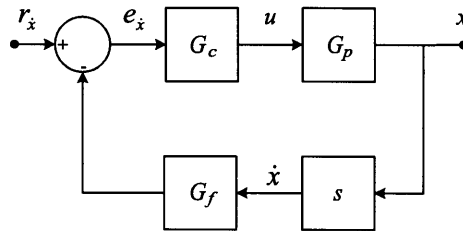
Figure 6-17: Centrifuge controller block diagram, showing transfer functions for the plant G_p, filter G_f, and compensator G_c. The position output of the plant x is differentiated for velocity control. The reference $r_{\dot{x}}$, error $e_{\dot{x}}$, and effort u signals are shown on the block diagram.

The encoder output x is differentiated find the instantaneous motor velocity $\dot{x}$. Care must be taken in the differentiator when the encoder is near its index, where the position counter resets to zero. In a discrete time controller with control period T, differentiation of an n line encoder can be accomplished with a piecewise discrete differentiator:

$$\dot{x} = \begin{cases} (x_t - x_{t-1} + n)/T & (x_t - x_{t-1}) < -n/2 \\ (x_t - x_{t-1})/T & -n/2 \leq (x_t - x_{t-1}) \leq n/2 \\ (x_t - x_{t-1} - n)/T & (x_t - x_{t-1}) > n/2 \end{cases} \tag{6.37}$$

The differentiated signal is filtered to remove the high frequency content that comes from differentiating a discrete spatial signal:

$$G_f(s) = \frac{1}{\tau_f s + 1} \tag{6.38}$$

226

The current-driven centrifuge is a second order system that appears as a pure mass (neglecting higher frequency dynamics):

$$G_p(s) = \frac{1}{(J_m + J_c)s^2} \tag{6.39}$$

where J_m is the motor inertia (Table 6.1) and J_c is the centrifuge inertia. With respect to velocity, the mechanical transfer function becomes first order and permits integral control without phase compensation. Hence, the centrifuge speed is controlled using proportional-integral (PI) control implemented as a lag compensator:

$$G_c(s) = K_c \frac{\tau_c s + 1}{s} \tag{6.40}$$

This controller can be tuned by setting the time constant τ_c at the desired bandwidth and gradually raising K_c until an appropriate amount of step response overshoot is observed. The achievable bandwidth is limited primarily by the flexible coupling between the motor and drum, which adds higher frequency factors to the plant transfer function G_p.

Stage Control

The controller architecture for the linear motion stage is shown in Figure 6-18. A velocity control loop is at the center of this control structure, nearly identical to that used for the centrifuge but with the addition of a feed forward term.

The idealized plant transfer function of the stage resembles

$$G_p(s) = \frac{1}{\left(J_m + m\left[\frac{p}{2\pi}\right]^2\right)s^2} \tag{6.41}$$

where the stage mass m has been reflected back through the lead screw of pitch p.

No integrator is required in G_{cx} in the position feedback loop for reference tracking; the inner velocity control loop already includes an integrator in G_c. This allows using a simple proportional control law in the position loop:
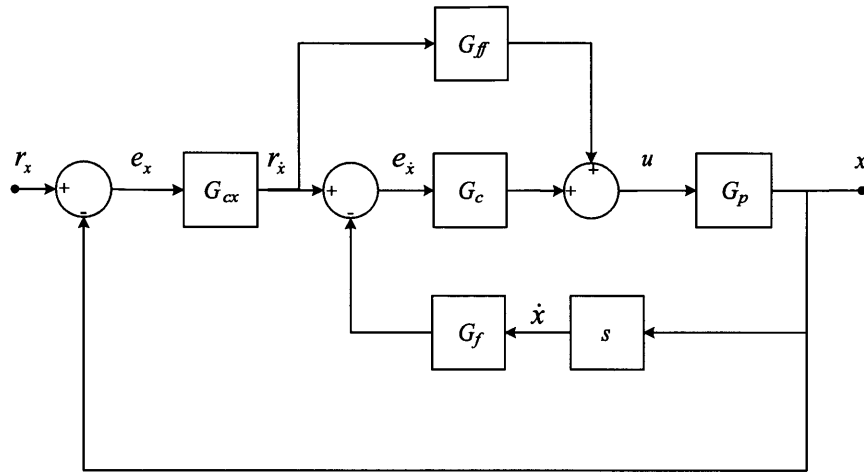
Figure 6-18: Optical stage controller block diagram, showing transfer functions for the plant G_p, filter G_f, position compensator G_{cx}, velocity compensator G_c, and feedforward G_{ff}. Nested state feedback loops are implemented, where the position output of the plant x is differentiated for velocity $\dot{x}$ control in the inner loop. The position referenece r_x, position error e_x, velocity reference $r_{\dot{x}}$, error $e_{\dot{x}}$, and effort ru signals are shown on the block diagram.

$$G_{cx} = K_{cx} \qquad (6.42)$$

The lead screw in the stage has a finite amount of friction, which presents particular problems when reversing direction. With no compensation, the integrator in G_c must slowly wind up to overcome the friction (which is often much greater than the inertial load of the stage). To counter this effect, a feedforward term G_{ff} is added to the velocity control loop, where

$$G_{ff} = \begin{cases} -K_{ff} & r_{\dot{x}} < 0 \\ 0 & r_{\dot{x}} = 0 \\ K_{ff} & r_{\dot{x}} > 0 \end{cases} \qquad (6.43)$$

This controller is tuned in three steps. First, K_{ff} is set to the effort required to maintain steady state motion. Second, G_c is tuned as described for the centrifuge

228

controller. Third, K_{cx} is slowly increased until acceptable overshoot is observed in the x/r_x response. The achievable bandwidth is limited by a flexible coupling between the motor and stage along with the Coulombic friction in the lead screw.

This control architecture has several advantages over a conventional proportional-integral-derivative (PID) or lead-lag compensator architecture. Isolating the velocity control loop decouples controller tuning, permits straightforward application of feed-forward to overcome Coulomb friction, and gives the option to jog the stage using velocity commands (for example from a joystick).

6.5 Experiment

The planarizing step is expected to create stamps with very low surface roughness, while the centrifuge action is expected to make stamps of very uniform thickness. A set of experiments and measurements were carried out to investigate these two hypotheses, as well as demonstrate the feasibility of developing direct-write pattern on the interior of the centrifuge drum.

6.5.1 Experimental Protocol

Stamps were created using the three coating steps proposed in this chapter (Figure 6-1): (i) a planarizing layer of photoresist, (ii) a patterned layer of photoresist, and (iii) a layer of PDMS.

SU8 is traditionally processed in five steps: (i) application via spin coating, (ii) a pre-exposure bake to evaporate solvent, (iii) selective UV exposure to release acid, (iv) a post-exposure bake to cross-link the photoresist with the acid catalyst, and (v) a developer bath to dissolve undeveloped photoresist. The following description shows how these traditional processing steps map to centrifugal coating and direct write developing.

Planarizing Layer

SU8 2015 (Microchem) was used for the planarizing layer. SU8 2015 has a solids fraction of $\beta = 0.63$, the drum has an internal radius of $r = 26.4$ mm, and the length of the cavity is $l_z = 60$ mm. This results in a ratio of 0.015 mL / μm of resist to final film thickness (6.30). 1.0 mL of resist was used for the planarizing layer (about 67 μm final thickness).

In the experiments, the resist was carefully metered from a 2.5 mL syringe into a small 10 mL glass beaker. SU8 thinner (cyclopentanone) was added to the beaker to bring the total volume to about 8 mL and mixed using a stirring rod. When fully mixed, the resist solution was stored in a 10 mL syringe for dispensing. Care was taken during mixing to not introduce bubbles into the solution.

The aluminum drum was rinsed with acetone and allowed to dry. The resist solution was introduced from the syringe into the centrifuge spinning at 50 rad/s, after which the centrifuge was ramped to 300 rad/s over a period of 5 s. Introducing the resist at a moderate speed prevents turbulence and bubbles, but still promotes formation of a uniform layer.

The solvent was evaporated from the photoresist solution by heating the centrifuge with a heat gun to about 95° C (as indicated by the material data sheet) for one hour. A thermocouple was used to measure the air temperature near the drum surface and adjust the heat gun accordingly (Figure 6-19).

The resist was exposed after the solvent evaporated and the drum cooled. The planarizing layer was exposed by a set of three 405 nm wavelength LED modules, each with a light output of 20 mW. With the drum spinning at 300 rad/s, the LED lights were translated along the drum axis $\hat{z}$ at a rate of 5 μ/s (determined empirically).

After exposure, the SU8 layer was again heated to about 95° C for one hour to cross link the resist. The planarizing layer was post baked at about 200° C for one additional hour to ensure full crosslinking and promote adhesion to the aluminum drum. Planarizing layers without this post bake delaminated from the drum when the resist solution was introduced for the patterning layer.

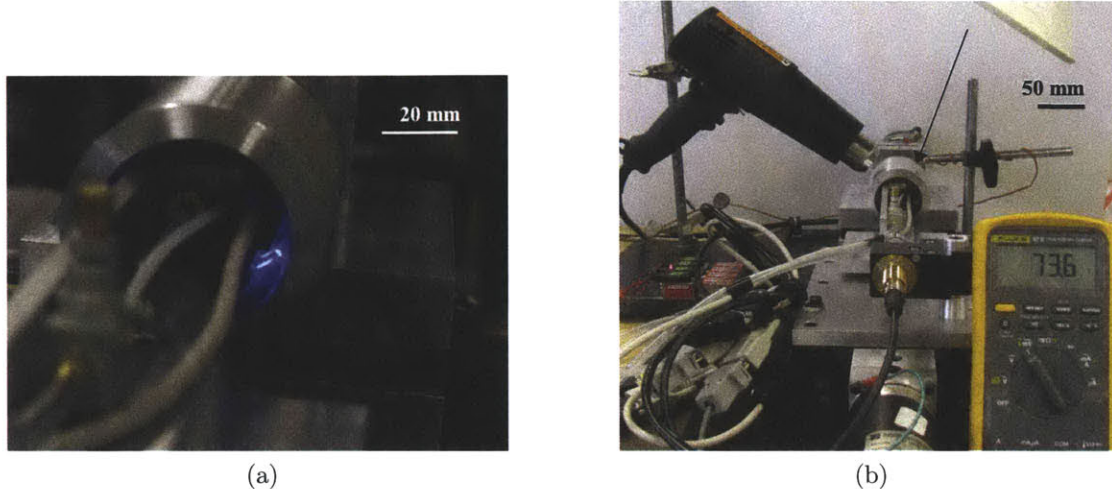(a)   (b)

Figure 6-19: Curing the planarizing layer of photoresist with (a) near-UV LED exposure and (b) thermal treatment with a heat gun and thermocouple (arrow).

Patterning Layer

The patterning layer also used SU8 2015. 0.5 mL of resist was used, corresponding to a final layer thickness of about 33 μm. The resist was prepared, introduced into the drum, and solvent evaporated in the same manner described previously.

The patterning layer was exposed with the laser and focusing optics in a set of exposure experiments. The drum was rotated at 300 rad/s while exposed with the laser for periods of 8, 10, 15, and 20 s. A series of lines were written with the laser head at each exposure level on a pitch of 50 μm using a step-and-expose routine.

Each of these exposures were at significantly higher energy levels than indicated by the material data sheet. The 405 nm wavelength near-UV light sources used have a significantly different effect than the intended 365 nm i-line UV wavelength. Figure 6-20 shows that the material transmittance is significantly higher at 405 nm than 365 nm, requiring much higher energy input to achieve the same absorption.

Cross linking of the photoresist was accomplished by heating to 95° C for one hour. After cooling, the resist was developed with SU8 developer (Microchem) and rinsed with isopropyl alcohol as described in the material data sheet.

PDMS

PDMS (Sylgard 184, Dow Corning) was mixed at the recommended 10:1 base:curing agent ratio in a 50 mL syringe. The PDMS was degassed under vacuum to remove bubbles. 10 mL (a slight excess) of PDMS was dispensed into the centrifuge drum while rotating at 50 rad/s, then the drum was ramped to 300 rad/s.

The centrifuge was allowed to operate for about 10 minutes to equilibriate the PDMS layer to a uniform thickness. Excess PDMS was allowed to exit through the open face of the drum so that the lip of the drum defined the exact inner diameter of the PDMS layer.

The heat gun was used to heat the spinning centrifgue drum to about 65 C for one hour to crosslink the PDMS.

After cooling, the cured PDMS stamp was removed from the drum using tweezers and rinsed with ethanol.
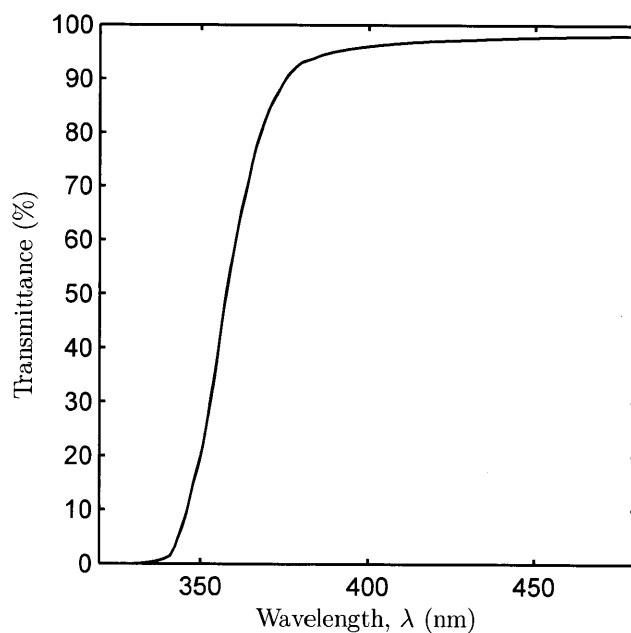

Figure 6-20: Transmittance of SU8 with respect to wavelength λ (Microchem).

Mounting

The cylindrical stamps are not trival to mount on rolls. In particular, attempting to slide the stamp over the roll is nearly impossible because the PDMS tends to cling to the roll surface.

An air cushing technique was developed to accurately mount stamps in a stress free state (Figure 6-21). A special bushing was fabricated to supply compressed air between the stamp and roll. The compressed air creates a fluid film that acts as a bearing and prevents the stamp and roll from contacting. This fluid bearing allows sliding the stamp over the roll in a stress free state. When the stamp is correctly positioned, the air pressure is released and the stamp collapses against the roll where it remains naturally adhered. The portion of the stamp connected to the bushing can be released, leaving only the cylindrical stamp wrapped around the roll.

(a)   (b)
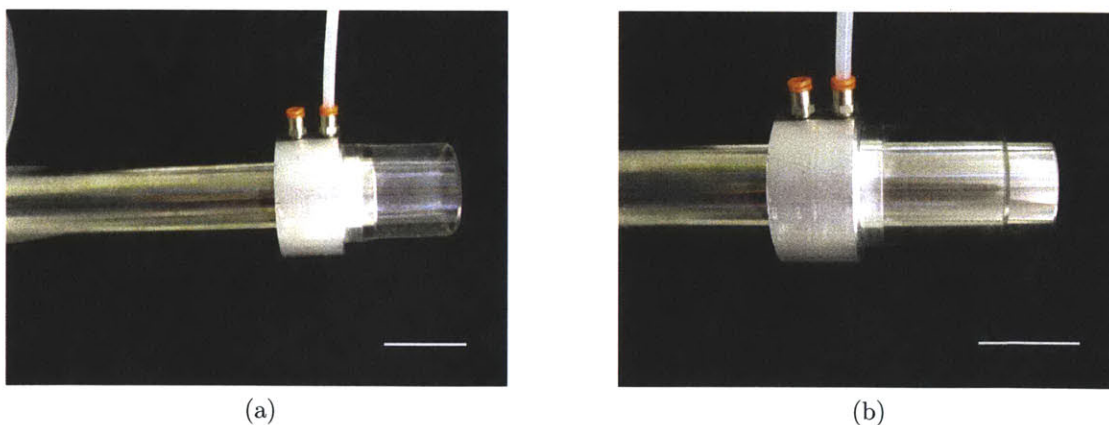
Figure 6-21: Cylindrical stamps are mounted to rolls using an air cushion. (a) The stamp is connected to a bushing that supplies compressed air between the roll and stamp. (b) The air creates a fluid bearing and prevents the stamp and roll from contacting, allowing the stamp to slide onto the roll in a stress-free state. Releasing the air pressure allows the stamp to collapse against the roll, where it remains fixed by the large work of adhesion between the two surfaces. Scale bars: 5 cm.

6.5.2 Measurement and Results

The experiments were successful in creating microfeatures in the SU8 patterning layer and replicating the same into the PDMS stamp (Figure 6-22).
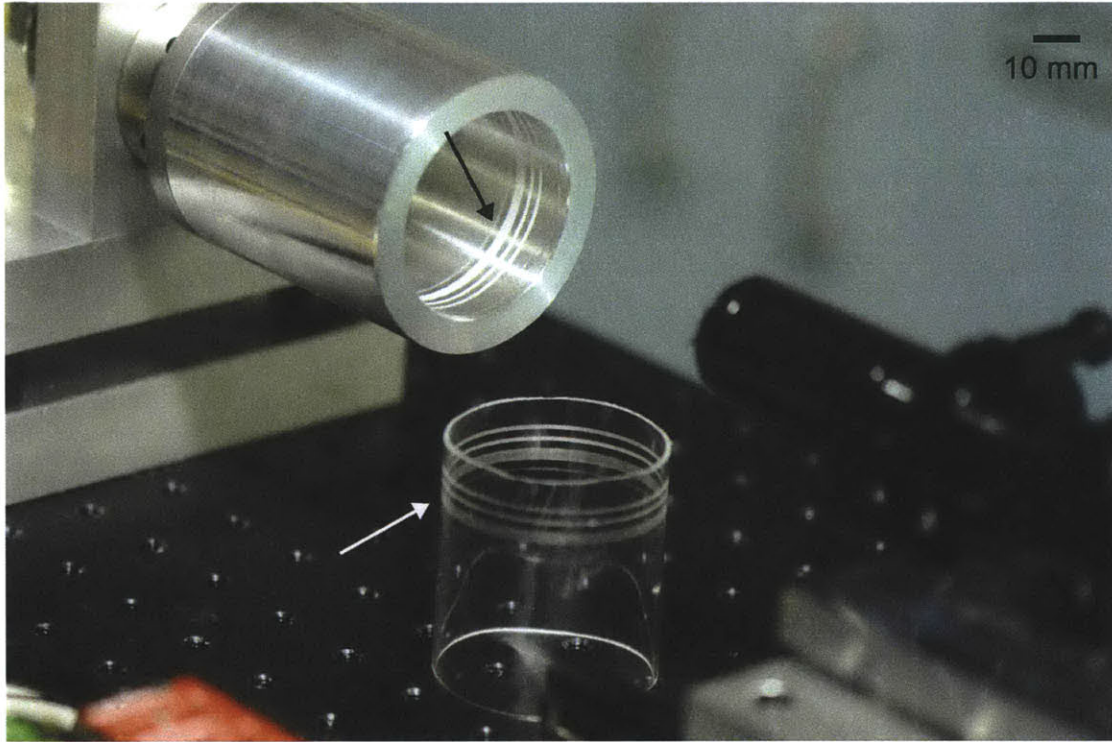
Figure 6-22: Image of centrifuge drum with planarizing and patterning layers, along with a cylindrical PDMS stamp. The direct write features on the inner diameter of the centrifuge drum (black arrow) were exactly replicated on the outer diameter of the stamp (white arrow).

Exposure Level

The laser exposures at 15 and 20 s created well defined features in the photoresist. The 10 s exposure created features that appeared well defined, though some delaminated from the underlying planarizing layer after casting the first PDMS stamp. Exposure at 8 s failed to create well defined features (Figure 6-23).
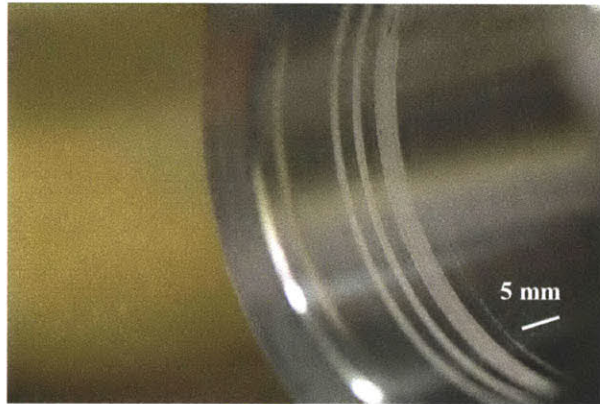
Figure 6-23: Laser exposure level experiment showing gratings formed by (from left to right) 20, 15, 10, and 8 s of exposure. Note delamination of 10 s features at the top of the frame and poor definition of 8 s features.

Surface Roughness

The surface roughness, feature definition, and uniformity of the photoresist layers could not be measured with conventional metrology equipment on the interior of the drum. Instead, measurements were made of the respective PDMS stamp features and the resulting data used to infer the quality of the photoresist.

Measurements of the PDMS surface with a white light interferometer (Zygo) showed very low surface roughness of 22 nm RMS (Figure 6-24).
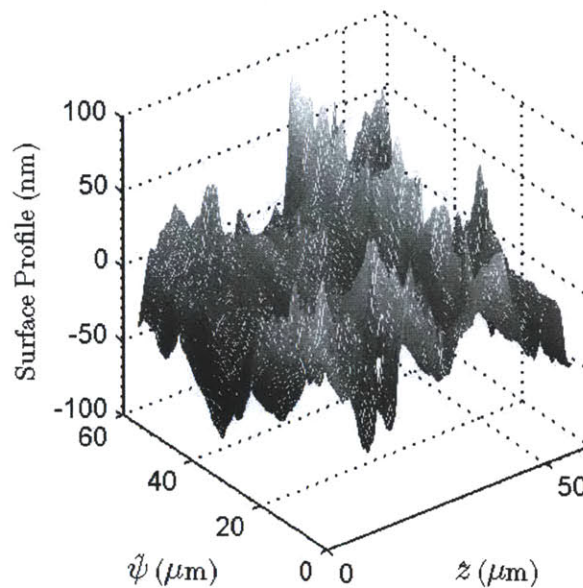
Figure 6-24: Surface map of planarizing layer shown 22 nm RMS roughness, as measured from a replicated PDMS stamp surface.

Thickness Uniformity

To evaluate the thickness uniformity of the stamp, 2 mm diameter cores were cut from the stamp at multiple locations (Figure 6-25a). These samples were mounted to a glass microscopy slide by floating on a layer of ethanol and allowing the ethanol to evaporate; this created a stress-free mount (Figure 6-25b).

236
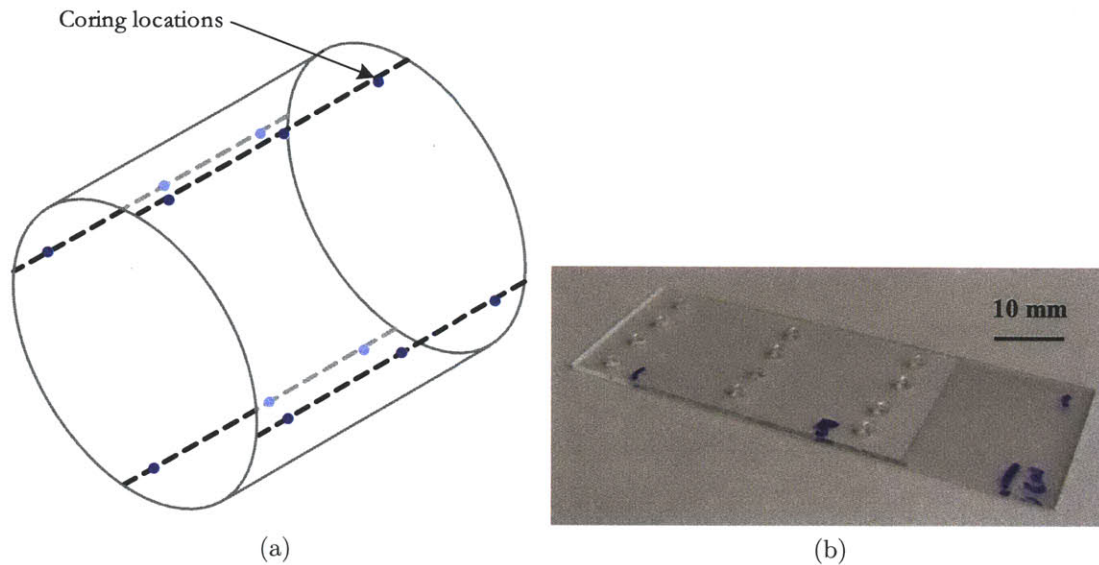
Figure 6-25: Core samples for stamp thickness measurement. (a) Location of core samples in stamp for thickness measurements and (b) cores mounted to a glass microscopy slide for measurement.

The height difference between the glass slide and top surface of the stamp core was measured using a white light interferometer (Zygo). A plane was fit to the data points corresponding to the glass slide. The height of the core was measured as the mean distance between this plane and the remaining data points (Figure 6-26).

The height of three sets of cores was measured to establish measurement repeatability: (i) from a first stamp, (ii) a second replicate from the same stamp, and (iii) from a second stamp. The first and second stamp were cast in the same centrifuge drum with the same planarizing layer. An analysis of variance (Table 6.3) showed a measurement repeatability variance of 3.73 μm^2, and that there was no significant effect due to the specific stamp or core replicate ($p > 0.05$). This implies that the core measurements are an accurate measure of stamp uniformity.

The analysis of variance showed a statistically significant effect due to both axial and angular core position ($p < 0.05$). The mean thickness residual is summarized in Figure 6-27 as a function of core location.

The thickness residuals indicate both a taper and an eccentricity in the stamps.
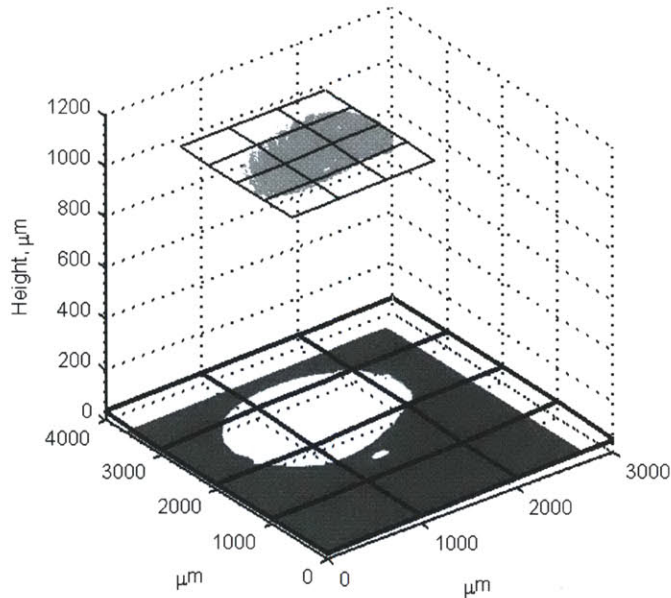
Figure 6-26: Interferometer data of core sample. The thickness of the sample was measured as the height between a best fit plane to the glass slide and a parallel plane at the mean height of the core surface.

The residual steadily decreases as a function of axial position, indicating a taper of about 200 μrad (10 μm over 60 mm). Eccentricity of about 10 μm TIR is indicated by the maximum and minimum residuals at opposite angular positions (0 and π).

Despite deviations of about 10 μm over a 1 mm stamp thickness, the drum runout has been attenuated. The thickness residuals are bounded by measurements of the

Table 6.3: Stamp thickness analysis of variance. The axial and angular core position are significant effects, while the casting replicate is not. This indicates that the measurements of variation in stamp thickness are statistically significant, with a repeatability variance of 3.73 μm.

Effect	Variance (μm^2)	p value
Casting Replicate	0.01	0.9973
Axial Position	339.07	<0.0001
Angular Position	148.36	<0.0001
Error	3.73	

238
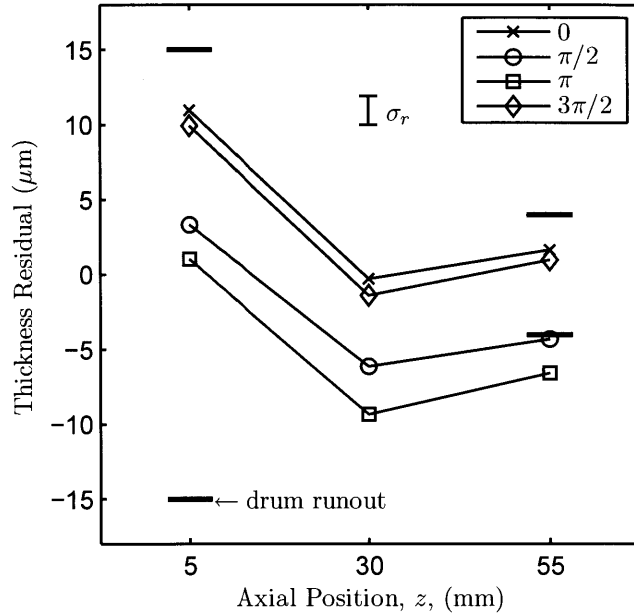
Figure 6-27: Stamp thickness residual as a function of axial position; separate curves indicate different positions along $\hat{\psi}$. The data suggests both a slight taper and eccentricity of about 10 μm.

drum runout after mounting on the centrifuge (30 μm and 8 μm TIR at each end of the drum as indicated on Figure 6-27).

It is hypothesized that the stamp residuals are due primariliy to errors in the free surface of the planarizing layer. While the PDMS is able to conform to a uniform free surface over time, the planarizing layer is subject to competing fluid dynamics and mass transfer phenomena because of solvent evaporation. It is believed that while the planarizing layer is able to *attenuate* runout and taper in the drum surface, it is unable to reach a perfectly cylindrical free surface like the PDMS.

Feature Definition

The quality of the direct-write features on the inner diameter of the centrifuge drum was assessed by casting a PDMS stamp in the drum and measuring the stamp. Figure 6-28 shows optical micrographs of features, both from a top view and a cross sectioned view, for three different exposure levels. These micrographs show that fea-

tures can indeed be produced using the centrifugal coating, direct write, and casting technique developed in this chapter.

An exposure level of 15 s produced features that were very near the 12 μm theoretical spot size of the laser system; exposure at 20 and 10 seconds resulted in either over- or under-exposure of the features. The edge roughness of the features is poor in this proof of concept demonstration, likely due to the low sensitivity of the photoresist to the 405 nm laser light, mechanical vibration over multiple turns of the drum, and reflection from the rough aluminum centrifuge surface or small bubbles in the photoresist. It is believed that better matching of the laser wavelength and photoresist sensitivity, improved centrifuge bearings, and an antireflective treatment on the drum surface will produce smooth feature edges. Feature resolution.

(a)   (b)   (c)
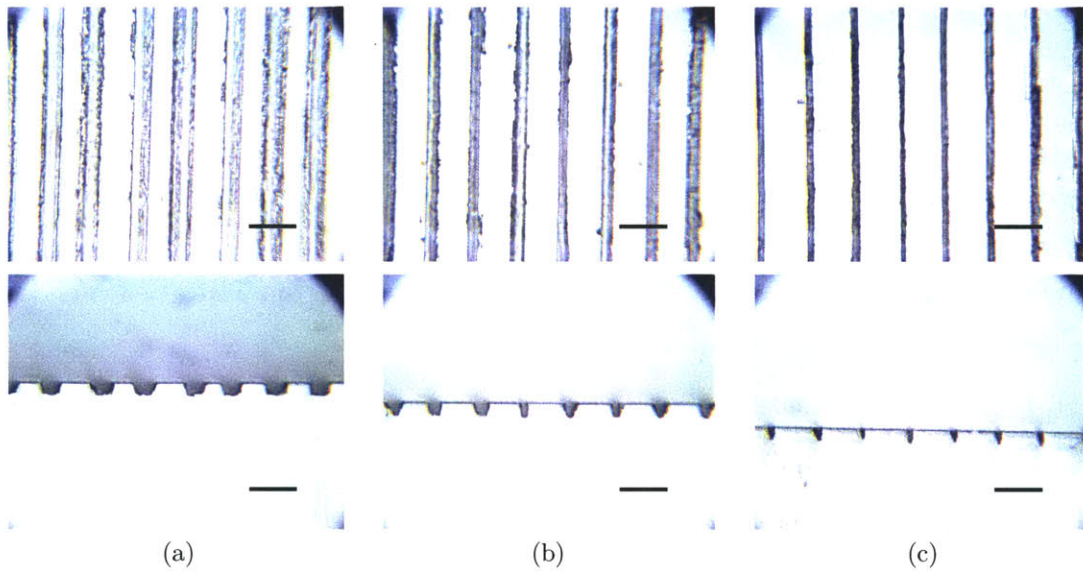
Figure 6-28: Micrograph of direct-write features replicated in PDMS stamps at (a) 20 s, (b) 15 s, and (c) 10 s exposure per line using an 80 mW laser in a 52.8 mm diameter centrifuge drum. The laser spot diameter was 12.8 μm and the drum was rotating at 300 rad/s during exposure. Scale bars: 50 μm.

Mounting Alignment

The stamp mounting uniformity was evaluated by fixing the mounted stamp and shaft in an air bushing, where it was held with opposing collars. A video camera captured

the location of the line features in the stamp as the roll freely rotated in the bushing. The video showed a periodic axial alignment error of about 100 μm over one rotation of the roll. It was unclear whether this error was entirely due to misalignment of the stamp or if the collars holding the shaft contributed to a periodic error.

It is emphasized that this level of accuracy was obtained using a very simple mounting method with no control mechanisms. It is expected that stamps could be mounted with single micron accuracy levels in an ideally stress free state with appropriate development of the technique.

6.6 Summary

This chapter developed a new process for casting large, dimensionally uniform stamps for roll-based soft lithography. Problems with conventional planar stamp casting, including scalability and roll mounting difficulties, were used to motivate a centrifuge based process. Three sequential fluid layers are applied in a horizontal centrifuge drum to create a continuously patterned cylindrical stamp: (*i*) a planarizing layer of photoresist, (*ii*) a patterned layer of photoresist, and (*iii*) a layer of PDMS that becomes the cylindrical stamp.

The fluid dynamics of a rimming flow in a centrifuge drum were analyzed to determine the time constant of asperity decay. If the centrifuge is operated for a sufficient number of time constants, the free surface of the fluid will converge to a perfect cylinder. This asperity decay results in very low surface roughness and exceptional dimensional uniformity when the fluid layers are cured with UV or thermal processing.

A proof of concept machine was constructed to demonstrate the feasibility of this stamp manufacturing process. A direct write laser system was used to create 10 micron features on the inner diameter of the centrifuge drum. Measurement of stamps produced in the patterned drum exhibited low surface roughness (22 nm), good dimensional uniformity (10 μm / 1 mm) and good feature replication.

A next generation prototype machine should incorporate improved bearing sys-

tems and large numerical apperture laser optics for patterning of small features at the diffraction limit. This direct write approach can be scaled to features with a half pitch of the laser wavelength being used. For smaller patterns, interference lithography or other advanced approaches will be required. At a minimum, the direct write approach can easily produce micron and sub-micron patterns for a large number of flexible electronics and metasurface applications.

This centrifuge technique can be adapted to other stamp materials. For example, harder polymers can be cast for use in NIL or self aligned imprint lithography (SAIL) stamps. Very durable nickel stamps can be produced for NIL through electrodeposition. With appropriate development, this centrifugal stamp casting process should find wide application in roll-to-roll technologies beyond μCP.

Part IV

Process Control

Chapter 7

Machine Design

7.1 Motivation

Roll based processes have long offered high processing rates and economies of scale, especially in the areas of surface coating and patterning. New methods of *contact lithography* have been developed that allow patterning micro and nanoscale features through mechanical contact of a patterned stamp to a substrate, including microcontact printing (μCP) [59, 106] and nanoimprint lithography (NIL). Adapting these contact lithography processes to roll based platforms [96, 4, 1] promises to functionalize large surface areas at low costs, with applications in engineered surfaces, flexible electronics, and photonics.

Implementing roll-based contact lithography requires extreme precision in associated roll based machinery. The characteristic dimensions of these processes are typically submicron, whether the stamp feature relief in μCP or the residual layer thickness in NIL. These dimensions require the utmost precision and accuracy in roll positioning equipment, below levels that are typically required in well established roll coating processes. Moreover, the characteristic contact force in μCP is on the order of 10 N per meter of roll length (Chapter 4), requiring very accurate machinery to observe or control contact pressure.

The objective of this work is to develop a precision positioning stage to control the height y and pitch θ of a roll over a substrate. These degrees of freedom allow

(i) experimental investigation of contact printing over a range of contact parameters and (ii) active compensation for non-uniformities in the contact printing stamp or substrate. In Chapter 5 develops a process model that includes some nominal roll displacement δ along $\hat{y}$, a spatially dependent error component $\epsilon(z, \theta)$, and a control effort u (5.4). For reference, this result is repeated here:

$$\delta^*(z, \psi) = \bar{\delta} + \epsilon(z, \psi) + u(z, \psi) \qquad \in (0, \delta_c) \qquad (7.1)$$

Developing a machine to control roll height y and pitch ψ allows exerting a control effort $u = y(\psi) + \theta(\psi)z$, where y and θ can have trajectories dependent on roll angle ψ. Substituting this expression for u gives

$$\delta^*(z, \psi) = \bar{\delta} + \epsilon(z, \psi) + y(\psi) + z\theta(\psi) \qquad \in (0, \delta_c) \qquad (7.2)$$

where the roll positioning stage is now able to compensate for errors at the contact interface that have low spatial frequencies in $\hat{z}$ or midrange spatial frequencies in $\hat{\psi}$.
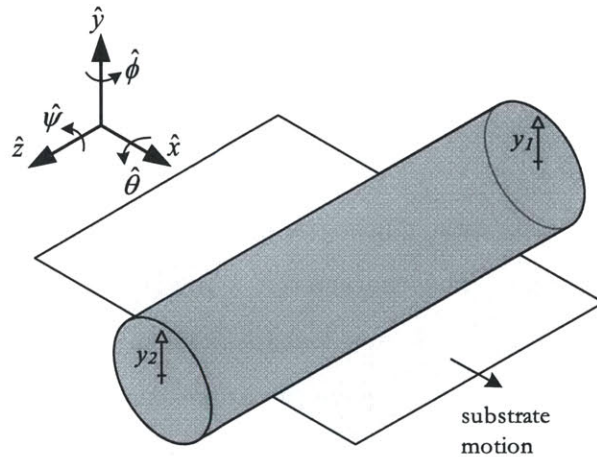

Figure 7-1: A simply supported shaft design can be moved relative to a printing substrate in the $\hat{y}$ and $\hat{\theta}$ directions by independently controlling the position y_i of each endpoint

The design and control principles developed here will provide models for both a

lab scale test bed and a future manufacturing scale machine.

7.2 Design

The lab scale printing considered here requires a mechanism that can accommodate 100 mm Si wafer substrates or 100 mm wide flexible webs with submicron position resolution and mN force sensitivity. Millimeter range of motion is required to accommodate a variety of stamp and substrate thicknesses. Accurate experiments of stamp contact mechanics will require a stiff structural loop, high sensor accuracy, and minimal hysteresis for repeatable load-displacement data between the roll and a substrate.

7.2.1 Design Concept

It is common for coating and printing machines to use a cantilever shaft design when printing widths are less than *ca.* 0.5 m. While this work targets a printing width of only 100 mm, a simply supported shaft design is employed that offers superior stiffness characteristics over cantilever designs. A simply supported shaft exhibits nearly ten times the stiffness in bending and eliminates large moments on the support bearings along with the corresponding angular deflections. Moreover, the height and pitch of the shaft in the $\hat{y}$ and $\hat{\theta}$ directions be controlled by independently manipulating the position of each end support (Figure 7-1).

To implement this concept, bearings at each end of the roll must provide the freedom of (*i*) shaft rotation $\hat{\psi}$, (*ii*) shaft translation in the lateral direction $\hat{z}$, (*iii*) vertical translation $\hat{y}$, and (*iv*) rotation $\hat{\theta}$ within the $y - z$ plane (Figure 7-2a). The first and second degrees of freedom allow the shaft to be kinematically constrained in the $\hat{z}$ and $\hat{\psi}$ directions by contact with the (eventual) substrate.

247

7.2.2 Bearings

The simply supported shaft design concept is implemented as a parallel kinematic mechanism, allowing design of identical bearing sets for both ends of the roll. A serial bearing design was chosen for simplicity of implementation and ease of actuation and sensing. The desired degrees of freedom are implemented by placing deep groove ball bearings ($\hat{\theta}$ motion) between ground and the box frame of a flexural bearing ($\hat{y}$ motion) that in turn supports an air bushing ($\hat{z}$, $\hat{\psi}$ motion) (Figure 7-2b). Ball bearings were chosen for high stiffness and economy; their associated nonlinear behavior at small angular displacements was not found to adversely affect the machine resolution. The flexural bearings provide repeatable motion throughout the desired vertical range, straightforward integration of position sensing through the use of strain gages, and can be absorb the weight of the shaft to minimize actuator power. Finally, the air bushings (NewWay S305001) provide frictionless, repeatable motion of the shaft.
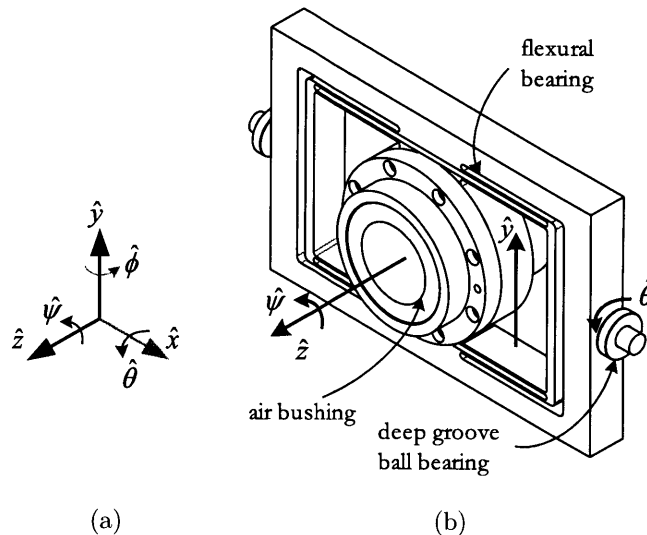
Figure 7-2: Degrees of freedom for end bearings of a simply supported shaft. (a) Desired Cartesian degrees of freedom at each shaft end point and (b) serial bearing design to provide desired degrees of freedom

Design of the flexural bearing thus becomes a key design challenge. A symmetric parallel flexure design is used (Figure 7-3) to achieve linear performance throughout

the range of motion, a thermally balanced design, and large range of motion. The load and actuators are easily placed through the center of stiffness of the flexure stage in this configuration.
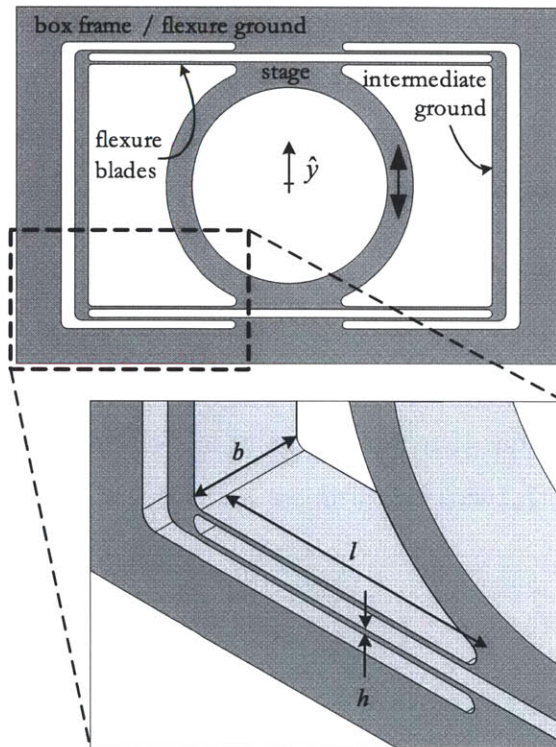
Figure 7-3: Parallel flexure design showing key design parameters and desired stage motion along $\hat{y}$.

The stiffness of each flexural bearing must be chosen to provide sufficient preload to offset the shaft weight while not requiring excessive actuator power to move throughout the range of motion.

Each flexure blade can be modeled using Euler beam theory to develop a set of design equations. Straightforward application of beam theory shows that the stiffness of each flexure blade is

$$k_{beam} = \frac{12EI}{l^3} \tag{7.3}$$

and that the maximum strain occurs at the root of each blade as a function of blade displacement δ_{beam}

$$\epsilon_{max} = \frac{3h}{l^2}\delta_{beam} \tag{7.4}$$

If the stress in the beam is to remain below some safety factor n of the yield stress, the following constraint is imposed:

$$\epsilon_{max} < \frac{\sigma_Y}{E}\frac{1}{n} \tag{7.5}$$

This bearing design has four parallel pairs of serial flexure blades (Figure 7-3), resulting in a stage with twice the stiffness and twice the displacement of a single blade:

$$k_{flexure} = 2k_{beam} = \frac{24EI}{l^3} \tag{7.6}$$

$$\delta_{flexure} = 2\delta_{beam} \tag{7.7}$$

The total displacement of the flexure must absorb both the preload of the shaft weight mg and the static range of motion imposed by the actuator force f_a:

$$k_{flexure}\delta_{flexure} > mg + f_i \tag{7.8}$$

The stiffness must also be low enough to permit the desired range of motion $|y_i|$ with actuator force $|f_i|$:

$$k_{flexure} < \frac{|f_i|}{|y_i|} \tag{7.9}$$

The formal design challenge is to minimize the actuator power requirements and

250

overall flexural bearing envelope (namely, length l) while satisfying the constraints of (7.5), (7.8), and (7.9). In doing so, each dimension in Figure 7-3 must be chosen along with the actuator sizing $|f_i|$. A heuristic solution method is used where the static actuator force $|f_i|$ is matched with the load weight mg in (7.8) rather than applying a rigorous optimization approach. A solution is chosen that lies on the boundaries of constraints (7.5) and (7.9), allowing deterministic calculation of the flexure height h and length l as a function of flexure thickness b.

Applying this heuristic method to the design at hand results in actuator sizing of 25 N each to support a total shaft weight of 50 N. The desired flexure stiffness $k_{flexure}$ is 25 N/mm from (7.9) to achieve 1 mm of motion $|y_i|$. Finally, using 6061-T6 aluminum ($E = 69$ GPa, σ_Y=240 MPa), this stiffness and range are satisfied using flexure blades that are $h = 1.25$ mm thick, $b = 25.4$ mm (1 in) wide, and $l = 65$ mm long with a safety factor $n = 4$.

This flexure design provides large range and exceptionally linear force-displacement behavior, but exhibits dynamic resonance from the intermediate flexure grounds. Numeric simulations (SolidWorks/COSMOS) verify linear load-displacement over the entire range of motion and validate the stiffness and maximum stress within 5%. The same simulations show the undesired modes of the flexural bearing were found to be at or above 150 Hz (Figure 7-4), about an order of magnitude greater than the desired system bandwidth.

The stiffness of each flexural bearing is very sensitive to the blade height h ((7.6)). As a matter of economy, the flexural bearings were machined using an abrasive waterjet, though ideally electric discharge machining (EDM) would be used to manufacture more accurate monolithic elements.

7.2.3 Actuators

The actuators must have sufficient force to both meet the requirements of (7.8) and (7.9) and to provide sufficient dynamic acceleration. The inertial dynamic impedance can be written in the frequency domain as

$$\frac{f_i(s)}{y_i(s)} = ms^2 \tag{7.10}$$

The supported mass is about 5 kg, the desired bandwidth is on the order of 30 Hz, and the typical range of motion required for control of the roll contact region is about 10 μm. Substituting these values into (7.10) gives a required dynamic force of 1.8 N. The actuator force sizing is thus dominated by the static requirements given in (7.8) and (7.9) rather than the dynamic requirement of (7.10).

Lorentz force actuators (voice coils) were chosen as actuators because they can provide bidirectional non-contact force over the range of force and displacement desired. While electromagnetic actuators require significantly more power for static load positioning than piezoelectric actuators, they are capable of much larger ranges and do not have the hysteresis typical of piezoelectrics. Coils capable of $\pm$ 25 N continuous force (H2W NCC03-15-050-2X) (Table 7.1) were chosen to satisfy the range requirement (7.9) given the stiffness of the flexural bearing (25 N/mm) and the desired range ($\pm$ 1 mm).

The actuators are placed directly between the flexural bearing box frame and the moving stage (Figure 7-5). This location places the resultant force through the center of stiffness and center of mass of the flexural bearing and load, respectively.

(a) (b)
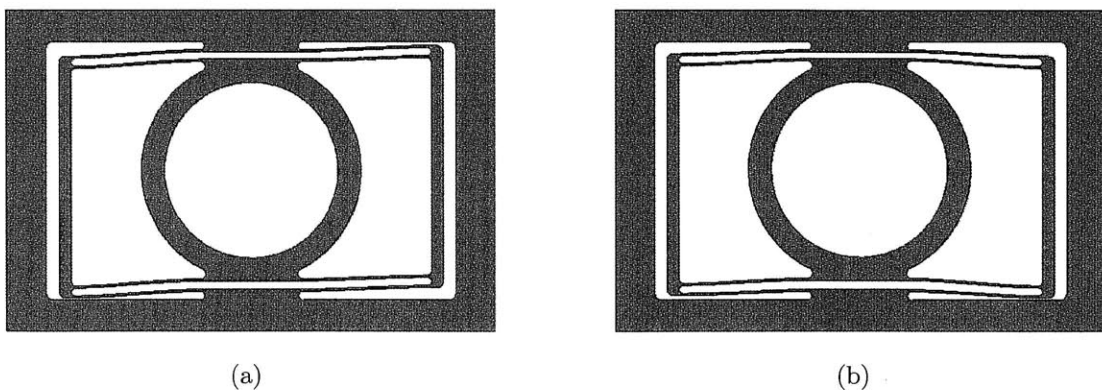
Figure 7-4: Flexural bearing design showing (a) second and (b) third dynamic modes of flexure stage from numeric simulation at 153 and 165 Hz, respectively.

Table 7.1: Actuator specifications

Specification	Value
Stroke	6.4 mm
Resistance	3.75 Ω
Inductance	1.30 mH
Motor Constant	11.9 N/A

The actuator coils and magnets are mounted with brass screws to avoid magnetic cogging.
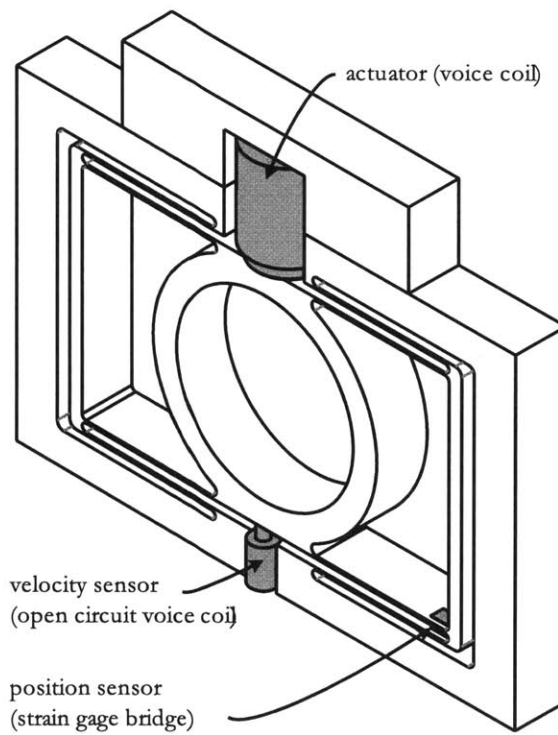
Figure 7-5: Actuator and sensor placement on each flexural bearing.

Each actuator is driven with a linear current amplifier.

7.2.4 Sensors

The position of the flexural bearing varies linearly with the strain in each flexure blade (7.4), allowing strain gages to be used as position sensors; [78] provides a detailed analysis of strain gage design for low noise position sensing. The large flexure blades employed here allow mounting a full Wheatstone bridge array on each flexural bearing without significant thermal effects; this provides a more sensitive and thermally stable measurement.

Each Wheatstone bridge is mounted on a pair of flexure blades opposite the actuator to minimize thermal drift from actuator heat dissipation. The bridge elements are arranged in a thermally balanced pattern on the flexure pair as shown in Figure 7-6.
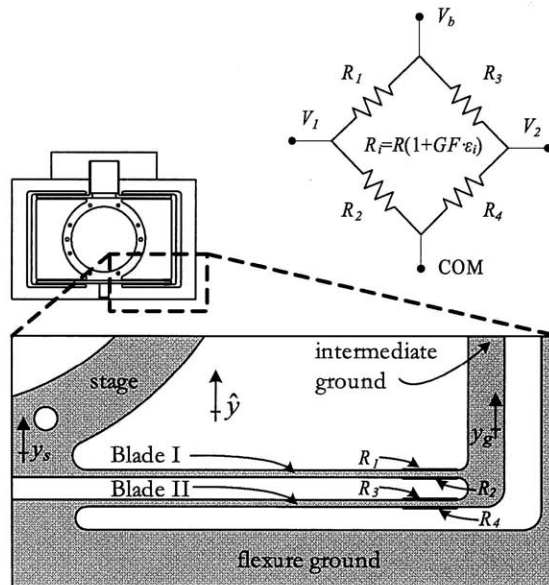
Figure 7-6: Circuit diagram of strain gage sensors in a full Wheatstone bridge configuration and corresponding mounting locations on each flexural bearing.

Referring to the notation in Figure 7-6, the output of this bridge can be derived by applying the identity $R_i = R \cdot (1 + GF \cdot \epsilon_i)$. The strain ϵ_i in each gage is governed by the deflection of the respective flexure blade as given in (7.4). Substituting $\epsilon_1 = -\epsilon_2 = \epsilon_I$

and $\epsilon_3 = -\epsilon_4 = \epsilon_{II}$, voltage divider equations find V_1 and V_2:

$$\frac{V_1}{V_b} = \frac{R(1 + GF \cdot \epsilon_I)}{R(1 + GF \cdot \epsilon_I) + R(1 - GF \cdot \epsilon_I)} \tag{7.11}$$

$$\frac{V_2}{V_b} = \frac{R(1 + GF \cdot \epsilon_{II})}{R(1 + GF \cdot \epsilon_{II}) + R(1 - GF \cdot \epsilon_{II})} \tag{7.12}$$

It follows that the bridge signal voltage signal is

$$\frac{V_1 - V_2}{V_b} = \frac{1}{2}GF\left(\epsilon_{II} - \epsilon_I\right) \tag{7.13}$$

The relationship in (7.4) shows that ϵ_{II} relates linearly to the position of the intermediate stage $\delta_{beam,II} = y_g$, while $-\epsilon_I$ relates linearly to the height difference between the flexure ground and stage $\delta_{beam,I} = y_s - y_g$. Substituting these identities give the voltage signal from the strain gage bridge:

$$\cdot\frac{V_1 - V_2}{V_b} = \frac{1}{2}GF\left(\frac{3h}{l^2}\right)\left(y_g + [y_s - y_g]\right) \tag{7.14}$$

Hence this Wheatstone bridge configuration thus observes only the position of the flexure stage with respect to ground and is nominally unaffected by the exact position z_g of the intermediate ground.

The small gage factor GF of the strain gages requires signal amplification. If an instrumentation amplifier with gain G_a is used, the position sensor gain K_{pi} can be determined:

$$V_s = K_{pi}y_i = \left[V_b G_a \frac{1}{2}GF\left(\frac{3h}{l^2}\right)\right] y_i \tag{7.15}$$

where K_{pi} relates position y_i and the sensor voltage signal V_s.

Metallic strain gages (Omega SGD-2/350-LY13, 350 ohm, $GF = 2.02$) were assembled to the flexure blades using cyanoacrylate (Loctite 401). Each bridge is driven with V_b=5 V and amplified by a commercial strain gage conditioner (Intronics Power 2B31K).

Velocity sensors are integrated into each flexural bearing to simplify full-state controller feedback without implementing differentiators or observers. Velocity is

measured using the open-circuit voltage V_s generated across secondary voice coils, determined by the velocity constant K_v of the coil.

$$V_s = K_{vi} \cdot \frac{dy_i}{dt} \tag{7.16}$$

These secondary coils are 12 mm diameter and 19 mm long with about 100 turns of wire; these are small enough to be embedded within the flexural bearing box frame opposite the actuator coils (Figure 7-5). Each velocity signal is amplified by an instrumentation amplifier (Analog Devices AD620ANZ).

7.2.5 Mounting

A schematic of the full parallel kinematic mechanism is shown in Figure 7-7, where two identical flexural bearing assemblies support the shaft at both endpoints. In practice, the ball bearings are supported in bearing blocks that can be adjusted vertically along mounting posts; this allows for coarse adjustment of the shaft height over different substrates and instrumentation. Figure 7-8 shows the fully assembled machine with such instrumentation.
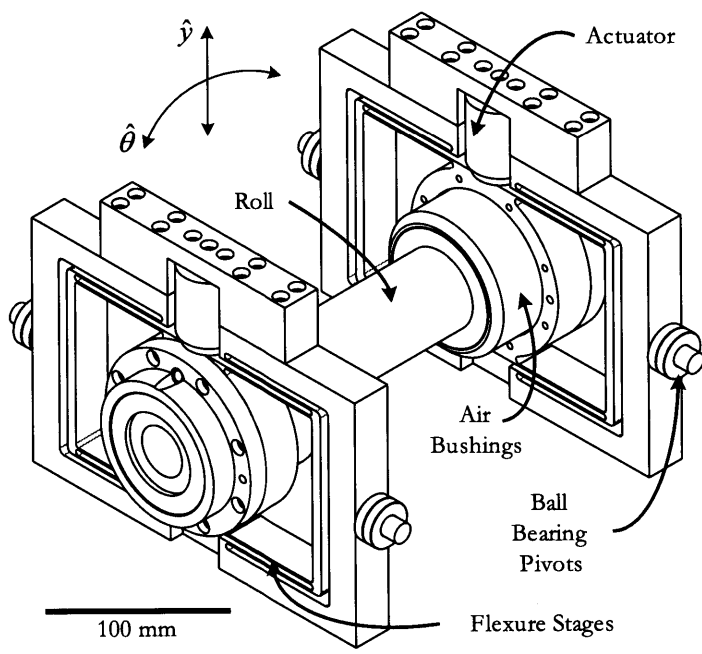
Figure 7-7: Schematic of complete kinematic stage design. Key mechanical elements are highlighted.
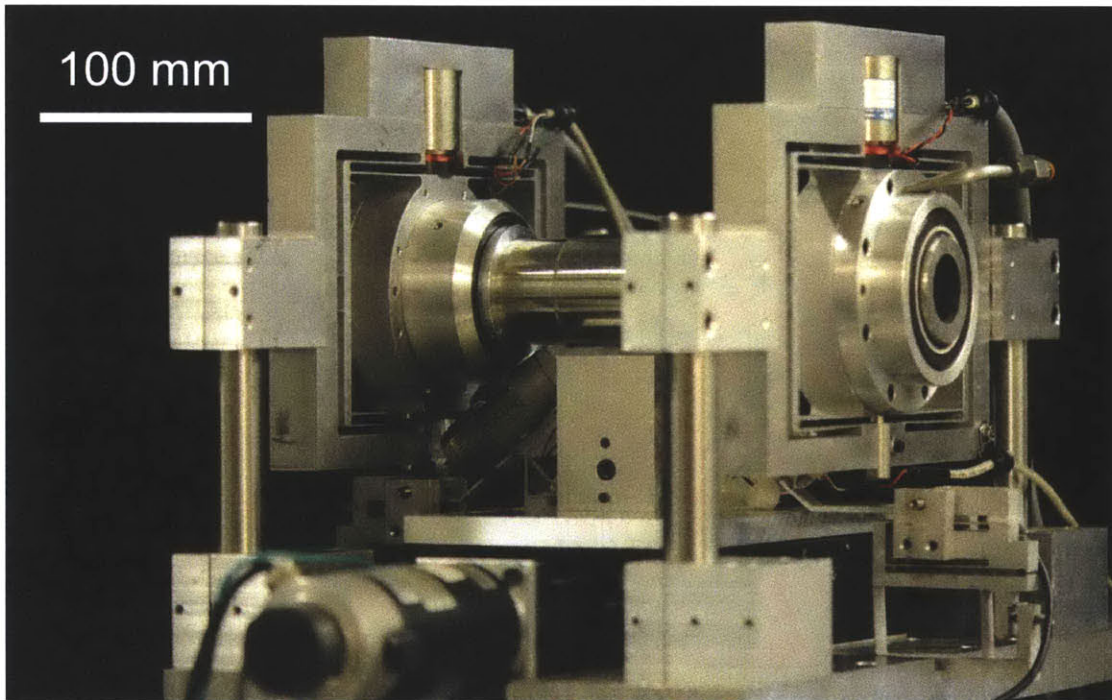
Figure 7-8: Precision roll positioning stage. The flexural bearing pivots are mounted on vertical shafts to provide coarse adjustment above various substrates. In the state shown, optical instrumentation is mounted beneath the roll for in situ stamp contact observation.

7.2.6 System Model

A kinematic model of the system is required to relate the forces and displacements exerted at each flexural bearing to the height and pitch of the supported shaft in a Cartesian coordinate frame (Figure 7-9). Each support point of the shaft can be represented by $\boldsymbol{p_1}$ and $\boldsymbol{p_2}$ as

$$\boldsymbol{p_i} = \begin{bmatrix} p_{iz} \\ p_{iy} \end{bmatrix} \tag{7.17a}$$

$$= \begin{bmatrix} \pm\frac{l}{2} - y_i \sin\theta \\ y_i \cos\theta \end{bmatrix}, \qquad i = 1, 2 \tag{7.17b}$$

Figure 7-9: Machine kinematics. Cross section schematic of (a) the flexural bearings and shaft at zero displacement and (b) the same with finite flexural bearing displacement.

The pitch θ of the shaft can be found from the slope between points $\boldsymbol{p_1}$ and $\boldsymbol{p_2}$:

259

$$\tan \theta = \frac{p_{1y} - p_{2y}}{p_{1z} - p_{2z}} \qquad (7.18a)$$

$$= \frac{(y_1 - y_2)\cos\theta}{l - (y_1 - y_2)\sin\theta} \qquad (7.18b)$$

And the height y of the center of the roll can be found by interpolating between points p_1 and p_2:
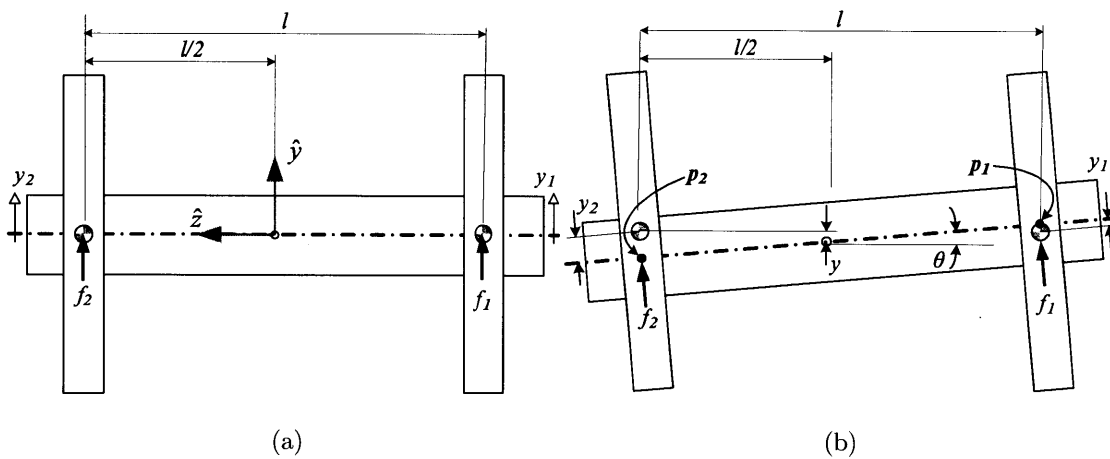
$$y = p_{1y} + \frac{p_{1z}}{p_{2z} - p_{1z}} \cdot (p_{2y} - p_{1y}) \qquad (7.19a)$$

$$= y_1 \cos\theta - \frac{\frac{l}{2} - y_1 \sin\theta}{l - (y_1 - y_2)\sin\theta} \cdot (y_1 - y_2)\cos\theta \qquad (7.19b)$$

The flexural bearings only permit motion of about 1 mm and l is 228 mm, restricting θ to a small angle. For this small angle case, (7.18a) and (7.19a) reduce to

$$\theta = \frac{1}{l}(y_1 - y_2) \qquad (7.20)$$

$$y = \frac{1}{2}(y_1 + y_2) \qquad (7.21)$$

Application of (7.20) and (7.21) gives the forward and reverse kinematic equations of the mechanism. Similarly, the net force f and torque τ on the shaft can be shown to reduce to

$$f = \frac{1}{2}(f_1 + f_2) \qquad (7.22)$$

$$\tau = \frac{1}{l}(f_1 - f_2) \qquad (7.23)$$

The dynamics of the system are developed in terms of these kinematic variables (y, θ, f, and τ) rather than the sensor and actuator variables (y_1, y_2, f_1, f_2) without

loss of generality. This transformation requires the following rotation matrices:

$$\begin{bmatrix} y \\ \theta \end{bmatrix} = \begin{bmatrix} 1/2 & 1/2 \\ 1/l & -1/l \end{bmatrix} \begin{bmatrix} y_1 \\ y_2 \end{bmatrix} \tag{7.24}$$

$$\begin{bmatrix} f \\ \tau \end{bmatrix} = \begin{bmatrix} 1 & 1 \\ l/2 & -l/2 \end{bmatrix} \begin{bmatrix} f_1 \\ f_2 \end{bmatrix} \tag{7.25}$$

The net force and torque on the roll can be written in the time domain as

$$f_1 - f_2 = k_1 y_1 + k_2 y_2 + b_1 \dot{y}_1 + b_2 \dot{y}_2 + \frac{m}{2}(\ddot{y}_1 + \ddot{y}_2) \tag{7.26}$$

$$\frac{1}{l}(f_1 - f_2) = \frac{l}{2}(k_1 y_1 - k_2 y_2)\frac{l}{2}(b_1 \dot{y}_1 - b_2 \dot{y}_2) + \frac{J}{l}(\ddot{y}_1 - \ddot{y}_2) \tag{7.27}$$

where k_i and b_i are the stiffness and damping of each flexural bearing ($i = 1, 2$), m is the equivalent mass of the shaft and air bushings, and J is the rotational inertia of the shaft, air bushings, and flexural bearings. (7.26) and (7.27) can be expressed in terms of the variables given in (7.24) and (7.25) and written in standard state space matrix form ($\dot{x} = Ax + Bu, y = Cx + Du$):

$$\dot{x} = \begin{bmatrix} 0 & 1 & 0 & 0 \\ -\frac{k_1+k_2}{m} & -\frac{b_1+b_2}{m} & -\frac{l(k_1+k_2)}{2m} & -\frac{l(b_1+b_2)}{2m} \\ 0 & 0 & 0 & 1 \\ -\frac{l(k_1-k_2)}{2J} & -\frac{l(b_1-b_2)}{2J} & -\frac{l^2(k_1+k_2)}{4J} & -\frac{l^2(b_1+b_2)}{4J} \end{bmatrix} x + \begin{bmatrix} 0 & 0 \\ 1/m & 0 \\ 0 & 0 \\ 0 & 1/J \end{bmatrix} u \tag{7.28}$$

$$y = \begin{bmatrix} 1 & 0 & 0 & 0 \\ 0 & 0 & 1 & 0 \end{bmatrix} x + 0 \cdot u \tag{7.29}$$

where the state vector, input vector, and output vector are

$$x = \begin{bmatrix} y & \dot{y} & \theta & \dot{\theta} \end{bmatrix}^{\mathsf{T}} \tag{7.30}$$

261

$$\boldsymbol{u} = \begin{bmatrix} f & \tau \end{bmatrix}^\mathsf{T} \tag{7.31}$$

$$\boldsymbol{y} = \begin{bmatrix} y & \theta \end{bmatrix}^\mathsf{T} \tag{7.32}$$

In this model, the $\boldsymbol{C}$ matrix has been chosen so that $\boldsymbol{y}$ includes only the position states of $\boldsymbol{x}$, resulting in a square system model ($\boldsymbol{u}$ and $\boldsymbol{y}$ are in the same vector space). Indeed each state in $\boldsymbol{x}$ is accessible from the position and velocity sensors on the machine and in the following sections it will be assumed that $\boldsymbol{x}$ can be accessed directly.

7.3 Characterization

7.3.1 Sensors

Each strain gage bridge was calibrated using a digital gage (Mitutoyo ID-F150HE) with 1 μm resolution and 3 μm accuracy (Table 7.2).
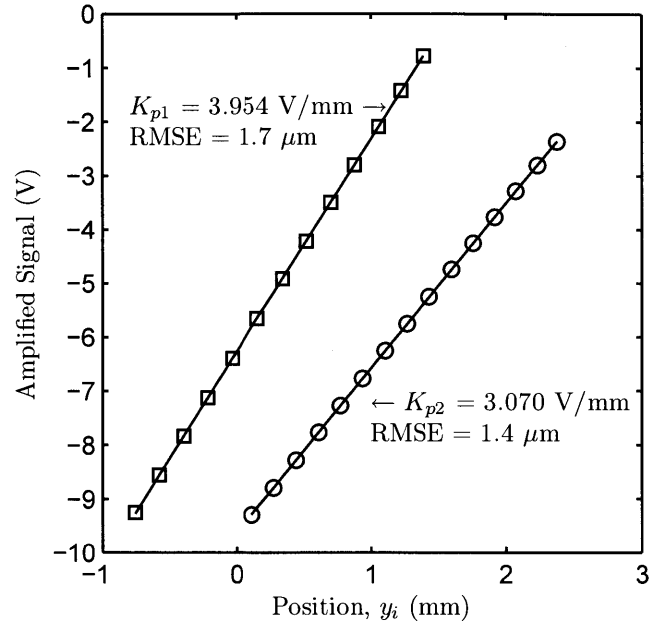
Figure 7-10: Position sensor calibration. Each experimental calibration point is shown with a least-squares fit superimposed. The RMSE error is within the calibration tool accuracy of 3 μm.

The velocity sensors are very short relative to the stage stroke, resulting in a position-dependent gain over their range of motion. To map this velocity sensor response, small sinusoidal oscillations (10 μm amplitude at 30 Hz) were performed about discrete points throughout the range of the flexural bearings. The amplitude of the position and velocity sensor signals were compared at each point to determine the local linearized velocity gain. A first order model provides an analytical function describing the velocity gain K_{vi} as a function of position y_i (Figure 7-11).

Table 7.2: Position and velocity sensor gains

	Flexural Bearing 1	Flexural Bearing 2
K_p	3.954 V/mm	3.070 V/mm
K_v	$(0.0984 + 0.0129z_1)$ V·s/m	$(0.0703 + 0.0111z_2)$ V·s/m
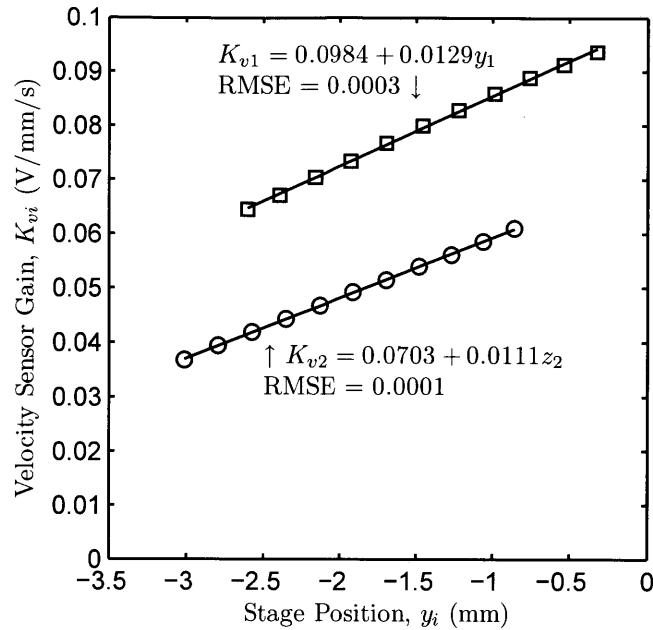
Figure 7-11: Velocity sensor calibration. The velocity sensors are non-linear, that is, the sensor gain is a function of position. The small-displacement sensor gain about different positions is shown for each of the velocity sensors, along with a least-squares fit of the position-dependent gain.

To measure the resolution and accuracy of the position sensors, the stage and each intermediate ground were clamped to the ground frame of each flexural bearing, effectively fixing sensor position. Sensor data was recorded for 15 minutes at a rate of 10 kHz and the power spectral density calculated for the noise in measurement y_i (Figure 7-13). The corner frequency between Johnson and flicker noise is 1 Hz. Rolloff from a 5 kHz hardware anti-aliasing filter is evident at high frequencies.

Using the spectral density in Figure 7-13a, the RMS noise above 10 Hz is 174 nm (representing the sensor noise above the approximate closed loop servo bandwidth). This noise level corresponds to a sensor dynamic range of 81 dB over the 2 mm range of motion.
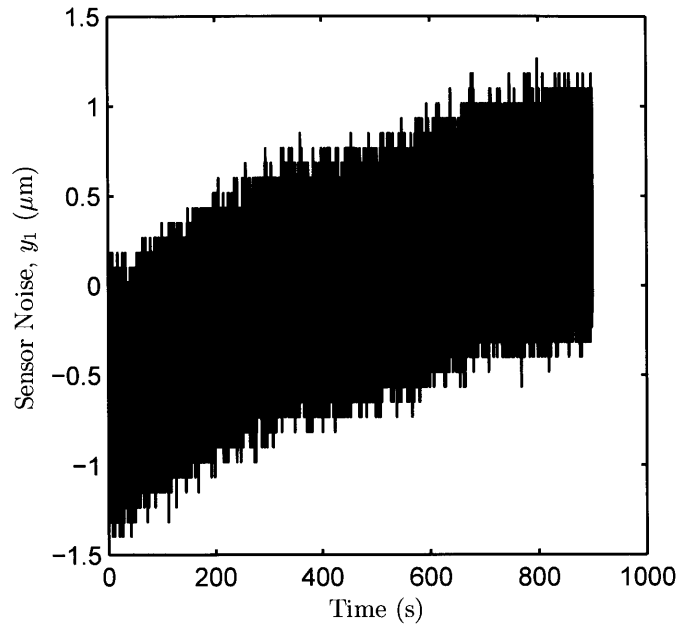
(a)
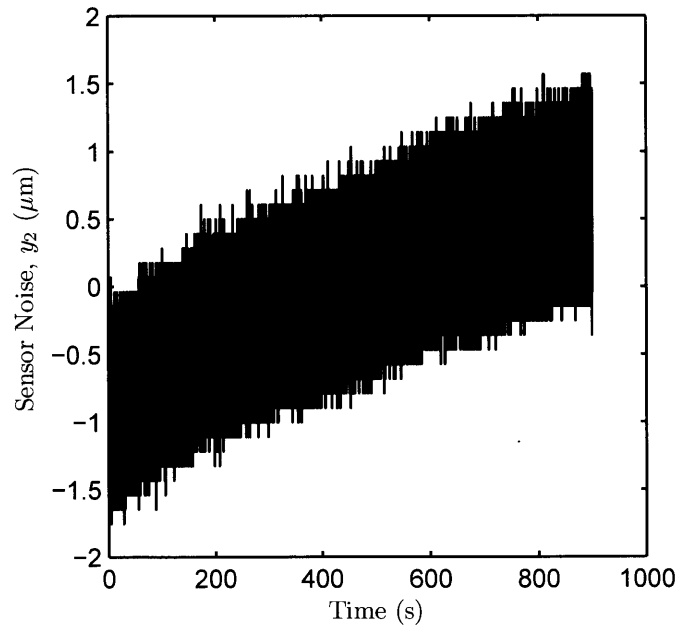
(b)

Figure 7-12: Time domain sensor noise of (a) y_1 and (b) y_2 position sensors. Low frequency thermal drift and digital to analog conversion discretization are clearly visible in these data.
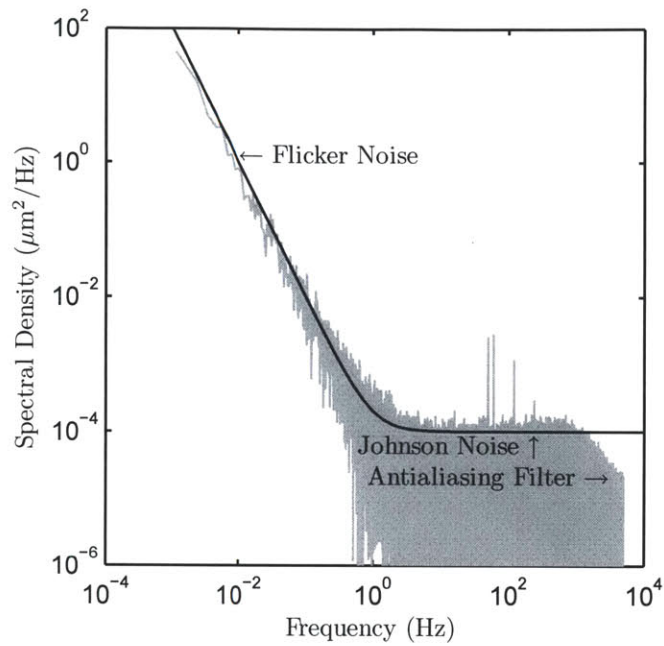
(a)
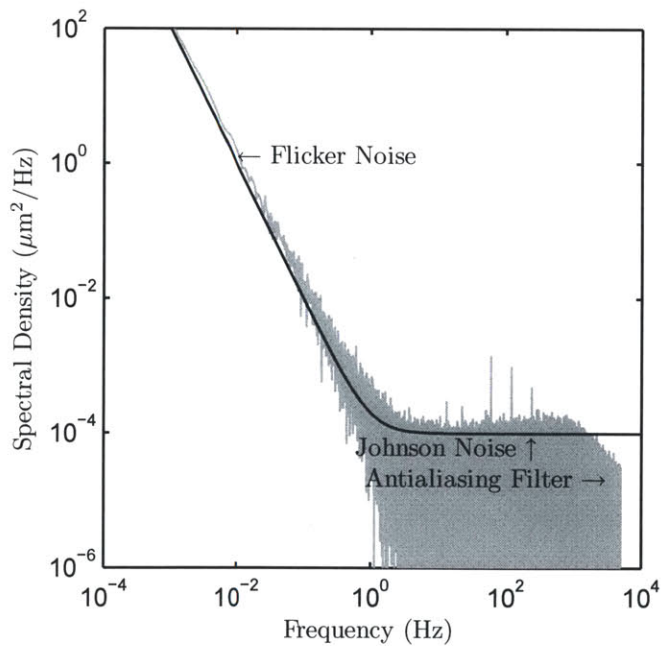
(b)

Figure 7-13: Power spectral density of (a) y_1 and (b) y_2 position sensor noise. Particular characteristics of the sensor noise are denoted on the plots, along with an approximate fit based on low frequency flicker noise and high frequency Johnson noise. Spikes are evident at 50, 60, 120, and 240 Hz, presumably from background electrical noise.

7.3.2 Flexural Bearings and Actuators

Each flexural bearing stiffness and actuator constant were calibrated experimentally by varying both the actuator signal and a known load on each stage. The actuator signals were changed in 0.5 V increments. A known load mg was created using a set of masses (20.1, 50.0, 100.4, and 200.5 g). At each combination of V_a and mg the position y_i of each stage was recorded using the calibrated strain gage sensors. The model in (7.33) was used to determine the each actuator constant K_{ai}, flexure stiffness k_i, and sensor bias y_{0i} by regression (Table 7.3).

$$k_i(y_i - y_{0i}) = mg + V_a K_{ai}, \qquad i = 1, 2 \tag{7.33}$$

Table 7.3: Calibrated flexure and actuator constants for the roll positioning stage.

	Flexural Bearing 1	Flexural Bearing 2
k_i	8600 N/m	9200 N/m
K_A	6.22 N/V	6.00 N/V
RMSE	0.088 N	0.088 N

The flexural bearings were cut from aluminum stock using an abrasive waterjet as a matter of economy and availability. Manufacturing tolerances in this process resulted in thinner flexure blades than the 1.25 mm design value, resulting in each calibrated flexural bearing stiffness being less than the 25000 N/m design value.

7.3.3 Linearity

The linearity of each flexural bearing stage was evaluated independently (without coupling by the shaft) by measuring the relationship between the actuator and sensor signals. Each stage was actuated sinusoidally over its entire range; the frequency of actuation was a 1/8 Hz so that the mechanical impedance was dominated by flexural bearing stiffness. The two flexural bearing stages had measured linearity of 0.48% and 0.29% with very little observable hysteresis.

7.3.4 Repeatability

Open loop repeatability was measured using a technique similar to the stage linearity evaluation. The stage was sinusoidally excited with a force f at 0.125 Hz and a torque τ at 0.1 Hz over a period of 15 minutes. Considering only static terms and incorporating an error term ϵ, the dynamic system equation (7.28) reduces to

$$0 = \begin{bmatrix} k_1 + k_2 & \frac{l}{2}(k_1 - k_2) \\ \frac{l}{2}(k_1 - k_2) & \frac{l^2}{4}(k_1 + k_2) \end{bmatrix} y + u + \epsilon \qquad (7.34)$$

The stiffness parameters k_1 and k_2 in (7.34) were fit to minimize the root mean square of error ϵ. Figure 7-14 shows ϵ plotted in the time domain.

The spectral density of ϵ indicates the open loop resolution and accuracy of the machine, important for measurements of printing contact forces. This spectral density is shown in Figure 7-15 with the sensor noise spectral density superimposed (scaled by the stage stiffness). The alignment of these curves suggests that the dominant source of low frequency error (i.e. drift affecting accuracy) can be attributed to the sensor drift.
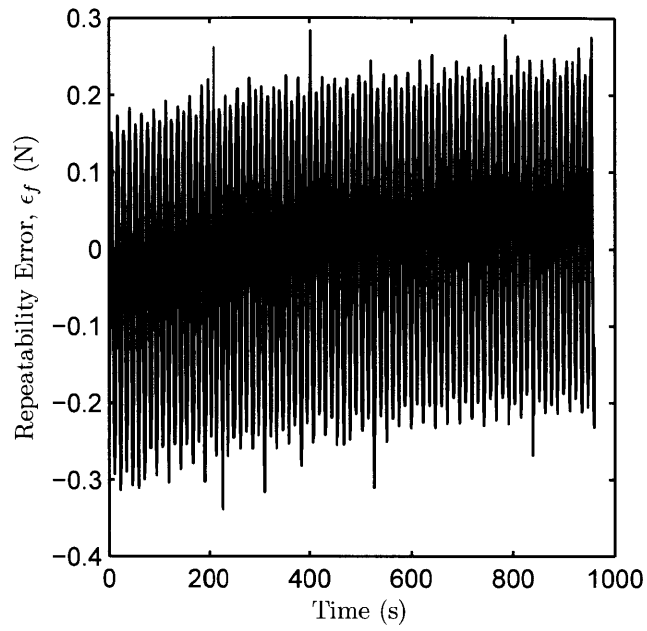
(a)
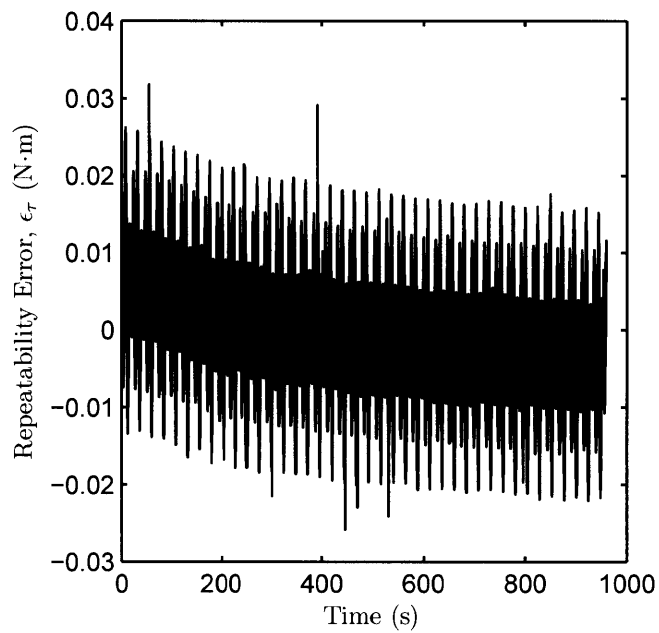
(b)

Figure 7-14: Time domain data of (a) f and (b) τ repeatability error ϵ. Low frequency thermal drift is evident in these data, along with the actuation frequencies of 1/12 Hz and 1/8 Hz.
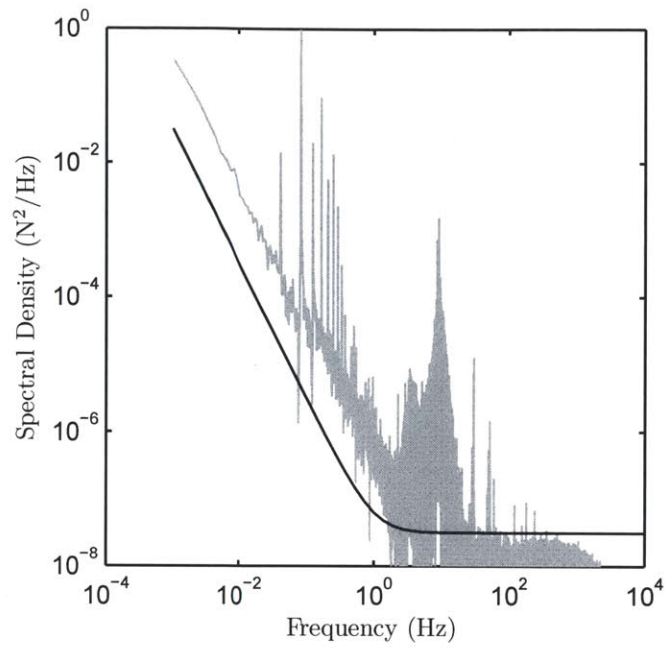
(a)
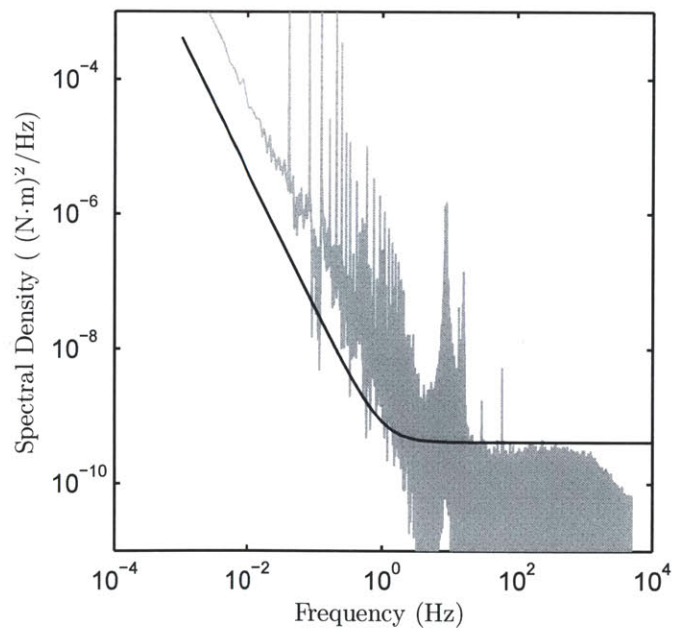
(b)

Figure 7-15: Power spectral density of of (a) f and (b) τ repeatability error ϵ. The apprpriately scaled model of sensor noise is superimposed on the data, showing that the low frequency error is due primarily to sensor drift. Spikes are evident at harmonics of the excitation frequencies (1/8 Hz and 1/12 Hz) and at the natural frequency of the rolling stage (10 Hz).

7.3.5 Shaft Runout

The shaft runout was measured in the fully assembled machine using a capacitive probe. Runout was measured at three points along the shaft as it was allowed to freewheel in the air bushings. The total indicated runout was 3.8 μm.

7.3.6 Structural Loop

The structural stiffness of the machine was measured using the actuator and sensor signals. The shaft was loaded using the actuators and the displacement measured using the strain gage sensors while supporting the shaft against the machine baseplate (shown in Figure 7-8). The structural loop data shows that the machine is much stiffer (0.1 μm/N) than could be attained using a cantilever design with the same shaft and bearings. The manufacturers data sheet lists the radial stiffness of each air bushing at 110 N/μm and the pitch stiffness at 23 N·m/mrad. If this live shaft were cantilevered over a 100 mm span, the pitch compliance would affect the structural loop by 0.44 μm/N.

7.3.7 Dynamic Response

The frequency domain transfer function between the inputs and outputs in the system equation (7.28) was measured using a swept sine input (Figure 7-16). The damping and inertia terms in (7.28) were fit visually to the frequency response data; all terms in the model are summarized in Table 7.4.

The system model (7.28) describes the primary dynamics of the system well, but fails to capture a number of high frequency dynamics. Because the flexure blade stiffness is lower than designed, the first mode of the flexural bearing intermediate grounds is at about 100 Hz instead of the 153 Hz predicted by numeric simulation in Figure 7-4. In addition to the dynamic modes shown in Figure 7-4, other unmodeled dynamics result from coupling the two flexural bearings with the rigid shaft. The measurement noise floor at -135 dB (equivalent to 180 nm/m sensor resolution) is evident in the frequency response measurements.

Table 7.4: Calibrated system model parameters for the roll positioning stage.

Parameter	Value
l	228 mm
m	5.50 kg
J	0.0805 kg·m^4 mm
k_1	8600 N/m
k_2	9200 N/m
b_1	10.0 N·s/m
b_2	10.0 N·s/m
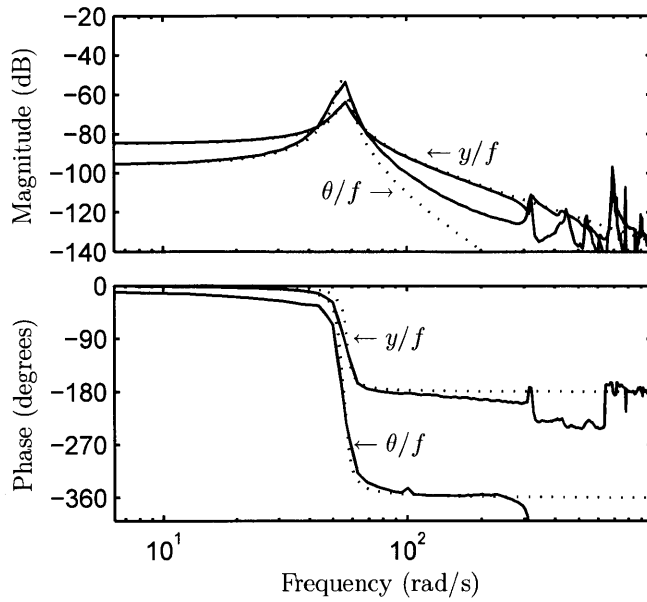
(a)
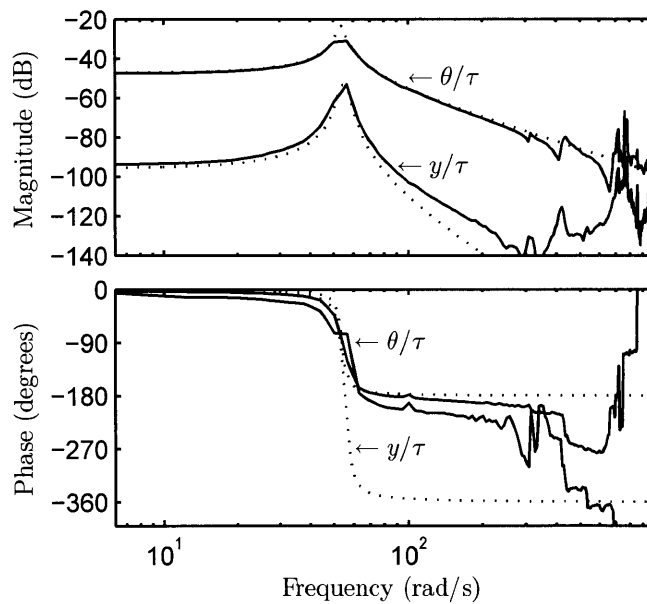
(b)

Figure 7-16: Experimental frequency response of roll height y and pitch θ with respect to inputs (a) force f and (b) torque θ. The system model shown dashed. The experimental data were collected using the swept sine method. Mode coupling and high frequency unmodelled dynamics are evident in the measurements.

273

7.4 Summary

This chapter presents the design and characterization of a precision rolling stage appropriate for laboratory scale manufacturing experiments. The design presented uses a simply supported shaft design, which results in symmetric machine design and high structural stiffness. The use of zero friction elements, including flexures, air bushings, and voice coil actuators, results in repeatable motion without significant hysteresis. The strain gage position sensors have good dynamic range and provide submicron resolution and accuracy.

The design concept of this machine can also be used in larger manufacturing scale implementations. While this machine used ball bearings and waterjet flexural bearings as a matter of economy, future machines can improve linearity by using frictionless bearings (air bushings) and match the designed stiffness using more a accurate manufacturing process for the flexural bearings (electric discharge machining).

Chapter 8

Machine Control

8.1   Parallel Kinematic Dynamics

Parallel kinematic mechanisms, like the roll positioning stage designed in the preceding chapter, offer a primary advantage of lower total mass, where the motion stage is coupled to ground through multiple parallel actuators rather than stacked serial stages. From a power perspective, this lower mass results in lower actuator efforts and higher accelerations. From a kinematic perspective, this parallel arrangement creates a coupling between each actuator degree of freedom, giving rise to the forward and reverse kinematic problems. When the full machine dynamics are considered, this coupling results in a complex multi-input multi-output (MIMO) plant that is quite difficult to control.

Attempts at parallel kinematic mechanisms in the machine tool industry can serve to illustrate this problem. Traditional three axis mills are constructed by stacking an $\hat{x}$ and $\hat{y}$ motion stage on top of each other in a serial arrangement. This arrangement allows independent tuning of the respective servo loops; the orthogonal axes see the same apparent mass regardless of the immediate behavior of the other stage. High stiffness can be obtained by appropriate design of each motion stage. The detriment of this design lies in the fact that the $\hat{y}$ stage must accelerate both its own weight *and* the weight of the $\hat{x}$ stage that it carries. The actuator efforts become even larger when trunions for four- or five-axis machining is added to the serial kinematic stack.

As one example, parallel kinematic designs are often employed in miniature precision motion stages, for example microelectromechanical systems (MEMS) for nanopositioning. These designs give superior performance in theoretical bandwidth as calculated from the ratio of actuator size to stage mass. However, the controller design is neither trivial nor straightforward and the theoretical bandwidth is rarely achieved. As one example, [23] uses a 39th order model to describe the dynamics of a 3-axis stage. Their design uses three 27 N actuators to move a stage with a mass of grams over a range of less than 100 μm. This combination gives a theoretical bandwidth over the entire range of motion in the range of kHz. In contrast, the resulting controller design achieves only 32 Hz and 57 Hz bandwidth in the $\hat{x}$ and $\hat{y}$ directions due to limiting system dynamics.

The dynamics of the roll positioning stage developed in Chapter 7 are likewise difficult to control at a high bandwidth despite having only two degrees of freedom. Measurements of dynamic system response (Figure 7-16) indicate a significant degree of cross-coupling between modes and unmodeled high frequency dynamics that emerge at about 50 Hz and above. This chapter introduces a nested control architecture that is able to effectively and intuitively achieve closed loop position control at 35 Hz.

8.2 Nested Control Architecture

The parallel kinematic stage designed here is an example of a multi-input multi-output (MIMO) dynamic system where the actuators and sensors are inherently coupled by the system kinematics. This machine also falls in a class of precision servomechanisms where the control objective is not simply regulation, but also good tracking of reference commands. A state space system of form $\dot{x} = Ax + Bu$ can be dynamically characterized by the Eigenvalues and Eigenvectors of the A matrix, where the Eigenvalues dictate the speed of system response and the Eigenvectors dictate the direction of the response (i.e. state interactions). While many MIMO control synthesis techniques seek to achieve a particular set of Eigenvalues with some degree of robustness, [97] suggests that the Eigenvectors are of equal import for servo tracking

performance. Ideally the Eigenvectors in a precision servomechanism are orthogonal so that each state can be independently controlled without perturbing any other state (e.g. in this case the height z and pitch θ of the roll should be independently manipulated).

Eigenstructure assignment (EA) is well known method of altering the dynamic characteristics of a plant using full state feedback [102]. A linear time invariant dynamic system given by $\dot{x} = Ax + Bu$ with a feedback law of $u = -Kx$ has a closed loop dynamic equation given by $\dot{x} = (A - BK)x$. The dynamic response of this closed loop system is governed by the Eigenvalues and Eigenvectors of $(A - BK)$, which can be assigned by the correct choice of feedback matrix K. If states are successfully decoupled using EA, then they can be treated as independent subsystems. In the case of servo control, each output in y is mapped to a reference r in the same vector space $\mathbb{R}^n$, allowing straightforward application of single-input single-output (SISO) compensators or feed forward paths for good reference tracking.

A challenge in this particular example is the resonance modes observed at high frequencies (Figure 7-16). These modes are impractical to fully model, leading to investigation of robust EA in the case of bounded uncertainty and unmodeled dynamics [95]. While these robust methods guarantee stability, exact decoupling is impossible with unmodeled dynamics and the stability of independent SISO compensators between y and u is correspondingly compromised.

In the case of this machine, the high frequency dynamics from the flexural bearings result in incomplete decoupling at those frequencies using EA. While loop shaping techniques allow intuitive evaluation of stability and sensitivity and can be based on experimental data, they fail to predict the interaction between coupled modes in a MIMO system. To combine the strengths of both state space methods and classical loop shaping techniques, this section presents an control architecture of nested decoupling and servo control loops, derives a criterion for adequate decoupling in the former, and ultimately applies these developments to this machine to achieve position control.

8.2.1 Controller Synthesis

A nested controller architecture is utilized to combine the strengths of both state feedback and classical loop shaping design techniques (Figure 8-1). This control architecture is synthesized in two steps:

(i) The K matrix is determined using well known EA methods to separate the dynamic modes of the plant, and

(ii) Compensators $C_i(s)$ are designed using loop shaping techniques to meet design specifications such as overshoot, sensitivity, and tracking error.
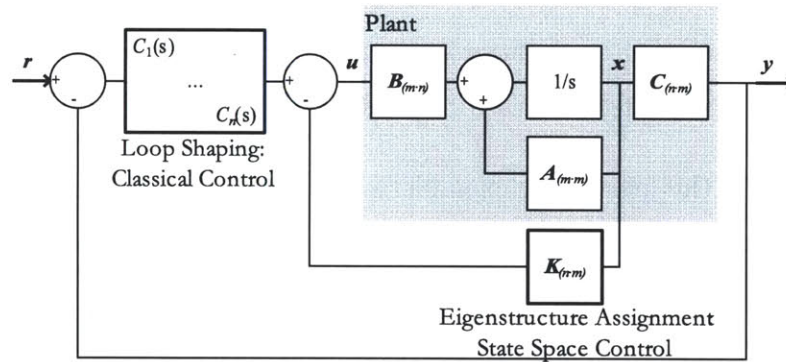
Figure 8-1: Block diagram of general square system in state-space representation with nested feedback loops. The inner loop allows shaping the plant dynamics via full state feedback and Eigenstructure assignment to decouple dynamical modes, while the outer loop provides intuitive servo loop design of independent modes via classical frequency domain techniques.

The application of this control architecture assumes full decoupling of all system modes during the first synthesis step. While state space feedback design is mathematically straightforward, it is sensitive to small variations in system parameters and, more importantly, unmodeled dynamics. Thus, while the compensators $C_i(s)$ are provided to more intuitively deal with unmodeled dynamics, the very presence of these dynamics precludes exact decoupling and blind application of SISO controllers.

278

8.2.2 Unmodeled Dynamics

An additional design criterion must be applied to the design of the loop shaping compensators $C_i(s)$ to address unmodeled system dynamics. To evaluate the quality of mode separation based on experimental data, a block diagram representation of the system is considered where each SISO transfer function is found in the transfer function matrix $\boldsymbol{G}(s)$:

$$\boldsymbol{G}(s) = \boldsymbol{C}(s\boldsymbol{I} - \boldsymbol{A})^{-1}\boldsymbol{B} + \boldsymbol{D} \qquad (8.1)$$

Arranging the elements of $\boldsymbol{G}(s)$ for a square system in $\mathbb{R}^2$ and adding the (as yet to be determined) SISO compensators $C_{1,2}(s)$ results in the block diagram shown in Figure 8-2a.

Rearranging this block diagram (Figure 8-2b) it is clear that the SISO control loops are separate if $G_{21}(s)$ and $G_{12}(s)$ are zero at all frequencies. Even if these two transfer functions have small finite values, the control loops are strongly decoupled if

$$|G_{11}| \gg \left| G_{21} \cdot \frac{-C_2}{1 + C_2 G_{22}} \cdot G_{12} \right|, \ \forall \omega \qquad (8.2)$$

Rearranging (8.3) provides a decoupling criterion $\mathcal{DC}(s)$:

$$\mathcal{DC}(s) = \left| \frac{G_{11} G_{22}}{G_{12} G_{21}} \right| \gg \left| \frac{C_i G_{ii}}{1 + C_i G_{ii}} \right|, \ i = 1, 2, \ \forall \omega \qquad (8.3)$$

This result shows that the closed loop response of each input-output pair (C_i and G_{ii}) must be much less than a criterion $\mathcal{DC}(s)$ defined by the plant transfer functions *at all frequencies*. The term $|G_{11} G_{22}/G_{12} G_{21}|$ can be determined experimentally from the state-space feedback result (8.1) and used as a design constraint for the closed loop transfer function. Each compensator C_i can be designed as if applied to a fully decoupled SISO subsystem as long as the closed loop transfer function satisfies the inequality in (8.3). The criterion $\mathcal{DC}(s)$ is less general than results for square systems

in $\mathbb{R}^n$ by other researchers (for example [104]) but is more exact for the case of a square system in $\mathbb{R}^2$.
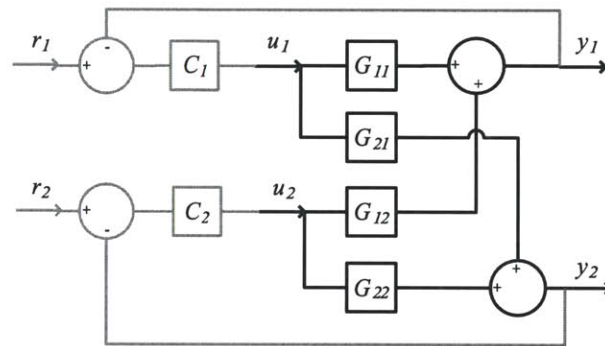
(a)
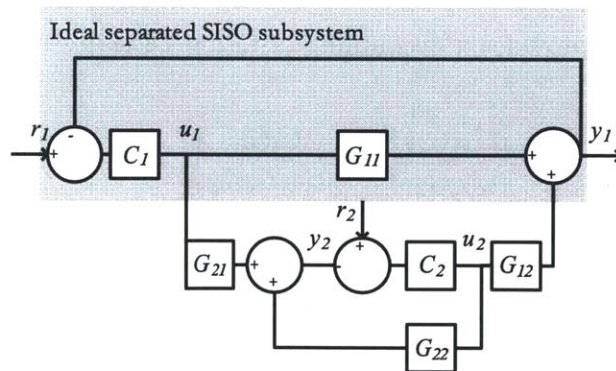
(b)

Figure 8-2: (a) Block diagram of a square (two input, two output) system with feedback compensation implemented between respective inputs and outputs; (b) rearranged block diagram used in deriving criteria for treating compensator designs independently

280

8.3 Position Control

In this section, the nested feedback architecture shown in Figure 8-1 is used as an example for controller synthesis. The machine dynamics (measured in Figure 7-16) are particularly appropriate because they (*i*) show a high degree of coupling between the y and θ modes and (*ii*) exhibit a number of high frequency unmodeled dynamics.

Control algorithms were implemented in C++ and executed on the CPU of a Dell T7500 workstation. Interfacing with the hardware was done through a 16-bit data acquisition board (National Instruments PCIe-6343) with a control sampling rate of 10 kHz. First order R-C anti-aliasing filters were placed on the analog inputs at 5 kHz.

Eigenstructure Assignment

Matrices $\boldsymbol{A}$ and $\boldsymbol{B}$ in the system equation (7.28) are in block diagonal form that allows algebraic determination of feedback matrix $\boldsymbol{K}$ without applying formal EA algorithms. Representing the elements of $\boldsymbol{K}$ as K_{ij} gives closed loop dynamic behavior determined by the Eigenstructure of

$$(\boldsymbol{A} - \boldsymbol{BK}) = \left[\begin{array}{cc|cc} 0 & 1 & 0 & 0 \\ -\frac{k_1+k_2+K_{11}}{m} & -\frac{b_1+b_2+K_{12}}{m} & -\frac{l(k_1+k_2)+2+K_{13}}{2m} & -\frac{l(b_1+b_2)+2K_{14}}{2m} \\ \hline 0 & 0 & 0 & 1 \\ -\frac{l(k_1-k_2)+2K_{21}}{2J} & -\frac{l(b_1-b_2)+2K_{22}}{2J} & -\frac{l^2(k_1+k_2)+4K_{23}}{4J} & -\frac{l^2(b_1+b_2)+4K_{24}}{4J} \end{array}\right]$$

(8.4)

The off-diagonal blocks should be $\boldsymbol{0}$ to eliminate cross coupling while the diagonal blocks can be shaped by second order matrices

$$\begin{bmatrix} 0 & 1 \\ -1/\omega_n^2 & -2\zeta/\omega_n \end{bmatrix}$$

(8.5)

where ω_n is the desired natural frequency and ζ the desired damping ratio. These requirements call for a closed loop system matrix of

281

$$(A - BK) = \left[\begin{array}{cc|cc} 0 & 1 & 0 & 0 \\ -1/\omega_{n1}^2 & -2\zeta_1/\omega_{n1} & 0 & 0 \\ \hline 0 & 0 & 0 & 1 \\ 0 & 0 & -1/\omega_{n2}^2 & -2\zeta_2/\omega_{n2} \end{array}\right] \qquad (8.6)$$

Matching terms in (8.4) and (8.6) gives the individual components of feedback matrix K:

$$K = \left[\begin{array}{cccc} \frac{m}{\omega_{n1}^2} - (k_1 + k_2) & \frac{2\zeta_1}{\omega_{n1}} - (b_1 + b_2) & -\frac{l}{2}(k_1 - k_2) & -\frac{l}{2}(b_1 - b_2) \\ -\frac{l}{2}(k_1 - k_2) & -\frac{l}{2}(b_1 - b_2) & \frac{J}{\omega_{n2}^2} - \frac{l^2}{4}(k_1 + k_2) & \frac{2\zeta_2}{\omega_{n2}} - \frac{l^2}{4}(b_1 + b_2) \end{array}\right] \quad (8.7)$$

The frequency ω_{ni} of each diagonal mode was left unaltered from the open loop plant (stiffness and inertia were not changed) in this design but the damping ratio ζ_i was set to unity (critical damping). The complete K matrix was calculated from (8.7) with the system parameters found in Table 7.4 and implemented on the hardware. The experimental frequency response of the shaped system (Figure 8-3) shows an improvement over the original plant response (Figure 7-16). The diagonal responses $z(s)/f(s)$ and $\theta(s)/\tau(s)$ exhibit critical damping, the low frequency response of the off-diagonal responses $z(s)/\tau(s)$ and $\theta(s)/f(s)$ have been reduced by 10 dB, and more importantly the separation between the diagonal and off-diagonal modes in the magnitude response remains strong over a much wider range of frequencies.
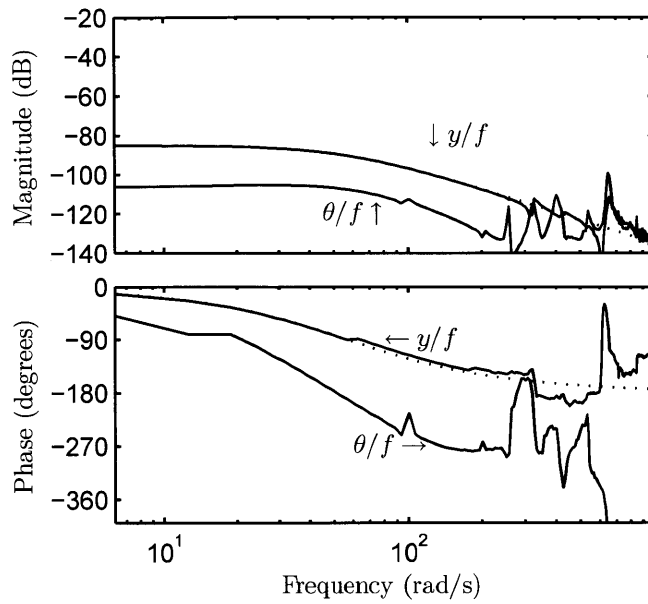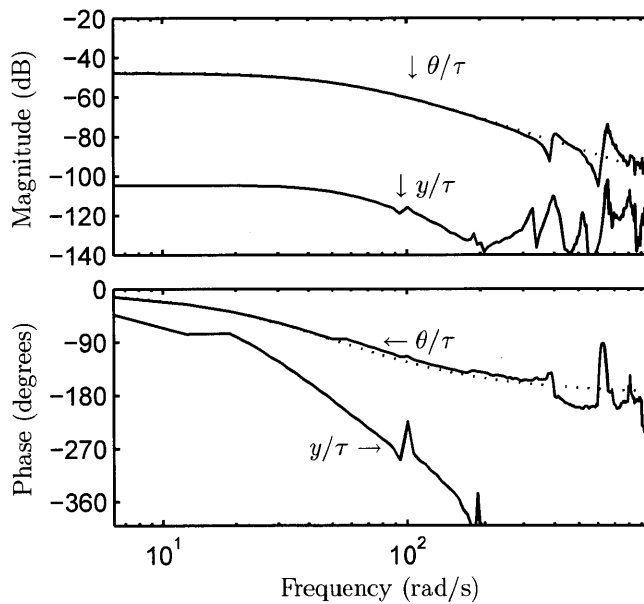
Figure 8-3: Plant frequency response after Eigenstructure assignment. Experimental frequency response of roll height y and pitch θ with respect to inputs (a) force f and (b) torque θ. The system model with identical feedback is shown dashed. In comparison to the original plant frequency response, this data shows superior mode separation and improved damping, but remaining high frequency unmodelled dynamics.

8.3.1 Loop Shaping

The dynamic response of the plant remains coupled at high frequencies above 300 rad/s. The result of (8.3) becomes invaluable in implementing the SISO compensators. The utility of $\mathcal{DC}(s)$ is demonstrated here by two compensator designs for $C_i(s)$.

As an initial controller design attempt, it is assumed that the plant has been completely diagonalized by EA. Lead-lag compensators are designed for each input-output pair:

$$C_i(s) = K_i \cdot \frac{\tau_{0i}s + 1}{s} \cdot \frac{\alpha_i \tau_i s + 1}{\tau_i s + 1} \tag{8.8}$$

Classical loop shaping techniques are applied to the experimental frequency response data to provided a phase margin of 45 degrees at about 20 Hz, with a sensitivity $S = [1 + C_i(s)G_{ii}(s)]^{-1}$ of less than 6 dB (dashed curve in Figure 8-4a). Despite meeting these well established frequency domain stability criteria, these compensators prove unstable when implemented on the hardware.

Applying the criterion of (8.3) to the experimental data clearly highlights frequencies above the closed loop bandwidth that were not well separated by the state feedback. The compensator design is repeated (solid curve in Figure8-4) with the decoupling criterion (8.3) as a constraint on the closed loop transfer function. To stabilize the plant, notch filters were added to each compensator at the overlapping frequencies in Figure 8-4b (400 rad/s and 680 rad/s) to attenuate the closed loop response at those points. Similar crossover frequencies, phase margins, and sensitivities were achieved but while also satisfying the constraint imposed by $\mathcal{DC}(s)$. The revised compensators are stable when implemented on the hardware.

The closed loop bandwidth of each mode is 35 Hz at -3 dB with this compensator design. The closed loop step response of each reference (y and θ) demonstrates excellent separation of each mode in the time domain (Figure 8-5).

This controller design illustrates the power of nested state space EA and classical loop shaping feedback. Using the mode separation criterion developed in (8.3)
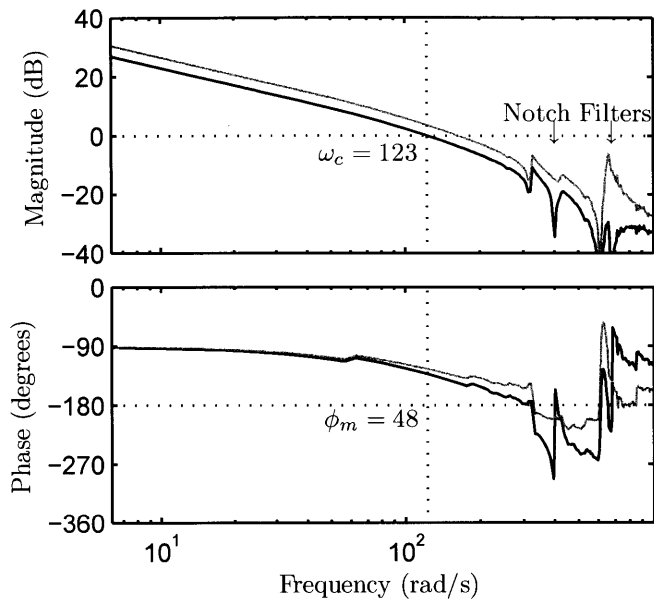
(a)
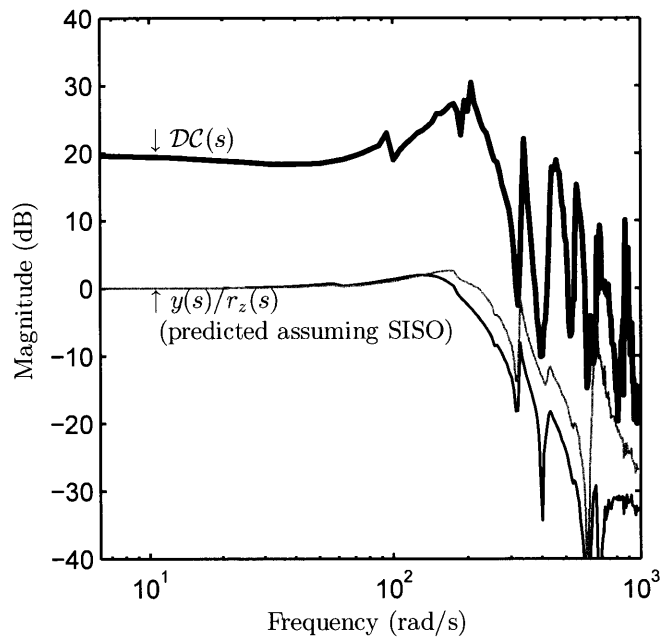
(b)

Figure 8-4: Compensator design. (a) Loop shaping of $y(s)/f(s)$ and (b) predicted closed loop response versus decoupling criterion $\mathcal{DC}(s)$. The gray curve in each plot is a simpler compensator design (no notch filters) that violates the constrain imposed by $\mathcal{DC}(s)$ and results in instability.
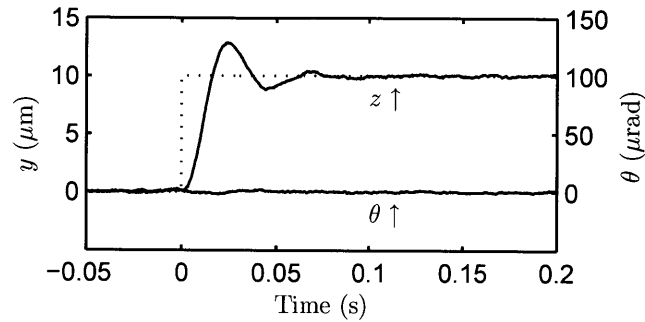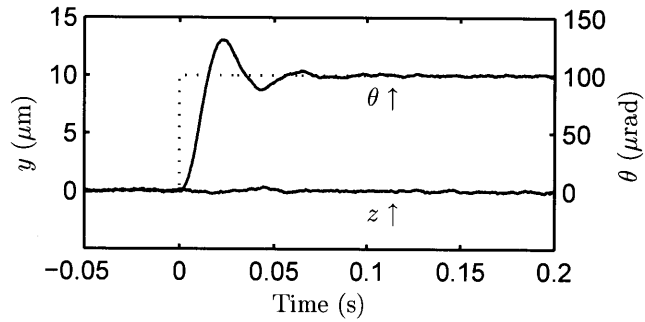
Figure 8-5: Closed loop time domain step response of roll positioning system. Independent step responses of (a) roll height y and (b) roll pitch θ; the step reference command is shown dashed. In each case, these experimental data show good response time and separation of modes.

provides a powerful tool to intuitively visualize and remedy incomplete decoupling during loop shaping design.

8.4 Summary

The simply supported shaft design results in a parallel kinematic machine. To decouple the modes of the machine, a strategy for nested state space and classical feedback loops is presented, including a criterion for the degree mode separation. In the controller design, the use of this criterion was shown to be a valuable design tool to achieve high system bandwidth despite coupled high frequency dynamics.

Chapter 9

Process Feedback Control

9.1 Process Control

Appropriate stamp design can greatly attenuate the sensitivity of stamp contact to local disturbances. Some level of process control is still required to compensate for errors at larger spatial and temporal wavelengths. To this end, this chapter explores active control of stamp contact by manipulation of the entire processing roll.

Chapter 7 developed a roll positioning stage capable of motion in two degrees of freedom: roll height y and pitch θ. It was shown that the process model developed in Chapter 5 could be rewritten in terms of these two degrees of freedom (7.2), repeated here:

$$\delta^*(z, \psi) = \hat{\delta} + \epsilon(z, \psi) + y(\psi) + z\theta(\psi) \qquad \in (0, \delta_c) \tag{9.1}$$

This chapter addresses appropriate choice of the $y(\psi)$ and $\theta(\psi)$ trajectories to keep the local roll displacement δ^* within the process window. The approach taken in this chapter is one of feedback control, where the stamp contact pattern is monitored and the trajectories adjusted accordingly. In comparison to a strategy of error mapping and subsequent open loop compensation, this feedback control method can compensate for both spatial and temporal errors.

The precision roll positioning stage developed in Chapters 7 and 8 is used as a platform for implementing process feedback control. The immediately following

section shows how instrumentation is incorporated in this machine to permit real time *in situ* observation of the stamp contact pattern. Following this, a feedback control law is implemented that uses the visualized contact pattern as a control variable. Finally, an impedance control scheme is used that maintains uniform contact through mechanical feedback between the roll and substrate.

9.2 Contact Imaging

9.2.1 Total Internal Reflection

In roll based processing opportunity rarely arises to visualize the contact behavior in situ: inspection is typically performed downstream or offline of the process and the process behavior is inferred from these measurements. The lab scale rolling stage developed in this thesis, combined with the optical properties of PDMS stamps, permit a unique opportunity to measure in situ contact behavior. The conventional printing substrate was replaced with a set of optical instrumentation in the lab scale machine to allow visualizing and actively manipulating the stamp contact region.

Other researchers have used high resolution microscopy and fringe methods to visualize the three dimensional contact behavior of collapsing PDMS structures [91, 31, 112]. In this thesis, an alternative method is used to visualize the two dimensional contact pattern using total internal reflection. While fringe based methods give better visualization of local behavior at the feature scale, the total internal reflection method is better suited for examining large areas of contact (for example, along the length of a roll) and can still identify when feature collapse occurs.

Reflection Criterion

A large optical prism was used as a substrate in the roll positioning stage to visualize contact at the stamp interface. Contact between the stamp and prism disrupts total internal reflection within the prism, allowing visualization with cameras (Figure 9-1).

When light passes through an interface between two mediums, the resulting angle

288
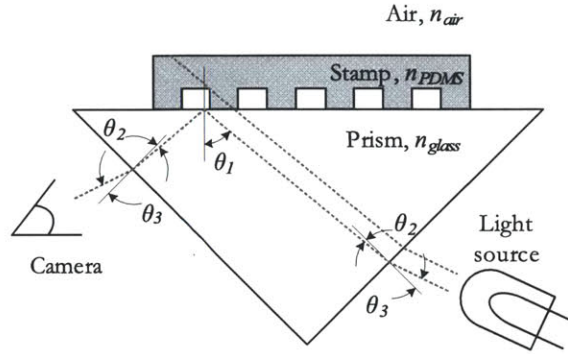
Figure 9-1: Stamp contact measurement using total internal reflection at the contact interface. Light incident within a certain range of θ_1 will escape the prism where the PDMS stamp makes contact, but internally reflect at the prism-air interface. This technique results in a high contrast image of the stamp contact pattern.

is given by Snell's Law

$$n_1 \sin \theta_1 = n_2 \sin \theta_2 \tag{9.2}$$

where n_1 and n_2 are the refractive indices of the two mediums and θ_i is given relative to the surface normal. When the angle of incidence θ_1 is large within a medium where $n_1 > n_2$, the light will fail to escape the interface and will reflect back into the first medium (*total internal reflection* (TIR)). This critical angle of incidence is

$$\sin \theta_1 = n_2/n_1 \tag{9.3}$$

These basic relationships from Snell's Law can be used to design the contact visualization optics in Figure 9-1. From (9.3) θ_1 must be large enough to force TIR at the glass-air interface

$$\theta_1 > \mathrm{asin} \, \frac{n_{\mathrm{air}}}{n_{\mathrm{glass}}} \tag{9.4}$$

but must be small enough that TIR does *not* occur at the glass-PDMS interface

$$\theta_1 < \mathrm{asin} \, \frac{n_{\mathrm{PDMS}}}{n_{\mathrm{glass}}} \tag{9.5}$$

289

Assuming use of a right angle prism,

$$\theta_2 = \theta_1 - \frac{\pi}{4} \qquad (9.6)$$

Refraction also occurs at the light and camera interfaces of the prism, giving

$$n_{\text{glass}} \sin \theta_2 = n_{\text{air}} \sin \theta_3 \qquad (9.7)$$

Combining the above equations gives a minimum viewing angle θ_3 of

$$\theta_3 > \text{asin} \left(\frac{\sqrt{2}}{2} \left[1 - \sqrt{\left(\frac{n_{\text{glass}}}{n_{\text{air}}} \right)^2 - 1} \right] \right) \qquad (9.8)$$

Table 9.1: Index of refraction for optical materials

Material	Index of Refraction, n
Air	≈ 1.0
Glass (N-BK7)	1.51
PDMS	1.4 [67]

Physical values for the index of refraction in different materials are summarized in Table 9.1. Applying these values to (9.8) gives the requirement that $\theta_3 > -5.3°$.

Image Distortion

While this technique results in a high contrast image of the stamp contact pattern, the required camera angle prevents an orthogonal view of the contact plane. The intersection of the camera view frustum and prism face result in imaging of a trapezoidal section of the image plane (Figure 9-2).

This camera view angle results in foreshortening of the real image when viewing a contact pattern on this prism surface. The contact interface incident angle θ_1 should be as small as possible to minimize this foreshortening and the variation in field depth. Equivalently, the viewing angle θ_3 should be as small as possible while satisfying (9.8).

290

Implementation

The TIR imaging concept was implemented using a 50 mm right angle prism (diagonal length 70 mm). The prism was epoxied to a custom mount. This mount was placed on a linear motion stage to control relative motion between the roll and prism.

Two cameras were mounted on opposite sides of the prism with $\theta_3 = +7°$. Rather than fixing the cameras to the prism, the cameras were mounted to the ground of the roll positioning stage. This strategy allowed focusing the cameras on specific points on the roll axis so that the contact region is always centered in the field of view. Compact CMOS sensors with integrated lenses (DinoLite AMS413T) were used to fit within the space constraints of the roll positing stage. These cameras were mounted to the frame using flexural mounts for fine alignment and adjustment.

Arrays of light emitting diodes were mounted behind the prism to provide stable backlighting.
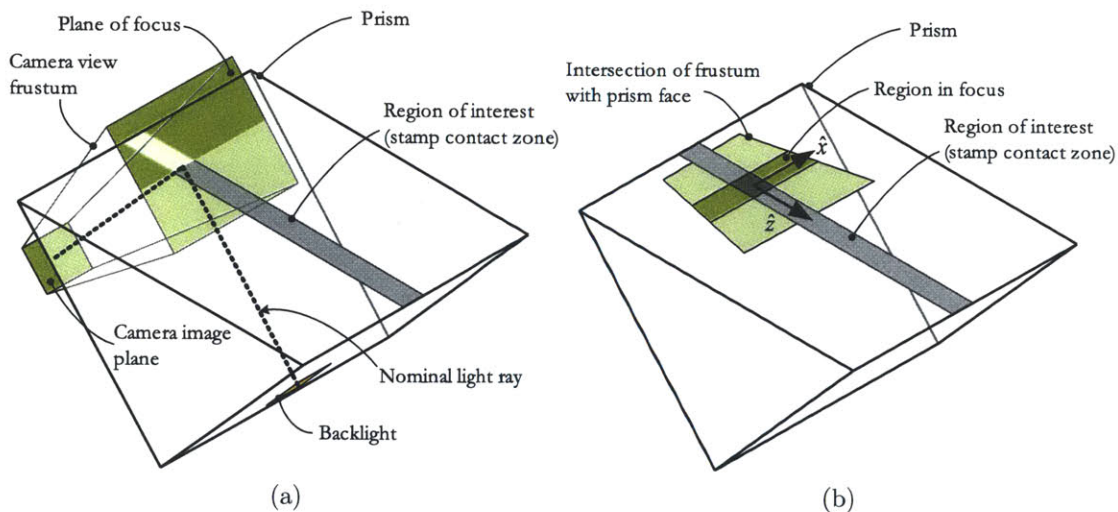
Figure 9-2: Perspective distortion of contact interface images. (a) Images at the contact interface are projected onto the camera image plane. Only a portion of the image is in focus where the plane of focus intersects the contact interface. (b) A trapezoidal region of the contact interface is projected onto the camera image plane, resulting in a perspective distortion and foreshortening of the image.

9.2.2 Perspective Correction

The inclination of the prism plane relative to the camera view vector results in three phenomena:(*i*) the image is distorted by perspective, (*ii*) it is foreshortened, and (*iii*) only a portion of the image is in focus (Figure 9-2). The detriment of these phenomena depends on the specific measurement task.

For example, if the goal is to detect local feature collapse, then the foreshortening and distortion may not be important, while the limited focus band would have a dramatic impact. Alternatively, if the intent is to measure the macroscopic contact area (*2l*), the perspective distortion would be much more important than either the foreshortening or focus.

A distortion free image is obtained by digital correction for the purposes of this thesis. In a high bandwidth imaging system, an equivalent effect could be obtained in the hardware by using additional optical prisms to refocus the image or a telecentric lens to eliminate perspective distortion.

The foreshortening and tapering cause by a perspective view can be compensated for computationally by a transformation to the image; a general case of this is examined by [90]. While image analysis are traditionally done in x, y coordinates, this discussion used a z, x coordinate system to remain consistent with the coordinate
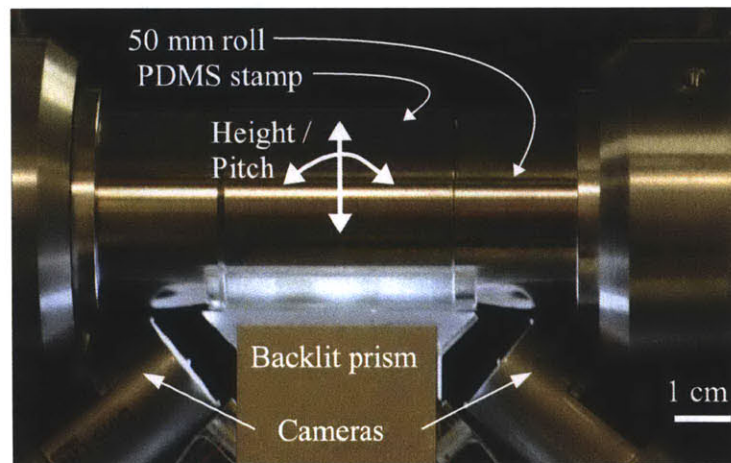
Figure 9-3: Positioning of optics in the roll positioning stage. Two sets of LED backlights and cameras are used to image two locations along the contact interface.

292

system used for roll based printing throughout this thesis. Taking the center of the image to be the origin (Figure 9-2b), the shear can be removed by mapping from the original image space z_i, x_j to a corrected space z_i^*, x_j^* (these spaces are written with subscripts i, j to remind that they are discrete pixel locations in an image). A ray tracing approach (Figure 9-4a) shows that this transformation is given by:

$$z_i^* = \alpha z_i \tag{9.9}$$

$$x_i^* = \left(1 + \beta \frac{z_i}{z_n}\right) x_i \tag{9.10}$$

(a)   (b)
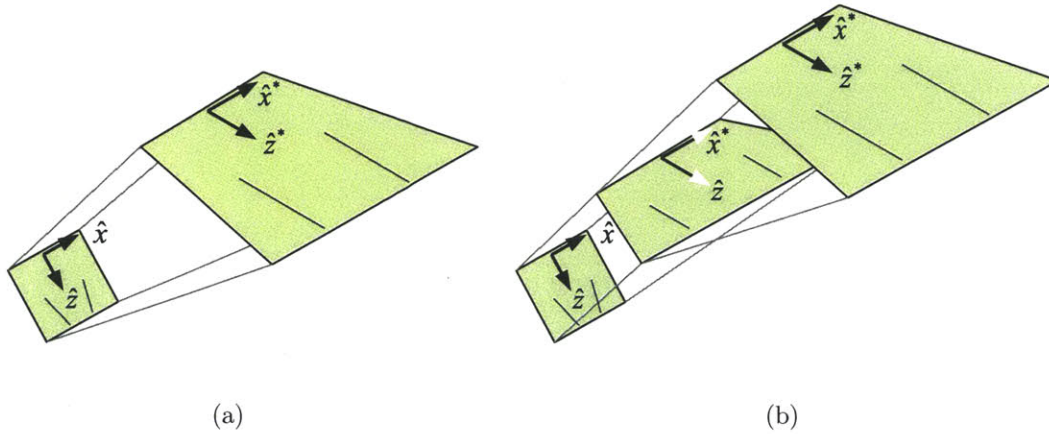
Figure 9-4: Mapping from the camera view plane to the contact interface for correction of contact images. (a) The camera view plane with coordinates z, x can be mapped back to the contact interface coordinates z^*, x^* with a ray-tracing approach. (b) This transformation can equivalently be performed in two steps, with an intermediate image in coordinates z, x^*. In both figures, parallel lines at the contact interface are projected through the transformations to illustrate the image distortion.

This transformation can be calibrated using a fiducial grid in two steps, illustrated in Figure 9-4b. First, the angular distortion in a calibration image is measured to determine β. Second, the image is transformed into space z, x^*, where the ratio of the vertical feature pitch p_x and the horizontal feature pitch p_z is measured to find

β. Knowledge of the precise pitch p_x also gives the scaling factor of the image.

In the first step, points p_i with coordinates z_i, x_i are selected from two horizontal rows of features at the top and bottom of the image ($p_{\bar{1}}p_2$ and $p_{\bar{3}}p_4$) (Figure 9-5a). After the transformation, the lines formed between these points should be parallel, giving equal slopes:

$$\frac{x_2^* - x_1^*}{z_2^* - z_1^*} = \frac{x_4^* - x_3^*}{z_4^* - z_3^*} \tag{9.11}$$

Substituting x^* and y^* gives

$$\beta = z_n \frac{(x_4 - x_3)(z_2 - z_1) - (x_2 - x_1)(z_4 - z_3)}{(z_2 x_2 - z_1 x_1)(z_4 - z_3) - (z_4 x_4 - z_3 x_3)(z_2 - z_1)} \tag{9.12}$$

Next, the feature pitch is examined to find α (Figure 9-5b). The three corners of a square (selected by z_i, x_i^*) must be transformed to be equidistant:

$$\sqrt{(z_2^* - z_1^*)^2 + (x_2^* - x_1^*)^2} = \sqrt{(z_3^* - z_2^*)^2 + (x_3^* - x_2^*)^2} \tag{9.13}$$

Substituting $z^* = \alpha z$ gives

$$\alpha = \sqrt{\frac{(x_3^* - x_2^*)^2 - (x_2^* - x_1^*)^2}{(z_3 - z_2)^2 - (z_2 - z_1)^2}} \tag{9.14}$$

This calibration procedure is illustrated in Figure 9-5 using a fiducial pattern of 50 μm posts on a 100 μm pitch. The results of the calibration procedure for each camera are summarized in Table 9.2.

Table 9.2: Camera perspective calibration constants from calibration

Parameter	Camera 1	Camera 2
α	1.66	1.65
β	0.075	0.077
Pixel resolution, μm/px	6.1	6.4
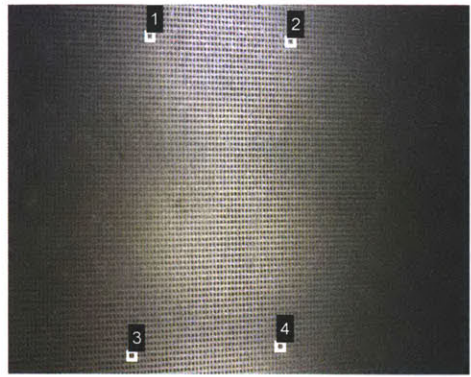
(a)
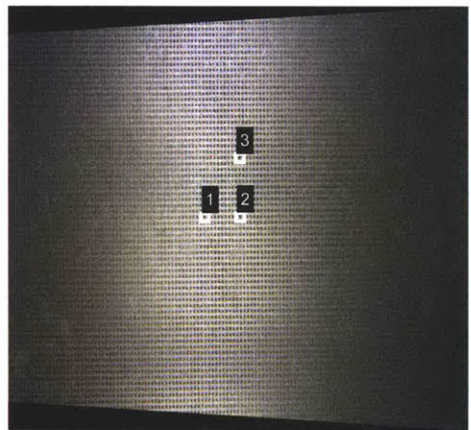
(b)

(c)

Figure 9-5: Example of camera perspective calibration. (a) Camera calibration image with 50 μm posts on a 100 μm pitch. The original image is mapped from space (a) z, x to (b) z, x^* and finally (c) z^*, x^* using the calibration procedure described in the text.

9.3   Contact Measurement

After obtaining images of the contact interface, some variable of interest must be extracted from the pixel data. A number of phenomena are of interest, for example contact width, feature collapse, or local contact defects. A fast, automatic, and repeatable measurement of contact width is required for a number of experimental and control components of this thesis.

The objective of the measurement strategies presented here is to extract the *mean* contact width in an image frame regardless of local behavior, collapse, or defects. In effect, the measurement techniques presented here act as a spatial filter F to convert a large number of pixels (typically one million or more) to a single variable describing the state of contact.

In this section two methods of contact width measurement are presented, based on well established image processing techniques of thresholding and edge finding.

9.3.1   Thresholding

The contact pattern formed by the total internal reflection mechanism is high contrast, offering an opportunity to measure contact area simply by measuring the ratio between light and dark pixels in the image frame.

As a roll-based stamp contacts the measurement prism a contact pattern of width pattern $2l(z)$ will form as a function of the coordinate along the roll axis $\hat{z}$. Assuming a uniform pattern ratio $P = a/w$, the area in contact along a differential element of the roll will be

$$\frac{d}{dz}A_{contact} = \frac{2l(z)}{P+1} \tag{9.15}$$

The total contact area can be measured by integrating across the camera field of view z_c (along the roll axis $\hat{z}$)

$$A_{contact} = \int_0^{z_c} \frac{2l(z)}{P+1} dz \tag{9.16}$$

296

The total viewing area will be $A = z_c x_c$ (where x_c is measured along the rolling direction $\hat{x}$), so that the fill factor C of the frame will be

$$C = \frac{A_{contact}}{A} = \frac{1}{x_c(P+1)}\frac{\int_0^{z_c} 2l(z)dz}{z_c} = \frac{1}{x_c(P+1)}2\bar{l} \qquad (9.17)$$

This relationship connects the dark/light fill factor C of the image frame to the mean contact width $2\bar{l}$.

The fill factor of a frame can be measured by converting a grayscale image to a black and white image by thresholding. The typical objective in choosing a threshold value is to separate data at the exact point that minimizes the variance within each of the two subsets.

To avoid a brute force approach to finding these two subsets, Otsu shows·that minimizing subset variance is identical to maximizing interset variance [77]. Otsu goes on to show that this dual of the problem can be accomplished in a single pass through a histogram of the pixel values, resulting in a fast and efficient thresholding algorithm.

The result of Otsu's method is shown in Figure 9-6a-b. The algorithm is able to clearly distinguish contact in the center of the image where the image is in sharp focus and the lighting is uniform. However, near the edges the algorithm gives incorrect results due to inconsistent lighting, poor focus, and vignetting. This difficulty is evident in a histogram of the pixel data (Figure 9-6c), where a poor signal-noise ratio is evident in the pixel data.

This thresholding measurement technique works quite well when lighting is uniform, the image is in focus, and the pixel resolution is sufficiently high to resolve each feature. In practice, this method was limited to a region of interest in the center of the image with good focus and uniform lighting for reliable results.
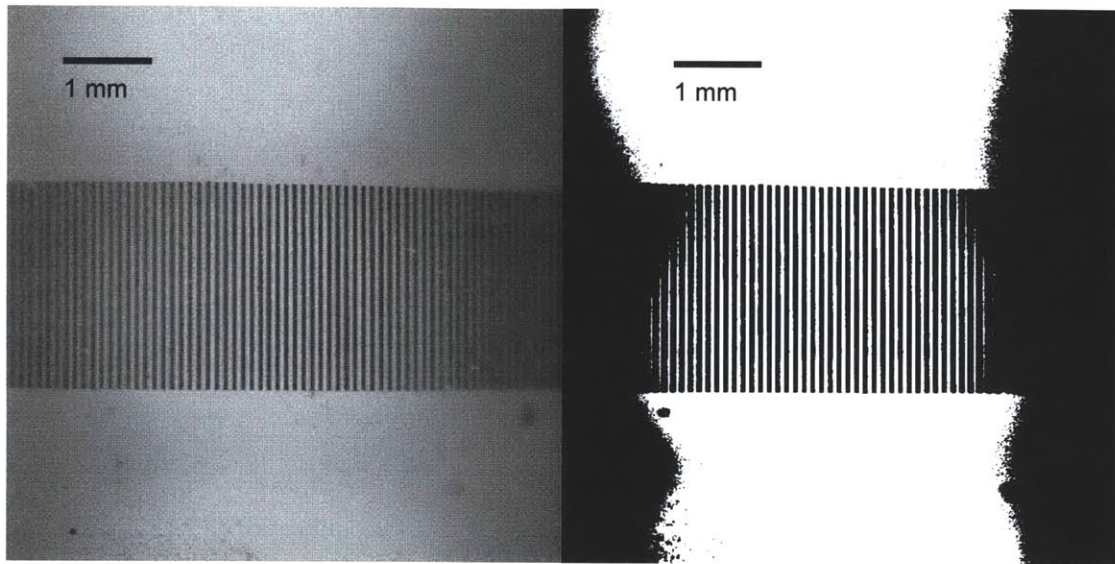
(a)   (b)
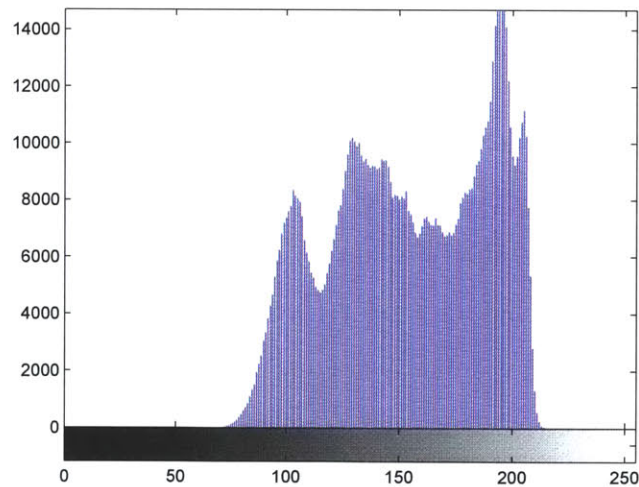
(c)

Figure 9-6: Thresholding method of contact measurement. The contact length in a raw image (a) can be measured by thresholding the image (b) and relating the resulting fill factor to the contact length as described in the text. This method works well when the pixel data is bimodal, but is not robust when the modes are not well separated (c) (i.e. low signal-to-noise ratio), such as caused by nonuniform lighting or vignetting.

9.3.2 Edge Finding

Edge finding techniques can be used to identify the extrema of the contact region, in contrast to the exact contact pattern within a region. The extrema of the contact region will be the edge, or point of maximum intesity gradient, in the image. An advantage of this technique is that it will work even when the features are smaller than the sensor pixel resolution, or even when they are smaller than the diffraction limit of light. Contact of these very small features will still impact the average degree of reflection within the observation prism, giving areas of lighter and darker intensity in the raw image.

The maximum gradient in images can be found by convolving the image data with a discrete gradient operator. In the case of Sobel edge detection, a 3×3 operator is convolved with the image I to find the z and x gradients:

$$\boldsymbol{G_z} = \left\{ \begin{matrix} -1 & 0 & +1 \\ -2 & 0 & +2 \\ -1 & 0 & +1 \end{matrix} \right\} * \boldsymbol{I} \tag{9.18a}$$

$$\boldsymbol{G_x} = \left\{ \begin{matrix} -1 & -2 & -1 \\ 0 & 0 & 0 \\ +1 & +2 & +1 \end{matrix} \right\} * \boldsymbol{I} \tag{9.18b}$$

The gradient is then calculated as

$$\boldsymbol{G} = \sqrt{\boldsymbol{G_z^2} + \boldsymbol{G_x^2}} \tag{9.19}$$

The Sobel method is a fast way of finding edges in an image, indicated by bright areas in $\boldsymbol{G}$. More sophisticated filters use larger kernal functions during the convolution that provide low pass filtering of high frequency pixel noise, for example for example Canny edge detection [10]. The disadvantage of these more sophisticated approaches is the large computation time required.

Measuring the stamp contact width does not require specific knowledge of the local

contact pattern, or even the gradient G_z. In this specific case of examining mean contact width $2\bar{l}$, a meaningful measurement can be extracted from the aggregate pixel data averaged along the roll axis $\hat{z}$, obtained by summing along z:

$$I^*(j) = \frac{1}{n}\sum_{i=1}^{n} I(i,j), \qquad \forall j \tag{9.20}$$

The problem is now reduced to edge finding in a one-dimensional vector I^*, which is much faster computationally that edge finding in a two dimensional array of pixels.

The edges corresponding to the contact width are difficult to discern when the contact pattern is highly periodic in the y direction. The periodic contact pattern creates a number of higher frequency variations in image intensity that have a gradients similar to the contact perimeter.

High frequency variations can be countered by using a low pass filter in conjunction with the gradient operator; see for example the convolution kernals suggested by [10]. A similar operation can be achieved using a linear filter.

Using a bandpass filter will provide a smoothed gradient with attenuation of high frequency content. This can be achieved by combining a differentiator with two poles at the bandpass frequency:

$$F(s) = \frac{s}{(\frac{f}{2\pi}s + 1)^2} \tag{9.21}$$

In the case of a periodic stamp pattern, the bandpass filter should accept frequencies at the contact scale of millimeters but reject frequencies at the pattern scale of microns.

In implementation, the filter in (9-5) is converted to the discrete domain with a sampling period T of 1 pixel (with break frequency f also in units of pixels). This filter is then applied to the aggregate image vector I^*, where the minimum and maximum points in the result give the contact edges in the original image.

This approach (aggregating data and finding the mean edge location by filtering) is illustrated in Figure 9-7. The aggregate intensity and filtered results are plotted to

illustrate the effect of the filter (9.21). Finally, the minimum and maximum points are annotated on both the filtered result and the original image.

(a) (b)
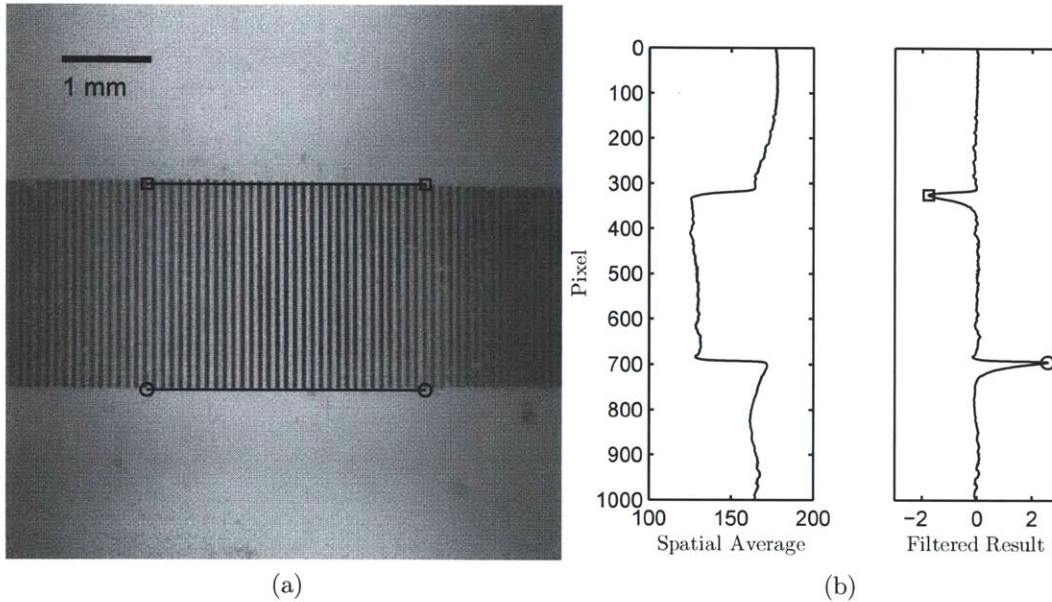
Figure 9-7: Example of contact measurement using edge finding. The raw image (a) is processed to find mean pixel values across the area of contact (b). Using a bandpass filter on this spatial average is able to easily identify the contact edges, even in the case of nonuniform lighting where the thresholding method fails.

In a second example, the filter is applied to a sparse hexagonal pattern with very small line features (Figure 9-8). Because P is large for this pattern, the signal-to-noise ratio is much smaller and thresholding methods would fail. The periodic nature of the pattern results in sharp gradients in the contact region. The filtered result is able to correctly identify the contact edges.

In each of these examples (Figures 9-7 and 9-8) the linear filter F (9.21) results in some finite level of phase shift (the contact edges are slightly lower in each image than the human eye would naturally identify). The relative distance between each edge is still maintained. A convolved kernel (e.g. [10]) would eliminate the phase shift, but require a more intense computation.
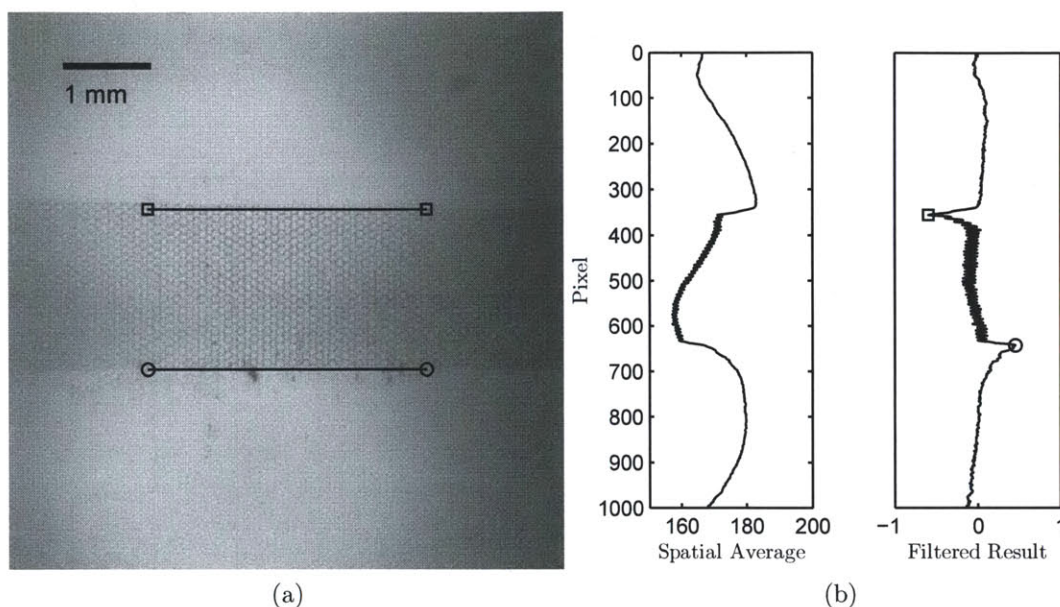
Figure 9-8: An example measuring the contact width of a stamp pattern (a) that is periodic along the direction of filtering. This example highlights the importance of using a bandpass filter F that identifies edges at the scale of the contact length rather than at the scale of the feature pattern. The contact edges are correctly identified despite the poor signal to noise ratio observed in the spatially averaged data (b).

9.3.3 Robustness

Each of the measurement methods proposed breaks down when features collapse or the stamp looses contact with the substrate. For example, stamp features with $P > 1$ will create a more significant signature during roof collapse than during ideal contact. To illustrate this phenomenon, Figure 9-9 shows the edge detection method applied to a hexagonal pattern exhibiting collapse. This example shows incorrect identification of the collapse boundary rather than the contact boundary.
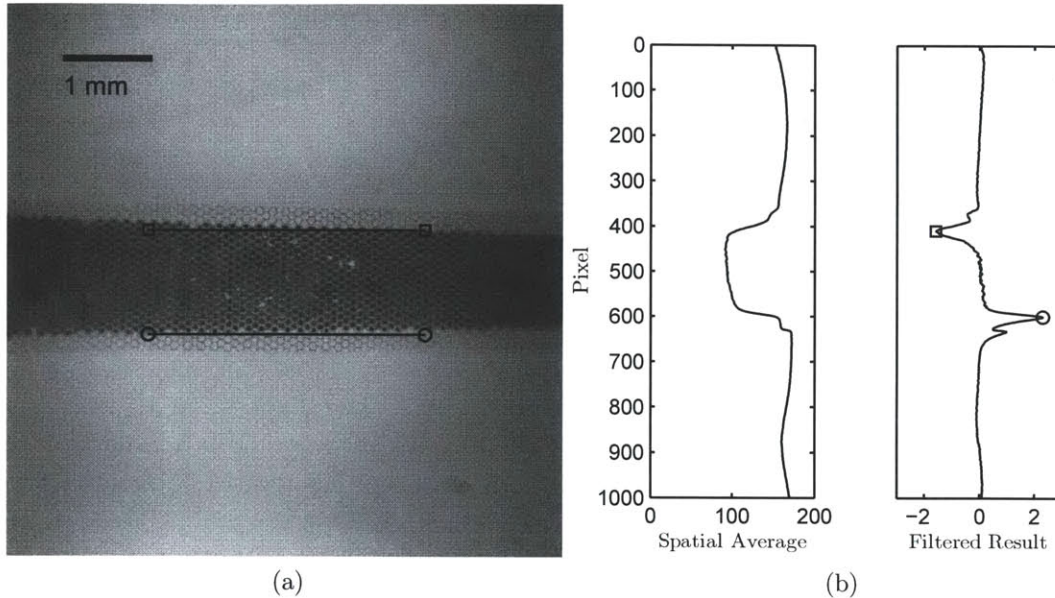
Figure 9-9: The contact measurement methods are only robust within a certain range of contact behavior. For example, when a sparse stamp collapses (a), the edge finding algorithm will incorrectly identify the edges of the collapse region (b) rather than the contact region. This error occurs the collapsed features have a stronger signature than uncollapsed features.

9.4 Contact Feedback Control

The camera images can be used not only for metrology, but also as an online control tool. If some characteristic of the contact area can be extracted with sufficient computational speed, that characteristic can be used a control variable.

A control architecture using camera images for feedback compensation is shown in Figure 9-10. The objective of this feedback compensation is to regulate contact area, and thus presumably contact integrity.

In this design, the plant consist of two elements: the roll positioning stage and the stamp, which are separated for the purposes of discussion. The positioning stage G_p has a transfer function defined by the closed loop dynamics of the servo controlled roll positioning stage. The stamp dynamics G_s relate the position to contact behavior.

The control task is thus to use the contact images to decide the position reference of the roll positioning stage. The camera images are passed through a filter F to
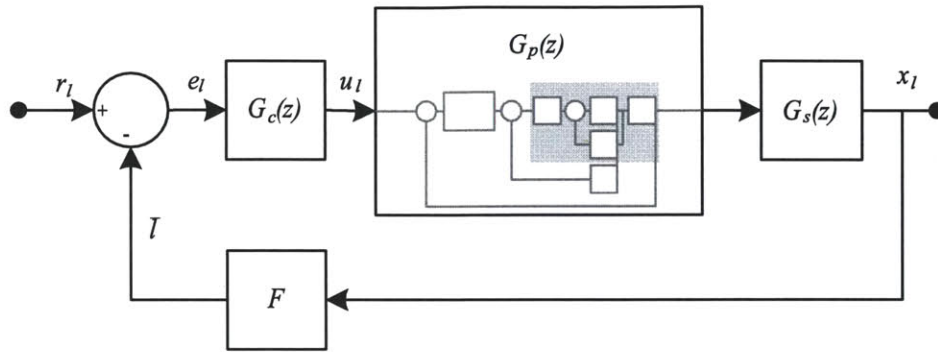
Figure 9-10: Block diagram of contact feedback control. The plant G_p is assumed to be the servo controlled roll positioning stage, where the roll position is related to the contact length x_l by stamp dynamics G_s. The image filter F is applied to the contact region images to supply the mean contact length $\bar{l}$ as a feedback signal.

determine the contact length l. The error e_l is calculated and passed through a controller G_c, which provides the control effort u_l. In this architecture, u_l is a vector that sets the position reference r for the positioning stage.

The primary design tasks are identification of the plant dynamics, the choice of filter F, and design of controller G_c. A discrete time sampling strategy will be assumed throughout, adopting the camera frame rate (10 fps) as the control clock.

9.4.1   Plant model

The positioning bandwidth of the stage is well over the camera bandwidth (35 Hz compared to 10 Hz) and the stage settling time is much less than $T=100$ ms (Figure 8-5). This justifies assuming that $G_p(z) = 1$.

Similarly, the stamp transfer function G_s is assumed constant, assuming that viscoelastic effects in the stamp have a negligible influence on contact area.

The gain of G_s is determined using the contact models from Part II of the thesis. It was shown that for large features, the contact length is given by

$$l = \sqrt{2r^*\delta} \tag{9.22}$$

304

This relationship is linearized by

$$l = l(\delta_0) + \frac{dl}{d\delta}\bigg|_{\delta_0}(\delta - \delta_0) \tag{9.23}$$

giving

$$l = \sqrt{2r^*\delta_0} + \sqrt{\frac{r^*}{2\delta_0}}(\delta - \delta_0) \tag{9.24}$$

and the system gain about the operating point δ_0 is

$$\frac{dl}{d\delta} = \sqrt{\frac{r^*}{2\delta_0}} \tag{9.25}$$

Often the specific displacement of the roll δ_0 is unknown, in which case the system gain can be written as a function of the operating contact length l_0:

$$\frac{dl}{d\delta} = \frac{r^*}{l} \tag{9.26}$$

Using a 25.4 mm radius roll gives a system gain of 25 mm/mm for a nominal contact length $2l_0 = 2$ mm.

9.4.2 Controller design

Image filter F was implemented as a thresholding measurement. In effect, this provides a spatial filter where localized contact defects do not appreciably influence the overall contact measurement.

Pure integral control can be used to (theoretically) achieve settling in a single time period when the system appears constant with respect to the discrete sampling period T. In the discrete z domain, this gives a compensator

$$G_c(z) = K\frac{z}{z - 1} \tag{9.27}$$

Using this compensator gives a closed loop transfer function

$$\frac{l(z)}{r_l(z)} = \frac{K\frac{z}{z-1}G_pG_sF}{1 + K\frac{z}{z-1}G_pGsFz^{-1}} \tag{9.28}$$

$$\frac{l(z)}{r_l(z)} = \frac{KG_pG_sFz}{z - 1 + KG_pG_sF} \tag{9.29}$$

l/r_l has a closed loop zero at the origin and a closed loop pole at $(1 - KG_pG_sF)$. The closed loop response will appear instantaneous if this pole is placed at the origin by setting $K = (G_pG_sF)^{-1}$:

$$\frac{l_i(z)}{r_{l,i}(z)} = \frac{(G_pG_sF)^{-1}G_pG_sFz}{z - 1 + (G_pG_sF)^{-1}G_pG_sF} = 1 \tag{9.30}$$

Values of K slightly lower or higher will result in a slower rise time or overshoot, respectively.

The compensator implementation becomes clear after dividing by z

$$G_c(z) = \frac{u_l}{e_l} = K\frac{1}{1 - z^{-1}} \tag{9.31}$$

and rearranging the transfer function

$$u_l = u_lz^{-1} + Ke_l \tag{9.32a}$$

$$u_{l,t} = u_{l,t-1} + Ke_{l,t} \tag{9.32b}$$

Finally, these controller efforts must be converted to the reference variables (y and θ) for the stage position. This can be accomplished using a linear transformation similar to (7.24):

$$\begin{bmatrix} y \\ \theta \end{bmatrix} = \begin{bmatrix} 1/2 & 1/2 \\ 1/l_c & -1/l_c \end{bmatrix} \begin{bmatrix} u_{l1} \\ u_{l2} \end{bmatrix} \tag{9.33}$$

where l_c is the distance between the camera viewpoints (about 50 mm).

9.4.3 Experimental Results

The camera control loop was implemented on the same Dell T7500 PC that controlled the positioning stage. The USB cameras were interfaced using drivers and an application programming interface (API) supplied by the camera manufacturer (DinoLite). A single Windows program was written in C++ to execute all of the control loops; multiple program threads and CPU cores were used for parallel camera frame acquisition at (sampling frequency 10 Hz), image processing, and stage position control (sampling frequency 10 kHz).

The camera controller G_c was tuned by starting at the calculated value of $K = (FG_pG_s)^{-1} = .04$ and adjusting K until an appropriate step response was achieved. Settling time was less than one second; a single step settling time could not be achieved because the system elements are not entirely static as modelled.

Two sets of data were taken using a stamp with $w = a = h = 50$ μm and a substrate speed of about 1 mm/s. In the first data set, the roll position was held constant and the camera images used simply to measure the observed stamp contact behavior (Figure 9-11a). In the second data set, the compensator G_c was activated and the roll position was actively modulated depending on the image information (Figure 9-11b). In both data sets, the same roll and substrate registration was maintained, allowing comparison of the two data sets.

These results demonstrate a clear improvement using closed loop process feedback control. The contact area is well regulated in the closed loop case. Disturbance rejection is quite clear: in the open loop case the maximum contact area occurs at a stage position of 12 mm; this corresponds to the control effort u_l maximum at 12 mm in the closed loop case.

These results also support earlier predictions of very high sensitivity of the contact region to displacements. While the open loop data shows significant variations in contact area, the closed loop data shows that changes of only single microns were required to maintain a uniform contact area.
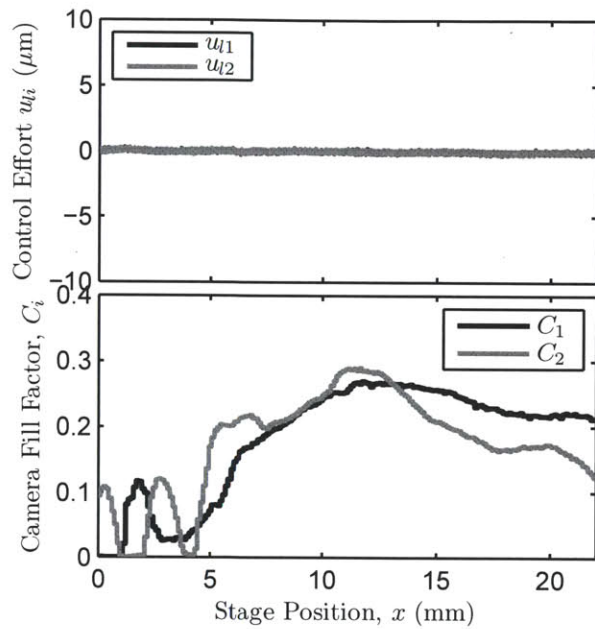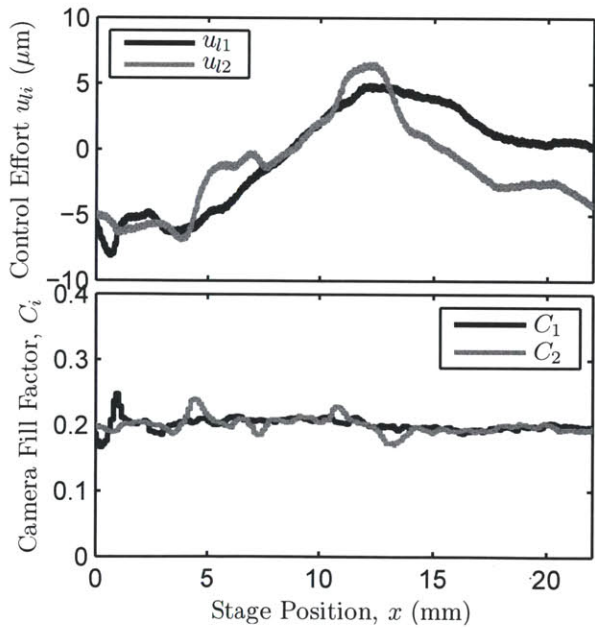
Figure 9-11: Contact feedback control results. (a) Contact behavior of a stamp in open loop (constant roll position operation) is erratic with large variations in contact area. (b) Closing the loop with control efforts u_{li} effectively regulates the contact behavior. Notice that the control effort in (b) tracks the behavior of the contact area in (a) to attenuate errors.

9.5 Impedance Control

Impedance control is investigated as an alternative method of regulating contact behavior. Compared to the prior method, which used contact images to determine changes in roll position, this method uses mechanical feedback between the roll, stamp, and substrate to determine roll position. In essence, all stiffness is intentionally removed from the processing equipment so that the roll can 'float' over the substrate.

9.5.1 Controller Design

The objective in servo control is to create a very stiff plant (with high mechanical impedance) that rejects disturbances to maintain a particular position trajectory. In contrast, impedance control uses feedback compensation to alter the dynamical characteristics of a plant, sometimes to create very low mechanical impedance. This form of control can make the plant appear to be an altogether different mechanical system. Applications are typically in robotics or haptics, where the interaction of a manipulator with the environment is very important for performance.

Feedback compensation for obtaining a particular plant impedance must satisfy the same stability criteria as any other feedback system, namely, poles must remain in the left half of the imaginary plane. Attempting to remove *all* stiffness and damping from a system will likely cause instability when unavoidable parameter variations result in apparent negative stiffness or damping. Attempting to alter the apparent inertia of a system is also quite difficult and unreliable unless accelerometers are included in the sensor design.

In this impedance control design, a feedback scheme is used that cancels out all stiffness in the machine. For stability, the damping and inertia are not altered.

The same EA method presented in Chapter 8 can be used to implement force control. By creating a low impedance mechanical plant, a reference force u_r can be superimposed on the actuators to create a constant-force controller (Figure 9-12). Operating the machine in this mode allows precise measurement of the force-

displacement relationships in roll based processes.
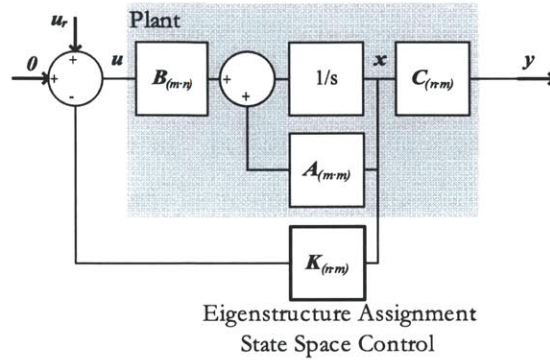
Figure 9-12: Controller architecture for impedance control of the roll positioning stage. Full state feedback matrix K is used to alter the dynamical characteristics of the plant with a zero reference. In this linear system, an external reference force u_r can be superimposed as a disturbance to provide a constant force to the printing interface.

The diagonal nature of the system equation (7.28) again makes Eigenstructure assignment simple. In this example, no attempt is made to alter the inertia or damping of the system. The damping is light and guarantees that the Eigenvalues of the closed loop system lie in the left half plane; attempts to remove both stiffness and damping results in feedback that is not robust to small parameter changes. The feedback matrix K is determined by examination of (8.4) and setting K_{11}, K_{13}, K_{21}, and K_{23} to cancel the machine stiffness components k_i.

This feedback matrix was implemented in the hardware. Impedance measurements (Figure 9-13) were made between y and u_r, demonstrating sufficiently low impedance for accurate experimental measurements of quasi-static contact behavior.

The accuracy of the applied force between the roll and substrate is dependent on the linearity and repeatability of the machine itself. In Section 7.3.4, the repeatability of the stage was shown to have a non-negligible low frequency variability (Figure 7-15). To address these long time scale parameter variations in the machine, a calibration procedure (similar to that described in Section 7.3.4) was run before each experimental set. The exact feedback matrix stiffness coefficients K_{ij} were determined from this
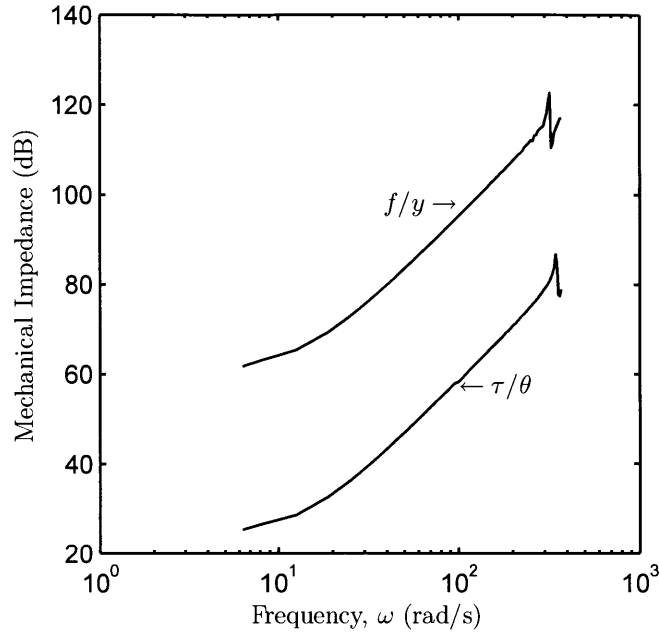
Figure 9-13: Experimental measurements of roll impedance using a swept sine method between u_r and y (units of N/m). The data show that the roll behaves as a pure mass (impedance slope + 20 dB/dec) after implementing feedback compensation to eliminate the flexure stiffness. High frequency dynamics are observed at about 300 rad/s and damping, stiffness, or parameter variations maintain a finite impedance at low frequencies.

calibration data by minimizing ϵ in (7.34).

Neglecting inertial effects, this roll control strategy results in a uniform contact force at the stamp interface regardless of substrate height. The roll is able to 'float' over step changes in substrate height, or equivalently reject displacement disturbances.

9.5.2 Experimental Results

Two experiments were performed using a 500 μm thick stamp with the honeycomb pattern shown in Figure 5-12. In each experiment, a force of 5 N was superimposed on the roll and the substrate was moved at a rate of 3 mm/s. The camera frames were not used for feedback, but rather recorded and measured using the edge finding

311

filter developed in this chapter (9.21).

In the first experiment, the stamp was mounted directly to the roll and traversed over the substrate. The results (Figure 9-14) show very good regulation of the contact area and automatic adjustment of the roll height through several μm of displacement.
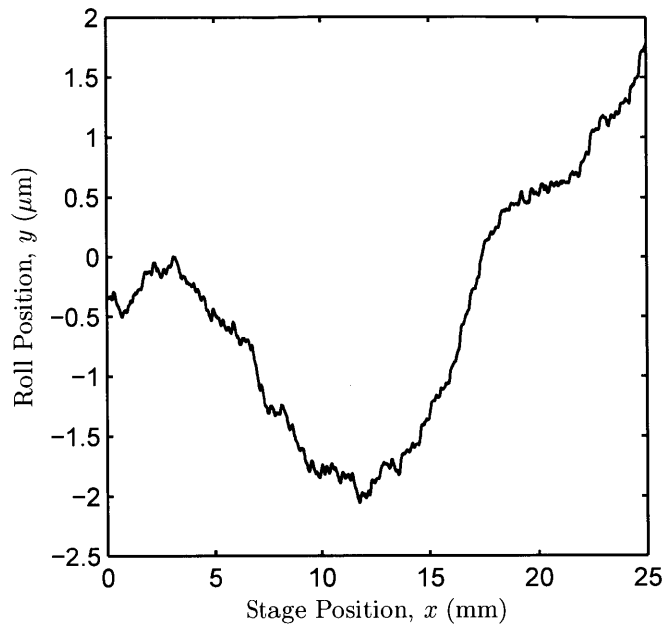
(a)
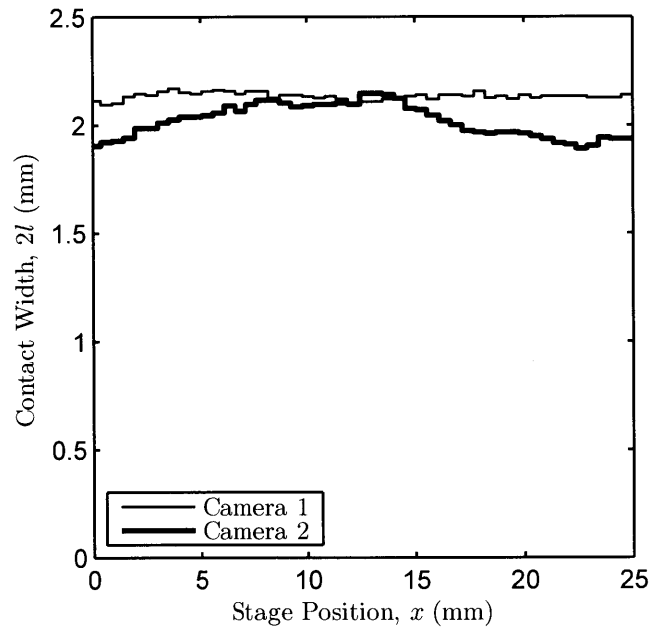
(b)

Figure 9-14: Impedance control experimental results showing (a) roll position and (b) contact area over a 25 mm range of substrate travel. These data show very good regulation of the contact area and automatic adjustment of the roll height over a ±2 μm.

313

In the second experiment, a piece of adhesive tape was mounted between the roll and stamp (Figure 9-15). The tape created a step disturbance about 40 μm high and 10 mm long.
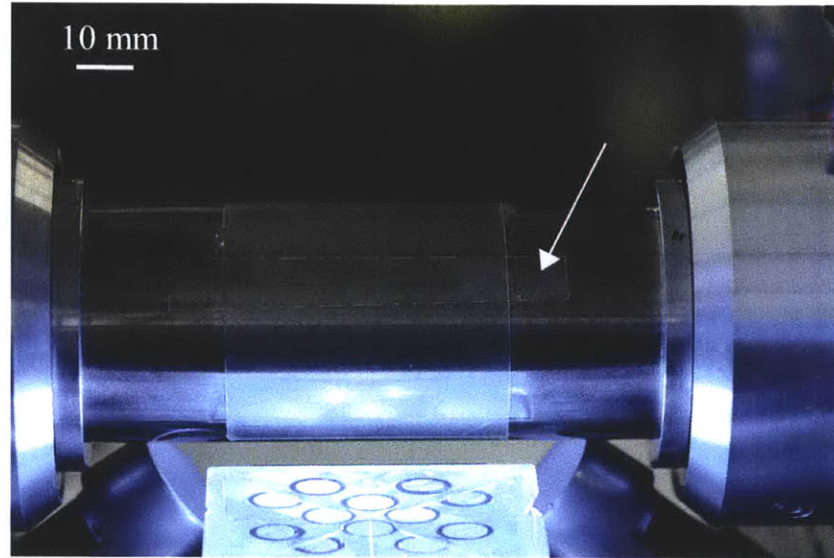
Figure 9-15: Impedance control disturbance rejection experiment. A piece of tape (arrow) was mounted between the stamp and roll to simulate a 40 μm step disturbance about 10 mm long.

The same impedance control experiment was repeated with a 5 N preload force on the roll. The results (Figure 9-16) clearly show the roll height moving over the disturbance. The contact area is well regulated with small dynamic effects evident at the step height changes.
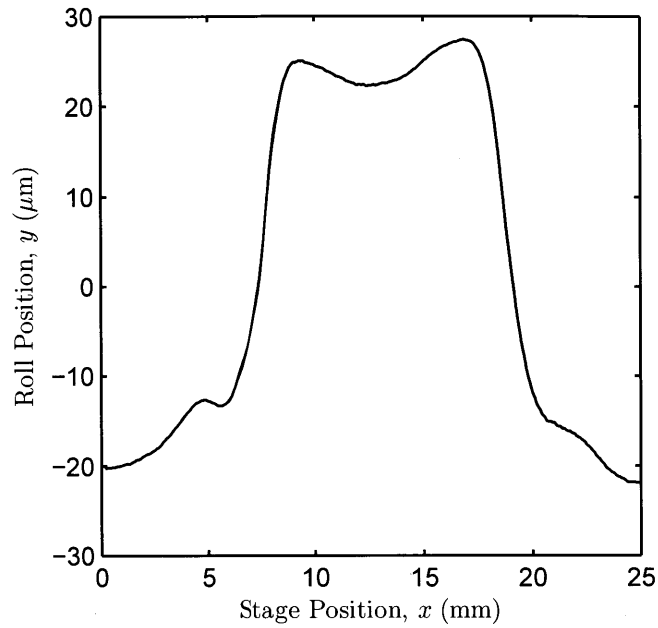
(a)
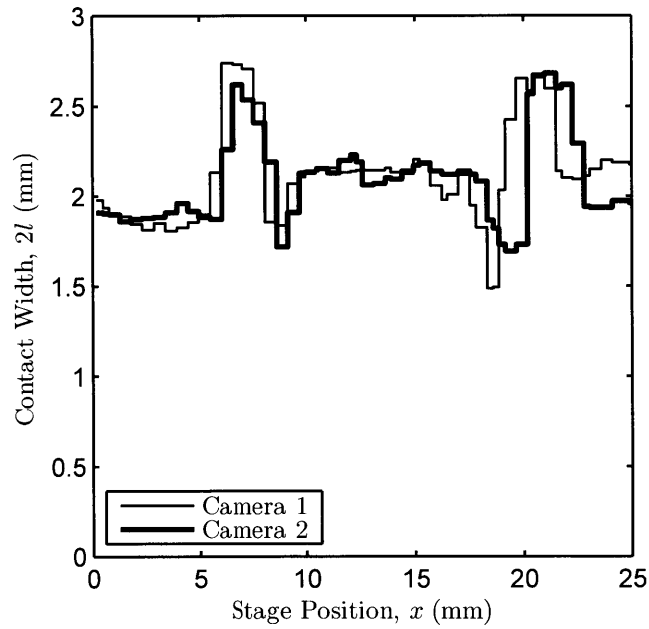
(b)

Figure 9-16: Experimental results of impedance control step disturbance rejection, showing (a) roll position and (b) contact area over a 25 mm range of substrate motion. The position of the roll clearly changes by about 40 μm over a range of about 10 mm as the 'step disturbance' is encounted. The contact area measurements show excellent disturbance rejection and contact area regulation, with some dynamics at each step location. No feature collapse was observed during the experiment.

The repeatability of the impedance control was outstanding. The substrate traversed and reversed under the roll a total of four times, plotted in Figure 9-17. The roll motion between passes replicated within 500 nm.
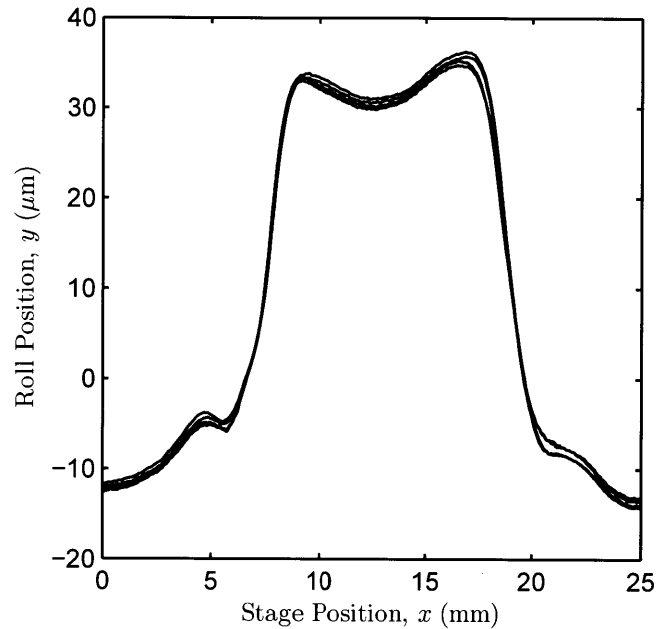
Figure 9-17: Repetition of the impedance control experiment over the same stamp-substrate contact region four times (the roll traversed forward and reverse twice). These data show very repeatable performance of position and contact area.

No collapse was evident at any point in the experiment despite the 40 μm step change, an exceptional observation given the fact that the fragile honeycomb pattern collapses at only a few microns of displacement. This demonstrates the ability of an impedance control strategy to effectively maintain a very sensitive contact area despite disturbances nearly an order of magnitude larger than the process window.

9.6   Summary and Outlook

Two control strategies were demonstrated in this chapter: (*i*) a feedback control method using contact images as a feedback variable for servo control and (*ii*) an impedance control method that regulates contact by maintaining a regular force.

Both were shown to regulate disturbances.

While a powerful experimental tool, the contact imaging approach is perhaps impractical in the demonstrated embodiment. This approach is essentially a brute force method of examining the contact region and making a position correction. The controller architecture is relatively complex. The image processing problem is nontrivial; the two methods of contact measurement shown are not particularly robust outside of a certain contact window (i.e. loss of contact or feature collapse). Finally, the physical arrangement of cameras viewing the contact interface is not possible in a general implementation of roll based printing.

In contrast, the impedance control strategy is simple and elegant. The controller architecture and implementation are far simpler; the only requirement is a linear and repeatable machine design. This control strategy is robust to phenomena like loss of contact and feature collapse. At very large scales the inertia of the processing rolls could require impedance control that alters the apparent inertia of the system.

One must acknowledge the host of other control requirements in a full scale roll-to-roll system. While this editorial has discounted vision systems as an immediate measure of contact integrity, they will likely be instrumental in detecting low frequency temporal drifts (i.e. fundamental limitations in machine accuracy), detecting inter-layer registration, or detecting the ink or thiol quality. While it may be difficult to directly examine the stamp contact region, vision systems mounted inline with the process and shortly downstream of the roll equipment can detect phenomena with a periodicity of the roll circumference, and then feed these back to the roll manipulation stage.

Ultimately, this chapter has demonstrated two feasible process feedback control techniques. It is likely that a successful manufacturing scale implementation will require perhaps a combination of at least these two methods to compensate for errors at different spatial and temporal scales.

317

Part V

Conclusion

Chapter 10

Conclusion

This thesis has examined stamp contact in roll based soft lithography. This final chapter assesses the unique contributions of this thesis, especially with respect to advancing the understanding in the field. This thesis has focused primarily on the ability to achieve and maintain faithful and robust stamp contact; a discussion is provided on the future extensions of this focus and the remaining challenges that lie ahead before manufacturing scale implementations of roll to roll lithography are likely to be realized. In closing, some comments are provided on the outlook of large area contact lithography.

10.1   Contributions

10.1.1   Stamp Deformation

The examination of stamp feature deformation in Chapter 3 of this thesis represents the first time that the stiffness of PDMS microfeatures have been systematically characterized. The rigorous development of a set of dimensionless parameters allowed exploring and characterizing the full design space of microfeatures.

These dimensionless number also provide a convenient and intuitive method of categorizing stamp defects to guide stamp design. Before this work, the most comprehensive and widely cited work on stamp collapse modes was that by Hui et al.

[47]. In this report, collapse boundaries were characterized by a series of dimension-less constraints κ that must not be violated. Unfortunately, these κ had no common meaning and did not bound an intuitive design space, such as feature aspect ratio. Using the dimensionless parameters in this thesis, namely pattern ratio P and aspect ratio A, collapse can be analyzed in term of intuitive parameters that translate directly to stamp design variables (Figure 3-24).

The individual models of feature collapse extend or improve upon those previously reported in the literature. In the case of lateral collapse, Timoshenko beam theory is used to explain the behavior of very low aspect ratio features (especially important at the nano-scale) and the correct cantilever beam deformation mode is identified through empirical observations (something missing in the purely analytical approach of [47]). Buckling models are augmented with a work of adhesion to explain the delayed buckling observed in experimental data. Most importantly, the limits between very large and very small aspect ratios were bridged to explain phenomena near practical aspect ratios of unity, a regime ignored in other studies.

The systematic study of microfeature stiffness allowed addressing the larger scale problem of roll-based stamp deformation. Results from classical contact mechanics were augmented with the specific load-displacement behavior of features to explain the behavior of soft elastomeric stamps mounted to rigid roll processing equipment.

The excessive contact pressures that develop in thin incompressible elastomeric stamps during roll contact is one of the core findings of this thesis. Moreover, these pressures can develop at single microns of roll displacement. This high sensitivity has not been clearly developed or explained in existing literature regarding roll based processing, and represents significant challenges from the perspective of robust man-ufacturing processes and precision machine design.

10.1.2   Stamp Design and Manufacture

The results developed from studying stamp deformation allowed developing a process model and exactly quantifying permissible contact pressures and roll displacements (5.12). This process model can guide machine and process design based on the funda-

322

mental physics of the printing process. Moreover, developing this model of permissible deformation allows straightforward determination of parameter sensitivity for robust stamp design.

The discussion in Section 5.2.2 shows that after designing robust features, the only remaining design variables are stamp thickness and stamp material. These design variables are shown to be bounded by several factors, limiting the ultimate process window that can be obtained for any particular stamp.

The limitation on ultimate process window motivated invention of an improved stamp architecture that includes a set of backing features at the stamp-roll interface. This set of features can be tailored to create a more compliant stamp construct that can absorb significantly more mechanical energy during contact before feature collapse, permitting both higher loads and greater displacements. Figure 5-13 summarized the results of a case study supporting this conclusion. Using this stamp architecture greatly desensitizes the stamp from disturbances with midrange spatial frequencies (Figure 5-2).

Stamp casting and mounting is one of the primary sources of dimensional errors in the contact zone: any imperfections in the stamp or mold are transferred and superimposed on the stamp features in the roll contact region. A new stamp casting process was invented to create a more uniform stamp in an inherently scalable manner. Using a centrifuge-based process, stabilizing fluid dynamics can be exploited to create very uniform layers of photoresist and PDMS precursor.

A prototype machine was constructed to demonstrate feasibility of this centrifugal stamp casting process. A laser was incorporated for direct-write patterning of microfeatures in photoresist. In initial demonstrations with this machine, 10 μm features were created on the surface of cylindrical PDMS stamps, which had a thickness uniformity of better than 10 μm out of 1 mm.

Future implementations with more precise motion stages, larger numerical apperature optics, and lower centrifuge runout should be able to create continuously patterned submicron features in stamps with single micron thickness uniformity. This cylindrical stamp casting process holds the potential to revolutionize microcon-

tact printing, but also other contact lithography processes like nanoimprint lithography (NIL) and self aligned imprint lithography (SAIL).

10.1.3 Process Control

A means of actuation is a requisite component for process feedback control. A new roll positioning stage was designed that can manipulate a simply supported roll with submicron resolution. The high precision and linearity of this stage were instrumental in making experimental measurements of roll based stamp contact.

A new control architecture and decoupling criterion $\mathcal{DC}$ (8.3)were developed for servo control of two-input, two-output MIMO systems. This architecture and synthesis technique were applied to the parallel kinematic roll positioning stage to achieve 35 Hz closed loop bandwidth. This bandwidth is well above that required to compensate for periodic errors in high speed (1 m/s) roll processing.

Two methods of regulating contact behavior were demonstrated. The most promising method uses the roll positioning stage in an impedance control mode, which allows the roll to 'float' over any asperities in the substrate. This control strategy effectively reverts from position control to pressure control, where the mean contact pressure is regulated (though asperities can still cause local collapse). The impedance control strategy was shown to effectively reject severe step disturbances on the order of 40 μm with out collapsing very sensitive stamp patterns (Figure 9-16).

These machine and control designs provide guidance for future implementations of roll based microcontact printing, including both next generation laboratory machines and full scale manufacturing implementations.

10.2 Design Example

This section uses two design examples to demonstrate the utility of the results reported in this thesis. First, a general design approach is developed drawing from results throughout the thesis. Second, separate examples of a submicron pattern (perhaps for an optical or mechanical metasurface) and a pattern with features at

different scales (such as that found in electronics) are examined using the design approach.

10.2.1 Design Approach

The goal in stamp design is to create an architecture that minimizes the sensitivity of feature collapse to roll displacement subject to constraints including feature distortion and roll bonding. The design problem can be decoupled into three separate stages to determine the printing feature aspect ratio, stamp body thickness, and backing feature pattern:

The contact pattern of printing features is determined by the desired pattern transfer, leaving the feature height (or aspect ratio A) as the only free design variable. The goal in choosing the aspect ratio is to maximize the resulting collapse pressure under loading (cf Figure 5-3). The models of feature behavior derived in Chapter 3 and summarized in Section 5.2 can be used to predict collapse pressure and choose the appropriate feature height.

Next, the stamp thickness is chosen to minimize sensitivity to variations in displacement, in other words, to maximize compliance. The results of Chapter 4 show that compliance increases monotonically with stamp thickness t. Constraints due to roll adhesion (5.17) and pattern distortion (5.14) must be observed when planar stamps are mounted to rolls (Section 5.2); these requirements are relaxed when cylindrical stamps are used (Chapter 6).

Finally, the backing features are designed to maximize compliance, identical to maximizing both pattern ratio and aspect ratio. The choice of aspect ratio A and pattern ratio P are constrained by pressure uniformity, roll adhesion, and collapse pressure. Pressure uniformity can be maintained by ensuring that the pitch $(a + w)$ of the backing features does not exceed $\frac{1}{3}$ of the stamp thickness t; this creates a uniform pressure at the printing interface by Saint Venant's principle. The effective work of adhesion W_{ad}^* (4.19) of the backing features should be at least that of the printing features to keep the stamp adhered to the roll during receding contact, requiring that the pattern ratio P of the backing features not be greater than the printing

features. The collapse pressure of the backing features should be at least that of the printing features so that their effect is utilized throughout the entire process window. Combining these requirement suggests using a backing pattern that has the same pattern ratio $P = a/w$ as the printing features, but at a scale such that $a + w = t/3$.

The process window can be estimated by δ_c (5.18). The derivation of δ_c involved kinematically admissible approximations, so that a conservative estimate of the process window is expected. To implement the impedance control developed in Chapter 9, a load-displacement curve from numerical simulation or experimental data should be used to determine the appropriate contact preload u_r (Figure 9-12). The force that results in one half the collapse displacement δ_c is suggested as an appropriate choice for u_r to permit equal bilateral variations in local roll displacement before either loss of contact or feature collapse.

10.2.2 Grating Example

A grating with 500 nm line widths is representative of a pattern that may be desired for an optical or mechanical metasurface. This pattern ($a_p = w_p = 500$ nm) is difficult to print because the pattern features will be unable to absorb a significant amount of mechanical energy before collapse.

In this example, it is assumed that printing is to be performed on a flexible substrate passed between a 100 mm diameter printing roll and a 100 mm backup (or impression) roll. Each of the design steps discussed above will be performed to create a stamp that maximizes the process window δ_c while keeping pattern distortion below 0.5%.

The printing features are designed by using the results of Chapter 3 to predict the failure mode and collapse stiffness of the grating features (pattern ratio $P = 1$). The feature height h_p (and thus aspect ratio A) is selected to maximize the collapse pressure based on these predictions (Figure 10-1). The result of this design is a feature height of about 500 nm, with a corresponding collapse pressure of $0.28E_0$.

Next, the stamp thickness is determined within the required constraints. Wrapping a flat stamp of thickness t around a roll of radius r will result in a pattern strain
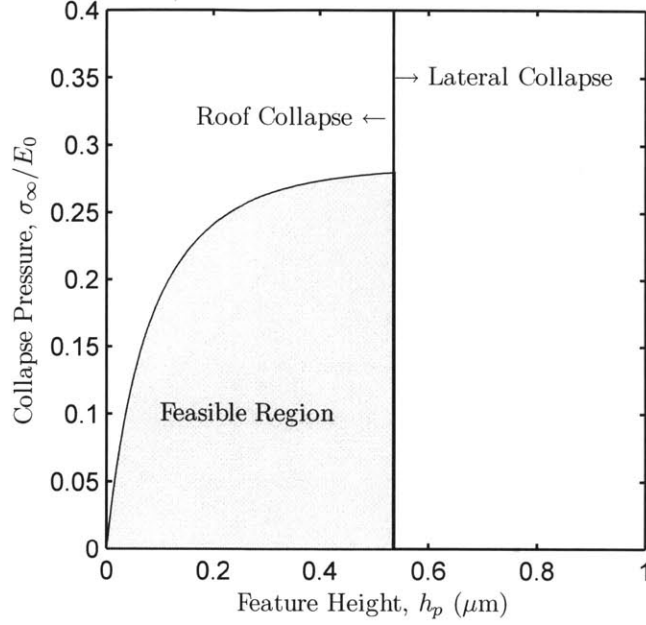
Figure 10-1: Collapse pressure σ_∞/E_0 as a function of feature height h_p for a grating pattern with $w = a = 500$ nm, assuming $E_0 = 1.5$ MPa, PDMS-PDMS $W_{ad} = 44$ mJ/m^2, and PDMS-substrate $W_{ad} = 200$ mJ/m^2. The ultimate feature height is limited by lateral collapse, where the most robust features are just over 500 nm tall and can tolerate a pressure of $\sigma_\infty/E_0 = 0.28$.

of $\epsilon = t/2r$. The maximum stamp thickness is thus 500 μm for a maximum distortion of 0.5% on a 100 mm diameter roll.

The backing pattern is designed using the guidelines developed above: the pattern ratio should be the same as the printing features and the pitch should be about one third of the stamp thickness. In this case, this requires a backing pattern with $P = a_b/w_b = 1$ and $a_b + w_b = t/3 \approx 150$ μm. These conditions call for a backing pattern with $a_b = w_b = 75$ μm. The results of Chapter 3 are again used to predict the failure mode and collapse pressure of the backing features (Figure 10-2). The height h_b of the backing features is selected as the maximum height that has a collapse pressure equal or greater than that of the printing features, in this case about 75 μm.

The full stamp design is summarized in Table 10.1, along with the predicted collapse displacement δ_c as determined by (5.18) and numerical simulation. Figure 10-
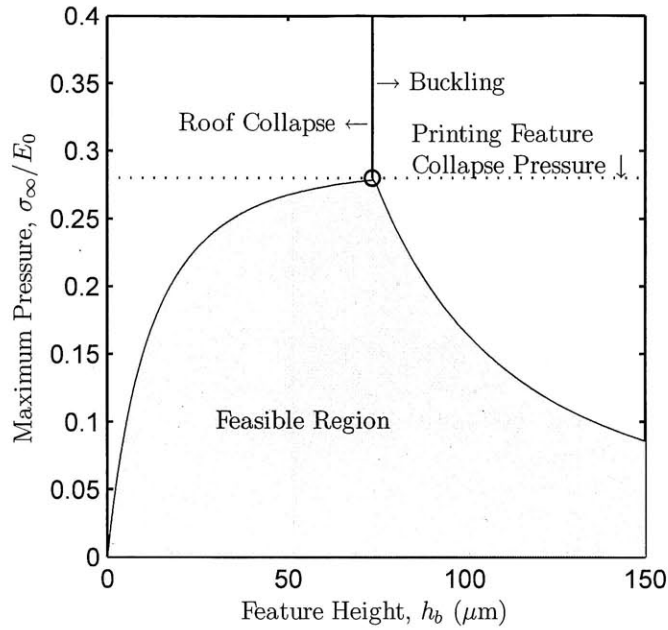
Figure 10-2: Collapse pressure σ_∞/E_0 as a function of feature height h_b for backing features with $w = a = 75$ μm, assuming $E_0 = 1.5$ MPa, PDMS-PDMS $W_{ad} = 44$ mJ/m^2, and PDMS-substrate $W_{ad} = 200$ mJ/m^2. The backing features must support at least the printing collapse pressure ($\sigma_\infty/E_0 = 0.28$; horizontal dashed curve). This criterion is met at the critical point between the roof collapse and buckling modes where the feature height is about 75 μm.

3 shows the predicted mechanical behavior of the stamp from simulation. Using the load-displacement results in the plot, a preload force of $u_r = 1.25 \cdot 10^{-4} E_0$ is selected as an appropriate operating point under impedance control ($E_0 = 1.5$ MPa gives u_r = 188 N per meter of roll length).

Table 10.1: Stamp dimensions and mechanical properties for the grating pattern design example. A backing layer is used to increase the roll collapse displacement δ_c using a thin stamp.

	Parameter	Value
Printing features	width, w_p	500 nm
	spacing, a_p	500 nm
	height, h_p	500 nm
	stiffness, K	0.36
	stiffness, k	$1.42 \cdot 10^6 E_0$ m^{-1}
	collapse mode	Roof Collapse
	collapse pressure, σ_∞	$0.28 E_0$
Stamp body	thickness, t	500 μm
Backing features	width, w_b	75 μm
	spacing, a_b	75 μm
	height, h_b	75 μm
	stiffness, K	0.36
	stiffness, k	$9.5 \cdot 10^3 E_0$ m^{-1}
	collapse mode	Roof Collapse
	collapse pressure, σ_∞	$0.28 E_0$
Process window	Collapse displacement, δ_c (5.18)	45 μm
	Collapse displacement, δ_c (simulation)	103 μm

Figure 10-3: Contact force and pressure as a function of roll displacement for the stamp designed in the grating example. Feature collapse occurs at a critical pressure of $p_c/E_0 = 0.28$, denoted by truncation of the load curves at $\delta_c = 103$ μm (marked ×). A proposed preload force is $f/E_0 = 1.25 \cdot 10^{-4}$ per meter of roll length (marked as ○), selected at half the collapse displacement.
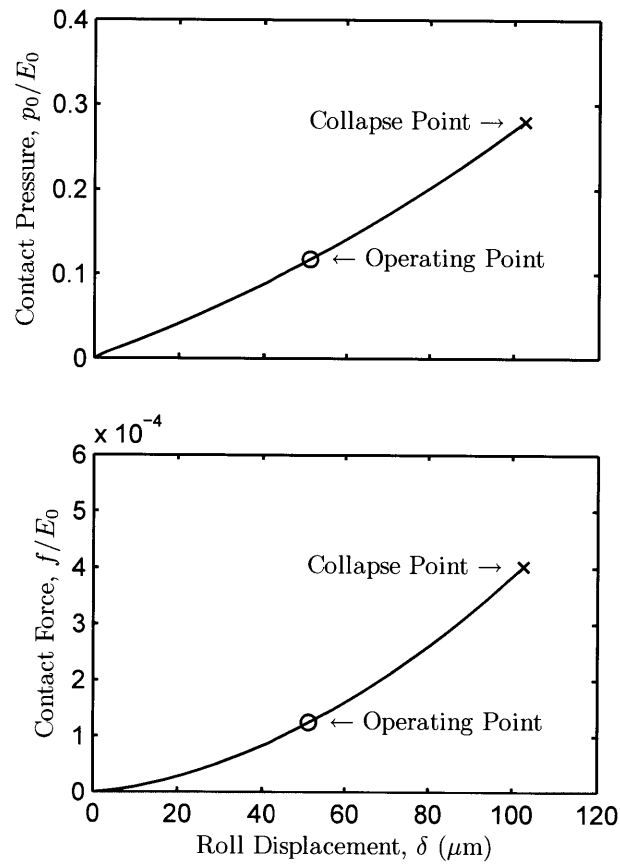
10.2.3 TFT Interconnect Example

A common application in flexible electronics is the thin film transistor (TFT). Large arrays of display pixels, sensors, or memory locations can be individually addressed with sets of horizontal and vertical interconnects. In the case of a display, selectively energizing the vertical and horizontal interconnects that address a particular pixel activates a transistor, which stores the interconnect voltage signal in a capacitor within the pixel. A typical layer of the device would include both one set of interconnects (e.g. vertical), the transistor gates, and a capacitive pad. Printing this pattern is challenging because the interconnects are very sparse pattern that will experience roof collapse at low pressures, while the transistor gates are very small with a very narrow channel between them and will be susceptible to lateral collapse. In this example, a pattern is considered that has these dual scale features: interconnects with dimensions $w_p = 5$ μm, $a_p = 45$ μm and transistor gates with dimensions $w_p = a_p = 1$ μm.

In this example, it is again assumed that printing is to be performed on a flexible substrate passed between a 100 mm diameter printing roll and a 100 mm backup (or impression) roll. Each of the design steps discussed above will be performed to create a stamp that maximizes the process window δ_c while keeping pattern distortion below 0.5%.

The printing features are designed by using the results of Chapter 3 to predict the failure mode and collapse stiffness of both the interconnect and gate features. The feature height h_p is selected to maximize the collapse pressure based on these predictions (Figure 10-4). The result of this design is a feature height of 1.4 μm, with a corresponding collapse pressure of $0.019E_0$.

Next, the stamp thickness is determined within the required constraints. Wrapping a flat stamp of thickness t around a roll of radius r will result in a pattern strain of $\epsilon = t/2r$. The maximum stamp thickness is thus 500 μm for a maximum distortion of 0.5% on a 100 mm diameter roll.

The backing pattern is designed using the guidelines developed above: the pattern

331
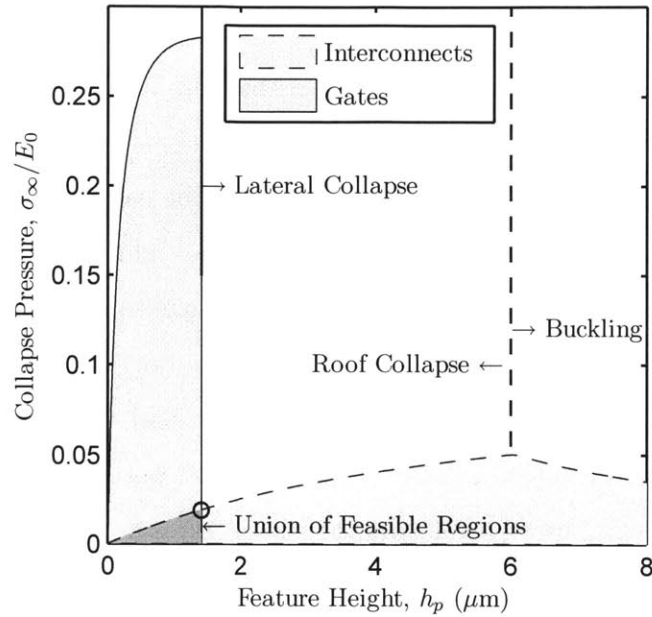
Figure 10-4: Collapse pressure σ_∞/E_0 as a function of feature height h_p for a thin film transistor gate pattern using interconnects with $w = 5$ μm, $a = 45$ μm and a transistor channel formed by gates with $a = w = 1$ μm, assuming $E_0 = 1.5$ MPa, PDMS-PDMS $W_{ad} = 44$ mJ/m^2, and PDMS-substrate $W_{ad} = 200$ mJ/m^2. The feature height is limited by lateral collapse of the smaller gate features at $h_p = 1.4$ μm. At this height the interconnects have a very low collapse pressure $\sigma_\infty/E_0 = 0.019$ (marked $\circ$), less than the maximum of 0.050 at the boundary between roof collapse and buckling.

ratio should be the same as the printing features and the pitch should be about one third of the stamp thickness. In this case, this requires a backing pattern with $P = a_b/w_b = 9$ and $a + w = t/3 \approx 150$ μm. These conditions call for a backing pattern with $w_b = 15$ μm and $a_b = 135$ μm. The results of Chapter 3 are again used to predict the failure mode and collapse pressure of these backing features (Figure 10-5). The height h_b of the backing features is selected as the maximum height that has a collapse pressure equal or greater than that of the printing features, in this case 32 μm.

The full stamp design is summarized in Table 10.2, along with the predicted collapse displacement δ_c as determined by (5.18) and numerical simulation. Figure 10-6 shows the predicted mechanical behavior of the stamp from simulation. Using the
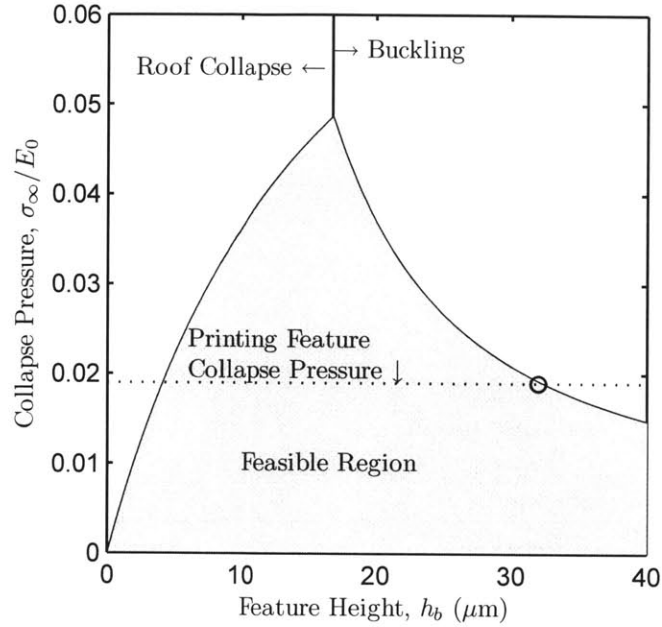
Figure 10-5: Collapse pressure σ_∞/E_0 as a function of feature height h_b for backing features with $w = 15$ μm, $a = 135$ μm, assuming $E_0 = 1.5$ MPa, PDMS-PDMS W_{ad} = 44 mJ/m^2, and PDMS-substrate $W_{ad} = 200$ mJ/m^2. The backing features must support at least the printing collapse pressure ($\sigma_\infty/E_0 = 0.28$; horizontal dashed curve). This criterion is satisfied for h_b between 4 μm and 32 μm; a height of 32 μm (marked o) is chosen for maximum backing feature compliance.

load-displacement results in the plot, a preload force of $u_r = 3.5 \cdot 10^{-6} E_0$ is selected as an appropriate operating point under impedance control ($E_0 = 1.5$ MPa gives u_r = 5.25 N per meter of roll length).

This compliant stamp design (using a backing layer) provides a process window of 12.8 μm. If the cylindrical stamp casting method developed in Chapter 6 is used, stamps of arbitrary thickness can be produced and mounted in a stress-free state. This relaxes the constraints on stamp thickness, so that for example a 3 mm thick stamp could be used with the TFT printing pattern. Even if no backing layer is used, this can provide a much larger processing window (Table 10.3). This tradeoff shows how the backing layer and cylindrical stamp casting can both be useful in creating stamps for robust printing.

Table 10.2: Stamp dimensions and mechanical properties for the TFT interconnect design example. A backing layer is used to increase the roll collapse displacement δ_c using a thin stamp.

	Parameter	Value
Printing features	width, w_p	5 μm
	spacing, a_p	45 μm
	height, h_p	1.4 μm
	stiffness, K	0.025
	stiffness, k	$1.94 \cdot 10^4 E_0$ m^{-1}
	collapse mode	Roof Collapse
	collapse pressure, σ_∞	$0.019 E_0$
Stamp body	thickness, t	500 μm
Backing features	width, w_b	15 μm
	spacing, a_b	135 μm
	height, h_b	32 μm
	stiffness, K	0.081
	stiffness, k	$2.8 \cdot 10^3 E_0$ m^{-1}
	collapse mode	Buckling
	collapse pressure, σ_∞	$0.019 E_0$
Process window	Collapse displacement, δ_c (5.18)	11.8 μm
	Collapse displacement, δ_c (simulation)	12.8 μm

Table 10.3: Stamp dimensions and mechanical properties for an alternate TFT interconnect design example. Cylindrical stamp casting is used to create a thick stamp with a large pattern collapse displacement $delta_c$ without the use of a backing layer.

	Parameter	Value
Printing features	width, w_p	5 μm
	spacing, a_p	45 μm
	height, h_p	1.4 μm
	stiffness, K	0.025
	stiffness, k	$1.94 \cdot 10^4 E_0$ m^{-1}
	collapse mode	Roof Collapse
	collapse pressure, σ_∞	$0.019 E_0$
Stamp body	thickness, t	3 mm
Process window	Collapse displacement, δ_c (5.18)	59 μm
	Collapse displacement, δ_c (simulation)	60 μm

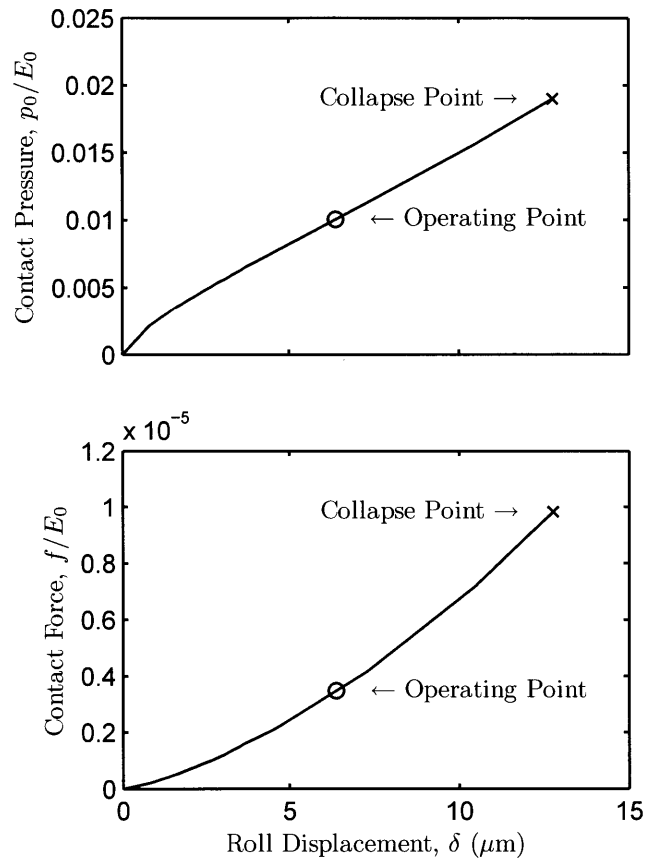Figure 10-6: Contact force and pressure as a function of roll displacement for the stamp designed in the thin film transistor example. Feature collapse occurs at a critical pressure of $p_c/E_0 = 0.019$, denoted by truncation of the load curves at $\delta_c = 12.8\ \mu$m (marked $\times$). A proposed preload force is $f/E_0 = 3.5 \cdot 10^{-6}$ per meter of roll length (marked as $\circ$), selected at half the collapse displacement.

10.3 Extensions

While the results in this thesis add significantly to understanding of roll based μCP, there are several directions in which these research approaches can be extended.

The study of microfeature behavior in Chapter 3 is limited to regular grating patterns. These grating patterns admit simpler plane strain analysis and provide a framework from which to derive general scaling laws and behavior. A logical extension of this work would be to characterize the behavior of two dimensional arrays of pillars and orthogonal lines, as would be found in superhydrophobic post arrays or grids of transistor interconnects, respectively. In the example of pillars, much of the existing analysis can be applied by replacing the plane strain modulus $E^* = E_0/(1 - \nu^2)$ with the plane stress modulus $E^* = E_0$.

A second important extension of the feature behavior models would include the effect of fluid inks. The models in this thesis have been developed using no slip boundary conditions at the stamp-substrate interface; the SAM inks used in classical μCP do not appreciably affect the surface adhesion between the stamp and substrate. An alternate and perhaps equally useful mode of printing uses the PDMS stamp as essentially a high resolution flexographic stamp to print liquid inks. The presence of a liquid at the stamp-substrate interface will dramatically change the boundary condition. Lubrication theory will show that the stamp will approach a nearly frictionless interaction with the substrate, changing the apparent stiffness and collapse modes of microfeatures. The presence of capillary forces from a liquid ink may result in new modes of collapse in very small features.

Chapter 4 develops contact pressure models that apply in the case of a rigid roll with a rigid substrate. These boundary conditions were chosen because they emulate printing on both rigid plates (i.e. display backplanes or photovoltaic cells) and flexible webs with a backup or impression roller; the latter has been shown to provide the best dimensional stability in flexography [99]. Use of a rigid impression roller makes the contact region very sensitive to disturbances; it may be advantageous to use either a very compliant impression roller or a positive wrap angle on the printing roller with

no backup roller. The analysis of contact pressure should be repeated for the cases of a compliant roller (in effect an additional elastic layer in Figure 4-6) and for a positive wrap angle on the roller (i.e. by applying a capstan model).

Chapter 5 introduces a new stamp architecture and shows that the use of a compliant backing layer can dramatically alter the stamp behavior and collapse point (Figure 5-13). This is a promising method for creating a robust printing process, but still has significant room for exploration. Use of different microfeature structures may improve the stiffness ratio of the backing layer so that it remains stiff in shear but becomes compliant in compression. As another example, there may be an optimal backing layer design for each printing pattern that depends not only on the mean stiffness k of each layer but also on the relative location of features.

Chapter 9 presents methods of contact inspection and control. New methods are needed for visualizing and rapidly evaluating the printed pattern once it has exited the contact region in a real process implementation. The new found understanding of feature stiffness and collapse points from Chapter 3 can be used to design test patterns into the final device architecture or along the edge of a flexible web to inspect for appropriate contact pressures. For example, a grating with a progressive pattern ratio P can be designed so that grating will have a corresponding progressive collapse sensitivity. Such a grating would provide a simple evaluation of the contact pressure in the rolls (i.e. the P ratio between collapsed and uncollapsed grating features would correspond to a particular contact pressure). Moreover, this approach could be designed to include microscale test patterns for inspection by optical means even if the desired device patterns are subwavelength.

10.4 Future Challenges

This thesis was motivated by noting that contact integrity is a necessary condition for printing. While this work addressed stamp contact fidelity from the perspective of modeling, sensitivity, and control, a number of other hurdles remain before a full manufacturing scale system can be realized. A turnkey printing system must provide

a means of contact actuation, stamp inking, web steering for layer registration, and online inspection.

The machine designed in Chapter 7 is capable of two degree of freedom motion to compensate for error with very long spatial wavelengths. New actuation schemes may be required that have higher spatial resolutions, for examples thermal actuation zones along the length of the roll to take advantage of the large coefficient of expansion of PDMS stamps. Other types of local actuation might be required to maintain tight control of pattern registration during printing.

Inking of thiol SAMs is quite different from inking techniques in the printing industry that are designed for fluid inks. It is possible that a similar approach can be adopted as flexography, where a separate set of inking rollers are used to apply a uniform layer of ink to the surface of the printing stamp. Bench level experiments have proven the efficacy of using a second PDMS slab as an 'ink pad' for the printing stamp [62]; this can potentially be applied to a separate inking roll.

Web steering and handling are well developed technologies. In their implementation of a roll-to-roll μCP machine, [4, 17, 56, 96, 92, 107] use off-the-shelf components for web tensioning and guiding. For precision patterning and registration, the accuracy of conventional web steering will need to be improved by at least two orders of magnitude, requiring both higher resolution sensors and actuators.

Metrology tools and techniques must be advanced to accomodate higher feature resolutions and tighter accuracy requirements. It will likely be impossible to perform 100% inspection of printed material; a significant challenge will be defining local measurements that are indicative of printing quality across a broader scale. A goal in metrology should be the development of online, real time measurement techniques that can be incorporated as a feedback control sensor in the processing equipment, similar to the optical control techniques demonstrated in Chapter 9.

10.5 Outlook

Methods of contact lithography, including μCP, NIL, and SAIL hold incredible promise for creating a new class of high speed, high resolution patterning systems. In the end, no single process will emerge as an end-all technology, advanced device architectures will require a combination of these technologies as appropriate.

The research community seems hopeful that mapping contact lithography to a roll will be simple, straightforward, and allow large area, high resolution printing with very low cost equipment. The experience gained through this thesis shows that this will be anything but a trivial endeavour.

If the ultimate goal is to achieve semiconductor resolutions, and possibly accuracies, it would be foolish to imagine roll based processing equipment any less sophisticated than the wafer steppers used in optical lithography. Achieving the desired performance is not impossible, but will require a number of innovations and engineering breakthroughs that redefine the capabilities of roll processing equipment.

Requirement will be the greatest driver: as an example, thin film transistors cannot currently be printed roll to roll with micron resolution and overlay because conventional roll-based lithography (i.e. flexography) has had no need for this level of precision. Achieving goals of resolution, accuracy, and rate will require coordinated efforts across academe and industry. These advances must progress in parallel with research and development in material systems and device architectures for flexible substrates.

The challenges facing roll-based contact lithography are numerous, but not insurmountable. Rather, these challenges represent a rich research area in the years to come. The work in this thesis aims to lay the foundation for further development of robust roll based μCP through the resulting holistic understanding of stamp contact behavior and examples of deterministic design of machines and processes for its implementation.

Bibliography

[1] S.H. Ahn and L.J. Guo. Large-area roll-to-roll and roll-to-plate nanoimprint lithography: a step toward high-throughput application of continuous nanoimprinting. *ACS Nano*, 3(8):2304–2310, 2009.

[2] D. Armani, C. Liu, and N. Aluru. Re-configurable fluid circuits by pdms elastomer micromachining. In *IEEE International Conference on Micro Electro Mechanical Systems*, pages 222–227, 1999.

[3] Ellen M. Arruda and Mary C. Boyce. A three-dimensional constitutive model for the large stretch behavior of rubber elastic materials. *Journal of the Mechanics and Physics of Solids*, 41(2):389 – 412, 1993.

[4] Paolo Baldesi. *Design and Development of High Precision Five-Axis Positioning System for Roll-to-Roll Multi-Layer Microcontact Printing*. Meng thesis, Massachusetts Institute of Technology, 2009.

[5] Tobias E. Balmer, Heinz Schmid, Richard Stutz, Emmanuel Delamarche, Bruno Michel, Nicholas D. Spencer, and Heiko Wolf. Diffusion of alkanethiols in pdms and its implications on microcontact printing. *Langmuir*, 21(2):622–632, 2005.

[6] R.H. Bentall and K.L. Johnson. An elastic strip in plane rolling contact. *International Journal of Mechanical Sciences*, 10(8):637 – 663, 1968.

[7] H.A. Biebuyck, N.B. Larsen, E. Delamarche, and B. Michel. Lithography beyond light: Microcontact printing with monolayer resists. *IBM Journal of Research and Development*, 41(1):159–170, 1997.

[8] Alexander Bietsch and Bruno Michel. Conformal contact and pattern stability of stamps used for soft lithography. *Journal of Applied Physics*, 88(7):4310, 2000.

[9] T. Burgin, Vi-En Choong, and G. Maracas. Large area submicrometer contact printing using a contact aligner. *Langmuir*, 16(12):5371–5375, 2000.

[10] John Canny. A computational approach to edge detection. *IEEE Transactions on Pattern Analysis and Machine Intelligence*, 8(6):679 –698, 1986.

[11] Manoj K. Chaudhury and George M. Whitesides. Direct measurement of interfacial interactions between semispherical lenses and flat sheets of poly(dimethylsiloxane) and their chemical derivatives. *Langmuir*, 7(5):1013–1025, 1991.

[12] Kyung M Choi and John A Rogers. A photocurable poly(dimethylsiloxane) chemistry designed for soft lithographic molding and printing in the nanometer regime. *Journal of the American Chemical Society*, 125(14):4060–1, 2003.

[13] Stephen Y. Chou, Peter R. Krauss, and Preston J. Renstrom. Imprint of sub-25 nm vias and trenches in polymers. *Applied Physics Letters*, 67(21):3114–3116, 1995.

[14] Stephen Y. Chou, Peter R. Krauss, and Preston J. Renstrom. Imprint lithography with 25-nanometer resolution. *Science*, 272(5258):85–87, 1996.

[15] Raymond Francis Cracauer, Rocky Ganske, M. Cynthia Goh, Jane B. Goh, Adam Brian Liederman, Richard Loo, and Pui Tam. Method and apparatus for micro-contact printing. *US Patent 6,981,445*.

[16] Gregory Philip. Crawford, editor. *Flexible flat panel displays*. John Wiley & Sons, Hoboken, N.J., 2005.

[17] Charudatta Achyut Datar. *Design and Development of High Precision Elastomeric-Stamp Wrapping System for Roll -to-Roll Multi-Layer Microcontact Printing*. Meng thesis, Massachusetts Institute of Technology, 2009.

[18] M.M.J. Decre, R. Schneider, D. Burdinski, J. Schellekens, M. Saalmink, and R. Dona. Wave printing (i): Towards large-area, multilayer microcontact printing. Number 2, pages 59–61, Boston, MA, 2004.

[19] E. Delamarche, Heinz Schmid, Bruno Michel, and H. Biebuyck. Stability of molded polydimethylsiloxane microstructures. *Advanced Materials*, 9(9):741–746, 1997.

[20] Emmanuel Delamarche. Microcontact processing for microtechnology and biology. *CHIMIA International Journal for Chemistry*, 61(4):126–132, 2007.

[21] Emmanuel Delamarche, James Vichiconti, Shawn A. Hall, Matthias Geissler, William Graham, Bruno Michel, and Ronald Nunes. Electroless deposition of cu on glass and patterning with microcontact printing. *Langmuir*, 19(17):6567–6569, 2003.

[22] Tao Deng, Kripa K. Varanasi, Ming Hsu, Nitin Bhate, Chris Keimel, Judith Stein, and Margaret Blohm. Nonwetting of impinging droplets on textured surfaces. *Applied Physics Letters*, 94(13):133109, 2009.

[23] Jingyan Dong, Srinivasa M. Salapaka, and Placid M. Ferreira. Robust control of a parallel- kinematic nanopositioner. *Journal of Dynamic Systems, Measurement, and Control*, 130(4):041007, 2008.

[24] D.S. Dugdale. Yielding of steel sheets containing slits. *Journal of the Mechanics and Physics of Solids*, 8(2):100 – 104, 1960.

[25] Mandy B. Esch, Sahil Kapur, Gizaida Irizarry, and Vincent Genova. Influence of master fabrication techniques on the characteristics of embossed microfluidic channels. *Lab Chip*, 3:121–127, 2003.

[26] Warren W. Flack, David S. Soong, Alexis T. Bell, and Dennis W. Hess. A mathematical model for spin coating of polymer resists. *Journal of Applied Physics*, 56(4):1199–1206, 1984.

[27] Matthias Geissler, Andr Bernard, Alexander Bietsch, Heinz Schmid, Bruno Michel, and Emmanuel Delamarche. Microcontact-printing chemical patterns with flat stamps. *Journal of the American Chemical Society*, 122(26):6303–6304, 2000.

[28] Matthias Geissler, Heinz Schmid, Alexander Bietsch, Bruno Michel, and Emmanuel Delamarche. Defect-tolerant and directional wet-etch systems for using monolayers as resists. *Langmuir*, 18(6):2374–2377, 2002.

[29] Matthias Geissler, Heiko Wolf, Richard Stutz, Emmanuel Delamarche, Ulrich-Walter Grummt, Bruno Michel, and Alexander Bietsch. Fabrication of metal nanowires using microcontact printing. *Langmuir*, 19(15):6301–6311, 2003.

[30] A. N. Gent. A new constitutive relation for rubber. *Rubber Chemistry and Technology*, 69(1):59–61, 1996.

[31] N. J. Glassmaker, A. Jagota, C.-Y. Hui, and J. Kim. Design of biomimetic fibrillar interfaces: 1. making contact. *Journal of The Royal Society Interface*, 1(1):23–33, 2004.

[32] Mikell P. Groover. *Fundamentals of modern manufacturing : materials, processes, and systems*. John Wiley & Sons, New York, 2nd edition, 2002.

[33] G M Guidoni, D Schillo, U Hangen, G Castellanos, E Arzt, RM McMeeking, and R Bennewitz. Discrete contact mechanics of a fibrillar surface with backing layer interactions. *Journal of the Mechanics and Physics of Solids*, 58:1571–1581, 2010.

[34] Jan Haisma, Martin Verheijen, Kees van den Heuvel, and Jan van den Berg. Mold-assisted nanolithography: A process for reliable pattern replication. *The 40th international conference on electron, ion, and photon beam technology and nanofabrication*, 14(6):4124–4128, 1996.

[35] E.B. Hansen and M.A. Kelmanson. Steady, viscous, free-surface flow on a rotating cylinder. *Journal of Fluid Mechanics*, 272:91–107, 1994.

[36] Eugene. Hecht. *Optics*. Addison-Wesley, Reading, Mass., 3rd ed. edition, 1998.

[37] Jo A Helmuth, Heinz Schmid, Richard Stutz, Andreas Stemmer, and Heiko Wolf. High-speed microcontact printing. *Journal of the American Chemical Society*, 128(29):9296–7, July 2006.

[38] David L Henann, Vikas Srivastava, Hayden K Taylor, Melinda R Hale, David E Hardt, and Lallit Anand. Metallic glasses: viable tool materials for the production of surface microstructures in amorphous polymers by micro-hot-embossing. *Journal of Micromechanics and Microengineering*, 19(11):115030, 2009.

[39] H. Hertz. On the contact of elastic solids. *J. reine und angewandte Mathematik*, 92:156–171.

[40] Gareth Hougham, Peter Fryer, and Ronald Nunes. Process of fabricating a precision microcontact printing stamp. *US Patent 6,656,308*.

[41] K J Hsia, Y Huang, E Menard, J.-U. Park, W Zhou, J Rogers, and J M Fulton. Collapse of stamps for soft lithography due to interfacial adhesion. *Applied Physics Letters*, 86:154106, 2005.

[42] Liangbing Hu, Hui Wu, and Yi Cui. Metal nanogrids, nanowires, and nanofibers for transparent electrodes. *MRS Bulletin*, 36(10):760–765, 2011.

[43] R Huang and L Anand. Non-linear mechanical behavior of the elastomer polydimethylsiloxane (pdms) used in the manufacture of microfluidic devices. *Innovation in manufacturing Systems and Technology (IMST)*, 2005.

[44] Shaoming Huang and Albert W. H. Mau. Selective growth of aligned carbon nanotubes on a silver-patterned substrate by the silver mirror reaction. *The Journal of Physical Chemistry B*, 107(15):3455–3458, 2003.

[45] Wilhelm T. S. Huck, Lin Yan, Abe Stroock, Rainer Haag, and George M. Whitesides. Patterned Polymer Multilayers as Etch Resists. *Langmuir*, 15(20):6862–6867, 1999.

[46] C.-Y. Hui, N. J. Glassmaker, T. Tang, and A. Jagota. Design of biomimetic fibrillar interfaces: 2. mechanics of enhanced adhesion. *Journal of The Royal Society Interface*, 1(1):35–48, 2004.

[47] C.Y. Hui, a. Jagota, Y.Y. Lin, and E.J. Kramer. Constraints on Microcontact Printing Imposed by Stamp Deformation. *Langmuir*, 18(4):1394–1407, February 2002.

[48] Anand Jagota, Kenneth G. Sharp, and David F. Kristunas. Stamp deformation during microcontact printing. *MRS Online Proceedings Library*, 728, 2002.

[49] Albert Jeans, Marcia Almanza-Workman, Robert Cobene, Richard Elder, Robert Garcia, Fernando Gomez-Pancorbo, Warren Jackson, Mehrban Jam, Han-Jun Kim, Ohseung Kwon, Hao Luo, John Maltabes, Ping Mei, Craig Perlov, Mark Smith, Carl Taussig, Frank Jeffrey, Steve Braymen, Jason Hauschildt, Kelly Junge, Don Larson, and Dan Stieler. Advances in roll-to-roll imprint lithography for display applications. *Alternative Lithographic Technologies II*, 7637(1):763719, 2010.

[50] Noo Li Jeon, Ralph G. Nuzzo, Younan Xia, Milan Mrksich, and George M. Whitesides. Patterned self-assembled monolayers formed by microcontact printing direct selective metalization by chemical vapor deposition on planar and nonplanar substrates. *Langmuir*, 11(8):3024–3026, 1995.

[51] K. L. Johnson. *Contact Mechanics*. 1985.

[52] KL Johnson, K. Kendall, and AD Roberts. Surface energy and the contact of elastic solids. *Proceedings of the Royal Society of London. Series A, Mathematical and Physical Sciences*, 324(1558):301–313, 1971.

[53] E. Karabut. Two regimes of liquid film flow on a rotating cylinder. *Journal of Applied Mechanics and Technical Physics*, 48:55–64, 2007.

[54] Tobias Kaufmann and Bart Jan Ravoo. Stamps, inks and substrates: polymers in microcontact printing. *Polym. Chem.*, 1:371–387, 2010.

[55] Amar Maruti Kendale. Automation of soft lithographic microcontact printing. Ms thesis, Massachusetts Institute of Technology, 2002.

[56] Kanika Khanna. *Analysis of the Capabilities of Continuous High-Speed Microcontact Printing*. Meng thesis, Massachusetts Institute of Technology, 2008.

[57] W. T. Koiter. An infinite row of collinear cracks in an infinite elastic sheet. *Archive of Applied Mechanics*, 28:168–172, 1959.

[58] Amit Kumar, Hans A. Biebuyck, and George M. Whitesides. Patterning self-assembled monolayers: Applications in materials science. *Langmuir*, 10(5):1498–1511, 1994.

[59] Amit Kumar and George M. Whitesides. Features of gold having micrometer to centimeter dimensions can be formed through a combination of stamping with an elastomeric stamp and an alkanethiol ink followed by chemical etching. *Applied Physics Letters*, 63(14):2002, 1993.

[60] Hee Hyun Lee, Etienne Menard, Nancy G. Tassi, John A. Rogers, and Graciela B. Blanchet. Large area microcontact printing presses for plastic electronics. *MRS Online Proceedings Library*, 846, 2004.

[61] Harry J. Levinson. *Principles of lithography*. SPIE, Bellingham, Wash. (1000 20th St. Bellingham WA 98225-6705 USA, 3rd ed. edition, 2010.

[62] Laurent Libioulle, Alexander Bietsch, Heinz Schmid, Bruno Michel, and Emmanuel Delamarche. Contact-inking stamps for microcontact printing of alkanethiols on gold. *Langmuir*, 15(2):300–304, 1999.

[63] I-Kuan Lin, Yen-Ming Liao, Yan Liu, Kuo-Shen Chen, and Xin Zhang. Elastic and viscoelastic characterization of polydimethylsiloxane (pdms) for cell-mechanics applications. *MRS Online Proceedings Library*, 1052:null–null, 2007.

[64] Ali G. Lopez and Harold G. Craighead. Subwavelength surface-relief gratings fabricated by microcontact printing of self-assembled monolayers. *Appl. Opt.*, 40(13):2068–2075, 2001.

[65] H. Lorenz, M. Despont, N. Fahrnl, N. LaBianca, P. Renaud, and P. Vettiger. Su-8: a low-cost negative resist for mems. volume 7, pages 121 – 4, UK, Sept. 1997.

[66] J Christopher Love, Lara a Estroff, Jennah K Kriebel, Ralph G Nuzzo, and George M Whitesides. Self-assembled monolayers of thiolates on metals as a form of nanotechnology. *Chemical reviews*, 105(4):1103–69, 2005.

[67] James E. Mark, editor. *Polymer data handbook*. Oxford University Press, New York, 1999.

[68] Yasufumi Matsumura, Yasushi Enomoto, Kensuke Akamatsu, and Hidemi Nawafune. Site-selective direct nickel metallization on precursor polyimide using microcontact printing. *Journal of The Surface Finishing Society of Japan*, 60(1):61, 2009.

[69] L. Maurin. Stability of fluid film on the surface of a rotating cylinder. *Journal of Applied Mechanics and Technical Physics*, 9:596–597, 1968.

[70] P Meijers. The contact problem of a rigid cylinder on an elastic layer. *Applied Scientific Research*, 18(1):353–383, 1968.

[71] H.K. Moffatt. Behaviour of a viscous film on the outer surface of a rotating cylinder. *Journal de Mecanique*, 16(5):651 – 673, 1977.

[72] Gordon Moore. Cramming more components onto integrated circuits. *Electronics*, 38(8), 1965.

[73] N. I. Muskhelishvili. *Some basic problems of the mathematical theory of elasticity: fundamental equations, plane theory of elasticity, torsion, and bending.* P. Noordhoff, Groningen, 1953.

[74] W L Noderer, L Shen, S Vajpayee, N J Glassmaker, A Jagota, and C Hui. Enhanced adhesion and compliance of film-terminated fibrillar surfaces Enhanced adhesion and compliance of. *Prooceedings of the Royal Society A*, 463:2631–2654, 2007.

[75] Ralph G. Nuzzo. The future of electronics manufacturing is revealed in the fine print. *Proceedings of the National Academy of Sciences*, 98(9):4827–4829, 2001.

[76] W. Shannan OShaughnessy, Sal Baxamusa, and Karen K. Gleason. Additively patterned polymer thin films by photo-initiated chemical vapor deposition (picvd). *Chemistry of Materials*, 19(24):5836–5838, 2007.

[77] Nobuyuki Otsu. A threshold selection method from gray-level histograms. *Systems, Man and Cybernetics, IEEE Transactions on*, 9(1):62–66, 1979.

[78] Robert M Panas, Michael A Cullinan, and Martin L Culpepper. Design of piezoresistive-based MEMS sensor systems for precision microsystems. *Precision Engineering*, 36(1):44–54, 2012.

[79] R. Parashkov, E. Becker, T. Riedl, H.-H. Johannes, and W. Kowalsky. Large area electronics using printing methods. *Proceedings of the IEEE*, 93(7):1321 –1329, 2005.

[80] Tae Hyun Park, Young Min Kim, Young Wook Park, Jin Hwan Choi, Jin-Wook Jeong, Kyung Cheol Choi, and Byeong-Kwon Ju. Self-assembled microarray of organic light-emitting diodes using a self-assembled monolayer by microcontact printing. *Applied Physics Letters*, 95(11):113310, 2009.

[81] András Perl, David N. Reinhoudt, and Jurriaan Huskens. Microcontact Printing: Limitations and Achievements. *Advanced Materials*, 21(22):2257–2268, 2009.

[82] Carlos Pina-Hernandez, Jin-sung Kim, L Jay Guo, and Peng-fei Fu. High-Throughput and Etch-Selective Nanoimprinting and Stamping Based on Fast-Thermal-Curing Poly(dimethylsiloxane)s. *Advanced Materials*, 19:1222–1227, 2007.

[83] Luigi Preziosi and Daniel D. Joseph. The run-off condition for coating and rimming flows. *Journal of Fluid Mechanics*, 187:99–113, 1988.

[84] Arjan P Quist, Elisabeth Pavlovic, and Sven Oscarsson. Recent advances in microcontact printing. *Analytical and bioanalytical chemistry*, 381(3):591–600, 2005.

[85] R. S. Rivlin. Large elastic deformations of isotropic materials. iv. further developments of the general theory. *Philosophical Transactions of the Royal Society of London. Series A, Mathematical and Physical Sciences*, 241(835):379–397, 1948.

[86] Pere Roca-Cusachs, Félix Rico, Elena Martínez, Jordi Toset, Ramon Farré, and Daniel Navajas. Stability of microfabricated high aspect ratio structures in poly(dimethylsiloxane). *Langmuir : the ACS journal of surfaces and colloids*, 21(12):5542–8, 2005.

[87] John A. Rogers, Zhenan Bao, Anita Makhija, and Paul Braun. Printing Process Suitable for Reel-to-Reel Production of High-Performance Organic Transistors and Circuits. *Advanced Materials*, 11(9):741–745, 1999.

[88] P. Ruchhoeft, M. Colburn, B. Choi, H. Nounu, S. Johnson, T. Bailey, S. Damle, M. Stewart, J. Ekerdt, S. V. Sreenivasan, J. C. Wolfe, and C. G. Willson. Patterning curved surfaces: Template generation by ion beam proximity lithography and relief transfer by step and flash imprint lithography. *Papers from the 43rd international conference on electron, ion, and photon beam technology and nanofabrication*, 17(6):2965–2969, 1999.

[89] H Schmid and B Michel. Siloxane Polymers for High-Resolution , High-Accuracy Soft Lithography. *Macromolecules*, 33:3042–3049, 2000.

[90] Theo E. Schouten and Egon L. van den Broek. Inverse perspective transformation for video surveillance. *Computational Imaging VI*, 6814(1):681415, 2008.

[91] Kenneth G Sharp, Gregory S Blackman, Nicholas J Glassmaker, Anand Jagota, and Chung-Yuen Hui. Effect of stamp deformation on the quality of microcontact printing: theory and experiment. *Langmuir : the ACS journal of surfaces and colloids*, 20(15):6430–8, July 2004.

[92] Xiao Shen. *Design and Analysis of High-Speed Continuous Micro-Contact Printing.* Meng thesis, Massachusetts Institute of Technology, 2008.

[93] Joseph Edward Shigley. *Mechanical engineering design.* McGraw-Hill, New York, 1963.

[94] Kenneth R. Shull, Dongchan Ahn, Wan-Lin Chen, Cynthia M. Flanigan, and Alfred J. Crosby. Axisymmetric adhesion tests of soft materials. *Macromolecular Chemistry and Physics*, 199(4):489–511, 1998.

[95] Kenneth M Sobel, Wangling Yu, Jean E Piou, James R Cloutier, and Robert Wilson. Robust eigenstructure assignment with structured state-space uncertainty and unmodelled dynamics. *International Journal of Systems Science*, 23(5):765–788, 1992.

[96] Adam Stagnaro. *Design and development of a roll-to-roll machine for continuous high-speed microcontact printing.* Meng thesis, Massachusetts Institute of Technology, 2008.

[97] Pradeep Subrahmanyan and David L. Trumper. Eigenvector Assignment. *Proceedings Of The American Control Conference*, pages 2238–2243, 1999.

[98] S. P. Timoshenko. *Theory of Elasticity.* McGraw-Hill, 1951.

[99] Arthur A. Tracton, editor. *Coatings technology handbook.* Taylor & Francis, 3rd edition, 2005.

[100] David Trimbach, Kirill Feldman, Nicholas D. Spencer, Dirk J. Broer, and Cees W. M. Bastiaansen. Block copolymer thermoplastic elastomers for microcontact printing. *Langmuir*, 19(26):10957–10961, 2003.

[101] R. v. Mises. On Saint Venant's principle. *Bull. Amer. Math. Soc.*, 51:555–562, 1945.

[102] B A White. Eigenstructure assignment: a survey. *Journal of Systems and Control Engineering*, 209:1–11, 1995.

[103] Eehern J. Wong. *Modeling and control of rapid cure in polydimethylsiloxane (PDMS) for microfluidic device applications.* Phd thesis, 2010.

[104] S-F Wu, W Wei, and M J Grimble. Robust MIMO control-system design using eigenstructure assignment and QFT. *Control Theory and Applications*, 151(2):198–209, 2004.

[105] Y. Xia, D. Qin, and G.M. Whitesides. Microcontact printing with a cylindrical rolling stamp: A practical step toward automatic manufacturing of patterns with submicrometer-sized features. *Advanced Materials*, 8(12):1015–1017, 1996.

[106] Y. Xia and George M. Whitesides. Soft Lithography. *Angewandte Chemie International Edition*, 37(5):550–575, August 1998.

[107] Wenzhuo Yang. *Design and Manufacturing of High Precision Roll-to-Roll Multilayer Printing Machine- Measurement and Experiment.* Meng thesis, Massachusetts Institute of Technology, 2009.

[108] Zhao Yapu. Stiction and anti-stiction in mems and nems. *Acta Mechanica Sinica*, 19:1–10, 2003.

[109] O.H. Yeoh. Some forms of the strain energy function for rubber. *Rubber Chemistry and Technology*, 66(5):754 – 771, 1993.

[110] S. S. Yoon, D. O. Kim, S. C. Park, Y. K. Lee, H. Y. Chae, S. B. Jung, and J. D. Nam. Direct metallization of gold patterns on polyimide substrate by microcontact printing and selective surface modification. *Microelectron. Eng.*, 85(1):136–142, January 2008.

[111] John A. Rogers Zhenan Bao, Anita Makhjita. High-resolution method for patterning a substrate with micro-printing. *US Patent 6,736,985*.

[112] W. Zhou, Y. Huang, E. Menard, N. R. Aluru, J. A. Rogers, and A. G. Alleyne. Mechanism for stamp collapse in soft lithography. *Applied Physics Letters*, 87(25):251925, 2005.